The internal magnetic field of the n2EDM experiment to probe CP symmetry : calculation of the magic field and control of non-uniformities

Thomas Bouillaud

THÈSE

Pour obtenir le grade de

DOCTEUR DE L'UNIVERSITÉ GRENOBLE ALPES

École doctorale : PHYS - Physique
Spécialité : Physique Subatomique et Astroparticules
Unité de recherche : Laboratoire de Physique Subatomique et Cosmologie

Le champ magnétique interne de l'expérience n2EDM pour sonder la symétrie CP : calcul du champ magique et maîtrise des non-uniformités

The internal magnetic field of the n2EDM experiment to probe CP symmetry: calculation of the magic field and control of non-uniformities

Présentée par :

Thomas BOUILLAUD

Direction de thèse :

Guillaume PIGNOL — Directeur de thèse
MAITRE DE CONFERENCES HDR, UNIVERSITE GRENOBLE ALPES

Rapporteurs :

GILLES BAN
PROFESSEUR DES UNIVERSITES, ENSI CAEN
CRISTINA CARLOGANU
DIRECTRICE DE RECHERCHE, CNRS DELEGATION RHONE AUVERGNE

Thèse soutenue publiquement le **20 novembre 2023**, devant le jury composé de :

LAURENT DEROME, PROFESSEUR DES UNIVERSITES, UNIVERSITE GRENOBLE ALPES	Président
GILLES BAN, PROFESSEUR DES UNIVERSITES, ENSI CAEN	Rapporteur
CRISTINA CARLOGANU, DIRECTRICE DE RECHERCHE, CNRS DELEGATION RHONE AUVERGNE	Rapporteure
ISABELLE RIPP-BAUDOT, DIRECTRICE DE RECHERCHE, CNRS DELEGATION ALSACE	Examinatrice
MATHIEU GUIGUE, MAITRE DE CONFERENCES, SORBONNE UNIVERSITE	Examinateur

Abstract

Electric Dipole Moments (EDMs) in spin 1/2 particles such as the neutron are highly sensitive probes for Charge-Parity (CP) violation Beyond the Standard Model (BSM), one of the requirements needed to fully explain the Baryon Asymmetry of the Universe (BAU). The n2EDM experiment, currently in the commissioning phase at the Paul Scherrer Institute in Switzerland, constitutes a leading effort to search for the neutron EDM. It relies on the principle of submitting spin-polarized Ultra-Cold Neutrons (UCNs) to parallel electric and magnetic fields and measuring their precession frequency. This experiment hopes to achieve a record sensitivity $\Delta d_n \leq 10^{-27}\, e\,\mathrm{cm}$, a goal which can only be reached by tackling statistical and systematical uncertainties affecting the measurement. The work we present here contributes to the control of systematic errors generated by non-uniform magnetic fields, through the calculation of a systematic effect and the precise characterization of the internal magnetic environment.

The first part of this thesis motivates and introduces the n2EDM experiment, particularly the theme of magnetic field uniformity. We begin with a review of the theoretical grounds on which EDM experiments stand, which are prompted by cosmological observations that *CP*-violating interactions must exist in nature, and by the inability of the Standard Model (SM) of particle physics to provide enough of these. We then present the n2EDM experiment, which relies at its core on the Ramsey method of separated rotating magnetic fields to determine the spin-precession frequency of UCNs. We finally give the stringent uniformity requirements that the internal magnetic environment of n2EDM must satisfy, and justify the existence of non-uniform contributions by studying the symmetries of the generated field.

The second part focuses on the so-called false EDM, a dire systematic effect in n2EDM arising from the unfortunate combination of a relativistic motional field and random non-uniformities. We first propose a new frequency-domain derivation of the false EDM *via* the Wiener-Khinchin theorem, before expanding on a recent approach to cancel this effect by tuning the coil-generated field to a "magic value". We conclude through our alternative calculation of the magic field, and its extension to dipole-like magnetic contaminations, that it is possible to suppress the total false EDM by at least one order of magnitude by setting the magnetic field to a value of $10.5\,\mu\mathrm{T}$.

The third part relies on magnetic field mapping to estimate and correct non-uniformities responsible for undesirable effects such as the false EDM. After establishing the accuracy of the mapping apparatus and taming unruly residual field patterns, we show through an analysis of the mapping data that the n2EDM magnetic environment fully satisfies the experiment's statistical and systematical requirements. We finally propose and apply a field optimization strategy to suppress residual non-uniformities even further. The optimized field generates a negligible false EDM and boasts an unprecedented level of uniformity, with a root mean square deviation on the vertical field component $\sigma(B_z) = 35\,\mathrm{pT}$ over the neutron's precession volume.

Résumé

Les Moments Dipolaires Électriques (EDMs) de particules de spin 1/2 telles que le neutron constituent des sondes privilégiées de violation Charge-Parité (CP) au-delà du Modèle Standard, l'une des conditions requises pour expliquer l'asymétrie baryonique de l'Univers. L'expérience n2EDM, actuellement en cours d'assemblage au Paul Scherrer Institute en Suisse, est un des efforts majeurs de recherche de l'EDM du neutron. Celle-ci consiste à soumettre des Neutrons Ultra-Froids (UCNs) polarisés à des champs magnétiques et électriques appliqués parallèlement et de mesurer leur fréquence de précession. Cette expérience a pour objectif d'atteindre une sensibilité inégalée $\Delta d_n \leq 10^{-27}\, e\,\mathrm{cm}$, à condition de satisfaire des exigences très strictes en matière de maîtrise des erreurs statistiques et systématiques. Le travail présenté dans ce manuscrit s'articule autour du contrôle d'effets systématiques induits par les non-uniformités du champ magnétique, à travers à la fois le calcul d'un de ces effets et la caractérisation du milieu magnétique de l'expérience.

La première partie de cette thèse justifie et présente n2EDM, en s'arrêtant sur le thème de l'uniformité magnétique de l'expérience. Nous commençons par rappeler les fondements théoriques sur lesquels reposent les recherches d'EDMs, qui découlent d'observations cosmologiques selon lesquelles les interactions violant CP doivent exister dans la nature et de l'incapacité du Modèle Standard (MS) à en fournir suffisamment. Nous présentons ensuite l'expérience n2EDM, en particulier la méthode de Ramsey sur laquelle celle-ci s'appuie pour déterminer la fréquence de précession des UCNs. Ceci nous permet enfin de détailler les exigences strictes d'uniformité que le champ magnétique interne doit satisfaire, ainsi que de justifier l'existence de contributions non uniformes en étudiant les symétries du champ généré.

La deuxième partie est axée autour du faux EDM, un effet systématique inquiétant pour n2EDM qui naît de la combinaison d'un champ magnétique relativiste et de non-uniformités aléatoires. Nous proposons d'abord une nouvelle expression du faux EDM dans le domaine fréquentiel *via* le théorème de Wiener-Khinchin, avant de l'étendre à une approche récente permettant d'annuler cet effet en ajustant le champ magnétique à une valeur dite "magique". Nous concluons grâce à notre calcul alternatif du champ magique et à son extension aux champs générés par des dipôles magnétiques qu'il est possible de supprimer le faux EDM d'au moins un ordre de grandeur en choisissant un champ magnétique de 10.5 µT.

La troisième partie s'appuie sur une cartographie du champ magnétique pour estimer et corriger les non-uniformités à l'origine d'effets indésirables tels que le faux EDM. Après avoir établi l'exactitude de l'instrument de cartographie et maitrisé les variations du champ résiduel, nous montrons à travers l'analyse des données de cartographie que l'environnement magnétique de n2EDM satisfait pleinement aux exigences statistiques et systématiques de l'expérience. Enfin, nous proposons et appliquons une stratégie d'optimisation du champ afin de réduire davantage les non-uniformités résiduelles. Notre champ optimisé génère un faux EDM négligeable et présente un niveau d'uniformité sans précédent, avec un écart quadratique moyen sur la composante verticale $\sigma(B_z) = 35\,\mathrm{pT}$ au sein du volume de précession.

Remerciements

Ce n'est pas par convention mais par sincère gratitude que je tiens à remercier en premier lieu Guillaume, mon directeur de thèse. Malgré tes nombreux engagements tu t'es toujours rendu disponible pour de longues discussions en face du tableau blanc, ou plus exotiquement sur un support papier de fortune lors du vol retour d'une réunion de collaboration.

Je tiens à remercier Stéphanie, Dominique, et Benoît. Je n'ai pas été souvent présent dans les locaux que nous avons partagés pendant trois années mais, au-delà de vos qualités de physiciens, vous m'avez marqué par votre humanité et votre dévouement à l'enseignement. Thank you Kseniia for bearing with me on our recurring trips and late night shifts at PSI. We made a pretty great team.

I would like to sincerely thank the n2EDM PSI team, which obviously made a huge part of this work possible. Thank you Georg, Michi, Bernhard, Philipp, Dieter, and Efrain for your guidance, expertise, and tireless on-site efforts. Thank you Klaus for your continued support.

Je te remercie Mathieu pour la relecture la plus consciencieuse qu'un doctorant puisse espérer et qui a certainement amélioré la qualité de ce manuscrit. Merci Gilles pour ta présence, scientifique et humaine.

Merci à mes parents, mes deux sœurs, mon Opa et ma Oma, ma Tatie, d'être là. Merci à mes amis, qui se reconnaîtront, de donner raison à ma procrastination. Et merci aux pompiers de la caserne de Grenoble pour m'avoir appris plus qu'un doctorat en physique des particules.

Alice, merci pour ton soutien indéfectible à travers les épreuves de la vie. Sans toi il est évident que je n'aurais pas pu rendre ce manuscrit.

Contents

PART I

The neutron EDM in the scope of new physics

Chapter 1

The motivation behind the search for EDMs

Contents

Electric Dipole Moments (EDMs) of elementary particles are uniquely appealing to physicists in that they constitute one of the most sensitive probes to new physics at the high precision frontier. The goal of this first chapter is to provide some insight on why this is the case in order to motivate EDM experiments, and in particular those concerned with the neutron EDM. We will begin with the non-relativistic picture of a fermion EDM (section 1.1), which will serve as a gradual introduction to both the concept of an EDM and to discrete symmetries of Charge conjugation (C) and Parity (P), before giving a brief summary of the cosmological grounds behind the search of physical processes that violate both C and P symmetries (section 1.2). We will then introduce the concepts that allow for the more appropriate, relativistic description of EDMs in the scope of the Standard Model of particle physics. First we will recall the definitions of discrete symmetries of quantum fields, give a brief overview of where CP violation occurs within the Standard Model, and finally attempt to reach the neutron EDM as a CP violating process beyond the Standard Model (section 1.3).

1.1 A first insight into the Electric Dipole Moment

In the classical sense, an electric dipole moment (EDM) is a physical quantity that describes the distribution of electrical charges within a system. Consider for instance two opposite charges $+q$ and $-q$ in space, and let $\mathbf{d}$ be the vector pointing from the negative to the positive one. The electric dipole moment is then defined as $q\mathbf{d}$. Any electric field $\mathbf{E}$ applied to this system will generate a torque $\tau = q\mathbf{d} \times \mathbf{E}$. The potential energy U of the system is then given by the work of this torque. Taking the origin of the potential energy for perpendicular $q\mathbf{d}$ and $\mathbf{E}$, we write it as:

$$U = -q\mathbf{d} \cdot \mathbf{E}. \tag{1.1}$$

If we consider instead of these two opposite charges a fundamental particle, more specifically a spin 1/2 particle, with a certain charge distribution, the story is a little different but fundamentally equivalent. In the quantum mechanical perspective, we replace the potential energy by an operator H that describes the interaction between the spin of the particle, given by the Pauli vector $\boldsymbol{\sigma} \equiv (\sigma_x, \sigma_y, \sigma_z)$, and the electric field:

$$H = -d\boldsymbol{\sigma} \cdot \mathbf{E}. \tag{1.2}$$

The dipole moment d is then the coupling constant between the spin and the electric field. One may notice a strong similarity between this Hamiltonian and another describing a much more familiar two-level system, which is the interaction between a spin 1/2 particle's spin and a magnetic field $\mathbf{B}$, coupled in this case by the magnetic moment μ:

$$H = -\mu\boldsymbol{\sigma} \cdot \mathbf{B}. \tag{1.3}$$

To gain some insight on the physical phenomenon, consider a simplified configuration where $\mathbf{B} = (0, 0, B_0)$, and let $\omega = (2\mu/\hbar) \times B_0$. Then $H = -\hbar\omega\sigma_z/2$ is diagonal in the basis of the σ_z operator, which is simply the up and down spin states $|+\rangle$ and $|-\rangle$. Both are then eigenstates of H with associated eigenvalues $E_+ = -\hbar\omega/2$ and $E_- = +\hbar\omega/2$. The spin dynamics are determined by the Schrödinger equation $i\hbar\left(d\left|\Psi(t)\right\rangle/dt\right) = H\left|\Psi(t)\right\rangle$, where the state of the system $|\Psi(t)\rangle$ is some time-dependent combination of both spin states $|\Psi(t)\rangle = c_+(t)\,|+\rangle + c_-(t)\,|-\rangle$. If we enforce the non-stationary initial condition $|\Psi(0)\rangle = (|+\rangle + |-\rangle)/\sqrt{2}$, we see that the wave function describes an oscillation between the two spin states at frequency ω:

$$|\Psi(t)\rangle = \frac{1}{\sqrt{2}}\left(e^{i\omega t/2}\,|+\rangle + e^{-i\omega t/2}\,|-\rangle\right). \tag{1.4}$$

The motion of the spin itself is given by the observable $\mathbf{S} = \hbar\boldsymbol{\sigma}/2$, measured in the system's state:

$$\langle\Psi(t)|\,\mathbf{S}\,|\Psi(t)\rangle = \frac{\hbar}{2}\begin{pmatrix}\langle\Psi(t)|\,\sigma_x\,|\Psi(t)\rangle\\ \langle\Psi(t)|\,\sigma_y\,|\Psi(t)\rangle\\ \langle\Psi(t)|\,\sigma_z\,|\Psi(t)\rangle\end{pmatrix} \tag{1.5}$$

$$= \frac{\hbar}{2}\begin{pmatrix}\cos(\omega t)\\ \sin(\omega t)\\ 0\end{pmatrix}, \tag{1.6}$$

which corresponds to a precession of the particle's spin around the vertical axis at an angular frequency ω.

Coming back to the analogous EDM Hamiltonian (1.2), we see that if a coupling such as the EDM exists for a spin 1/2 particle, it should have an effect equivalent to that of the magnetic moment. The applied electric field would produce a precession of the particle's spin around the field's axis, with a frequency proportional this time to the coupling d and the electric field's strength E_0. The drawings on the left-hand side of figure 1.1 depict this precession motion for magnetic and electric couplings.

There is however one fundamental distinction between the two couplings, whose significance to particle physics will become clear in the next section. If we so to speak "play" both processes backwards in time, the magnetic coupling will remain identical to its forward time process but the electric coupling will be opposite. In other words, the electric coupling violates time reversal symmetry T while the magnetic coupling conserves it. By the CPT theorem the neutron EDM interaction then violates CP symmetry. This can be understood by considering a rudimentary version

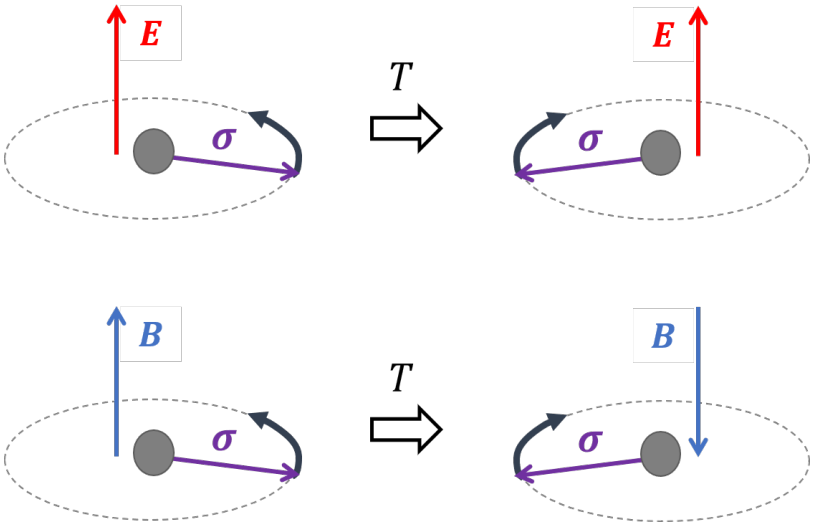

FIGURE 1.1: The topmost figure shows the action of time reversal symmetry T on the coupling of a spin 1/2 particle's spin σ with an electric field $\mathbf{E}$. This process is T-odd. The bottom-most figure shows the same transformation for the equivalent system involving a magnetic field $\mathbf{B}$. This process is T-even.

of the charge conjugation C, parity P, and T transformations, wherein C reverses the sign of charges, effectively exchanging particles and antiparticles, P reverses the sign of a position vector, and T reverses time:

$$C : e^+ \longrightarrow e^-, \tag{1.7}$$
$$P : \mathbf{r} \longrightarrow -\mathbf{r}, \tag{1.8}$$
$$T : t \longrightarrow -t. \tag{1.9}$$

It is clear that for both the magnetic and the electric couplings, the precession motion described by (1.6) is reversed in time. In addition, time reversal somehow acts on the magnetic and electric fields by reversing the motion of charges. This has the effect of reversing the direction of the magnetic field but preserving the direction of the electric field. So overall T is violated only for the electric coupling, as figure 1.1 demonstrates. Also note that only the electric coupling violates parity. This can be intuited by writing $\mathbf{E} = \boldsymbol{\nabla}\varphi + \partial\mathbf{A}/\partial t$ and $\mathbf{B} = \boldsymbol{\nabla} \times \mathbf{A}$ and noticing that the vector potential $\mathbf{A}$ and the spatial derivative $\boldsymbol{\nabla}$ are P-odd. By the CPT theorem C is then conserved for both couplings.

As we will now try to show, the fact that the interaction describing the neutron EDM violates CP symmetry is what motivates its search.

1.2 A cosmological motivation

When confronted with cosmological observations, the Standard Model of particle physics faces one question it pains to answer: why does the universe evidently contain more matter than antimatter? This fundamental discrepancy between the observed number density of baryons n_B and anti-baryons $n_{\overline{B}}$ is referred to as the

Baryon Asymmetry in the Universe (BAU), and is characterized by the ratio

$$\eta = \frac{n_B - n_{\overline{B}}}{n_\gamma}, \tag{1.10}$$

where n_γ is the number density of photons. Evidence of this asymmetry is glaring as it comes from two independent sources. The first is the abundance of certain atoms that allow a measurement of η via Big Bang nucleosynthesis. The second is given to us by more recent observations of the cosmic microwave background by the Planck collaboration. Both agree on a value of $\eta = 6.10 \times 10^{-10}$ (Aghanim et al., 2020).

Through a series of articles published starting in 1967, Andrei Sakharov proposed a set of three conditions for baryon asymmetry (Sakharov, 1967):

1. Baryon number violation.
2. Departure from thermal equilibrium.
3. C and CP violation.

The first condition is perhaps the most obvious, as there must have been some mechanism in the primordial universe allowing the creation of baryons or annihilation of anti-baryons. In the Standard Model, baryon number violation is allowed through the sphaleron process, which converts baryons to anti-leptons and vice versa, effectively transferring baryon number B to lepton number L while conserving $B - L$. The most recent theoretical framework for this process is known as electroweak baryogenesis (Morrissey and Ramsey-Musolf, 2012).

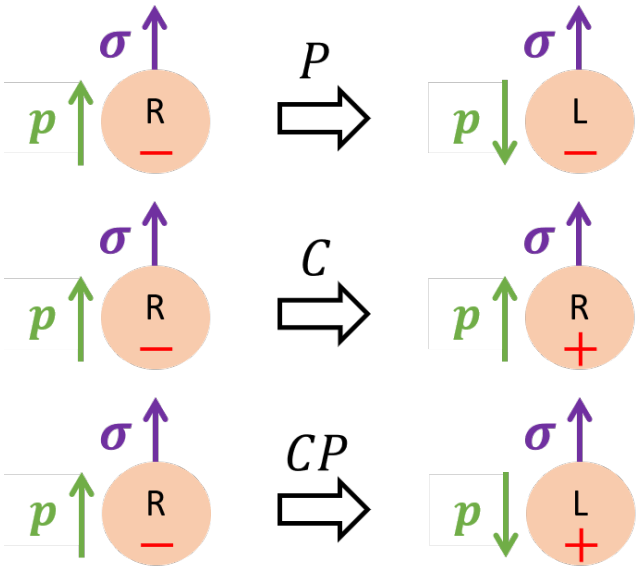

FIGURE 1.2: Schematic representation of parity P and charge conjugation C symmetries on a chiral charged particle. P reverses momentum and chirality, while C reverses charge.

The second condition can be understood by considering a baryon creation process $X \to Y + B$, where X and Y have a zero baryon number, and B represents the number of produced baryons. Thermal equilibrium implies that the rate of change of this process equals the rate of change of the inverse process, meaning

$$\Gamma(X \to Y + B) = \Gamma(Y + B \to X). \tag{1.11}$$

If this is true then the created baryons B (or anti-baryons $\overline{B}$) would at some point annihilate again. Therefore departure from thermal equilibrium is necessary in order for there to be baryon asymmetry.

The final condition is not as straightforward but coincidentally is the one we are most interested in. Before we investigate it let us consider again the preliminary definitions of C and P symmetries (1.7) and (1.8). In the case of a spin $1/2$ particle, its momentum $\mathbf{p}$ is P-odd just like its position vector. Its spin however is not affected by parity, consequently P reverses the projection of the momentum on the spin $\mathbf{p} \cdot \boldsymbol{\sigma}$, that is, parity reverses *chirality*. Since charge conjugation C refers to the conversion of particles and antiparticles, CP then exchanges left handed particles with right handed antiparticles and vice versa. This pivotal fact will be discussed further when we generalize the transformations (1.7), (1.8), and (1.9) to quantum fields. A visual summary of these properties of C and P is shown in figure 1.2.

Coming back to the third Sakharov condition, we consider again the process $X \to Y + B$ as well as its charge conjugate $\overline{X} \to \overline{Y} + \overline{B}$. We can then think of the baryon production rate dB/dt as some quantity proportional to the difference between the process that creates baryon and the process that creates anti-baryons:

$$\frac{dB}{dt} \propto \Gamma(X \to Y + B) - \Gamma(\overline{X} \to \overline{Y} + \overline{B}). \tag{1.12}$$

Clearly if C is violated then this rate is non-zero. However in a more complete picture where we decompose the final state into quarks of both left (q_L) and right (q_R) chirality, the rate would look more like this:

$$\frac{dB}{dt} \propto \left[\Gamma(X \to q_L q_L) + \Gamma(X \to q_R q_R)\right] - \left[\Gamma(\overline{X} \to \overline{q}_L \overline{q}_L) + \Gamma(\overline{X} \to \overline{q}_R \overline{q}_R)\right]. \tag{1.13}$$

Since CP swaps particles of one chirality with antiparticles of the other, we now need CP violation on top of C violation in order for the baryon production rate to be non-zero. This constitutes the last of Sakharov's conditions for baryogenesis. For a much more thorough review of the Sakharov conditions, refer to James M. Cline's lectures (Cline, 2007).

In order to show how we can fulfill this last condition, we will now see in more detail how the C and P symmetries are implemented and where CP violation arises in the Standard Model. Before doing so, we can point out that predictions based on one of these CP violation sources, the so-called δ phase of the CKM matrix, give a baryon asymmetry of the order of 10^{-26}, which evidently fails to account for all of the observed quantity by a huge margin (Huet and Sather, 1995). This is why beyond the Standard Model CP-violating processes such as the potential neutron EDM are so coveted.

1.3 From CP violation to the neutron EDM

During this section, we will write the 4*-vector as* $x = (t, \mathbf{r})$*. The gamma matrices* γ^μ *will be expressed in the Weyl representation. We then use the notation* $\overline{\psi} = \psi\gamma^0$ *for Lorentz invariance of the bilinear fermion field* $\overline{\psi}\psi$*.*

1.3.1 CP symmetry of quantum fields

The interest of particle physicists for the neutron EDM lies in its CP-violating nature. However our preliminary definition of CP symmetry (1.7) and (1.8) does not explicitly describe the action of parity on chirality and of charge conjugation on particle and antiparticle exchange. In order to do this we need to recall briefly the transformation properties of C and P on scalar, fermionic, and spin-1 vector fields.

Scalar fields:
The spin-0 scalar field

$$\phi(x) = \int \frac{d^3p}{(2\pi^3)\sqrt{2E_p}} \left[a(p)e^{-ipx} + b^\dagger(p)e^{ipx}\right], \tag{1.14}$$

$$\phi^\dagger(x) = \int \frac{d^3p}{(2\pi^3)\sqrt{2E_p}} \left[b(p)e^{-ipx} + a^\dagger(p)e^{ipx}\right], \tag{1.15}$$

makes obvious its function of creating and annihilating particles and antiparticles through its operators $a(p)^\dagger, a(p)$ (creates/annihilates particle with 4-momentum p) and $b(p)^\dagger, b(p)$ (creates/annihilates antiparticle with 4-momentum p). Accordingly, we define charge conjugation as the transformation that swaps particles and antiparticles:

$$Ca(p)C^{-1} = b(p), \qquad Cb(p)C^{-1} = a(p), \tag{1.16}$$

and parity as one that reverses momentum and multiplies the field by a phase $\eta = \pm 1$:

$$Pa(p,s)P^{-1} = \eta a(-p,s), \qquad Pb(p,s)P^{-1} = \eta b(-p,s). \tag{1.17}$$

Applying these transformations to the scalar fields themselves, we see that, effectively, parity simply reverses the spatial part of the position vector, while charge conjugation acts as complex conjugation:

$$P : \phi(t,\mathbf{r}) \longrightarrow P\phi(t,\mathbf{r})P^{-1} = \eta\phi(t,-\mathbf{r}), \tag{1.18}$$

$$C : \phi(t,\mathbf{r}) \longrightarrow C\phi(t,\mathbf{r})C^{-1} = \phi^\dagger(t,\mathbf{r}), \tag{1.19}$$

Since applying either P or C twice reverts the field to its initial state, note that both operators are Hermitian and unitary ($P^2 = 1 \Rightarrow P^\dagger = P^{-1} = P$).

Spin-$1/2$ fields:
The next step is to extend this definition to solutions of the Dirac equation, which are not scalars but spinors and thus add chirality to the scalar field. The fermionic fields are expanded on a basis of 4-vectors $u(p,s)$ and $v(p,s)$, whose top two components describe the state of the left-handed particle and the bottom two of the right-handed particle, with momentum p and spin state s:

$$\psi(x) = \int \frac{d^3p}{(2\pi^3)\sqrt{2E_p}} \sum_{s=\pm} \left[a(p,s)u(p,s)e^{-ipx} + b^\dagger(p,s)v(p,s)e^{ipx}\right], \tag{1.20}$$

$$\psi^\dagger(x) = \int \frac{d^3p}{(2\pi^3)\sqrt{2E_p}} \sum_{s=\pm} \left[b(p,s)u(p,s)e^{-ipx} + a^\dagger(p,s)v(p,s)e^{ipx}\right], \tag{1.21}$$

Transforming the creation and annihilation operators equivalently to the scalar field, we can show that parity and charge conjugation act on the fermionic field as follows:

$$P : \psi(t,\mathbf{r}) \longrightarrow P\psi P^{-1}(t,\mathbf{r}) = \gamma^0\psi(t,-\mathbf{r}), \tag{1.22}$$

$$C : \psi(t,\mathbf{r}) \longrightarrow C\psi C^{-1}(t,\mathbf{r}) = -i\left(\overline{\psi}\gamma^0\gamma^2\right)^T(t,\mathbf{r}), \tag{1.23}$$

with the transformations on $\overline{\psi}$ being deducible from the above. As mentioned earlier, parity indeed exchanges left-handed with right handed particles, through the γ^0 matrix, on top of flipping the spatial vector's sign. Charge conjugation also mixes chirality as it exchanges left-handed and right-handed spinors with each other's complex conjugates (to a $\pm\sigma^2$ factor). In combination, CP thus exchanges a right-handed particle with a left-handed antiparticle.

As a first application, consider a Yukawa coupling $g\overline{\psi}\phi\psi$, where ϕ is a scalar field and g a coupling constant. Using the definitions of C and P above we can show that that the bilinear $\overline{\psi}\psi$ is CP-invariant (first column of table 1.1), and that

$$CP : g\overline{\psi}\phi\psi \longrightarrow g\overline{\psi}\phi^\dagger\psi. \tag{1.24}$$

Therefore wherever couplings of the form $g\overline{\psi}\phi\psi + g^*\overline{\psi}\phi^\dagger\psi$ arise, in order for CP symmetry to be conserved the coupling constant g should be real.

Spin-1 vector fields:
For spin-1 vector fields, parity acts on the spatial and time components in an opposite fashion, while charge conjugation does not discriminate between indices. By convention we write:

$$P : V^\mu(t,\mathbf{r}) \longrightarrow PV^\mu P^{-1}(t,\mathbf{r}) = \begin{cases} V^\mu(t,-\mathbf{r}) & \text{if } \mu = 0 \\ -V^\mu(t,-\mathbf{r}) & \text{if } \mu = 1,2,3 \end{cases} \tag{1.25}$$

$$C : V^\mu(t,\mathbf{r}) \longrightarrow CV^\mu C^{-1}(t,\mathbf{r}) = -V^\mu(t,\mathbf{r}) \tag{1.26}$$

We can use all the transformation rules above to compute C and P transformations of some useful field bilinears. The results are summarized in table 1.1.

	$\overline{\psi}\psi$	$\overline{\psi}\gamma^\mu\psi$	$\overline{\psi}\gamma^5\psi$	$\overline{\psi}\gamma^\mu\gamma^5\psi$	$\overline{\psi}\sigma^{\mu\nu}\psi$	$\overline{\psi}\sigma^{\mu\nu}\gamma^5\psi$	V^μ	∂^μ	$F^{\mu\nu}$
P	1	$(-1)^\mu$	-1	$-(-1)^\mu$	$(-1)^\mu(-1)^\nu$	$-(-1)^\mu(-1)^\nu$	$(-1)^\mu$	$(-1)^\mu$	$(-1)^\mu(-1)^\nu$
C	1	-1	1	1	-1	-1	-1	1	-1
CP	1	$-(-1)^\mu$	-1	$-(-1)^\mu$	$-(-1)^\mu(-1)^\nu$	$(-1)^\mu(-1)^\nu$	$-(-1)^\mu$	$(-1)^\mu$	$-(-1)^\mu(-1)^\nu$

TABLE 1.1: Transformation properties of some field bilinears, as well as spin-1 vectors and the derivative operator, under parity and charge conjugation. Here, $\sigma^{\mu\nu} = \frac{i}{2}[\gamma^\mu,\gamma^\nu]$ and $F^{\mu\nu} = \partial^\mu A^\nu - \partial^\nu A^\mu$. We use the notation $(-1)^\mu = 1$ if $\mu = 0$ and $(-1)^\mu = -1$ if $\mu = 1,2,3$.

As another example, consider an interaction of the form $F_{\mu\nu}\tilde{F}^{\mu\nu}$, with $\tilde{F}^{\mu\nu} = \epsilon^{\mu\nu\alpha\beta}F_{\alpha\beta}$, $F_{\mu\nu} = \partial_\mu A_\nu - \partial_\nu A_\mu$, and A_μ the electromagnetic potential. Using the antisymmetry of $F_{\mu\nu}$, which implies $\epsilon_{\mu\nu\alpha\beta}F^{\mu\nu}F^{\alpha\beta} = 4\epsilon_{ijk}F^{0i}F^{jk}$, as well as the transformation properties of A^μ and ∂^μ, we can show that this term is CP-violating:

$$CP : F_{\mu\nu}\tilde{F}^{\mu\nu} \longrightarrow -F_{\mu\nu}\tilde{F}^{\mu\nu} \tag{1.27}$$

The examples above will hopefully shed some light on the two crucial CP-violating sources of the Standard Model that we will mention in the following section.

1.3.2 CP violation in the Standard Model

The Standard Model is a quantum field theory invariant under gauge symmetry $SU(3)_C \times SU(2)_L \times SU(1)_Y$ and described by the following Lagrangian:

$$\mathcal{L}_{\text{SM}} = \mathcal{L}_{\text{Gauge}} + \mathcal{L}_{\text{Matter}} + \mathcal{L}_{\text{Higgs}} + \mathcal{L}_{\text{Yukawa}}, \tag{1.28}$$

where the gauge vector boson interactions of the strong and weak sector are given by

$$\mathcal{L}_{\text{Gauge}} = -\frac{1}{4} G^a_{\mu\nu} G^{a\mu\nu} - \frac{1}{4} W^b_{\mu\nu} W^{b\mu\nu} - \frac{1}{4} B_{\mu\nu} B^{\mu\nu}, \tag{1.29}$$

and the matter content by

$$\mathcal{L}_{\text{Matter}} = \sum_f \overline{f} D_\mu \gamma^\mu f, \tag{1.30}$$

with the covariant derivative $D_\mu = \partial_\mu + i g_s \lambda^a G^a_\mu/2 + i g \sigma^b W^b_\mu/2 + i g' Y G_\mu/2$. The λ^a, σ^b, and Y refer to the Gell-Mann matrices, Pauli matrices, and to hypercharge, generators of $SU(3)$, $SU(2)$, and $SU(1)$ respectively. The sum runs over all fermions f, more specifically the left handed quark and lepton doublets, and the right handed quark and lepton singlets

$$Q^i_L = \begin{pmatrix} u^i \\ d^i \end{pmatrix}, \qquad L^i_L = \begin{pmatrix} \nu^i \\ e^i \end{pmatrix}, \qquad u^i_R, \qquad d^i_R, \qquad e^i_R, \tag{1.31}$$

for three generations ($i = 1, 2, 3$ for (u, d), (c, s), and (t, b)), which characterizes the fact that only fermions of left chirality couple to the weak interaction. The left and right handed fermion notations imply a projection on both chiralities of the Dirac spinor f, with $f_L = (1 - \gamma^5) f/2$ and $f_R = (1 + \gamma^5) f/2$.

The Higgs sector is described by

$$\mathcal{L}_{\text{Higgs}} = (D_\mu \phi)^\dagger (D^\mu \phi) - V(\phi), \tag{1.32}$$

with Higgs doublet $\phi = (\phi^+, \phi^0)$ and Higgs potential $V(\phi)$.

Lastly, the Yukawa interaction with the fermions is given by

$$\mathcal{L}_{\text{Yukawa}} = -\Upsilon^{ij}_u \overline{Q}^i_L \epsilon \phi^* u^j_R - \Upsilon^{ij}_d \overline{Q}^i_L \phi d^j_R - \Upsilon^{ij}_l \overline{L}^i_L \phi e^j_R \tag{1.33}$$

where again i, j run over quark and lepton generations. It is through this interaction that the fermions acquire masses after electroweak symmetry breaking (EWSB). This will in turn generate one of the CP-violating terms of the SM through their coupling with the charged currents, in a process that we will now briefly recall.

CP violation in the weak sector:
After EWSB, the Higgs potential acquires a non-zero minimum $\phi = (0, v/\sqrt{2})$, with $v = 246\,\text{GeV}$ defining the electroweak scale. Mass terms appear explicitly for fermions when we express the Yukawa interaction in terms of mass eigenstates (denoted $u'_L, \ldots$) instead of flavor eigenstates (denoted $u_L, \ldots$) by diagonalizing the Yukawa matrices Υ^{jk}_f, $f = u, d$. This is done through the unitary transformations V_{f_L}

and V_{f_R}, with

$$u_L^i = [V_{u_L}]_{ij} u_L'^j, \qquad d_L^i = [V_{d_L}]_{ij} d_L'^j, \qquad u_R^i = [V_{u_R}]_{ij} u_R'^j, \qquad d_R^i = [V_{d_R}]_{ij} d_R'^j. \tag{1.34}$$

The diagonal fermion mass matrices M_u, M_d, with $[M_u]_{ij} = m_u^i \delta^{ij}$ and $[M_d]_{ij} = m_d^i \delta^{ij}$, are then given by:

$$M_u = V_{u_L}^\dagger Y_u V_{u_R} \qquad\qquad M_d = V_{d_L}^\dagger Y_d V_{d_R} \tag{1.35}$$

Of particular significance is how these transformations affect, inside the matter term of the Lagrangian, the quarks and charged current (CC) interaction

$$\mathcal{L}_{\text{CC}} = g V_{\text{CKM}}^{jk} \overline{u}_L'^j W_\mu^- \gamma^\mu d_L'^k + g V_{\text{CKM}}^{*jk} \overline{d}_L'^j W_\mu^+ \gamma^\mu u_L'^k, \tag{1.36}$$

through the Cabibbo-Kobayashi-Maskawa (CKM) matrix, defined as

$$V_{\text{CKM}} = V_{u_L}^\dagger V_{d_L}. \tag{1.37}$$

Note that by construction, the CKM matrix is unitary ($V_{\text{CKM}}^\dagger V_{\text{CKM}} = 1$). Using the combined charge conjugation and parity transformations defined in the previous section, we see that

$$CP : \mathcal{L}_{\text{CC}} \longrightarrow g V_{\text{CKM}}^{jk} \overline{d}_L'^j W_\mu^+ \gamma^\mu u_L'^k + g V_{\text{CKM}}^{*jk} \overline{u}_L'^j W_\mu^- \gamma^\mu d_L'^k. \tag{1.38}$$

which is only equal to $\mathcal{L}_{\text{CC}}$ if the CKM matrix elements are real. Nothing however indicates that they should be. The only constraints on the elements of this matrix come from its unitarity, and after re-absorption of some of the complex phases in the quark fields, its most general parametrizations depend on three Euler angles θ_i, $i = 1, 2, 3$, and a complex phase δ. Note that it is only because there are more than two generations of quarks that a complex phase δ persists after phase redefinition. The original parametrization proposed by the three authors is (Kobayashi and Maskawa, 1973):

$$V_{\text{CKM}} = \begin{pmatrix} c_1 & -s_1 c_3 & -s_1 s_3 \\ s_1 c_2 & c_1 c_2 c_3 - s_2 s_3 e^{i\delta} & c_1 c_2 s_3 + s_2 c_3 e^{i\delta} \\ s_1 s_2 & c_1 s_2 c_3 + c_2 s_3 e^{i\delta} & c_1 s_2 s_3 - c_2 c_3 e^{i\delta} \end{pmatrix} \tag{1.39}$$

with $c_i = \cos\theta_i$ and $s_i = \sin\theta_i$. The presence of the complex phase is then what makes the quarks and charged current interaction CP violating. Nevertheless this source of CP violation fails to account for much of the baryon asymmetry η, as mentioned in the previous section. This is what drives the search for new sources of CP violating interactions.

The largest SM contribution to the neutron EDM arising from this CP-violating phase is found only at the three-loop level, *via* a so-called "strong Penguin" diagram (depicted in figure 1.3) (Engel, Ramsey-Musolf, and van Kolck, 2013). This mechanism could lead to an EDM of the order of $10^{-32}\, e\,\text{cm}$, which is five to six order of magnitude below the sensitivity of even the most ambitious neutron EDM experiments.

CP violation in the strong sector:
The second type of CP-violating couplings of the Standard Model arises in the strong sector. Isolating gluonic terms from the gauge and matter Lagrangians in (1.28) and

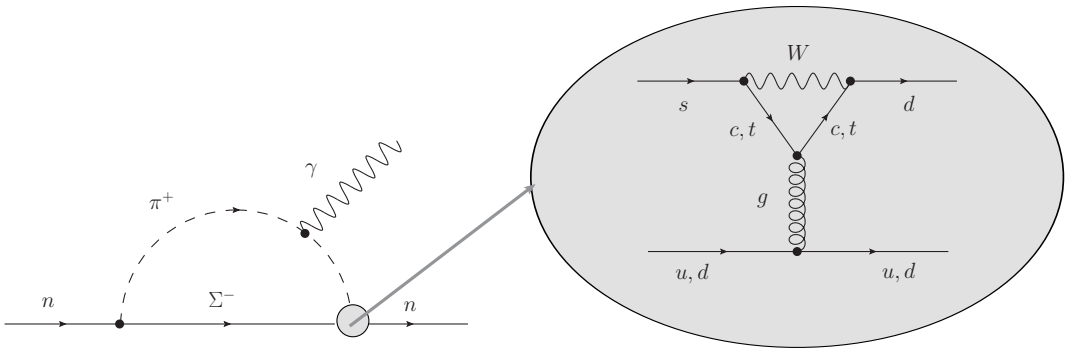

FIGURE 1.3: The largest SM contribution to the neutron EDM. A four-quark operator generated by a strong penguin (to the right) is enhanced via a chiral π^+ loop (to the left).

adding a topological term $\mathcal{L}_\theta$, we write the Quantum Chromo-Dynamics (QCD) part of the SM Lagrangian as

$$\mathcal{L}_{\text{QCD}} = \mathcal{L}_{\text{Gluons}} + \mathcal{L}_{\text{Quarks}} + \mathcal{L}_\theta \tag{1.40}$$

$$= -\frac{1}{4} G^a_{\mu\nu} G^{a\mu\nu} - \frac{g_s}{2} \sum_q \bar{q} \lambda^a G^a_\mu \gamma^\mu q - \theta \frac{g^2}{32\pi^2} \tilde{G}^a_{\mu\nu} G^{a\mu\nu}, \tag{1.41}$$

with $\tilde{G}^{\mu\nu} = \epsilon^{\mu\nu\alpha\beta} G_{\alpha\beta}$. We know from the previous section that the last term is CP-violating. The phase θ it is proportional to is referred to as the QCD vacuum angle, and is transformed after EWSB by the flavour to mass change of basis mentioned above. The diagonalization of the mass matrices M_u, M_d, has the effect of a chiral rotation $q^i_L = e^{i\theta'} q'_L$, $q^i_R = e^{i\theta'} q'_R$ ($q = u, d$), with $\theta' = \arg(\det\{M_u M_d\})$. The parameter $\bar{\theta}$ of the transformed Lagrangian $\mathcal{L}_{\bar{\theta}}$ is then:

$$\bar{\theta} = \theta - \arg(\det\{M_u M_d\}). \tag{1.42}$$

In other words, the CP-violating phase of the strong sector is the difference between the QCD parameter θ and a phase associated with the quark mass matrices. It so happens that the most stringent constraint on $\bar{\theta}$ is given by the neutron electric dipole moment (Pospelov and Ritz, 2005):

$$d_n(\bar{\theta}) = \bar{\theta} \frac{e m_*}{m_n \Lambda_{\text{QCD}}}, \tag{1.43}$$

with $m_* = m_u m_d / (m_u + m_d)$ and Λ_{QCD} the QCD energy scale. Using the current limit on the neutron EDM $d_n \leq 10^{-26}\, e\,\text{cm}$ set by the nEDM collaboration in 2020 (Abel et al., 2020), recent lattice QCD calculations predict an upper bound on the strong CP phase $\bar{\theta} \leq 10^{-10}$ (Dragos et al., 2021). The fact that the two seemingly unrelated phases involved in $\bar{\theta}$ are set so arbitrarily close to one another is what constitutes the *strong CP problem*.

1.3.3 Beyond the Standard Model CP violation and the neutron EDM

Having observed that CP violation occurs in two sectors of the Standard Model, one may legitimately wonder if further violation could take place beyond the Standard Model. Since new physics is expected to be found at higher energies, the effective field theory approach to this question is to artificially add higher-dimensional mass

terms to the SM Lagrangian, on the natural condition that they satisfy the $SU(3)_C \times SU(2)_L \times SU(1)_Y$ gauge symmetry, and select among these the CP-violating terms ((Pospelov and Ritz, 2005), (Engel, Ramsey-Musolf, and van Kolck, 2013)). The effective CP-violating (CPV) Lagrangian would then look like this:

$$\mathcal{L}_{\text{CPV}} = \mathcal{L}_{\bar{\theta}} + \mathcal{L}_{\text{CC}} + \mathcal{L}_{\text{BSM}} \tag{1.44}$$

with the two first SM terms having been discussed in the previous section, and the BSM term taking the form

$$\mathcal{L}_{\text{BSM}} = \sum_i \frac{\alpha_i}{\Lambda^2} O_i^{(6)} \tag{1.45}$$

In this case we only consider up to mass dimension six operators $O_i^{(6)}$ generated at the energy scale $\Lambda > v$, the α being dimensionless couplings. The effective term $\mathcal{L}_{\text{BSM}}$ is then just as the entire Lagrangian of mass dimension four. The reason we are interested in these BSM CP-violating operators is that a subset of these generate EDM interactions when descending to lower energies. After EWSB, the effective theory below the electroweak scale, accessed by integrating out the W bosons from these dimension six operators, describes in particular the neutron EDM through the fermion EDM interactions (EDM), the quark chromo-electric dipole moment (CEDM), and the three-gluon Weinberg operator ($\tilde{G}$) (Engel, Ramsey-Musolf, and van Kolck, 2013):

$$\mathcal{L}_{\text{BSM}}^{\text{EW}} \supset \mathcal{L}_{\text{EDM}} + \mathcal{L}_{\text{CEDM}} + \mathcal{L}_{\tilde{G}} \tag{1.46}$$

$$= -\frac{i}{2}\sum_f d_f \bar{f}\sigma^{\mu\nu}\gamma_5 f F_{\mu\nu} - i\frac{g_s}{4}\sum_q \tilde{d}_q \bar{q}\sigma^{\mu\nu}\lambda^a\gamma_5 q G^a_{\mu\nu} + \frac{g_s}{3}\tilde{d}_G f^{abc}\tilde{G}^a_{\mu\nu}G^b_{\mu\rho}G^c_{\nu\rho} \tag{1.47}$$

Focusing on the first term, one may bridge the conceptual gap with the introductory section by considering that, in the non-relativistic limit, this term yields the EDM interaction (1.2) for a spin 1/2 particle. Using identities in 1.1, we can confirm that this type of interaction is indeed CP-violating. The neutron itself only explicitly appears at even lower energies in a hadronic scale Lagrangian describing nucleon interactions (Chupp and Ramsey-Musolf, 2015):

$$\mathcal{L}_{\text{BSM}}^{\text{Hadron}} \supset \mathcal{L}_{\text{nEDM}} + \mathcal{L}_{\text{NSID}}$$

$$= -i\frac{d_n}{2}\bar{n}\sigma^{\mu\nu}\gamma_5 n F_{\mu\nu} - i\frac{G_F}{\sqrt{2}}\bar{e}\gamma_5 e\,\bar{n}\left[C_S^{(0)} + C_S^{(1)}\tau_3\right] n. \tag{1.48}$$

The first term is just the nucleon (n) equivalent of the fermionic EDM interaction, while the second term represents the nuclear spin-independent (NSID) interaction between electrons (e) and nucleons. The C_S are dimensionless coefficients, G_F is the Fermi constant, and τ_3 is the nucleon isospin Pauli matrix. A measurement of the coupling constant d_n at this scale would then constrain not only the QCD phase $\bar{\theta}$ but also EDM, cEDM, and gluonic couplings in (1.47), by climbing the energy ladder back to below the electroweak scale. Recent theoretical efforts, especially through lattice QCD calculations, give a numerical estimate of the dependency between these couplings (Dragos et al., 2021; Bhattacharya et al., 2021b; Bhattacharya et al., 2021a; Gupta et al., 2018; Bhattacharya et al., 2015; Pospelov and Ritz, 2001; Lebedev et al.,

2004; Hisano et al., 2012; Demir, Pospelov, and Ritz, 2003):

$$\begin{aligned} d_n = &-(1.5 \pm 0.7)10^{-3}\bar{\theta}\, e\,\text{fm} \\ &-(0.20 \pm 0.01)d_u + (0.78 \pm 0.03)d_d + (0.0027 \pm 0.016)d_s \\ &-(0.55 \pm 0.28)\, e\,\tilde{d}_u - (1.1 \pm 0.55)\, e\,\tilde{d}_d + (50 \pm 40)\,\text{MeV}\, e\tilde{d}_G. \end{aligned} \tag{1.49}$$

The coefficients constrained by d_n can in turn be expressed in terms of Wilson coefficients $C_i \equiv \alpha_i/\Lambda^2$ at the new energy scale Λ (Chupp and Ramsey-Musolf, 2015). For instance, the up quark term of the fermion EDM contribution constrains the Wilson coefficient $[C_{uB}]_{11}$ through $d_u = (ev\cos\theta_W/\sqrt{2})[C_{uB}]_{11}$, with θ_W the Weinberg weak-mixing angle. The most recent $10^{-26}\, e$ cm bound on the neutron EDM results in $\text{Im}\,|[C_{uB}]_{11}| \lesssim 1/(1300\,\text{TeV})^2$ at 95% confidence level (Engel, Ramsey-Musolf, and van Kolck, 2013), probing energies at the 10^3 TeV scale.

1.4 Conclusion

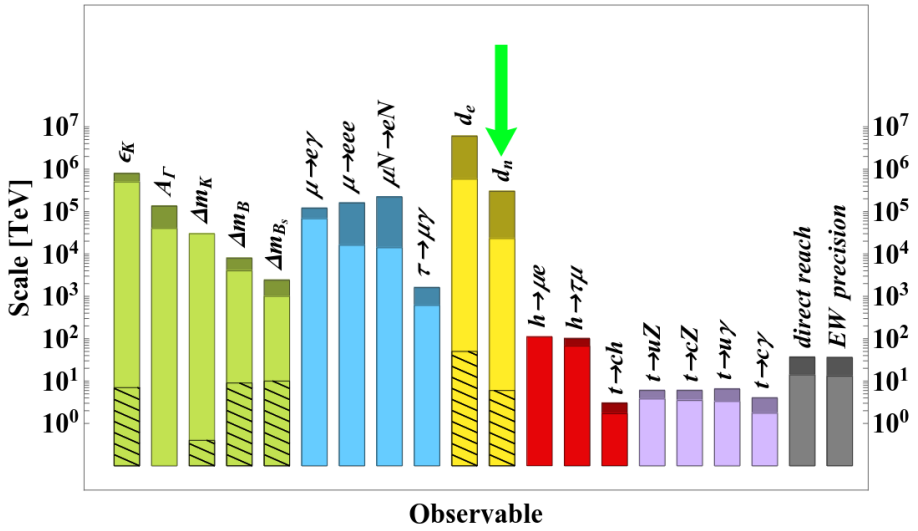

FIGURE 1.4: Energy scale reach of present and future experiments from dimension six EFTs $(\alpha_i/\Lambda^2)O_i^{(6)}$. The coefficients α_i are set either to 1 (plain colored columns) or suppressed by Minimal Flavor Violation factors (hatched out areas). The upper grey areas correspond to the intended reach of ongoing experiments. The neutron EDM, pointed to in green, probes new physics up to 10^6 TeV. Picture modified from (Particle Physics Preparatory Group, 2020).

Throughout this chapter we have introduced both the interaction which EDM experiments seek to measure and the underlying motivations behind these searches. We began our discussion with the dynamics of fermion spins subjected to an electric field, which we showed corresponded to a precession of the spin around the field's axis. We found that the precession frequency was proportional to the coupling between the spin and the electric field, a quantity known as the Electric Dipole Moment. This also allowed us to give a rudimentary taste of the charge conjugation, parity, and time symmetries by observing that the coupling in question violated the combined CP symmetry. This fundamental fact is what motivates the search for the

neutron EDM. The following section attempted to shed some light on the cosmological grounds on which this motivation stands, by recalling the famous Sakharov conditions for baryogenesis and providing some basic understanding of these. One of their conclusions is that CP violation is needed in order to explain the baryon asymmetry in the Universe.

We then brought our discussion over to the Standard Model of particle physics, by first recalling how C and P symmetries were defined on scalar fields, fermionic fields, and spin-1 vector fields, and arrived at the well-known observation that CP exchanges particles and anti-particles of opposite chirality. Through this process we also summarized the combination of CP transformations on relevant interactions. With these tools in hand we turned to the SM Lagrangian and recalled that CP violation occurs in both the weak sector through the complex CKM phase and in the strong sector *via* the $\bar{\theta}$ parameter. However the former does not provide enough CP violation to successfully address the issue of baryon asymmetry, and the latter is coincidentally constrained by the neutron EDM to an arbitrarily small value in what is referred to as the strong CP problem. We also remarked that the CKM contribution to the neutron EDM was incredibly suppressed, about five orders of magnitude below the sensitivity of future experiments.

This naturally led us to examine the place of the neutron EDM in the realm of CP violating BSM interactions. We recalled from the literature that the neutron EDM interaction, which we showed to be CP violating, was generated by a subset of dimension 6 CP violating operators by climbing the energy scale all the way down to the hadronic scale. The reciprocal process is what allows us to think of the neutron EDM as a possible constraint on high-energy parameters. Indeed, the neutron EDM provides bounds on a number of Wilson coefficients, most notably through the up and down quark EDMs, and through this sets the energy scale for new physics. We conclude this discussion with a look at figure 1.4, which shows that the neutron EDM serves as a far-reaching probe for new physics, up to a potential 10^6 TeV energy scale for the most competitive current experiments such as n2EDM. We can now introduce the experimental concept of n2EDM, which is just one of many endeavours hoping to measure this promising interaction.

Chapter 2

Measurement of the neutron EDM with the n2EDM experiment

Contents

The justified quest for P and then CP violating couplings, in and beyond the Standard Model, is not a recent one. n2EDM inserts itself in a long line of experiments that first went through drastic increases in sensitivity but are now seemingly stalling. The next-generation experiments must muster the most cutting edge technologies in order to increase the neutron EDM measurement sensitivity by one order of magnitude. After a brief history of neutron EDM experiments (section 2.1), we will explain the core concept of neutron EDM experiments (section 2.2), introduce ultra-cold neutrons (section 2.3), before turning to a more specific description of the n2EDM apparatus. We will go through key features of the measurement process which relies for sensitivity on a mercury co-magnetometer (section 2.4) and is based on the well-known *Ramsey method* of separated oscillating magnetic fields (section 2.5). Finally we will give a general overview of the core components of n2EDM, focusing on those related to the control of the magnetic environment (section 2.6).

2.1 A brief history of neutron EDM experiments

The first proposal of a measurement of the neutron EDM is attributed to Ramsey and Purcell and their 1950 letter (Purcell and Ramsey, 1950). Along with Smith, the three physicists conducted the experiment but did not publish their results straight away. Although the conservation of parity had at the time only been tested in the electromagnetic and strong interactions, there was no reason to believe that it would not also be verified elsewhere, so there was little interest in a measurement of a P-violating coupling involving fermions. This was before however that Wu showed

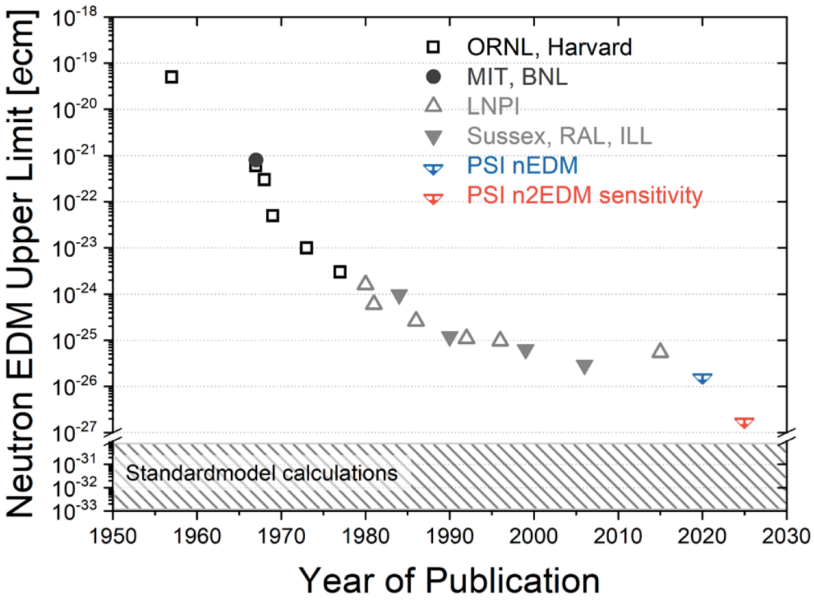

FIGURE 2.1: A history of upper limits on the neutron EDM published by various collaborations, ranging from the Smith-Ramsey-Purcell experiment to the projected n2EDM measurement. The previous limit obtained by the nEDM collaboration is represented by the blue point and the projected sensitivity of n2EDM by the red point. The plot is featured in reference (Kirch and Lauss, 2020).

concrete evidence of parity violation in the weak sector in the seminal 1956 experiment of beta decays, that later won her colleagues the Nobel prize (Wu et al., 1957). Emboldened by the discovery, Ramsey, Purcell, and Smith published in 1957 the first limit on the electric dipole moment of the neutron, $|d_n| < 5 \times 10^{-20}\, e\,\text{cm}$ (Smith, Purcell, and Ramsey, 1957), plotted as the leftmost dot of figure 2.1. Their experiment consisted in subjecting polarized neutrons, generated by the same neutron beam they previously used to determine the neutron's magnetic moment, to a strong electric field. The technique used to extract the neutron spin precession frequency, which as we indicated in section 1.1 allows the determination of the dipole moment, was Ramsey's very own method of "separated oscillating magnetic fields". This procedure is still at the foundation of modern neutron EDM experiments such as n2EDM. We will describe it in more detail in section 2.5.

Neutron beam experiments continued both on the European continent and in the USA well into the 1970s until reaching their limit in sensitivity $|d_n| < 3 \times 10^{-24}\, e\,\text{cm}$ with the Dress and collab. experiment (Dress et al., 1977). All beam-type measurements are represented as black points in figure 2.1. The limiting factors were attributed to both a low neutron precession time, which is a limitation in statistics, and to a systematic effect arising from the presence of a relativistic *motional field* $\mathbf{v} \times \mathbf{E}/c^2$. The latter is coincidentally one of the focal points of this thesis, as part II is dedicated to its study. As for the poor statistics, the solution the experimental physicists of that time came up with was to replace the beam with slow, cold neutrons which by virtue of their low energy could be stored for a longer period of time. The loss in the number of interacting neutrons N would then be largely compensated by the tremendous increase in precession time T. For this to make sense one should have in mind that the sensitivity the neutron EDM scales as $\sigma(d_n) \sim 1/(T\sqrt{N})$.

This led to the age of Ultra-Cold neutron (UCN) experiments, the properties of

which we will detail in section 2.3. The first limit on the neutron EDM obtained thanks to the use of UCNs was that of Altarev and collab. (Altarev et al., 1980) ($|d_n| < 1.6 \times 10^{-24}\, e\,\text{cm}$), pictured as the leftmost gray point of figure 2.1. Neutrons in this experiment were successfully stored for about 5 seconds, three orders of magnitudes longer than in previous neutron beam experiments. Significant improvements on this limit arrived in the next years, both by the soviet group at LNPI that continued to build on their 1980 result, and by the western Sussex/RAL/ILL collaboration operated at the Institut Laue-Langevin (ILL) in Grenoble. The latter most notably brought the limit down to $|d_n| < 3 \times 10^{-26}\, e\,\text{cm}$ in 2006 (Baker et al., 2006). Part of this experiment was then moved close to the UCN source of the Paul Scherrer Institute (PSI) in Villigen, Switzerland and upgraded by the new nEDM collaboration. The upgraded apparatus featured most notably cesium magnetometers for online field measurements, as well as a dual spin detection system, while retaining the ILL's mercury co-magnetometer for the correction of magnetic field fluctuations. This allowed the collaboration to publish in 2020 the best limit to date on the neutron EDM $|d_n| < 1.8 \times 10^{-26}\, e\,\text{cm}$ (Abel et al., 2020).

Having stretched the technical capabilities of the apparatus to their limits, there was a definite need for a new system in order to continue to push the d_n sensitivity up by another order of magnitude. This is what gave way to the much larger twin chamber system of n2EDM, that would allow for much greater neutron statistics as well as simultaneous data taking in opposite electric and magnetic field configurations. Figure 2.2 shows a geometrical comparison of nEDM and n2EDM precession chambers. The next sections will cover the most salient novelties of n2EDM, especially regarding the control of the magnetic field as this is what this thesis is concerned with.

Today, there are a number of experiments outside n2EDM hoping to improve on the neutron EDM limit (Ito et al., 2018; Ahmed et al., 2019; Chanel, Estelle et al., 2019; Picker, n.d.; Wurm, David et al., 2019), which can be broadly split in two categories: those relying on the well-established solid Deuterium UCN sources, and those working on next-generation superfluid Helium UCN sources. The former category includes n2EDM as well as the upgraded apparatus of Los Alamos National Laboratory (Ito et al., 2018), both aiming for a one order of magnitude increase in sensitivity. The latter features a remarkably innovative cryogenic apparatus filled with superfluid ^{4}He as well as ^{3}He for co-magnetometry, promising to deliver much greater statistics that could in principle lower the EDM limit by two orders of magnitude (Ahmed et al., 2019). Two other experiments rely on superfluid ^{4}He as a UCN source: one at ILL (Chanel, Estelle et al., 2019), and another at TRIUMF (Picker, n.d.), both hoping to increase the nEDM sensitivity by one order of magnitude. Finally, the ILL also hosts a novel pulsed neutron beam EDM experiment (Wurm, David et al., 2019).

While being the limiting factor in the most recent measurement of d_n, greater neutron statistics alone cannot bring the 10^{-27} limit down if the control of systematic effects does not scale along with them, which is the focus of this thesis. Nevertheless these effects can only be covered after introducing the main components of this experiment, some of which may significantly bias the neutron EDM measurement while at the same time improving our sensitivity.

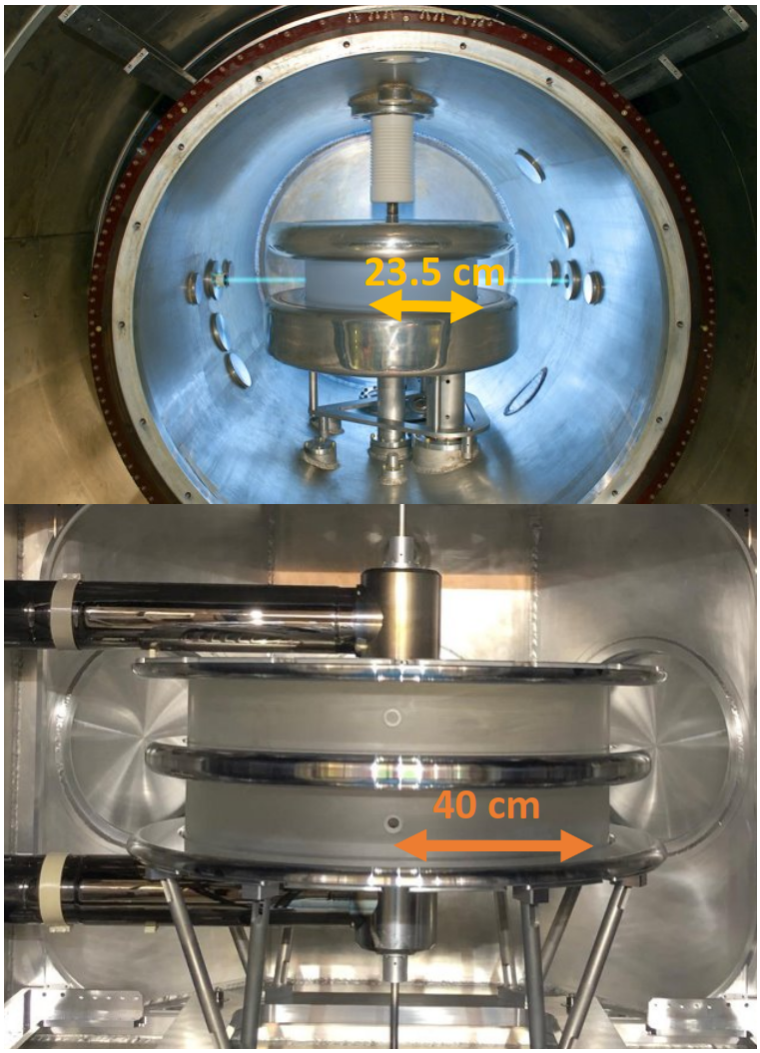

FIGURE 2.2: Scaled pictures of the nEDM (top) and n2EDM (bottom) precession chambers. The radius of each of the new experiment's chamber is nearly twice that of the previous experiment, thus granting increased statistics. The double chamber configuration allows simultaneous measurements in $\uparrow\uparrow$ and $\uparrow\downarrow$ magnetic-electric configurations.

2.2 The neutron EDM measurement concept

The core concept of neutron EDM experiments such as n2EDM is to have neutrons precess in both a strong electric field and a weak magnetic field and try to extract the neutron EDM as the electrical contribution to the precession frequency. Such an interaction is described by a combination of the electric and magnetic couplings (1.2) and (1.3) introduced in the first section:

$$H = -\mu_n \boldsymbol{\sigma} \cdot \mathbf{B} - d_n \boldsymbol{\sigma} \cdot \mathbf{E}, \tag{2.1}$$

where μ_n is the (known) neutron magnetic moment, and d_n is the hypothetical neutron EDM. If both fields are applied vertically ($\mathbf{B} = (0, 0, B_0)$ and $\mathbf{E} = (0, 0, E_0)$), we know from the introductory example in section 1.1 that the neutrons' spins will

precess around these at a frequency

$$f_n = \frac{-1}{\pi\hbar}\left(\mu_n B_0 + d_n E_0\right). \tag{2.2}$$

The manner in which the electrical contribution is isolated is by applying the magnetic and electric fields in parallel (↑↑) and anti-parallel (↑↓) configurations, and comparing the precession frequencies

$$f_{n\uparrow\uparrow} = \frac{-1}{\pi\hbar}\left(\mu_n B_0 + d_n E_0\right), \qquad f_{n\uparrow\downarrow} = \frac{-1}{\pi\hbar}\left(\mu_n B_0 - d_n E_0\right), \tag{2.3}$$

measured in both configurations. The EDM is then expressed as

$$d_n = \frac{\pi\hbar}{2E_0}\left(f_{n\uparrow\downarrow} - f_{n\uparrow\uparrow}\right). \tag{2.4}$$

The equality above is of course an idealization of the experimental reality. The next chapters will be dedicated to more intricate systematic errors plaguing d_n, but for the moment we will focus on the most potent source of uncertainty which has to do with the fluctuations of the magnetic field. In the likely scenario where the value of B_0 changes between parallel and anti-parallel configurations but E_0 remains identical, the magnetic terms in $f_{n,\uparrow\uparrow}$ and $f_{n,\uparrow\downarrow}$ do not cancel out in d_n and lead to uncertainties that dominate the statistical errors. The top-plot of figure 2.4 shows such a scenario with data taken during the previous installment of the experiment (nEDM). We will see in the next section how this major systematic effect is accounted for in the measurement.

One of the novelties of n2EDM is that the precession frequencies for both field configurations can be extracted at the same time so as to minimize time-dependent field fluctuations. This is made possible by the double chamber configuration, in which two precession chambers of radius $R = 40\,\text{cm}$ and height $H = 12\,\text{cm}$ are stacked vertically at the center of the apparatus. A high-voltage electrode separates the two and generates in conjunction with ground electrodes, situated both below the bottom chamber and above the top chamber, electric fields of opposite polarities in the two chambers. Figure 2.3 demonstrates how the double chamber configuration allows simultaneous data-taking in opposite field configurations. The magnetic field is taken care of by a sophisticated coil system whose main mission is to produce the vertical B_0 field but is also capable of generating multi-directional optimizing fields. Figure 2.7 offers a more distant view of the apparatus, where we see that the coil system encases a vacuum vessel containing the two chambers.

In numbers, the applied vertical field has a magnitude of $B_0 = 1\,\mu\text{T}$ while the electric field strength is of $E_0 = 15\,\text{kV}\,\text{cm}^{-1}$. Subjected to the magnetic field only, the neutrons precess at a frequency $f \approx 30\,\text{s}^{-1}$. Subjected to the electric field only, the current limit on the dipole moment $d_n < 10^{-26}\,e\,\text{cm}$ predicts $f < 2\,\text{year}^{-1}$. This is why the electrical contribution to the neutrons' precession frequency is incredibly difficult to detect. Broadly speaking, the experimental parameters of n2EDM are adjusted in order to enhance the accuracy of this measurement, by

- **Maximizing the interaction time**. Ultra-Cold Neutrons (UCNs) are used in n2EDM specifically for this reason. Because of their extremely low kinetic energy, they are easily storable and therefore remain in the precession chambers for a longer period of time. This simply allows more precession cycles to be performed on the same particles. We will briefly cover in the next section the properties which make UCNs storable.

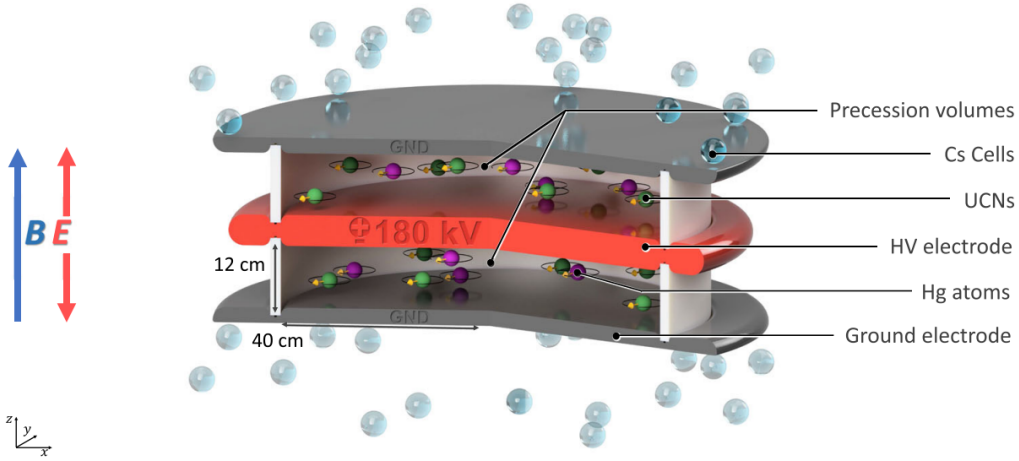

FIGURE 2.3: A sketch of the two precession chambers separated by the high voltage electrode and encased between two ground electrodes, as shown in (al., 2022). This double chamber configuration allows for simultaneous data-taking in parallel and anti-parallel electric and magnetic field configurations. Both neutrons and mercury atoms see their spins precess in the two chambers. Around the chambers, cesium cells offer a real-time measurement of the magnetic field.

- **Maximizing the statistics**. The precursor of n2EDM, nEDM, was limited in its statistical sensitivity by neutron counting statistics. The neutron source at PSI remaining identical, n2EDM will maximize its statistics thanks to a larger UCN storage volume ($R = 23.5\,\text{cm}$ for nEDM compared to $R = 40\,\text{cm}$ for n2EDM, see figure 2.2), and an optimized UCN transport system. It is important to keep in mind that an increase in the cell volume necessarily leads to an increase in field-related systematic errors, which requires a better control of the magnetic environment.

- **Controlling the magnetic field**. Control of the magnetic field encompasses both its stability in time and its spatial uniformity. As we just mentioned, a fluctuating magnetic field completely spoils the EDM extraction. As we will later see, a non-uniform magnetic field negatively impacts both the sensitivity and the accuracy of the measurements. The fluctuations are dealt with thanks to mercury co-magnetometry. The non-uniformities are tackled through precise field measurement, which includes both *online* (during data-taking) monitoring and *offline* (before and after data-taking) mapping of the magnetic field, as well as a control of related systematic effects.

We will now briefly cover the properties of UCNs, before moving on to the control of the magnetic field with mercury co-magnetometry.

2.3 A few properties of ultra-cold neutrons

Ultra-Cold Neutrons (UCNs) are defined as neutrons with a total kinetic energy of less than 250 neV. By virtue of this incredibly low energy they are easily storable (their velocity is of the order of $v < 7\,\text{m}\,\text{s}^{-1}$), which is especially useful in spin-counting experiments which seek to maximize the interaction time between the particles and the applied fields. UCNs are sensitive to fundamental forces among which

three need to be taken into consideration for the experiment: gravity, the electromagnetic interaction, and the strong interaction.

Gravity has a strong influence on these low energy particles that can be used to control their velocity and that produces non-negligible systematic effects. Indeed, the gravitational potential

$$V_g = m_n g z \tag{2.5}$$

is of the order of 100 neV at a 1m height for a neutron of mass $m_n = 1.675 \times 10^{-27}$ kg, which is of the order of magnitude of the UCNs kinetic energy.

We are already familiar with the way the UCNs interact with electric and magnetic fields as it is the foundation of this experiment. The interaction of the neutron's spin with the magnetic field, with a magnetic moment $\mu_n = -60.3\,\text{neV}\,\text{T}^{-1}$, is what not only allows the UCNs to precess in the chambers but also polarizes them before precession.

Finally, the strong interaction is what allows the UCNs to be stored effectively inside the precession chamber. At the interface of the chamber walls, the wavelength of the low energy UCNs is larger than the typical inter-nuclei distance of the wall's material. In this case the neutrons possess an optical-like behavior which allows them to be reflected on the walls of the chamber. More specifically, a neutron is described by a wave function satisfying Shrödinger's equation with a potential barrier called the *Fermi potential*, written as

$$V_F = \frac{2\pi\hbar^2}{m_n} n b, \tag{2.6}$$

where n is the medium's nuclei number density, and b is a constant referred to as the *bound scattering length*, dependent on the nuclear radius of the material involved. For most materials V_F is around a few hundred neV. Reflection occurs when the projection of the neutron's kinetic energy normal to the surface of the wall is lower than the potential barrier, which constitutes the *Fermi-Zimm condition*

$$E \cos^2\theta < V_F, \tag{2.7}$$

where θ is the neutron's incidence angle and E is its kinetic energy. The UCN regime $E < V_F = 250\,\text{neV}$ is precisely defined so that this condition is satisfied at any angle, therefore granting the neutrons a fully ballistic behavior. A useful review of this interaction can be found in (Pignol, 2015).

2.4 Mercury co-magnetometry to compensate for magnetic fluctuations

As mentioned in section 2.2 and pictured in the top plot of 2.4, the extraction of d_n through a straightforward measurement of the precession frequencies $f_{n\uparrow\uparrow}$ and $f_{n\uparrow\downarrow}$ (equation (2.4)) is spoiled by fluctuations in the vertical amplitude B_0 of the magnetic field. This major hurdle is crossed by injecting a mercury gas in the precession chambers alongside the neutrons, and measuring instead a ratio between the precession frequencies of neutrons and of mercury atoms. Figure 2.3 shows the mercury and neutron's spins precessing inside the two chambers. Because the limit on the mercury EDM is much lower than that of the neutron EDM (Graner et al., 2016) ($d_{\text{Hg}} < 10^{-30}\,e\,\text{cm}$), the mercury's electrical term can be neglected so that it is still possible to isolate d_n from the ratio while at the same time canceling out the

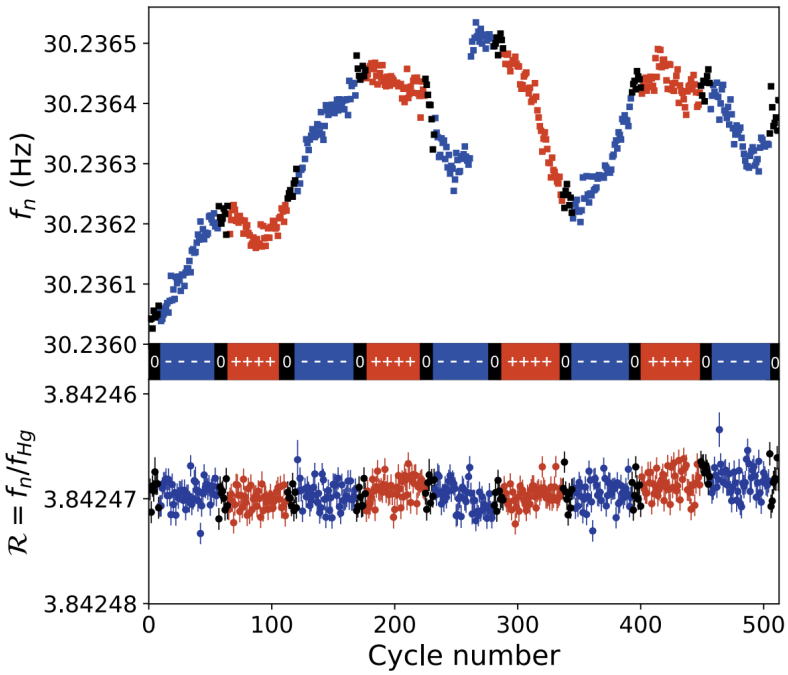

FIGURE 2.4: Data from the nEDM experiment taken in 2016 (Abel et al., 2020). Each red, blue, and black point corresponds to a measurement cycle performed in the positive, negative, and zero electric field polarity respectively. The top plot shows the measurement of the neutron precession frequency alone, while the bottom plot shows instead the ratio of mercury and neutron precession frequencies.

magnetic field contribution. This B_0-free ratio is then

$$\mathcal{R} = \left|\frac{f_n}{f_{\mathrm{Hg}}}\right| = \left|\frac{\gamma_n}{\gamma_{\mathrm{Hg}}}\right| \mp \frac{E_0}{\pi\hbar|f_{\mathrm{Hg}}|}|d_n|, \tag{2.8}$$

where we wrote f_n using equation (2.2) and f_{Hg} equivalently but without the electrical term, and introduced the neutron and mercury gyromagnetic moments $\gamma = 2\mu/\hbar$. The minus sign is for the parallel configuration $\uparrow\uparrow$ and the plus sign for the anti-parallel configuration $\uparrow\downarrow$. The bottom plot of figure 2.4 shows that this ratio is now dominated by statistical uncertainties. Following the same reasoning that led to equation (2.4), the neutron EDM can be extracted from the difference in the ratios measured in $\uparrow\uparrow$ and $\uparrow\downarrow$. Since the electric field polarity is reversible, we can actually form two ratios per chamber (one for each field configuration), and use this to our advantage to compensate for potential gravitational shifts in $\mathcal{R}$. The neutron EDM is then calculated as

$$|d_n| = \frac{\pi\hbar|f_{\mathrm{Hg}}|}{4E_0}\left(\mathcal{R}^{\mathrm{TOP}}_{\uparrow\downarrow} - \mathcal{R}^{\mathrm{TOP}}_{\uparrow\uparrow} + \mathcal{R}^{\mathrm{BOT}}_{\uparrow\downarrow} - \mathcal{R}^{\mathrm{BOT}}_{\uparrow\uparrow}\right). \tag{2.9}$$

What is left to measure in order for this approach to make sense is the precession frequency of mercury atoms f_{Hg}. Polarized ^{199}Hg atoms are injected inside the precession chambers at the beginning of each measurement cycle so that their spins precess freely around the vertical field, much like the neutron spins which we will soon cover. Their precession frequency is then measured optically from the modulated transmission of a polarized horizontal UV beam. This along with the extraction

of f_n allows a calculation of (2.9).

Mercury co-magnetometry does have some drawbacks however, which we will go through in much more detail in chapter 3 but still need to be introduced here. In a nutshell, non-uniformities in the magnetic field in combination with some relativistic effect shift the precession frequencies of both neutrons and mercury atoms, but more so of mercury atoms. Since we measure a ratio of the two frequencies, the shift in the precession frequencies of those mercury atoms negatively impacts the extraction of the neutron EDM d_n. Effectively, we extract "false" EDMs along with the "true" EDM d_n, the most potent of which is the *mercury-induced false neutron EDM* $d^{\text{false}}_{n\leftarrow\text{Hg}}$. It appears in this more realistic version of the precession frequency ratio:

$$\mathcal{R} = \left|\frac{\gamma_n}{\gamma_{\text{Hg}}}\right| \mp \frac{E_0}{\pi\hbar|f_{\text{Hg}}|}\left|d_n + d_n^{\text{false}} + d^{\text{false}}_{n\leftarrow\text{Hg}} + \dots\right|, \tag{2.10}$$

where we have omitted other less relevant systematic effects. As we seek to measure d_n at a sensitivity of $10^{-27}\,e\,\text{cm}$, we constrain other experimental parameters such that this systematic effect is kept below the following limit:

$$d^{\text{false}}_{\text{n}\leftarrow\text{Hg}} < 3\times10^{-28}\,e\,\text{cm}. \tag{2.11}$$

Of course this systematic effect is in a more general perspective completely outweighed by the benefits that mercury co-magnetometry brings to the experiment. Now that we have introduced the main observables of the experiment, let us briefly explain how the most crucial of these, the precession frequency f_n, is obtained in each chamber.

2.5 Precession frequency measurement with the Ramsey method

The neutron precession frequency $f_n = \omega_0/(2\pi)$ [1] used in the determination of the neutron to mercury frequencies ratios $\mathcal{R}$ is extracted using Ramsey's method of separated oscillating fields (Ramsey, 1950). Applied to spin counting in n2EDM, this method consists in the measurement of a probability $P_{+\to-}$ of a neutron transitioning from an up to a down spin state over the course of a specific cycle which is illustrated in figure 2.5 and described below.

0. At $t = 0$, neutrons polarized in the up $|+\rangle$ spin state are injected in the precession chambers, where a vertical magnetic field $(0, 0, B_0)$ is applied.

1. A transverse rotating field, of angular frequency ω chosen close to $\omega_0 = \gamma_n B_0$ and magnitude B_1, is superimposed to the existing field for a time $\tau = 2\,\text{s}$. The interaction time and the field amplitude are chosen according to the Rabi condition $\gamma_n B_1 \tau = \pi/2$, so that the spins perform a $\pi/2$ flip in the transverse plane. Note that the angular frequency ω is close to but cannot be exactly at resonance ω_0.

2. The neutrons are left to precess freely for a time $T = 180\,\text{s}$ in the strictly vertical field, at angular frequency ω_0. This frequency should in principle be slightly different for the two chambers.

3. The rotating field is applied again for a time τ in order to flip the spins back onto the vertical axis.

[1] By convention we will use angular frequencies ω over frequencies f for more computational sections such as this one.

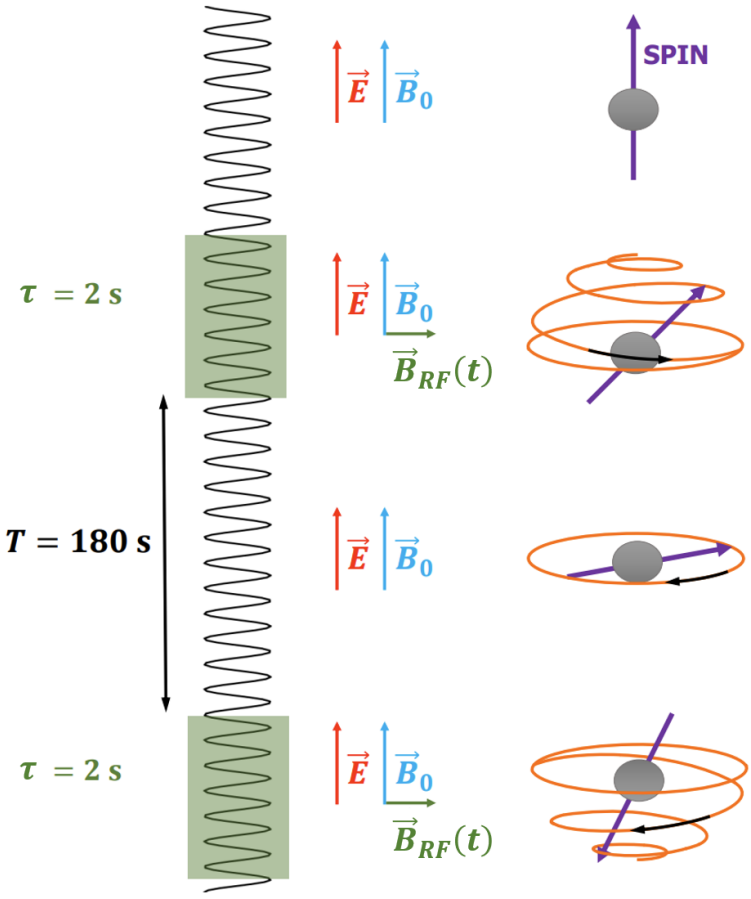

FIGURE 2.5: A schematic representation of the Ramsey method of separated oscillating magnetic fields, modified from a drawing by Laura Ferraris-Bouchez (Ferraris-Bouchez, 2020). The four sections of this sketch follow from top to bottom the steps $0-3$ detailed in section 2.5. The green highlights on the sinusoidal curve shows that the oscillating magnetic field B_{RF} is only applied during steps 1 and 3, in order to flip the spin onto the vertical axis.

In each step of the process, the spin of the neutrons have a probability of preserving their polarization or transitioning to the opposite state. Therefore the total transition probability $P_{+\to\pm}$ will be expressed as a function of these individual amplitudes, which can be derived in steps 1, 2, and 3 of the process by solving the Shrödinger equation

$$i\hbar\frac{d\,|\Psi(t)\rangle}{dt} = H\,|\Psi(t)\rangle \tag{2.12}$$

in the rotating frame, where we write the state of the system as

$$|\Psi(t)\rangle = c_+(t)e^{i\omega t/2}\,|+\rangle + c_-(t)e^{-i\omega t/2}\,|-\rangle\,. \tag{2.13}$$

This is just a more general form of (1.4), where the coefficients $c_+(t)$ and $c_-(t)$ correspond to the probability amplitudes of finding the neutron's spin in state $|+\rangle$ or $|-\rangle$. The Schrödinger equation must then be solved in two cases: (1) for a uniform vertical field, and (2) for the combination of a uniform vertical field and a transverse rotating field.

Vertical field
In the case where only a vertical field is applied, the Hamiltonian is just like in the first section's example proportional to σ_z. Letting $\omega_0 = \gamma_n B_0$, we write it as:

$$H = H_0 = -\frac{\hbar}{2}\begin{pmatrix}\omega_0 & 0\\ 0 & -\omega_0\end{pmatrix} \tag{2.14}$$

The state coefficients of $|\Psi_{\mathrm{VF}}(t)\rangle$ are then given by:

$$\begin{pmatrix}\dot{c}_{\mathrm{VF}+}\\ \dot{c}_{\mathrm{VF}-}\end{pmatrix} = \frac{-i}{2}\begin{pmatrix}\omega-\omega_0 & 0\\ 0 & -(\omega-\omega_0)\end{pmatrix}\begin{pmatrix}c_{\mathrm{VF}+}\\ c_{\mathrm{VF}-}\end{pmatrix} \tag{2.15}$$

As these are uncoupled differential equations the solutions are transparent:

$$\begin{pmatrix}c_{\mathrm{VF}+}\\ c_{\mathrm{VF}-}\end{pmatrix} = \begin{pmatrix}e^{-i\delta\omega t/2}\\ e^{i\delta\omega t/2}\end{pmatrix} \tag{2.16}$$

where $\delta\omega = \omega - \omega_0$.

Rotating field
Applying a transverse rotating field amounts to adding a perturbation V to the initial Hamiltonian H_0. Since the field is of the form $(B_1\cos(\omega t), B_1\sin(\omega t), B_0)$, we let $\omega_1 = \gamma_n B_1$ and write the Hamiltonian as:

$$H = H_0 + V = -\frac{\hbar}{2}\begin{pmatrix}\omega_0 & \omega_1 e^{-i\omega t}\\ \omega_1 e^{i\omega t} & -\omega_0\end{pmatrix} \tag{2.17}$$

The state coefficients of $|\Psi_{\mathrm{RF}}(t)\rangle$ are then given by:

$$\begin{pmatrix}\dot{c}_{\mathrm{RF}+}\\ \dot{c}_{\mathrm{RF}-}\end{pmatrix} = \frac{-i}{2}\begin{pmatrix}\omega-\omega_0 & \omega_1 e^{-i\omega t}\\ \omega_1 e^{i\omega t} & -(\omega-\omega_0)\end{pmatrix}\begin{pmatrix}c_{\mathrm{RF}+}\\ c_{\mathrm{RF}-}\end{pmatrix} \tag{2.18}$$

This set of coupled differential equations can be solved by diagonalizing H and then expressing $|\Psi_{\mathrm{RF}}(t)\rangle$ in the eigenvector basis of H. We then project $|\Psi_{\mathrm{RF}}(t)\rangle$ on $|+\rangle$ and $|-\rangle$ to obtain:

$$\begin{pmatrix}c_{\mathrm{RF}+}\\ c_{\mathrm{RF}-}\end{pmatrix} = \begin{pmatrix}e^{i\omega t/2}\left[\cos(\Omega t) + i((\omega_1^2-\delta\omega^2)/\Omega^2)\sin(\Omega t)\right]\\ ie^{-i\omega t/2}(\omega_1/\Omega)\sin(\Omega t)\end{pmatrix} \tag{2.19}$$

with $\Omega = \sqrt{\delta\omega^2+\omega_1^2}$.

The state amplitudes at steps 1 and 3 are then solutions of the rotating field equation (2.18) $c_{\mathrm{RF}\pm}$, while the state amplitudes at step 2 are solutions of the vertical field equation (2.15) $c_{\mathrm{VF}\pm}$. We can then write the neutron's transition probability from the up to either the up or the down spin state as the sum of two possible "paths" through the three step process:

$$P_{+\to+} = \left|c_{\mathrm{RF}+}(\tau)c_{\mathrm{VF}+}(T)c_{\mathrm{RF}+}(\tau) + c_{\mathrm{RF}-}(\tau)c_{\mathrm{VF}-}(T)c_{\mathrm{RF}+}(\tau)\right|^2, \tag{2.20}$$

$$P_{+\to-} = \left|c_{\mathrm{RF}+}(\tau)c_{\mathrm{VF}+}(T)c_{\mathrm{RF}-}(\tau) + c_{\mathrm{RF}-}(\tau)c_{\mathrm{VF}-}(T)c_{\mathrm{RF}-}(\tau)\right|^2. \tag{2.21}$$

In the limit $\tau \ll T$, we can derive the following expression for the transition probabilities:

$$P_{+\to\pm} = \frac{1}{2}\left[1 \mp \alpha \cos\left(\pi \frac{f_{\mathrm{RF}} - f_n}{\Delta\nu}\right)\right], \tag{2.22}$$

where $f_{\mathrm{RF}} = \omega/(2\pi)$ is the rotating field frequency and $\Delta\nu = 1/(2T + (8\tau/\pi))$ corresponds to the half-width of the resonance. We also introduced as an amplitude factor a parameter α known as the *visibility* of the resonance, which corresponds to the measured neutron polarization at the end of the Ramsey cycle. In the ideal scenario discussed here, neutrons remain polarized so that we naturally have $\alpha = 1$. However in past experiments we observed a depolarization of the neutrons, which can be mainly attributed to non-uniformities in the magnetic field. We will show how to both control the extraction of α and keep it as close to one as possible in section 3.2.

In the case of a non-zero neutron EDM, these transition probabilities will be slightly different for the two chambers because the precession frequencies f_n will differ. What is actually measured in n2EDM, for both precession chambers, is an asymmetry between the number of neutrons found in the up state N_+ and down state N_- at the end of the Ramsey cycle involving a total of N neutrons:

$$A = \frac{N_+ - N_-}{N_+ + N_-}. \tag{2.23}$$

Using equation (2.22) and the fact that $N_- = NP_{+\to-}$ and $N_+ = NP_{+\to+}$, we write the expression for the asymmetry as

$$A = -\alpha \cos\left(\pi \frac{f_{\mathrm{RF}} - f_n}{\Delta\nu}\right). \tag{2.24}$$

The neutron precession frequency in both chambers and for both field configurations is finally obtained by inverting equation (2.24) for f_n, which along with the optical measurement of mercury precession frequency allows the calculation of the neutron EDM through equation (2.9). A plot of the measured asymmetry A for several values of the applied rotating field frequency f_{RF} is shown as the blue points of figure 2.6. What is referred to as the Ramsey resonance is obtained by fitting these points with the expression for the asymmetry (2.24) (black curve of figure 2.6). Notice that $\Delta\nu$ corresponds indeed to the half width of this curve.

In order to maximize our statistical sensitivity, we cannot simply extract f_n from the asymmetry at any value of f_{RF}. Consider the statistical error for one measurement cycle of f_n given by

$$\sigma(f_n) = \frac{\Delta\nu}{\pi\alpha\sqrt{N}}\left(1 - \frac{A^2}{\alpha^2}\right)^{-\frac{1}{2}}. \tag{2.25}$$

We see in the expression above that the statistical error is minimal at $A = 0$, where the slope of the asymmetry curve is the highest. So once we obtain the asymmetry curve we could in principle set f_{RF} to $f_{n,0} \equiv f_n(A = 0)$, by calculating $f_{n,0}$ from a previous cycle, and then extract f_n at maximal sensitivity. However at $A = 0$ we are not sensitive to the amplitude of the curve, represented by the visibility α. The precession frequency f_n will then be extracted from four “working points"

$$f_{\mathrm{RF}} = f_{n,0} \pm (1 \pm 0.1) \times \Delta\nu/2, \tag{2.26}$$

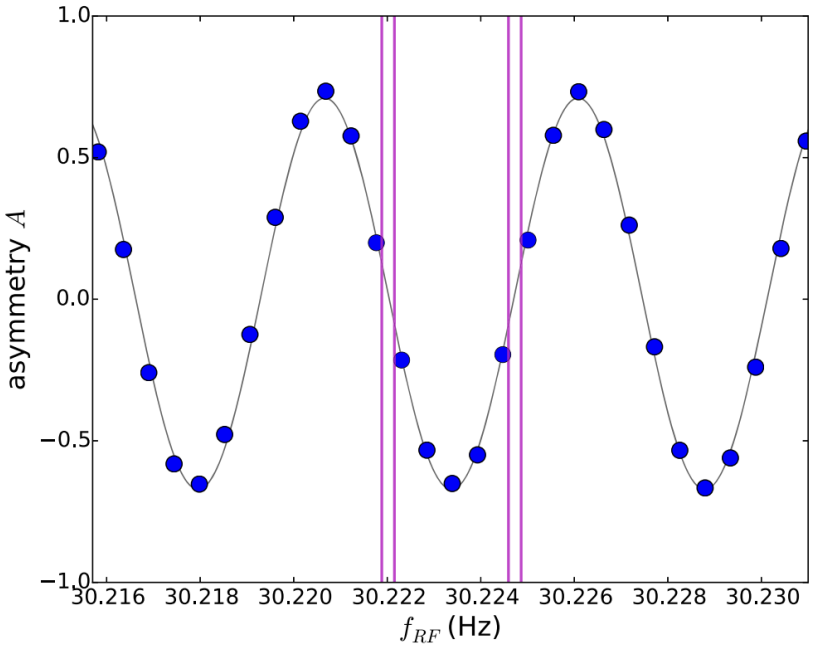

FIGURE 2.6: A set of measurements of the spin asymmetry (2.23) for different values of the transverse rotating field frequency (blue points), fitted according to equation (2.24) (black curve). The purple lines correspond to the four working points given by equation (2.26), set around the points where slope of the asymmetry, hence the sensitivity on f_n, is maximal. This result appears in the article announcing the nEDM limit (Abel et al., 2020).

chosen close to the maximal sensitivity points. These are shown as the purple vertical lines in figure 2.6. Note that since the applied frequency f_{RF} is common to the two precession chambers, the resonance curves of both chambers should be close enough for the points (2.26) to be optimal. This translates to a requirement on the vertical gradient of the magnetic field that will be explicitly stated in the next chapter.

Finally, the statistical sensitivity on the EDM value d_n can be derived by propagating the error on the precession frequency (2.25), taken at $A = 0$, with the expression for d_n (2.4):

$$\sigma(d_n) = \frac{\hbar}{2\alpha E_0 T\sqrt{N}}. \tag{2.27}$$

Looking back at the three concluding remarks of section 2.2 in the light of equality (2.27), we now have clear evidence that, in order to maximize the neutron EDM measurement's sensitivity, we require: a long exposure of the precessing neutrons to the magnetic field ($\sigma(d_n) \propto 1/T$), a strong electric field ($\sigma(d_n) \propto 1/E_0$), and more neutrons ($\sigma(d_n) \propto 1/\sqrt{N}$).

2.6 Overview of the n2EDM apparatus

Before we move on to the more specific subject of magnetic field uniformity in n2EDM, we will take a moment to look at the n2EDM apparatus in its entirety. As very thorough descriptions of this apparatus have already been given by previous PhD students (Chiu, 2021; Pais, 2021), we will only give a general overview of the main components of n2EDM, and leave to part III of this thesis the full description

of those related to magnetic field generation (B_0 coil), characterization (magnetic field mapper), and optimization (trim coils). We will from now on speak in the coordinate system of n2EDM, where the origin is the geometrical center of both the coil system and the double chamber system, the x axis points in the direction of the vacuum tubes in the horizontal plane, the y axis is normal to the x axis in the horizontal plane, and the z axis points opposite to gravity. The axes are represented at the bottom of figure 2.7, which gives an almost complete picture of the apparatus.

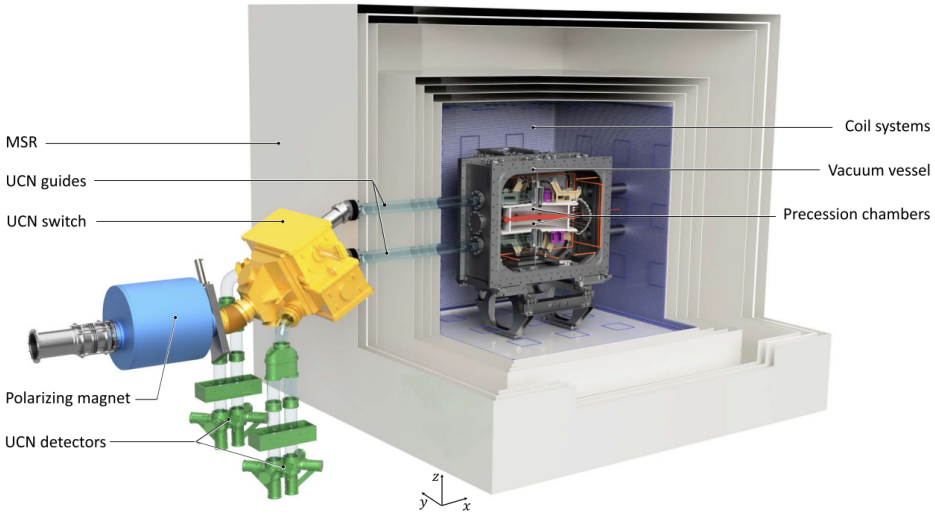

FIGURE 2.7: The n2EDM experimental setup as shown in the design article (al., 2022). The UCNs are polarized by the superconducting magnets and let into the glass guides via the UCN switch. Traveling inside the guides, the neutrons go through the six layers of magnetic shielding that constitute the magnetically shielding room, the coil system responsible mainly for the vertical magnetic field, the vacuum-tight aluminum vessel, and eventually are let into the precession chambers. Inside the vacuum vessel and around the precession chambers reside the cesium magnetometers and the RF coils responsible for the spin-flipping field of the Ramsey cycle. After completing a Ramsey cycle the neutrons follow a reverse path back to the UCN detectors where the up and down spins are counted. The coordinate system of n2EDM is specified at the foot of the apparatus.

2.6.1 UCN transport and detection

The n2EDM experiment resides at PSI in part for its UCN source. UCNs are produced by nuclear spallation: a beam of protons strikes a lead spallation target, thereby ejecting neutrons from the lead nuclei. The neutrons then reach the UCN regime by going through a superthermal converter, where they are slowed down in heavy water and in solid deuterium.

The UCNs reach the n2EDM apparatus where they are polarized thanks to a 5 T superconducting magnet. They are then directed towards the **UCN switch**, which can operate in two configurations: *filling* and *counting*. In filling configuration the switch lets the UCNs into the guides leading them to the chambers. In counting configuration it guides the UCNs into the spin detectors. At first the UCNs are let inside by the switch in filling mode, and after completing a Ramsey cycle, are let out in counting mode.

They eventually land in the two **UCN detectors**, which simultaneously count the number of neutrons in the up and down spin states. This provides a measurement of the asymmetry (2.23). The PhD thesis (Saenz, 2022) provides a very thorough description of those detectors.

2.6.2 The layers of n2EDM: magnetic shield, coil system, and vacuum vessel

FIGURE 2.8: View of the aluminum vacuum vessel, placed at the center of the MSR (in white), from inside the n2EDM thermohouse at PSI. The precession chamber walls and the electrodes are waiting to be moved into the vacuum vessel. The AMS wiring is visible on the inner walls of the thermohouse.

The precession chambers of n2EDM sit at the center of a multi-layered apparatus, responsible mainly for magnetic shielding and magnetic field generation.

The outermost layer consists in a **thermohouse** of dimensions $8.6 \times 10.3 \times 8.9\,\mathrm{m}^3$, which as its name suggests provides thermal insulation for the rest of the apparatus. An interior view of the thermohouse is pictured in 2.8. Much later in chapter 8 we will see that thermal stability of the inner components is crucial as it is correlated to the stability of the remnant magnetic field.

On the inner walls of the thermohouse are wired a set of coils responsible for actively compensating the outside magnetic field and referred to as the **Active Magnetic Shield (AMS)**. These are visible in figure 2.8. The necessity for the AMS arose from the presence of nearby experiments that produce unpredictable fields of amplitude comparable to the earth's magnetic field (tens of µT). The AMS compensates for this varying magnetic noise in real-time through actively controlled coils, with an accuracy of the order of 1 µT. A recent PhD thesis was in part dedicated to the upgrade of the AMS coil system (Rawlik, 2018).

The next layer, or rather set of layers, is that of the **Magnetically Shielded Room (MSR)**. Its outermost layer is of dimensions $5.2 \times 5.2 \times 4.8\,\mathrm{m}^3$ and is shown both as the large white cube at the center of 2.8 and as the outermost "box" of figure 2.7. This passive magnetic shield suppresses through 6 layers of mu-metal the static external field by about five orders of magnitude. The quantity used to evaluate the performance of a magnetic shield is the magnetic *shielding factor*, defined as the ratio between the amplitude of the magnetic field at the center of the shield with the shield, and that same amplitude without the shield. When applying an oscillating magnetic field with a peak-to-peak amplitude of 2 µT (which is of the order of what should remain after AMS shielding), in all three directions, it was demonstrated that the MSR possesses a shielding factor of 1×10^5 at 0.01 Hz which rises up to 1×10^8 at 1 Hz (Ayres et al., 2022).

The innermost layer of the MSR is followed by the n2EDM **coil system**, pictured in figure 2.9. Chapter 9 will be dedicated to the characterization of its main component, the B_0 coil. The design of these coils is mostly the work of another PhD student (Flaux, 2019), whose manuscript contains all the references our characterization efforts rely on. In n2EDM, the term coil system generically refers to four sets of coils that can serve very different purposes:

- The B_0 **coil**, its main component, is responsible for producing the 1 µT vertical field that the neutrons and mercury atoms precess around. It is wired horizontally on the inner vertical walls of the MSR (black lines of figure 2.9).
- The 7 **gradient coils** are coils designed to generate specific magnetic field gradients. These are useful for cancelling the main contributions to the non-uniform field. Figure 2.9 shows only one of these as an example: the vertical linear gradient coil (or G_{10} coil in the harmonic description, which will make more sense after chapter 3).
- The 56 **trim coils**, are much smaller square-shaped coils placed on all six inner walls of the MSR (shown in yellow on figure 2.9). These work in conjunction with one another to produce the wider array of magnetic modes demanded by the field optimization process.
- The 4 **RF coils**, in red on figure 2.9, generate as their name indicates the rotating field responsible for the $\pi/2$ flips of the Ramsey cycle.

Deeper inside the apparatus stands an aluminum tank of about $1.6 \times 1.6 \times 1.2\,\mathrm{m}^3$ which will be in vacuum during data-taking. Accordingly, this component is referred to as the **vacuum vessel**. It is visible in figure 2.8 inside the MSR. Vacuum is achieved through pumping *via* vacuum tubes, shown on the right of the vacuum vessel of figure 2.7, opposite to the UCN guides. The precession chambers are installed inside it such that the neutron guides, after having gone through all of the layers of the apparatus, enter the two precession chambers *via* holes in the center of the top and bottom electrodes. The mercury atoms are let in for co-magnetometry

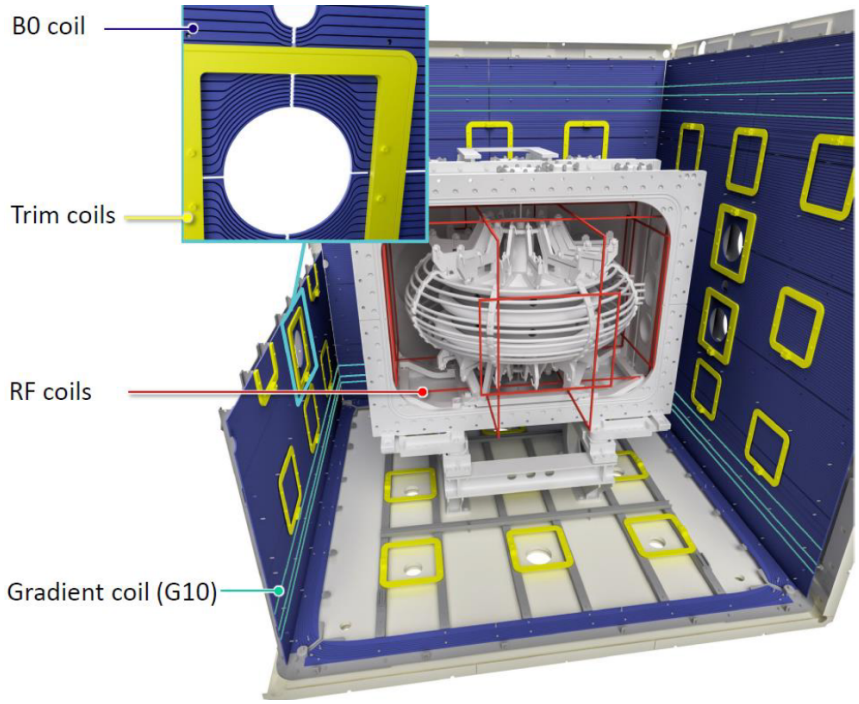

FIGURE 2.9: The n2EDM coil system as presented in the design article (al., 2022). The B_0 coil produces the 1 µT vertical field. The G_{10} coil is one of the seven gradient coils generating specific modes, assisted by the trim coils. The RF coils serve for the $\pi/2$ flips of the Ramsey cycle.

through similar but off-centered holes in the electrodes. Finally, an array of about a hundred **cesium (CS) magnetometers** are mounted above and below the double chamber in order to provide an online measurement of the magnetic field. These were fully designed and assembled by a recent PhD student (Pais, 2021).

2.7 Conclusion

Over the course of this chapter we have introduced n2EDM as one of the most sensitive upcoming experiments on the neutron EDM with its goal of $\Delta d_n \leq 10^{-27}\, e\,\text{cm}$. The apparatus currently under assembly at the Paul Scherrer Institut by the nEDM collaboration inherits from its Sussex/RAL/ILL predecessor a long legacy of successful experimental techniques, most notably the use of Ultra-Cold Neutrons and mercury co-magnetometry. The measurement principle itself however, has remained mostly unchanged since the Ramsey method of separated oscillating fields was introduced in the early 1950's.

Before diving into the description of these techniques, we laid out the very simple core concept of EDM experiments. These measure the precession frequency f_n of polarized neutrons in two electromagnetic configurations: parallel electric and magnetic fields, and anti-parallel fields where the electric field is reversed. Since the precession frequency should carry contributions from both the (huge) magnetic coupling μ_n and the sought-after but tiny electric coupling d_n, the f_n given by opposite configurations should differ slightly by a quantity proportional to the electric coupling. The neutron EDM is thus extracted from the difference of the two precession frequencies.

The bulk of the experimental work relies on the measurement of these precession frequencies. Because of this we went through a step-by-step application of the Ramsey concept to the case of n2EDM. Spin-polarized UCNs are injected into two precession chambers with opposite field configurations. The Ramsey technique is then applied in order to have some of the UCNs change spin-states, with a transition probability, which we re-derived, that depends on the precession frequency f_n. What is actually measured is the asymmetry between the number of up and down spin-states counted by the detectors at the end of the measurement process, for each chamber, which naturally yields f_n. The simultaneous precession frequency measurement for the two chambers allows a very precise extraction of d_n.

This discussion allowed us to highlight two natural yet crucial implications of the Ramsey method, which is that the nEDM sensitivity scales with the number of neutrons N and their precession time T, as $\sigma(d_n) \sim 1/(T\sqrt{N})$. n2EDM promises increased neutron statistics with its much larger precession chambers, shown in 2.2, and deals with the need for a long interaction by using Ultra-Cold Neutrons. We spent a section of this chapter recalling a few important properties of UCNs, the key message being that these are neutrons with a kinetic energy low enough for them to satisfy a full reflection condition at the interface of an appropriate material, at any given incidence angle. This is what allows these particles to be stored for over 180 s in n2EDM's precession chambers.

A third albeit less obvious requirement for n2EDM to reach its targeted sensitivity is a strict control of the magnetic field, both in terms of fluctuations in time and spatial uniformity. As magnetic field control happens to be the subject of this thesis, we dedicated a full section to mercury co-magnetometry. This absolutely essential tool compensates field fluctuations by measuring the ratio of neutron to mercury precession frequencies instead of the neutron frequency alone. Still, the boons of this technique come with a bane: the mercury atoms' precession frequency is shifted by non-uniformities in the magnetic field combined with a relativistic motional field, and this naturally impedes on the extraction of the neutron EDM through the so-called *false EDM*. This in itself drives our need for a more uniform field. Over the course of a general overview of the apparatus we presented the n2EDM coil system but also advanced magnetic shielding devices, the Active Magnetic Shield and the Magnetic Shielding Room, specifically designed to deal with field non-uniformities.

Having examined the core concept of n2EDM and the role that magnetic field control plays in its sensitivity goal, we may now introduce our work which focuses on the control of magnetic uniformity in n2EDM. After thoroughly laying out the n2EDM requirements on its magnetic environment, the next chapter will investigate the symmetries of the B_0 coil in order to uncover the origins of non-uniformities in the magnetic field.

Chapter 3

The challenges of magnetic field uniformity in n2EDM

Contents

This last introductory chapter presents the subject of this thesis: the control of magnetic field uniformity in n2EDM. We will begin by introducing a polynomial decomposition of the field extensively relied on in the collaboration and known as the “harmonic expansion" (section 3.1). We will then explain why a non-uniform field lowers the sensitivity of n2EDM and give the requirements that allow us to reach the desired sensitivity (section 3.2). This section will serve as the central reference for the remaining chapters. As it is responsible for the generation of the experiment’s magnetic field, the B_0 coil will be the focal point of the last section (section 3.3). Here we will propose a novel group-theoretical perspective on the symmetries of the coil system in order to show that, although the generated field is intended to be purely uniform and vertical, one can expect a specific set of non-uniform magnetic “modes” to appear in its harmonic spectrum, depending on the chosen coil geometry. This knowledge will prove paramount to the control of the generated magnetic field discussed in the last chapters of this thesis.

3.1 The harmonic parametrization of the magnetic field

Before we can discuss the uniformity requirements that the n2EDM magnetic field must satisfy, we need to present a systematic way of classifying non-uniformities. This naturally calls for a polynomial development of the magnetic field, which allows one to identify the zero-order modes with the uniform field contribution and the remaining orders with different classes of non-uniformities.

Fortunately the nEDM collaboration has over the years tailored a sophisticated polynomial field expansion, known as the **harmonic expansion**, to its experiment. Here we will briefly recall its construction, as presented in a 2019 paper (Abel et al.,

2019). The general idea is to express each component of the magnetic field as a sum of polynomial functions of different degree l. One such polynomial expansion is the following:

$$\mathbf{B}(x,y,z) = \sum_{l,m} G_{lm}\mathbf{\Pi}_{lm}(x,y,z) \tag{3.1}$$

$$\begin{pmatrix} B_x(x,y,z) \\ B_y(x,y,z) \\ B_z(x,y,z) \end{pmatrix} = \sum_{l,m} G_{lm} \begin{pmatrix} \Pi_{x,lm}(x,y,z) \\ \Pi_{y,lm}(x,y,z) \\ \Pi_{z,lm}(x,y,z) \end{pmatrix}, \tag{3.2}$$

where the entries of $\mathbf{\Pi}_{lm}$ are, for a given m, polynomial functions of degree l, and the G_{lm} are real coefficients. Note that the double-index expansion is not accidental but is as we will soon explain motivated by the form of the field. The polynomial functions are not arbitrarily chosen since the total field $\mathbf{B}$ must satisfy Maxwell's equations. In a region with no current or magnetization, which applies to n2EDM, Gauss's law for magnetism and Ampere's law reduce to:

$$\boldsymbol{\nabla} \cdot \mathbf{B} = 0, \tag{3.3}$$

$$\boldsymbol{\nabla} \times \mathbf{B} = 0. \tag{3.4}$$

Equation (3.4) implies that the field can be written as the gradient of a potential V, with $\mathbf{B} = \boldsymbol{\nabla} V$. Equation (3.3) imposes that this potential is a solution of Laplace's equation $\Delta V = 0$, which in this case is expressed in the spherical coordinate system (ρ, θ, φ):

$$\frac{1}{\rho^2}\frac{\partial}{\partial\rho}\left(\rho^2\frac{\partial V}{\partial\rho}\right) + \frac{1}{\rho^2\sin\theta}\frac{\partial}{\partial\theta}\left(\sin\theta\frac{\partial V}{\partial\theta}\right) + \frac{1}{\rho^2\sin^2\theta}\frac{\partial^2 V}{\partial\varphi^2} = 0. \tag{3.5}$$

The Laplace equation can be solved by separation of variables $V(\rho,\theta,\varphi) = R(\rho)\Theta(\theta)\Phi(\varphi)$. This allows to rewrite equation (3.5) as a sum of terms of independent variables which satisfy

$$\frac{1}{\rho^2 R(\rho)}\frac{\partial}{\partial\rho}\left(\rho^2\frac{\partial R(\rho)}{\partial\rho}\right) = \lambda \tag{3.6}$$

$$\frac{1}{\rho^2\sin\theta\Phi(\varphi)}\frac{\partial}{\partial\theta}\left(\sin\theta\frac{\partial\Theta(\theta)}{\partial\theta}\right) + \frac{1}{\rho^2\sin^2\theta\Theta(\theta)}\frac{\partial^2\Phi(\varphi)}{\partial\varphi^2} = -\lambda, \tag{3.7}$$

with λ a real constant. The convergence of the angular solutions will impose $\lambda = l(l+1)$, with $l \in \mathbb{N}$, leading to l radial solutions of the form

$$R_l(\rho) = a\rho^l + b\rho^{-l-1}, \tag{3.8}$$

but we throw out the ρ^{-l-1} term by requiring that the field be bounded at the origin. As for the angular solutions $Y(\theta,\varphi) \equiv \Theta(\theta)\Phi(\varphi)$, function of the remaining two variables, these will similarly be indexed by two indices l, m, with $-l \leq m \leq l$. These solutions take the form of the so-called *spherical harmonics*, given here as

$$Y_{lm}(\theta,\varphi) = \sqrt{\frac{2l+1}{4\pi}\frac{(l-m)!}{(l+m)!}}P_l^m(\cos\theta)e^{im\varphi}, \tag{3.9}$$

where the P_l^m are the associated Legendre polynomials, given explicitly in appendix A. The real-valued basis of the field potential is constructed by taking the real and

imaginary parts of the spherical harmonics (3.9). With another choice of normalization, the field potential is then written as

$$V_{lm}(\rho,\theta,\varphi) = \frac{(l-1)!(-2)^{|m|}}{(l+|m|)!}\rho^l P_l^{|m|}(\cos(\theta)) \times \begin{cases} \cos(|m|\varphi) & \text{if } m \geq 0 \\ \sin(|m|\varphi) & \text{if } m < 0 \end{cases}. \tag{3.10}$$

The magnetic field $\mathbf{B}$ is finally obtained by differentiation of this potential. In terms of parametrization (3.2) this means that the l-degree polynomial functions contained in $\mathbf{\Pi}_{lm}$, now referred to as the *harmonic polynomials*, are determined by the $l-1$-degree field potential:

$$\mathbf{\Pi}_{l,m} = \boldsymbol{\nabla} V_{l+1,m}. \tag{3.11}$$

Expressing (3.11) in either a cylindrical or a Cartesian coordinate system one can then derive all harmonic polynomials found in appendix A. Their coefficients G_{lm} are referred to as the *generalized gradients*. Lastly, note that in the n2EDM coordinate system, the magnetic field expansion considers as its origin the geometrical center of the coil system, which should correspond to the center of the two precession chambers.

With this convenient tool in hand we can define a (vertically) *uniform field* as a field whose harmonic expansion is $\mathbf{B} = B_0\mathbf{\Pi}_{00}$. Any mode other than $\mathbf{\Pi}_{00}$ is then considered a non-uniformity. The next section will explain which of these are considered problematic w.r.t. to experimental requirements. The final section will show that, although the main component of the coil system, the B_0 coil, is only meant to produce a single magnetic mode $\mathbf{\Pi}_{00}$, a specific set of other modes are allowed by the symmetries of the n2EDM apparatus.

3.2 The n2EDM requirements on magnetic field uniformity

In order to achieve the desired sensitivity of $10^{-27}\,e\,$cm on the measurement of the neutron EDM d_n, a certain number of requirements on the uniformity of the magnetic field must be met. These requirements can be conveniently expressed in the harmonic field language and are split in two broad categories: those related to statistical errors, and those related to systematical errors.

First, magnetic field uniformity has a strong influence on the statistical sensitivity of the precession frequency measurement in n2EDM. By setting the maximal loss in sensitivity to 2% after 180 seconds of neutrons storage, we effectively impose that the generated magnetic field matches two requirements.

Statistical requirement 1: the top-bottom resonance matching condition

$$\left|\frac{\partial B_z}{\partial z}\right| < 0.6\ \text{pT/cm}. \tag{3.12}$$

As explained in section 2.5, we measure the spin asymmetry on the Ramsey resonance curve at a value of the applied frequency f_{RF} that minimizes the statistical error (blue bars of figure 2.6, masked by the points). This requirement ensures that the optimal f_{RF} is as similar as possible between the two chambers. As the two resonance curves shift with the vertical magnetic field, we require that the vertical field gradient stays below a value that minimizes this drift. A 2% loss in sensitivity corresponds to a $0.2 \times \Delta\nu/2$ shift between the two resonance curves. With a precession time $T = 180$s and a vertical distance $H' = 18$cm between the centers of the two

chambers, this corresponds to the maximally allowed vertical gradient coefficient given by (3.12). Note that in the harmonic gradient decomposition, $\frac{\partial B_z}{\partial z}\Big|_{z=0} = G_{10}$ is the main contribution to this vertical gradient. We will rely on this much more convenient coefficient formulation when looking at mapping data.

Statistical requirement 2: vertical field component uniformity

$$\sigma(B_z) < 170\,\text{pT}, \tag{3.13}$$

where $\sigma(B_z) = \sqrt{\langle (B_z - \langle B_z \rangle)^2 \rangle}$. This stems from a requirement on the final neutron spin polarization α after the Ramsey procedure, which corresponds to the amplitude of the Ramsey resonance curve. It turns out that non-uniformities in the vertical field component lead to a depolarization of the neutron spins which in turn reduces the visibility α as time goes. These non-uniformities are described at a given time t by the quantity $b_z(t) = B_z(\mathbf{r}(t)) - \langle B_z(t) \rangle$, which represents the field seen by a neutron or mercury atom moving through the cylindrical volume with a trajectory $\mathbf{r}(t)$. Spin-relaxation theory (Redfield, 1957) tells us that the decay rate of the transverse polarization due to this noise is given, to second order in the perturbation, by

$$\frac{1}{T_2} = \gamma_n^2 \int_0^\infty \langle b_z(t) b_z(t+\tau) \rangle \, d\tau = \gamma_n^2 \langle b_z^2 \rangle \, \tau_c, \tag{3.14}$$

where γ_n is the neutron's gyromagnetic ratio, τ_c is the correlation time, estimated to $\tau_c = 120\,\text{ms}$ in n2EDM, and $\langle b_z(t) b_z(t+\tau) \rangle$ is the auto-correlation of the non-uniform magnetic noise. The angle brackets indicate an average over all particles in the precession chamber, which here amounts to a volume average. The right-hand term tells us that this depolarization is proportional to the average vertical non-uniformity in the (considered static) magnetic field. The upper bound in (3.13) corresponds to a 2% decrease in α due to these non-uniformities after $T = 180\text{s}$ of storage, which yields a decay rate limit $T_2 > 9000\text{s}$. Further details on the origins of this effect are given in section 4.1. The following section will show that, by design of the B_0 coil, only a specific set of modes $\mathbf{\Pi}_{lm}$ should contribute to $\sigma(B_z)$.

Second, the generated magnetic field should be stable enough to allow us to account for systematic errors, and its offline measurement should be accurate enough for the same purpose. As mentioned in section 2.4 of the previous chapter, the most stringent systematical requirement is a limit on the non-negligible mercury-induced false neutron EDM:

$$d^{\text{false}}_{\text{n}\leftarrow\text{Hg}} < 3 \times 10^{-28}\, e\,\text{cm} \tag{3.15}$$

It will become clearer in the next part why this turns into a requirement on the magnetic field. For now let us say that this effect is produced by two different combinations of harmonic modes, one more potent than the other. The first, referred to as the top-bottom gradient G_{TB}, is monitored during data-taking, thus precisely controlled. The second is a combination of all $m = 0$, l-odd G_{lm} generalized gradients that we normalize to first order gradients $\acute{G}_{2k+1}$, and call **phantom modes** specifically because they do not generate a top-bottom gradient. Expressed as a function of the top-bottom gradient and the phantom modes, the false EDM[1] is written as:

[1] Shorthand for mercury-induced false neutron EDM hereafter.

$$d^{\text{false}}_{\text{n}\leftarrow\text{Hg}} = \frac{\hbar\left|\gamma_n\gamma_{\text{Hg}}\right|}{8\pi c^2} R^2 \left(G_{\text{TB}} + \acute{G}_3 + \acute{G}_5 + \acute{G}_7 + \dots\right). \tag{3.16}$$

Notice that this effect scales quadratically with the characteristic size of the precession chamber R, which makes it much more problematic in n2EDM than in nEDM. It is important to point out that all these modes are not controlled in the same way. The third order mode can be monitored online thanks to the cesium magnetometers, while the other two can only be determined offline with magnetic field mapping. By construction, the phantom modes carry all the "invisible" contribution of the magnetic field to the false EDM in the online measurement *via* the top-bottom gradient. It is therefore the task of the offline mapping system to ensure that they are measured accurately enough so as to later be able to either cancel them thanks to auxiliary coils or account for them through a calculation of equation (3.16). This amounts to requiring that the magnetic field satisfies two conditions: one on the generation of the magnetic field, the other on its measurement.

Systematical requirement 1: Phantom mode reproducibility

$$\sigma(\acute{G}_3) < 20\,\text{fT/cm}, \qquad \sigma(\acute{G}_5) < 20\,\text{fT/cm}, \qquad \sigma(\acute{G}_7) < 20\,\text{fT/cm}, \tag{3.17}$$

The quantities above[2] represent the difference between the magnetic field measured before or after data-taking, and the actual magnetic field during data-taking, with values chosen such that each phantom mode generates an error on the false EDM less than the one given by the core systematical requirement (3.15). In practice, we will see in the third part of this thesis that the reproducibility of the phantom modes corresponds to the standard deviation of the phantom modes over different magnetic configurations that mimic the typical field fluctuations before and during data-taking.

Systematical requirement 2: Phantom mode accuracy

$$\delta\acute{G}_3 < 20\,\text{fT/cm}, \qquad \delta\acute{G}_5 < 20\,\text{fT/cm}, \qquad \delta\acute{G}_7 < 20\,\text{fT/cm}, \tag{3.18}$$

Here the condition applies to the accuracy of the magnetic field mapping system. We should not only be able to *generate* a reproducible field, but also be able to *measure* it accurately enough. In this case the error on the phantom modes should be understood as their standard deviation over measurements taken in the exact same magnetic configuration, so that it only reflects the shortcomings of the mapping apparatus

Table 3.1 summarizes the four main conditions laid out above. The analysis of the magnetic field measurements featured in third part of this thesis will show that n2EDM should be able to operate within these requirements.

3.3 Symmetries of the B_0 coil and allowed non-uniformities

While most requirements presented above target specific modes of the harmonic expansion, the condition (3.13) on the vertical uniformity $\sigma(B_z)$ concerns in principle

[2] In this case the σ notation does *not* refer to an RMSE as it does for $\sigma(B_z)$, but to a standard deviation.

all modes of the expansion. As we will now aim to show however, there are reasons to believe that the harmonic spectrum of the vertical field generated by the B_0 coil should be dominated by a well-defined set of modes. The explanation for this resides in the symmetrical design of the coil system. We will define these symmetries as elements of a symmetry group, establish the symmetry of the coil system as a representation of this group, and finally look for another representation which describes the symmetries of the generated magnetic field.

3.3.1 Symmetry group of the B_0 coil

Our starting point will be the most intuitive picture of the B_0 coil, considered as a purely geometrical object consisting of the blue wires visible in figure 2.9. Figure 3.1 provides a drawing of the B_0 coil alone, where we see that the current loops (in grey) are wired horizontally along the walls of a cube - the inner layer of the MSR - in order to produce a vertical field, and go around several other parts of the apparatus (in color). In this chapter we focus on an idealized version of the coil where we disregard these extra features. This object turns out to be invariant under a set of transformations defined as *symmetries* of the B_0 coil. Considering that the coil is centered at the origin of the n2EDM coordinate system, one can intuitively work out these symmetries to be:

- I: the identity.
- P: the point reflection with respect to the origin.
- R_z: the $\pi/2$ rotation around the z axis.
- R_x^2, R_y^2, R_z^2: the π rotations around the x, y, z axes.
- $\sigma_x, \sigma_y, \sigma_z$: the reflections on planes orthogonal to the x, y, z axes.
- and all combinations of the above.

In our introductory picture the B_0 coil is just a set of points in the euclidean space, so these transformations are 3×3 invertible matrices that send a point in space to

Statistical requirements	
Vertical uniformity $\sigma(B_z)$	< 170 pT
Top-bottom resonance matching condition $\lvert G_{10}\rvert$	< 0.6 pT/cm
Systematical requirements	
$\sigma(\acute{G}_{2k+1})$ on field generation	< 20 fT/cm
$\delta\acute{G}_{2k+1}$ on field measurement	< 20 fT/cm

TABLE 3.1: n2EDM requirements on magnetic field generation for statistical and systematical errors. The systematical requirements concerns the error on the false EDM generated by phantom modes up to degree 7, both due to non-reproducibility of the field (field generation) and to mapping inaccuracy (field measurement).

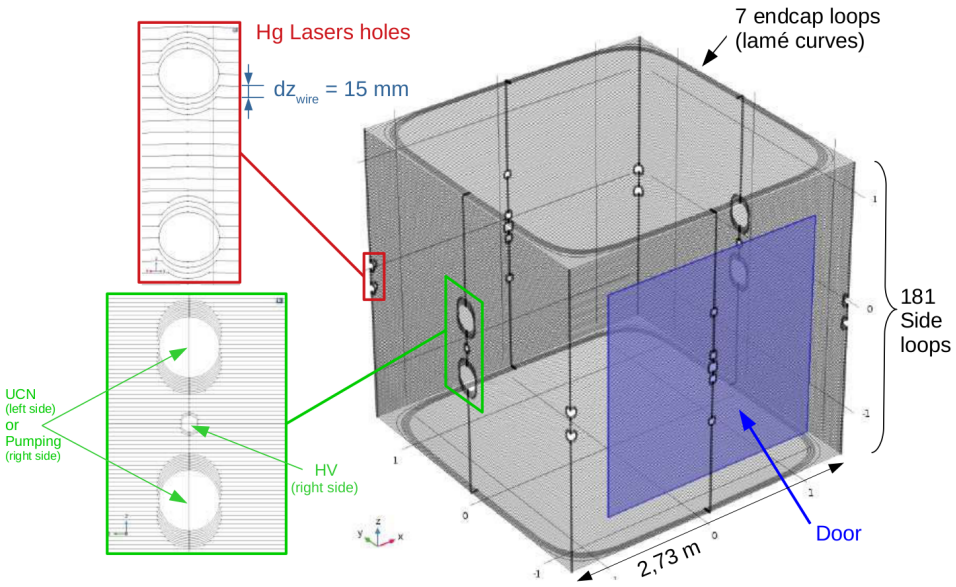

FIGURE 3.1: Schematic drawing of the B_0 coil as presented in Pierrick Flaux's thesis (Flaux, 2019). In the ideal geometry scenario, in which we disregard the presence of symmetry-breaking features (in blue, green, and red), the coil is invariant under all transformations in $\mathcal{D}_{4h}$. One can visually check that the three generating transformations σ_x, σ_z, and R_z, are symmetries of the B_0 coil. Non-ideal geometries are discussed in chapter 9.

another point in space. With all possible combinations of the 9 symmetries presented above, we find a set of 16 symmetries of the B_0 coil that we write

$$\mathcal{D}_{4h} = \{I, P, \sigma_x, \sigma_y, \sigma_z, R_x^2, R_y^2, R_z^2, R_z, R_z^{-1}, \sigma_{xy}, \sigma_{-xy}, R_z', R_z'^{-1}, \sigma_{xy}', \sigma_{-xy}'\}, \tag{3.19}$$

where the name $\mathcal{D}_{4h}$ alludes to the equivalent point group used by chemists. Explicitly these are:

$$I = \begin{pmatrix} 1 & 0 & 0 \\ 0 & 1 & 0 \\ 0 & 0 & 1 \end{pmatrix} \qquad P = \begin{pmatrix} -1 & 0 & 0 \\ 0 & -1 & 0 \\ 0 & 0 & -1 \end{pmatrix}$$

$$\sigma_x = \begin{pmatrix} -1 & 0 & 0 \\ 0 & 1 & 0 \\ 0 & 0 & 1 \end{pmatrix} \qquad \sigma_y = \begin{pmatrix} 1 & 0 & 0 \\ 0 & -1 & 0 \\ 0 & 0 & 1 \end{pmatrix} \qquad \sigma_z = \begin{pmatrix} 1 & 0 & 0 \\ 0 & 1 & 0 \\ 0 & 0 & -1 \end{pmatrix}$$

$$R_x^2 = \begin{pmatrix} 1 & 0 & 0 \\ 0 & -1 & 0 \\ 0 & 0 & -1 \end{pmatrix} \qquad R_y^2 = \begin{pmatrix} -1 & 0 & 0 \\ 0 & 1 & 0 \\ 0 & 0 & -1 \end{pmatrix} \qquad R_z^2 = \begin{pmatrix} -1 & 0 & 0 \\ 0 & -1 & 0 \\ 0 & 0 & 1 \end{pmatrix}$$

$$R_z = \begin{pmatrix} 0 & -1 & 0 \\ 1 & 0 & 0 \\ 0 & 0 & 1 \end{pmatrix} \quad R_z^{-1} = \begin{pmatrix} 0 & 1 & 0 \\ -1 & 0 & 0 \\ 0 & 0 & 1 \end{pmatrix} \quad \sigma_{xy} = \begin{pmatrix} 0 & 1 & 0 \\ 1 & 0 & 0 \\ 0 & 0 & 1 \end{pmatrix} \quad \sigma_{-xy} = \begin{pmatrix} 0 & -1 & 0 \\ -1 & 0 & 0 \\ 0 & 0 & 1 \end{pmatrix}$$

$$R'_z = \begin{pmatrix} 0 & -1 & 0 \\ 1 & 0 & 0 \\ 0 & 0 & -1 \end{pmatrix} \quad R'^{-1}_z = \begin{pmatrix} 0 & 1 & 0 \\ -1 & 0 & 0 \\ 0 & 0 & -1 \end{pmatrix} \quad \sigma'_{xy} = \begin{pmatrix} 0 & 1 & 0 \\ 1 & 0 & 0 \\ 0 & 0 & -1 \end{pmatrix} \quad \sigma'_{-xy} = \begin{pmatrix} 0 & -1 & 0 \\ -1 & 0 & 0 \\ 0 & 0 & -1 \end{pmatrix} \tag{3.20}$$

The fact that all combinations of these symmetries are also symmetries hints to a group structure. Indeed, these transformations together with matrix multiplication $(\mathcal{D}_{4h}, \times)$ possess the mathematical structure of a group, defined entirely by the Cayley table 3.2, which shows all combinations of elements within this group. One may check from this table that all group axioms are satisfied: the identity element is I, each element $M \in \mathcal{D}_{4h}$ has an inverse element $M^{-1} \in \mathcal{D}_{4h}$, and associativity holds. The definitions related to groups and group representations that are the most useful to this discussion are recalled in the second section of appendix B. Furthermore, a few useful remarks can be made:

$\times$	I	P	σ_x	σ_y	σ_z	R_x^2	R_y^2	R_z^2	R_z	R_z^{-1}	σ_{xy}	σ_{-xy}	R'_z	R'^{-1}_z	σ'_{xy}	σ'_{-xy}
I	I	P	σ_x	σ_y	σ_z	R_x^2	R_y^2	R_z^2	R_z	R_z^{-1}	σ_{xy}	σ_{-xy}	R'_z	R'^{-1}_z	σ'_{xy}	σ'_{-xy}
P	P	I	R_x^2	R_y^2	R_z^2	σ_x	σ_y	σ_z	R'^{-1}_z	R'_z	σ'_{-xy}	σ'_{xy}	R_z^{-1}	R_z	σ_{-xy}	σ_{xy}
σ_x	σ_x	R_x^2	I	R_z^2	R_y^2	P	σ_z	σ_y	σ_{xy}	σ_{-xy}	R_z	R_z^{-1}	σ'_{xy}	σ'_{-xy}	R'_z	R'^{-1}_z
σ_y	σ_y	R_y^2	R_z^2	I	R_x^2	σ_z	P	σ_x	σ_{-xy}	σ_{xy}	R_z^{-1}	R_z	σ'_{-xy}	σ'_{xy}	R'^{-1}_z	R'_z
σ_z	σ_z	R_z^2	R_y^2	R_x^2	I	σ_y	σ_x	P	R'_z	R'^{-1}_z	σ'_{xy}	σ'_{-xy}	R_z	R_z^{-1}	σ_{xy}	σ_{-xy}
R_x^2	R_x^2	σ_x	P	σ_z	σ_y	I	R_z^2	R_y^2	σ'_{-xy}	σ'_{xy}	R'^{-1}_z	R'_z	σ_{-xy}	σ_{xy}	R_z^{-1}	R_z
R_y^2	R_y^2	σ_y	σ_z	P	σ_x	R_z^2	I	R_x^2	σ'_{xy}	σ'_{-xy}	R'_z	R'^{-1}_z	σ_{xy}	σ_{-xy}	R_z	R_z^{-1}
R_z^2	R_z^2	σ_z	σ_y	σ_x	P	R_y^2	R_x^2	I	R_z^{-1}	R_z	σ_{-xy}	σ_{xy}	R'^{-1}_z	R'_z	σ'_{-xy}	σ'_{xy}
R_z	R_z	R'^{-1}_z	σ_{-xy}	σ_{xy}	R'_z	σ'_{xy}	σ'_{-xy}	R_z^{-1}	R_z^2	I	σ_x	σ_y	P	σ_z	R_y^2	R_x^2
R_z^{-1}	R_z^{-1}	R'_z	σ_{xy}	σ_{-xy}	R'^{-1}_z	σ'_{-xy}	σ'_{xy}	R_z	I	R_z^2	σ_y	σ_x	σ_z	P	R_x^2	R_y^2
σ_{xy}	σ_{xy}	σ'_{-xy}	R_z^{-1}	R_z	σ'_{xy}	R'_z	R'^{-1}_z	σ_{-xy}	σ_y	σ_x	I	R_z^2	R_x^2	R_y^2	σ_x	P
σ_{-xy}	σ_{-xy}	σ'_{xy}	R_z	R_z^{-1}	σ'_{-xy}	R'^{-1}_z	R'_z	σ_{xy}	σ_x	σ_y	R_z^2	I	R_y^2	R_x^2	P	R_z^2
R'_z	R'_z	R_z^{-1}	σ'_{-xy}	σ'_{xy}	R_z	σ_{xy}	σ_{-xy}	R'^{-1}_z	P	σ_z	R_y^2	R_x^2	R_z^2	I	σ_x	σ_y
R'^{-1}_z	R'^{-1}_z	R_z	σ'_{xy}	σ'_{-xy}	R_z^{-1}	σ_{-xy}	σ_{xy}	R'_z	σ_z	P	R_x^2	R_y^2	I	R_z^2	σ_y	σ_x
σ'_{xy}	σ'_{xy}	σ_{-xy}	R'^{-1}_z	R'_z	σ_{xy}	R_z	R_z^{-1}	σ'_{-xy}	R_x^2	R_y^2	σ_z	P	σ_y	σ_x	I	R_z^2
σ'_{-xy}	σ'_{-xy}	σ_{xy}	R'_z	R'^{-1}_z	σ_{-xy}	R_z^{-1}	R_z	σ'_{xy}	R_y^2	R_x^2	P	σ_z	σ_x	σ_y	R_z^2	I

TABLE 3.2: Cayley table of the $(\mathcal{D}_{4h}, \times)$ group.

- $\mathcal{D}_{4h}$ is non-abelian.
- $\mathcal{D}_{4h}$ is a sub-group of the *orthogonal group* $\mathcal{O}(3) = \{M \in GL(\mathbb{R}^3) \mid M^\intercal M = I\}$, where $GL(\mathbb{R}^3)$ refers to the general linear group of $\mathbb{R}^3$, consisting of all invertible 3×3 matrices.
- The group elements R_z, σ_x, σ_z are *generators* of $\mathcal{D}_{4h}$ (definition B.1.3). Indeed, consider the subgroup of $\mathcal{D}_{4h}$ generated by R_z and denoted $\langle R_z \rangle = \{I, R_z, R_z^2, R_z^{-1}\}$. Then we can show by applying σ_x and σ_z to $\langle R_z \rangle$ that the subgroup generated by R_z, σ_x and σ_z is the group itself: $\langle R_z, \sigma_x, \sigma_z \rangle = \mathcal{D}_{4h}$. Note that this choice of generators is not unique.

So how do these group symmetry considerations help us in determining what kind of magnetic field the B_0 coil will generate? We know from basic electromagnetism that there is a causal relationship between the geometrical shape of a coil and the magnetic field that it produces. Following the Curie principle that symmetries in the causes are to be found in the effects, the geometrical symmetries in $\mathcal{D}_{4h}$ will somehow translate to symmetries in the magnetic field. As we will now see, this shift is operated by representations of the $\mathcal{D}_{4h}$ group.

3.3.2 Current representation of the coil symmetry group

Before we move to a magnetic representation, we need to consider the B_0 coil not as a simple geometrical object but as a set of currents and determine what the corresponding symmetries are. The coil's *current system* can be thought of as a vector field depicting a current flow through a rectangular box of height H and base $L \times L$:

$$\mathbf{I}(x,y,z) = \begin{cases} (0, I_0, 0) & \text{if } x = L,\ |y| < L, \text{ and } |z| < H \\ (-I_0, 0, 0) & \text{if } y = L,\ |x| < L, \text{ and } |z| < H \\ (0, -I_0, 0) & \text{if } x = -L,\ |y| < L, \text{ and } |z| < H \\ (I_0, 0, 0) & \text{if } y = -L,\ |x| < L, \text{ and } |z| < H \end{cases} \tag{3.21}$$

The connection between this current system and the geometrical coil is made by considering that the current system lives in a vector space V_c, on which act elements of a **current representation** (V_c, ρ_c) of the group $\mathcal{D}_{4h}$. This representation is defined as:

$$\rho_c : \mathcal{D}_{4h} \longrightarrow GL(V_c), \tag{3.22}$$

where the elements of $\rho_c(\mathcal{D}_{4h})$ satisfy by definition

$$\rho_c(M_1 M_2) = \rho_c(M_1)\rho_c(M_2), \forall M_1, M_2 \in \mathcal{D}_{4h}. \tag{3.23}$$

In short this means that the elements of this representation are linear transformations of V_c that combine according to the Cayley table above.

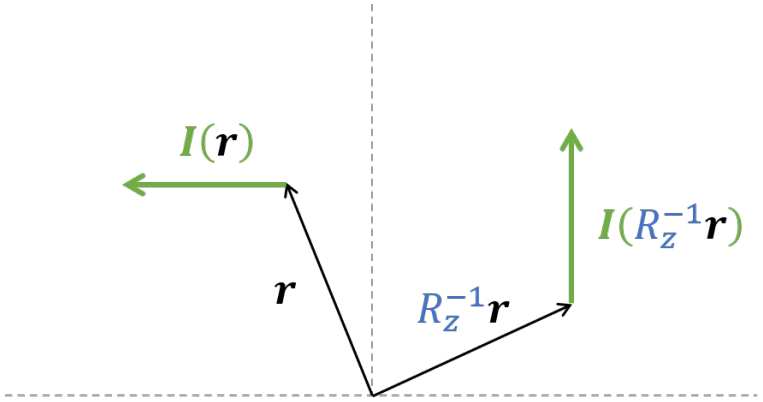

FIGURE 3.2: The current I evaluated at position r and at a $-\pi/2$ rotated position $R_z^{-1}r$.

So how is the current system transformed under the symmetries of the B_0 coil? Using elements M of the geometrical group $\mathcal{D}_{4h}$, we can write the transformed current $\mathbf{I}'(\mathbf{r})$ as the rotation of a current evaluated at a position taken before rotation:

$$\mathbf{I}'(\mathbf{r}) = M\mathbf{I}(M^{-1}\mathbf{r}). \tag{3.24}$$

Figure 3.2 should give a clearer picture of this transformation with $M = R_z$. In this case, $\mathbf{I}'(\mathbf{r})$ is obtained by applying R_z to $\mathbf{I}(R_z^{-1}\mathbf{r})$. Because of the coil symmetries it turns out that $\mathbf{I}'(\mathbf{r})$ is equal to $\mathbf{I}(\mathbf{r})$. What is left to do is to determine linear transformations $\rho_c(M)$, with

$$\rho_c(M) : \mathbf{I}(\mathbf{r}) \longmapsto \mathbf{I}'(\mathbf{r}) = \rho_c(M)\mathbf{I}(\mathbf{r}) \tag{3.25}$$

that are equivalent to the transformations given by (3.24). In other words we solve

$$\rho_c(M)\mathbf{I}(\mathbf{r}) = M\mathbf{I}(M^{-1}\mathbf{r}) \tag{3.26}$$

for all $\rho_c(M), M \in \mathcal{D}_{4h}$, using $\mathbf{I}(\mathbf{r})$ from equation (3.21). It is enough to do this for the three chosen group generators R_z, σ_z, and σ_x and then use table 3.2 to determine all other linear transformations. The results are stored in the so-called *character table* 3.3.

irrep	$Cl(I)$	$Cl(P)$	$Cl(\sigma_x)$	$Cl(\sigma_z)$	$Cl(R_x^2)$	$Cl(R_z^2)$	$Cl(R_z)$	$Cl(\sigma_{xy})$	$Cl(R_z')$	$Cl(\sigma_{xy}')$
ρ_c	1	1	-1	1	-1	1	1	-1	1	-1

TABLE 3.3: Character table of $\rho_c(\mathcal{D}_{4h})$. The characters of the generators conjugacy classes (see definitions B.1.11 and B.1.4), highlighted in blue, sufficiently describe the character of the entire group. $Cl(\sigma_x) = \{\sigma_x, \sigma_y\}$, $Cl(R_x^2) = \{R_x^2, R_y^2\}$, $Cl(\sigma_{xy}) = \{\sigma_{xy}, \sigma_{-xy}\}$, $Cl(R_z) = \{R_z, R_z^{-1}\}$, and so on for prime transformations...

Note that:

- We refer to the transformations with character $\rho_c(M) = 1$ as **symmetries** of the coil system, and to those with character $\rho_c(M) = -1$ as **anti-symmetries**.
- $\rho_c(M) = \pm 1$ for all $M \in \mathcal{D}_{4h}$, so ρ_c is a dimension 1 representation. It is then an irreducible representation or *irrep* (by definition B.1.9).

From now on we will consider the character given by the ρ_c row of table 3.3 as the symmetry of the B_0 coil system. Our goal is now to find irreps describing the magnetic field that share the same character as ρ_c, or in other words, symmetries of the magnetic field inherited from symmetries of the B_0 coil.

3.3.3 Magnetic representation of the coil symmetry group

The magnetic field should instinctively transform similarly to the current field in (3.24). However $\mathbf{B}$ is a pseudo-vector so this doesn't quite work out for all symmetries M and we need to introduce a $\det(M)$ factor into the expression for $\mathbf{B}'$, as such:

$$\mathbf{B}'(\mathbf{r}) = \det(M)M\mathbf{B}(M^{-1}r). \tag{3.27}$$

One way to understand this is to see that if a so-called improper transformation, such as a reflection σ, is a symmetry of a current loop, then it is an anti-symmetry of the magnetic field generated by that current. The determinant $\det(\sigma)$ is thus introduced to account for the sign change of improper transformations, and sign preservation of proper transformations. Just as before, our goal is to find a representation ρ_b of $\mathcal{D}_{4h}$ on a vector space V_b where the magnetic field lives, which we will refer to as the

magnetic representation. This is done by looking for linear transformations

$$\rho_b(M) : \mathbf{B}(\mathbf{r}) \longmapsto \mathbf{B}'(\mathbf{r}) = \rho_b(M)\mathbf{B}(\mathbf{r}) \tag{3.28}$$

equivalent to (3.27), again by solving

$$\rho_b(M)\mathbf{B}(\mathbf{r}) = \det(M)M\mathbf{B}(M^{-1}\mathbf{r}) \tag{3.29}$$

for all $M \in \mathcal{D}_{4h}$. This process was straightforward for the current representation because we knew what $\mathbf{I}(\mathbf{r})$ looked like. In the case of magnetic representation we should determine the $\rho_b(M)$ for all possible magnetic fields $\mathbf{B}(\mathbf{r})$. One generic approach to this task is to introduce a parametrization of the magnetic field and determine the magnetic representation for each element of the expansion.

Before engaging in this tedious process, we can try to figure out what a magnetic field that preserves the symmetries of the B_0 coil would look like. To do this we impose $\rho_b(M) = \rho_c(M)$ for all $M \in \mathcal{D}_{4h}$, and look for fields that satisfy equation (3.29). Let us briefly detail this process for the three generators.

(i) For σ_x we want $\rho_b(\sigma_x) = -1$ (see table 3.3). Equation (3.29) yields:

$$\begin{pmatrix} B_x \\ B_y \\ B_z \end{pmatrix}(x,y,z) = \begin{pmatrix} -B_x \\ B_y \\ B_z \end{pmatrix}(-x,y,z) \tag{3.30}$$

(ii) For σ_z we want $\rho_b(\sigma_z) = 1$. Equation (3.29) yields:

$$\begin{pmatrix} B_x \\ B_y \\ B_z \end{pmatrix}(x,y,z) = \begin{pmatrix} -B_x \\ -B_y \\ B_z \end{pmatrix}(x,y,-z) \tag{3.31}$$

(iii) For R_z we want $\rho_b(R_z) = 1$. Equation (3.29) yields:

$$\begin{pmatrix} B_x \\ B_y \\ B_z \end{pmatrix}(x,y,z) = \begin{pmatrix} -B_y \\ B_x \\ B_z \end{pmatrix}(y,-x,z) \tag{3.32}$$

We have determined a set of conditions on the shape of the magnetic field that preserves the symmetries of the B_0 coil. Let us briefly try to guess the shape of the B_0 field by applying these conditions to a completely arbitrary polynomial expansion of the field

$$\mathbf{B} = \mathbf{\Pi}'_0 + \mathbf{\Pi}'_1 + \mathbf{\Pi}'_2, \tag{3.33}$$

where the $\mathbf{\Pi}'_l = (\Pi'_{x,l}, \Pi'_{y,l}, \Pi'_{z,l})$ are polynomials of degree l. We start with the zeroth degree polynomial $\mathbf{\Pi}'_0$. Since B_x and B_y must be odd functions of z they cannot have a non-zero constant term. B_z must be even in z so it can. We thus recover a uniform field of the form $\mathbf{\Pi}'_0 = (0,0,a)$, with a a real coefficient. It is easy to check that no first degree polynomial satisfies all three conditions at the same time. Moving to the second degree polynomial, consider for each coordinate $i = x,y,z$ the most general polynomial function

$$\Pi'_{i,2} = a_i xy + b_i xz + c_i yz + d_i x^2 + e_i y^2 + f_i z^2, \tag{3.34}$$

with $a_i, b_i, c_i, d_i, e_i, f_i$ real coefficients. Regarding $\Pi'_{x,2}$, condition (3.30) selects only the x-odd terms, condition (3.31) selects among those the z-odd terms, so $\Pi'_{x,2} = b_x xz$. The same reasoning leads to $\Pi'_{y,2} = b_y yz$. Applying condition (3.32) to both polynomials sets $b_x = b_y$. Similarly we find $\Pi'_{z,2} = d_z x^2 + e_z y^2 + f_z z^2$. The second degree polynomial field is then of the form

$$\mathbf{B}(x,y,z) = \begin{pmatrix} 0 \\ 0 \\ a \end{pmatrix} + \begin{pmatrix} bxz \\ byz \\ cx^2 + dy^2 + ez^2 \end{pmatrix}, \tag{3.35}$$

As mentioned earlier, the coefficients a, b, c, d, e are constrained by requiring that the field satisfies Gauss' and Ampere's laws in a region with not current or magnetization. Plugging in our polynomial expansion (3.35) into equation (3.3) we net the condition $e = -b$. Equation (3.4) imposes $2d = b$ and $2c = b$. The Maxwellian field is then

$$\mathbf{B}(x,y,z) = a \begin{pmatrix} 0 \\ 0 \\ 1 \end{pmatrix} + b \begin{pmatrix} xz \\ yz \\ (x^2 + y^2)/2 - z^2 \end{pmatrix}, \tag{3.36}$$

and must correspond to a combination of modes of the harmonic expansion given in appendix A. Looking at the zero and second order polynomials of table A.2 we find that the symmetry preserving harmonic field expansion, up to order 2, is

$$\mathbf{B} = G_{00}\mathbf{\Pi}_{00} + G_{20}\mathbf{\Pi}_{20}. \tag{3.37}$$

What have just found an example of a non-uniform field that conserves the symmetries of the B_0 coil. The uniform $\mathbf{\Pi}_{00}$ mode is of course expected to appear, but more noteworthy is the presence of a non-uniform mode, $\mathbf{\Pi}_{20}$. These modes are said to be **allowed** by the symmetries of the coil, in that the existence of a magnetic field consisting of these modes does not violate the symmetries in $\mathcal{D}_{4h}$. The modes that do violate these symmetries are said to be **forbidden**.

Instead of pushing this naive procedure to further polynomial degrees, we will now replace the magnetic field with its harmonic expansion and present a generic way of determining which magnetic modes, apart from $\mathbf{\Pi}_{20}$, are allowed by the symmetries of the B_0 coil.

3.3.4 Harmonic representations of the coil symmetry group

In light of the harmonic parametrization, we can turn equation (3.29) into a set of equations on each harmonic mode in order to determine which of these are allowed by the coil symmetry group $\mathcal{D}_{4h}$. For convenience we rewrite the harmonic expansion in matrix form:

$$\mathbf{B}(\mathbf{r}) = \Pi(\mathbf{r})\mathbf{G}, \tag{3.38}$$

where $\mathbf{G} = (G_{0,-1}, G_{0,0}, G_{0,1}, G_{1,-2}, \ldots, G_{L,L+1})$ is a vector of length $n = (L+1)(L+3)$, with L the maximum l-order of the expansion, and $\Pi(\mathbf{r})$ is a $3 \times n$ matrix in which the harmonic polynomials are stored (one row for each coordinate). Using this expansion we can now determine the character of a final representation ρ_h whose elements act on the harmonic gradient vector $\mathbf{G} \in \mathbb{R}^n$. We will call this representation $(\mathbb{R}^n, \rho_h)$ the **harmonic representation** of the $\mathcal{D}_{4h}$ group. Plugging (3.38) in equation

(3.29), we determine the elements of this representation by solving

$$\Pi(\mathbf{r})\rho_h(M)\mathbf{G} = \det(M)M\Pi(M^{-1}\mathbf{r})\mathbf{G} \tag{3.39}$$

for the representation of the three group generators σ_x, σ_z, R_z. Using appendix table A.2 we can show that the $\rho_h(M)$, $M = \sigma_x, \sigma_z, R_z$, are equivalent to block-diagonal $n \times n$ matrices (equivalence is to be understood as in B.1.7). This implies that ρ_h is decomposable in a direct sum of irreducible representations (one block for each irrep), each of these acting on a subset of $\mathbf{G}$. The dimension of each irrep corresponds to the rank of the matrix block. Regarding $\rho_h(\sigma_x)$ and $\rho_h(\sigma_z)$ these irreps are all of dimension 1 and act on a single G_{lm}. The left-hand table of figure 3.4 gives the values of the rank-1 matrices as a function of the harmonic indices l and m. Regarding $\rho_h(R_z)$ however, the irreps are of dimensions 1 and 2. The second dimension irreps are rank-2 matrices that act on couples $(G_{lm}, G_{l,-m})$, as shown by the right-hand table of 3.4. Recall that the current irrep ρ_c is of dimension 1, meaning harmonic modes transformed by dimension 2 irreps, which in this case are m-odd, are not allowed by the symmetries of the coil.

m	σ_x	σ_y	σ_z
$m \geq 0$	$(-1)^{m+1}$	-1	$(-1)^{l+m}$
$m < 0$	$(-1)^{m}$	1	$(-1)^{l+m}$

m	R_z
$0+4n$	1
$(1+4n, -1-4n)$	$\begin{matrix} 0 & 1 \\ -1 & 0 \end{matrix}$
$2+4n$	-1
$(3+4n, -3-4n)$	$\begin{matrix} 0 & -1 \\ 1 & 0 \end{matrix}$

m	σ_x	σ_y	σ_z	R_z
$0+4n$	-1	-1	1	1
$(1+4n, -1-4n)$	$\begin{matrix} 1 & 0 \\ 0 & -1 \end{matrix}$	$\begin{matrix} -1 & 0 \\ 0 & 1 \end{matrix}$	$(-1)^{l+1}\mathbb{I}_2$	$\begin{matrix} 0 & 1 \\ -1 & 0 \end{matrix}$
$2+4n$	-1	-1	$(-1)^{l}$	-1
$-2-4n$	1	1	$(-1)^{l}$	-1
$(3+4n, -3-4n)$	$\begin{matrix} 1 & 0 \\ 0 & -1 \end{matrix}$	$\begin{matrix} -1 & 0 \\ 0 & 1 \end{matrix}$	$(-1)^{l+1}\mathbb{I}_2$	$\begin{matrix} 0 & -1 \\ 1 & 0 \end{matrix}$
$-4-4n$	1	1	$(-1)^{l}$	1

TABLE 3.4: Harmonic representations of the three reflections (upper-left table), $\pi/2$ z-axis rotation (upper-right table), and both combined (bottom table), of the $\mathcal{D}_{4h}$ group, for all harmonic indices l and m, with $n \in \mathbb{N}$. The tables should be read as follows: for a given transformation M, the matrix $\rho_h(M)$ is block-diagonal, with each rank 1 block acting on a single entry $G_{l,m}$ of $\mathbf{G}$, and each rank 2 block acting on a couple $(G_{l,m}, G_{l,-m})$ of $\mathbf{G}$. The columns correspond to different transformations M, and the lines to distinct blocks of the matrix $\rho_h(M)$.

Overall, $\rho_h(\mathcal{D}_{4h})$ is a direct sum of irreps of dimensions 1 and 2, which are indexed in the bottom table of 3.4 for different values of l and m. The result we care about for our investigation on the symmetries of the B_0 coil is featured in table 3.3, which gives the character of these irreps ρ_{lm}, or more explicitly the traces of the matrices $\rho_{lm}(M)$, for the group generators. For first dimension irreps these are just ± 1 factors that, for a given symmetry, act on a specific set of G_{lm} just as the symmetry acts on the coil. Figure 3.3 also features a visual representation of the harmonic spectrum, decomposed in the 8 subspaces of $\mathbb{R}^n$ associated to the 8 harmonic irreps given by the table above. We note that:

- One can verify that the harmonic representations are indeed irreps by applying the orthogonality theorem B.1.1 to the representation characters found in the cells of table 3.3.
- There are 8 inequivalent irreps of dimension 1, and 2 inequivalent irreps of dimension 2, which make up the 8 lines of table 3.3. The linear map between equivalent dimension 1 irreps is trivially 1. For dimension 2 irreps, consider for instance representations ρ_{21} and ρ_{23}. These can be shown to be equivalent by considering the invertible linear map $T = \begin{pmatrix} -1 & 0 \\ 0 & 1 \end{pmatrix}$. Then for all $M \in \mathcal{D}_{4h}$, we can show using table 3.4 that $\rho_{23}(M) = T\rho_{23}(M)T^{-1}$.

For now, what we can conclude from table 3.3 is that the only harmonic irrep that shares the same character as the current irrep ρ_c is ρ_{00} (dark green line). This implies that modes $\{\mathbf{\Pi}_{2k,4n}\}_{k,n\in\mathbb{N}}$, affected by irreps equivalent to ρ_{00} in the group-theoretical sense, are allowed by the B_0 coil symmetry. For $l > 0$ these are non-uniform modes, which we expect to appear in the coil's harmonic spectrum. The modes are also displayed in dark green in the drawing of the harmonic spectrum 3.3. We can check that a polynomial expansion of the field up to order 2 among modes allowed by the coil's symmetry indeed consists of only $\mathbf{\Pi}_{00}$ and $\mathbf{\Pi}_{20}$, as predicted in the previous section by equation (3.37). For a visual of representation of these symmetrically allowed modes, one may turn to figure 3.4 where are plotted the first few modes affected by $\rho_{2k,4n}$ in the horizontal plane at $z = 0$. It is then easy to verify through equation (3.29) that these are indeed anti-symmetries of σ_x and σ_y, and symmetries of R_z.

irrep	l	m	$Cl(\sigma_x)$	$Cl(\sigma_z)$	$Cl(R_z)$
$\rho_{0,0}$	$2k$	$0+4n$	-1	1	1
$\rho_{0,2}$	$2k$	$2+4n$	-1	1	-1
$\rho_{0,-2}$	$2k$	$-2-4n$	1	1	-1
$\rho_{0,-4}$	$2k$	$-4-4n$	1	1	1
$\rho_{1,0}$	$2k+1$	$0+4n$	-1	-1	1
$\rho_{1,2}$	$2k+1$	$2+4n$	-1	-1	-1
$\rho_{1,-2}$	$2k+1$	$-2-4n$	1	-1	-1
$\rho_{1,-4}$	$2k+1$	$-4-4n$	1	-1	1
$\mathrm{Tr}[\rho_{0,1}]$	$2k$	$(1+2n,-1-2n)$	0	-2	0
$\mathrm{Tr}[\rho_{1,1}]$	$2k+1$	$(1+2n,-1-2n)$	0	2	0

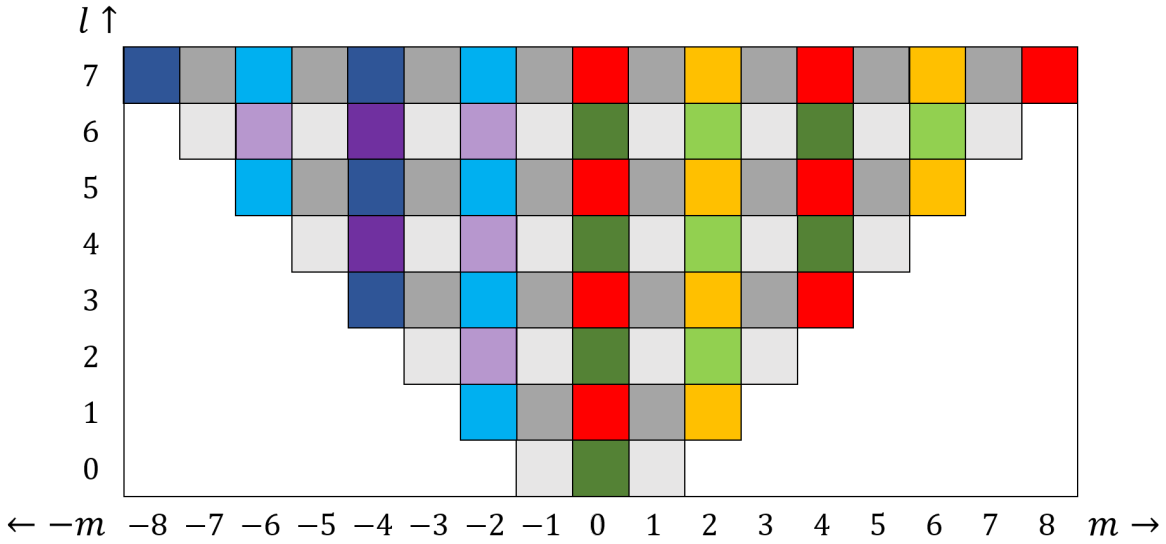

FIGURE 3.3: Top: character table of the 3 generators of the $\mathcal{D}_{4h}$ group, for all 8 inequivalent harmonic irreps. In each row, the irreps indexed by l and m, with $k, n \in \mathbb{N}$, are all equivalent. Bottom: visual decomposition of the harmonic modes in 8 subspaces of $\mathbb{R}^n$ acted on by the 8 harmonic irreps.

3.4 Conclusion

We began this chapter by a technical but unavoidable step in any discussion about magnetic fields in n2EDM, which is the introduction to the harmonic parametrization. Given some polynomial expansion of the magnetic field on a basis of polynomials $\mathbf{\Pi}_{lm}$, with associated coefficients, or *generalized gradients*, G_{lm}, Maxwell's equations grant an explicit form to these polynomials, summarized in A.

We were then able to present in the appropriate language the four main requirements that the n2EDM magnetic field must satisfy in order to achieve the desired sensitivity. Two of these are related to statistics and generated by non-uniform modes of the harmonic field spectrum, while the two other are constrained by a dire systematic effect, the mercury-induced false neutron EDM, which is generated by an intricate combination of non-uniform magnetic modes. The summary of those requirements in table 3.1 will serve as an indispensable reference for the later parts

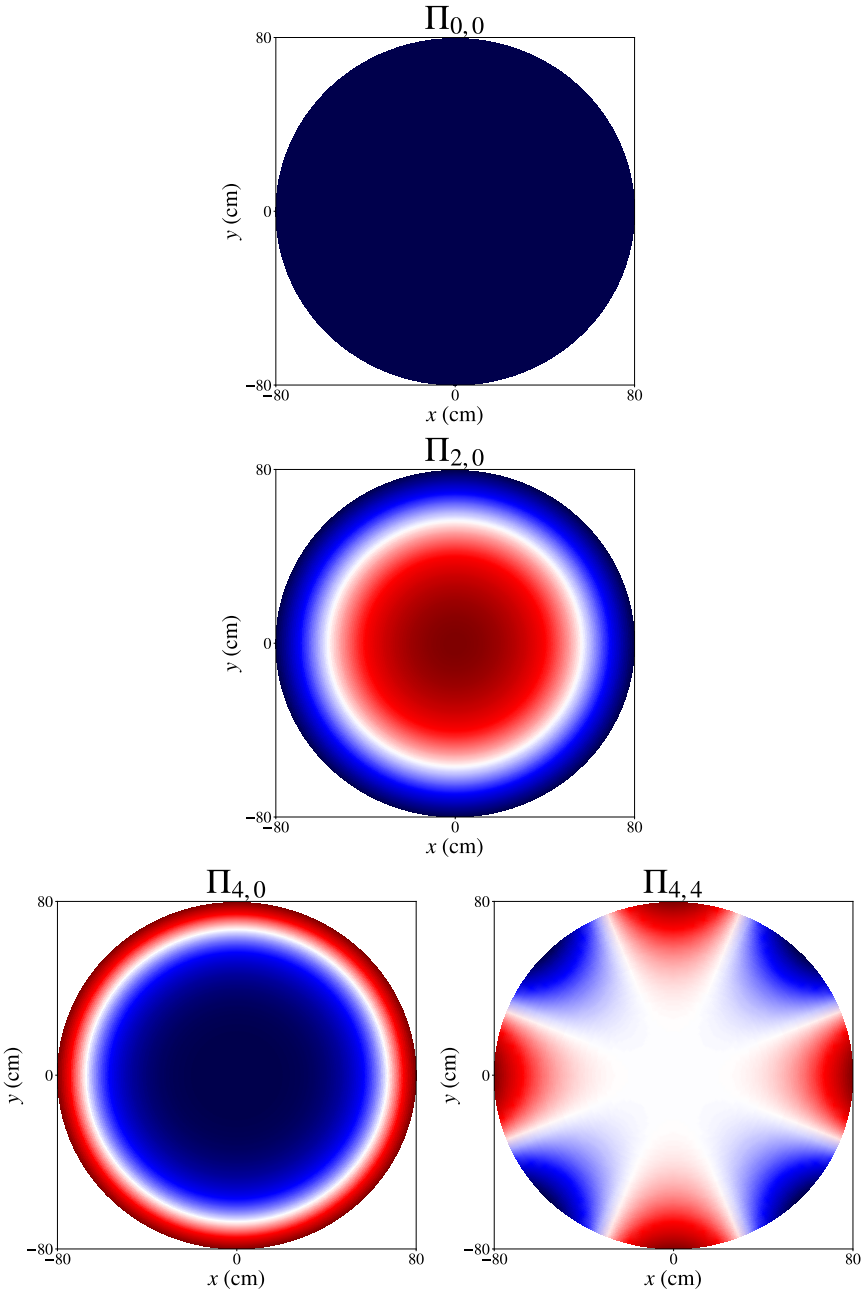

FIGURE 3.4: Horizontal cut at $z = 0$ of the harmonic modes $\mathbf{\Pi}_{2k,4n}$, $k, n \in \mathbb{N}$ allowed by the symmetries of the B_0 coil, up to $l = 4$.

of this manuscript.

Before addressing these requirements, we wished to give reasons for the existence of non-uniformities in the magnetic field generated by n2EDM's B_0 coil. To this end we proposed a group-theoretical approach to propagating symmetries of the geometrical B_0 coil to the magnetic field it generates. We began by determining the symmetry group of the ideal coil, along with its representation on a vector space associated with the coil's current system, in order to arrive at the symmetry, or *character*, of the B_0 coil. From there we turned to the representation of this symmetry group on the magnetic field's vector space, and showed that this representation was a direct sum of irreducible representations (irreps), all of which act on different gradients G_{lm} of the harmonic decomposition. We were finally able to determine the

character of each of these irreps, and found that the irrep acting on gradients $G_{2k,4n}$ shared the coil's character. In other words, we showed that a specific set of harmonic modes of the form $\mathbf{\Pi}_{2k,4n}$, depicted in figure 3.4, were allowed by the B_0 coil's innate symmetries.

This perhaps obscure observation will prove to be extremely useful in chapter 9 when looking at measurements of the harmonic spectrum of the B_0 coil. We will then expect the spectrum to consist not only of the vertically uniform mode $G_{0,0}$ but of many more well-determined modes, and strive to keep these under control as they will constitute the main contribution to the crucial vertical field RMSE $\sigma(B_z)$. We will moreover resume the group-theoretical discussion in order to associate the presence of unexpected gradients with symmetry-breaking mechanical features.

The subject of the remaining two parts of this thesis is the false EDM. In part II we will show from calculations of this pivotal quantity for relevant magnetic configurations that it is possible to suppress it or even cancel it entirely. In part III we will rely on magnetic field measurements to estimate the false EDM and propose field optimization strategies that fulfill our systematical requirement.

PART II

The false neutron EDM

Chapter 4

Fundamental aspects of the false EDM

Contents

The focal point of the second part of this thesis is n2EDM's core systematic effect, the false EDM. Although this quantity was introduced in chapter 2 and its maximal permitted value has already been established (section 3.2), we have yet to justify its existence. The issue of a relativistic *motional field* in EDM experiments, that would induce precession frequency shifts quadratic in the electric field, was first raised in 1996 (Lamoreaux, 1996). It was then formalized after the introduction of mercury co-magnetometry (Pendlebury et al., 2004), and concluded that more potent linear-in-E shifts, which would lead to a false EDM signal, were also expected. This led to further theoretical endeavours (Lamoreaux and Golub, 2005; Barabanov, Golub, and Lamoreaux, 2006; Clayton, 2011; Swank, Petukhov, and Golub, 2012; Pignol and Roccia, 2012; Pignol, 2015; Golub et al., 2015; Swank, Petukhov, and Golub, 2016; Pignol et al., 2015; Pignol, 2019) and experimental verification (Abel et al., 2019; Afach et al., 2015).

This first chapter dedicated to the fundamental study of systematic effects both serves as an introduction and offers conceptual developments to the false EDM. In the first section, we will recall its derivation from spin-relaxation theory (section 4.1). This will establish the false EDM as a correlation between a non-uniform magnetic field and a relativistic effect affecting moving particles in an electric field. We will then briefly study the high and low frequency regimes of this systematic effect (section 4.2). In a third section, we will propose an alternate derivation of the false EDM based on a frequency domain approach, which involves a quantity known as the *power spectral density* of false EDM-generating processes (section 4.3). A fourth

section will finally illustrate through a simple case study the main quantities previously defined: the correlation function and the power spectral density of processes describing both the magnetic field and position of mercury atoms, as well as the false EDM generated by these processes (section 4.4).

4.1 From spin-relaxation theory to false EDMs

4.1.1 Field non-uniformity and precession frequency shift

As we hinted at in section 2.4, the vital use of mercury co-magnetometry comes at the cost of a significant systematic uncertainty on the extraction of the neutron EDM, referred to as the mercury-induced false neutron EDM $d^{\text{false}}_{n\leftarrow\text{Hg}}$. This effect arises from the fact that the magnetic field is in reality not perfectly uniform, and because mobile particles inside an electric field generate a relativistic motional field. The combination of both non-vertical fields leads to a shift in the precession frequency of the neutrons and most importantly of the mercury atoms, which negatively impacts the extraction of the neutron EDM d_n from the measured neutron and mercury precession frequencies. This is why we express false EDMs as errors in the neutron to mercury precession frequency ratio

$$\frac{f_n}{f_{\text{Hg}}} = \left|\frac{\gamma_n}{\gamma_{\text{Hg}}}\right| \mp \frac{E_0}{\pi\hbar|f_{\text{Hg}}|}\left|d_n + d^{\text{false}}_n + d^{\text{false}}_{n\leftarrow\text{Hg}} + \dots\right|, \tag{4.1}$$

where the false neutron EDM d^{false}_n is a manifestation in this ratio of shifts in the neutron precession frequency, and similarly $d^{\text{false}}_{n\leftarrow\text{Hg}}$ comes from shifts in the mercury precession frequency. The framework that allows for a description of those precession frequency shifts is the spin relaxation theory (Redfield, 1957), which we already invoked to define the decay rate of the transverse polarization as equation (3.14). We will briefly present some important results of this theory in order to better understand how false EDMs arise from field non-uniformities.

We consider the non-uniform magnetic field seen by a spin-1/2 particle, with a random trajectory $\mathbf{r}(t)$ inside a precession chamber, as a perturbation $\mathbf{b}(t) = \mathbf{B}(t) - \langle\mathbf{B}(t)\rangle$ to the total field $\mathbf{B}(t)$, and define its longitudinal and transverse components as

$$b_z(t) = \mathbf{b}(t)\cdot\mathbf{h_z} \qquad\qquad b_T(t) = \mathbf{b}(t)\cdot\left(\mathbf{h_x} + i\mathbf{h_y}\right), \tag{4.2}$$

where the basis $(\mathbf{h_x}, \mathbf{h_y}, \mathbf{h_z})$ is chosen so that $\mathbf{h_z}$ is aligned with the average perturbed field $\langle\mathbf{B}(t)\rangle$. As we know from our introductory picture 1.1, the spins of the considered particle, described by the observables S_x, S_y, S_z, precess about the direction of the magnetic field $\mathbf{B}(t)$ with a frequency ω. Spin-relaxation theory tells us that the relaxation rates of the longitudinal and transverse spin components $\langle\Psi(t)|\,S_z\,|\Psi(t)\rangle$ and $\langle\Psi(t)|\,(S_x + iS_y)\,|\Psi(t)\rangle$, as well as the shift in the precession frequency, depend on the perturbation $\mathbf{b}(t)$ (Redfield, 1957; Pignol et al., 2015; Lamoreaux and Golub, 2005). At second order in the perturbation, these can be written as, respectively:

$$\frac{1}{T_1}(\omega) = \gamma^2 \,\mathrm{Re}\left\{\int_0^\infty d\tau \,\langle b_T(0) b_T^*(\tau)\rangle \, e^{-i\omega\tau}\right\}, \tag{4.3}$$

$$\frac{1}{T_2}(\omega) = \frac{1}{2T_1} + \gamma^2 \,\mathrm{Re}\left\{\int_0^\infty d\tau \,\langle b_z(0) b_z(\tau)\rangle\right\}, \tag{4.4}$$

$$\delta\omega(\omega) = -\frac{\gamma^2}{2} \,\mathrm{Im}\left\{\int_0^\infty d\tau \,\langle b_T(0) b_T^*(\tau)\rangle \, e^{-i\omega\tau}\right\}, \tag{4.5}$$

with γ the particle's gyromagnetic ratio. Among these, equation (4.5) will be the focal point of the following discussions. The terms of the form $C_{ij}(t_1, t_2) \equiv \left\langle b_i(t_1) b_j^*(t_2)\right\rangle$, that here describe the auto-correlation of the magnetic perturbation, are in more general terms correlation functions of two stochastic processes, where the angle brackets indicate an ensemble average over all particles in the precession chamber. The next subsection will take care of defining these terms appropriately.

But before diving any deeper, let us try to get some intuition on the form of this frequency shift. Consider the simplified, static scenario of a particle precessing about a perfectly uniform and vertical magnetic field $\mathbf{B} = B_0 \mathbf{h_z}$ with a frequency $\omega = \gamma B_0$, with γ the particle's gyromagnetic ratio. If we add a small non-uniform transverse perturbation $\mathbf{b} = b_x \mathbf{h_x} + b_y \mathbf{h_y}$ to this vertical field, in a static field picture the precession frequency becomes $\omega + \delta\omega = \gamma\,|\mathbf{B} + \mathbf{b}|$. Considering that $|\mathbf{b}| \ll B_0$ and $\mathbf{b} \cdot \mathbf{h_z} = 0$, a first-order approximation gives $\omega + \delta\omega \approx \gamma B_0 \left(1 + \frac{\mathbf{b}\cdot\mathbf{h_z}}{B_0} + \frac{\mathbf{b}^2}{2B_0^2}\right) = \gamma B_0 + \frac{\mathbf{b}^2}{2B_0}$. This tells us that the precession frequency shift directly depends on the magnitude of the perturbed field B_0. Furthermore at high field values, or high frequency ω, it is inversely proportional to the initial frequency value. To acquire a more complete picture of the frequency shift, especially for low precession frequencies, we need to invoke the more involved, non-static, spin-relaxation formulation of the precession frequency shift (4.5).

4.1.2 A detour through the correlation of stochastic processes

The core components of the spin-relaxation equations (4.3), (4.4), and (4.5) are correlation functions of a particular class of stochastic processes, which are both stationary and ergodic. As these terms are of particular importance for the discussion that will follow, we will begin by providing a few key definitions, loosely based on a reading of Papoulis and Pillai's (Papoulis and Pillai, 2002).

Definition 4.1.1. A **stochastic process** is as a collection of complex-valued random variables $\{X(t) \mid t \in T\}$, defined on a probability space Ω and indexed by a set T.

We focus here on so-called *continuous* processes, for which $T = \mathbb{R}$. Much like a random variable X can be thought of as a rule for assigning to an event $\omega \in \Omega$ a complex-number $x = X(\omega)$, a stochastic process $\{X(t) \mid t \in T\}$ can be thought of as a rule for assigning to that event a complex-valued time series $x(t) = \{X(t, \omega) \mid t \in T\}$. In our scenario of moving particles inside a precession chamber, if X assigns to a given particle a coordinate x inside the precession volume, then $\{X(t) \mid t \in T\}$ assigns to that particle a coordinate trajectory $x(t)$[1].

[1] We will commonly use the shorthand $x(t)$ for a realization $\{X(t, \omega) \mid t \in T\}$ of the stochastic process $\{X(t) \mid t \in T\}$.

Stationarity and correlation functions

Definition 4.1.2. A stochastic process $\{X(t) \mid t \in T\}$ is said to be **strict-sense stationary** if all its random variables are identically distributed. That is, for any $\tau \in T$, the random variables

$$X(t_1), X(t_2), \ldots, X(t_n), \qquad \text{and} \qquad X(t_1+\tau), X(t_2+\tau), \ldots, X(t_n+\tau), \tag{4.6}$$

have the same probability distribution.

Definition 4.1.3. A stochastic process $\{X(t) \mid t \in T\}$ is said to be **wide-sense stationary**, or here simply stationary, if

(i) Its expectation value, referred to in this case as the *ensemble average*, is constant in time:

$$\langle X(t) \rangle = \langle X \rangle , \tag{4.7}$$

(ii) Its covariance, defined as $C_X(t_1, t_2) = \langle (X(t_1) - \langle X \rangle)\,(X^*(t_2) - \langle X^* \rangle) \rangle$, is invariant with time:

$$C_X(t_1, t_2) = C_X(t_1 + t_0, t_2 + t_0), \forall t_0 \in T. \tag{4.8}$$

An important consequence of this definition is that, since we can always choose $t_0 = -t_1$, we can write the covariance as $C_X(t_1, t_2) = C_X(0, t_2 - t_1) \equiv C_X(\tau)$, with $\tau = t_2 - t_1$. So for a stationary stochastic process the covariance depends only on the time difference τ. In the case of processes with null expectation value, the covariance $C_X(\tau) = \langle X(0)X(\tau) \rangle$ is known as the *auto-correlation function* of the stochastic process $\{X(t) \mid t \in T\}$. More generally,

Definition 4.1.4. The **correlation function** of two stationary stochastic processes $\{X(t) \mid t \in T\}$ and $\{Y(t) \mid t \in T\}$ is defined by:

$$C_{XY}(\tau) = \langle X(0)Y^*(\tau) \rangle . \tag{4.9}$$

These functions satisfy a number of important properties. The first three of these are valid for any cross-correlation function.

(i) *Reflectivity*:

$$C_{XY}(-\tau) = C^*_{YX}(\tau). \tag{4.10}$$

This is deduced from the stationarity property 4.1.3(ii).

(ii) Cauchy-Schwartz inequality:

$$|\langle X(0)Y^*(\tau) \rangle|^2 \leq \langle |X|^2 \rangle \langle |Y|^2 \rangle \tag{4.11}$$

(iii) It is always possible to define a **correlation time**

$$\tau_c = \frac{1}{\langle XY^* \rangle} \int_0^\infty dt\, \langle X^*(0)Y(t) \rangle \tag{4.12}$$

as the characteristic time scale for the correlation function to decay to zero. Indeed, in the case of a decreasing exponential $C(\tau) = C(0)e^{-|\tau|/\tau_c}$, the correlation time *is* the function's characteristic time.

We will often limit ourselves to the auto-correlation of a real-valued process $\{X(t) \mid t \in T\}$, of the form $C_X(\tau) = \langle X(0)X(\tau)\rangle$. This particular subset of correlation functions satisfies a further set of very useful properties.

(iv) At initial time $\tau = 0$, the auto-correlation function reaches its maximum:

$$C_X(\tau) \leq C_X(0) = \left\langle |X|^2 \right\rangle \tag{4.13}$$

(v) In the long time limit, the process decorrelates with itself[2] and

$$\lim_{\tau\to\infty} C_X(\tau) = \langle X(0)\rangle \langle X(\tau)\rangle = \langle X\rangle^2 = 0 \tag{4.14}$$

(vi) The auto-correlation function of a real process is a real-valued, even function of time:

$$\langle X(0)X(\tau)\rangle = \langle X(0)X(-\tau)\rangle . \tag{4.15}$$

This is a consequence of reflectivity 4.1.4(i). Note that because of this, the time-derivative of a continuously differentiable correlation function goes to zero at initial time $\tau = 0$:

$$\left.\frac{dC_X(\tau)}{d\tau}\right|_{\tau=0} = 0 \tag{4.16}$$

Ergodicity

Definition 4.1.5. A stochastic process $\{X(t) \mid t \in T\}$ is said to be **mean-ergodic** if its time average tends to its ensemble average at infinite time, i.e.

$$\lim_{T\to\infty} \frac{1}{2T} \int_{-T}^{T} dt\, x(t) = \langle X\rangle . \tag{4.17}$$

Similarly, it is said that

Definition 4.1.6. A correlation function between two processes $\{X(t) \mid t \in T\}$ and $\{Y(t) \mid t \in T\}$ is **ergodic** if

$$\lim_{T_0\to\infty} \frac{1}{2T_0} \int_{-T_0}^{T_0} dt\, x(t)y^*(t+\tau) = \langle X(0)Y(\tau)\rangle . \tag{4.18}$$

Considering an ensemble of particle trajectories, this equivalency between averages of outcome and time can be understood by considering that, over infinite time, a particle travels to all the locations that other particles occupy at a given time.

We will end with a few comments that help conclude on the ergodicity of stationary processes:

(i) **(Slutsky's theorem)** A stationary process $\{X(t) \mid t \in T\}$ with auto-correlation C_X is mean-ergodic iff

$$\lim_{T\to 0} \frac{1}{T} \int_0^T d\tau\, C_X(\tau) = 0. \tag{4.19}$$

(ii) If X is a regular stationary process, such that $\lim_{\tau\to\infty} C_X(\tau) = 0$, then it is mean-ergodic.

[2] This is actually only true for so-called *regular* processes, defined as linearly equivalent to a white noise (Papoulis and Pillai, 2002). Here all stochastic processes are considered regular.

(iii) If for two stationary processes X and Y, $\lim_{\tau\to\infty} C_X(\tau) = 0$, $\lim_{\tau\to\infty} C_Y(\tau) = 0$, and $\lim_{\tau\to\infty} C_{XY}(\tau) = 0$, then their cross-correlation $C_{XY}(\tau)$ is ergodic.

This last property is particularly useful as it applies to the majority of stationary processes considered in this chapter, which are then automatically ergodic.

4.1.3 Frequency shifts and false EDMs

In the context of an experiment such as n2EDM, particle trajectories $\mathbf{r}(t) = (x(t), y(t), z(t))$ as well as magnetic noises $\mathbf{b}(t) = (b_x(t), b_y(t), b_z(t))$ are realizations of stationary and ergodic stochastic processes with null expectation value. This is because the particle trajectories are random and because the magnetic noise is specifically defined as the random contribution $\mathbf{b}(t) = \mathbf{B}(t) - \langle \mathbf{B}(t) \rangle$ to a mostly uniform magnetic field $\mathbf{B}(t)$. The total magnetic noise of n2EDM receives two main contributions: the null-average non-uniform field $\mathbf{b}(\mathbf{r}(t))$ at a position of the particle inside the chamber, as well as a relativistic *motional field* which depends on the applied electric field and the particle's velocity $\dot{\mathbf{r}}(t)$. We write the total magnetic noise as

$$\mathbf{b}_{\text{tot}}(t) = \mathbf{b}(\mathbf{r}(t)) + \frac{\mathbf{E}}{c^2} \times \dot{\mathbf{r}}(t), \tag{4.20}$$

with in this case $\mathbf{E} = E_0 \mathbf{h_z}$ [3]. We have already encountered the non-uniform field contribution $\mathbf{b}(\mathbf{r}(t))$ in equation (4.2) but the motional field needs to be introduced. By the laws of special relativity, a particle moving in an electric field $\mathbf{E}$ with velocity $\mathbf{v}$ experiences a magnetic field, expressed as $\mathbf{v} \times \mathbf{E}/c^2$ in the $|\mathbf{v}| \ll c$ limit. As mentioned earlier this relativistic field was first examined in 1996 (Lamoreaux, 1996), and is at the origin of a systematic effect that has troubled EDM experiments since then. Both UCNs and mercury atoms experience this field in n2EDM, to varying degrees that match their velocity. Since the n2EDM electric field is vertical, their motional field is a purely transverse magnetic noise, which also has zero expectation value as $\langle \dot{x} \rangle = \langle \dot{y} \rangle = 0$. Figure 4.1 shows a plot of the non-uniform noise $\mathbf{b}(\mathbf{r}(t))$ and the motional noise along UCN and Hg atom trajectories.

We know by equation (4.5) that these magnetic noises generate a shift in the precession frequency of the considered particles. Plugging (4.20) in (4.5) yields an expression that we decompose for convenience in powers of the electric field amplitude:

$$\delta\omega = \delta\omega_1 + \delta\omega_E + \delta\omega_{E^2}. \tag{4.21}$$

We recall from equation (2.4) that the neutron EDM is extracted from the difference of precession frequencies measured in **opposite** electric field polarities. Therefore, only frequency shifts with **odd** powers of E_0 will contribute to the neutron EDM. The E-even terms could in principle also contribute if the electric field is not exactly equal in magnitude in both precession chambers, but to a lesser extent. The design article (al., 2022) deals extensively with these considerations. One crucial thing to remember is that a linear-in-E frequency shift can only be generated by a **combination** of a non-uniform field $\mathbf{b}(\mathbf{r}(t))$ and a motional field $\dot{\mathbf{r}} \times \mathbf{E}/c^2$.

So we focus on the E_0 linear term. Plugging the (4.20) into the frequency shift expression (4.5) one can show that the latter reduces to (Pignol, 2015):

$$\delta\omega_E(\omega) = \frac{E_0\gamma^2}{c^2} \int_0^\infty d\tau \cos(\omega\tau) \frac{d}{d\tau} \left\langle x(\tau)b_x(0) + y(\tau)b_y(0) \right\rangle. \tag{4.22}$$

[3] In reality the total magnetic noise also consists of the so-called *Johnson noise* $\mathbf{b}_J(t)$ due to the electrode (Chiu, 2021). As this term does not contribute to the false EDM we remove it from the discussion.

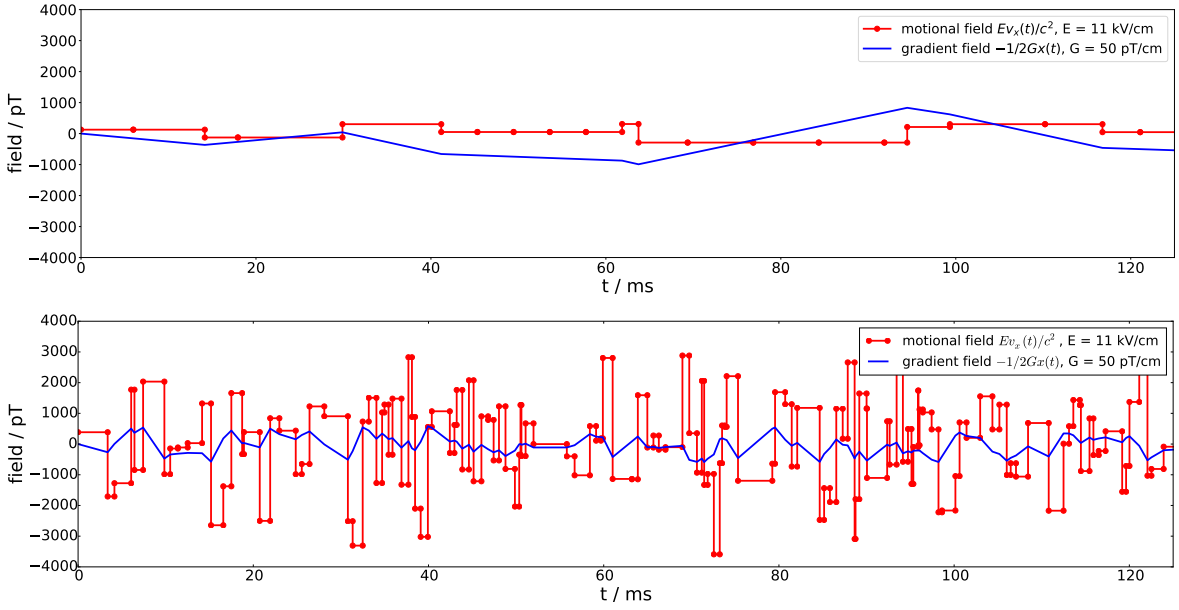

FIGURE 4.1: Magnetic field seen by UCNs (top plot) and mercury atoms (bottom plot) as a function of time. The red curve represents the motional field contribution $v \times E/c^2$, proportional to the horizontal velocity of the particles, while the blue curve represents a simplified gradient field configuration for the non-uniform magnetic field contribution. Plots obtained from the Monte-Carlo simulation tool TOMAt, showcased in (Pignol, 2019).

This derivation makes use of the stationarity 4.1.3(ii) and parity 4.1.4(vi) of autocorrelation terms of the form $\langle x(0)x(t)\rangle$ to show that $\langle x(0)\dot{x}(t)\rangle = -\langle x(t)\dot{x}(0)\rangle$. Recalling from equation (2.9) that the neutron EDM d_n is given by the difference of precession frequencies in opposite field configurations, the **false** neutron EDM is simply the equivalent difference of frequency **shifts**, so

$$d_n^{\text{false}}(\omega_n) = \frac{\hbar}{4E_0}\left(\delta\omega_E(\omega_n) - \delta\omega_{-E}(\omega_n)\right) \tag{4.23}$$

$$= \frac{\hbar\gamma_n^2}{2c^2}\int_0^\infty d\tau \cos(\omega_n\tau)\frac{d}{d\tau}\left\langle x(\tau)b_x(0) + y(\tau)b_y(0)\right\rangle. \tag{4.24}$$

We then get the expression for the false mercury EDM $d_{\text{Hg}}^{\text{false}}$ by replacing γ_n with γ_{Hg}. The false mercury EDM affects the extraction of the neutron EDM through the frequency ratio $\mathcal{R}$ in the form of the mercury-induced false neutron EDM $d_{n\leftarrow\text{Hg}}^{\text{false}}(\omega_{\text{Hg}}) = \left|\gamma_n/\gamma_{\text{Hg}}\right| d_{\text{Hg}}^{\text{false}}(\omega_{\text{Hg}})$. The above equality then yields

$$d_{n\leftarrow\text{Hg}}^{\text{false}}(\omega_{\text{Hg}}) = \frac{\hbar|\gamma_n\gamma_{\text{Hg}}|}{2c^2}\int_0^\infty d\tau \cos(\omega_{\text{Hg}}\tau)\frac{d}{d\tau}\left\langle x(\tau)b_x(0) + y(\tau)b_y(0)\right\rangle. \tag{4.25}$$

The important message is that the core systematic effect $d_{n\leftarrow\text{Hg}}^{\text{false}}$ depends on a function $C(\tau) = \langle x(\tau)b_x(0) + y(\tau)b_y(0)\rangle$ which describes the correlation between two noises: the random trajectory of a mercury atom inside the chamber, and the

magnetic field seen by that atom[4]. The characteristic time scale of a correlation function is its correlation time τ_c, defined in 4.1.4(iii). Since these functions generally decay with time (by properties 4.1.4(iv) and 4.1.4(v)), τ_c can be thought of as the characteristic time of an exponential decay that shares the same asymptotic behavior. In the n2EDM scenario, the correlation time of neutrons and mercury atoms scale with the characteristic size of the chamber R as $\tau_c \propto R/v_h$, with v_h the particle's horizontal velocity. For slow ultra-cold neutrons which travel longer between wall collisions, $\tau_c(\mathrm{UCN}) \approx 120\,\mathrm{ms}$. For faster mercury atoms however, the correlation time is much shorter: $\tau_c(\mathrm{Hg}) \approx 5\,\mathrm{ms}$ (al., 2022). Figure 4.1 represents the field seen by both UCNs and mercury atoms as a function of time. Clearly the faster Hg particles experience a stronger motional field. Since E odd frequency shifts, which false EDMs are proportional to, arise from a combination of a non-uniform field and a motional field, one can already guess that, at a given precession frequency, the mercury-induced false neutron EDM will be greater than the false neutron EDM. The two particles' precession frequencies however differ slightly: with $B_0 = 1\,\mu\mathrm{T}$, $\omega_{\mathrm{Hg}} = \gamma_{\mathrm{Hg}} B_0 \approx 48 \times 10^{-3}\,\mathrm{ms}^{-1}$ while $\omega_n = \gamma_n B_0 \approx -183 \times 10^{-3}\,\mathrm{ms}^{-1}$. The magnitude of the false EDMs will then depend on the dimensionless quantity $\omega\tau_c$ that can be used to compare this effect for both particles. For the UCNs, $|\omega_n \tau_c(\mathrm{UCN})| = 22 \gg 1$, while for the mercury atoms $|\omega_{\mathrm{Hg}} \tau_c(\mathrm{Hg})| = 0.24 \ll 1$. Because of this the UCNs are said to be in the *high-frequency regime* while the mercury atoms are in the *low-frequency regime*.

Before setting the mercury precession frequency to its experimental value $\omega_{\mathrm{Hg}}\tau_c(\mathrm{Hg}) \ll 1$, let us first focus on the general false EDM $d^{\mathrm{false}}_{n\leftarrow\mathrm{Hg}}(\omega)$. As an intuitive example, consider that the correlation function takes the form of a decreasing exponential function $C(\tau) = C(0)e^{-|\tau|/\tau_c}$, with $C(0) = \langle x b_x + y b_y \rangle$ [5]. The mercury-induced false neutron EDM expression (4.25) becomes

$$\begin{aligned} d^{\mathrm{false}}_{n\leftarrow\mathrm{Hg}}(\omega) &= \frac{\hbar|\gamma_n\gamma_{\mathrm{Hg}}|}{2c^2}\int_0^\infty d\tau \cos(\omega\tau)\left(\frac{-C(0)}{\tau_c}e^{-\tau/\tau_c}\right) \\ &= \frac{\hbar|\gamma_n\gamma_{\mathrm{Hg}}|}{2c^2}\frac{-C(0)}{1+\omega^2\tau_c^2}. \end{aligned} \tag{4.26}$$

It is then easy to compare the mercury-induced false neutron EDM with the neutron false EDM:

$$\left|\frac{d_n^{\mathrm{false}}}{d^{\mathrm{false}}_{n\leftarrow\mathrm{Hg}}}\right| = \left|\frac{\gamma_n}{\gamma_{\mathrm{Hg}}}\right|\left|\frac{1+\omega_{\mathrm{Hg}}^2\tau_c^2(\mathrm{Hg})}{1+\omega_n^2\tau_c^2(\mathrm{UCN})}\right|. \tag{4.27}$$

With $|\gamma_n/\gamma_{\mathrm{Hg}}| \approx 3.84$ (Graner et al., 2016), we get $|d_n^{\mathrm{false}}/d^{\mathrm{false}}_{n\leftarrow\mathrm{Hg}}| \approx 7 \times 10^{-3} \ll 1$ at $B_0 = 1\,\mu\mathrm{T}$. This is why the mercury-induced false neutron EDM is the most concerning systematic effect in n2EDM, on which many field uniformity requirements depend. Because the false neutron EDM is so negligible, from now on we will simply refer to the mercury-induced false neutron EDM as *the false EDM* when no confusion is possible.

In chapter 6, we will determine a more realistic false EDM from the numerical calculation of the field-position correlation function $C(\tau)$. The next section should give an idea of what to expect from a direct calculation in asymptotic cases.

[4] Unless stated otherwise, the notation $C(\tau)$, although implicit, will always refer to the false EDM generating correlation function $\langle x(\tau)b_x(0) + y(\tau)b_y(0)\rangle$

[5] In reality, this example is a valid correlation function only for $\tau > 0$

4.2 The false EDM in extreme frequency regimes

4.2.1 The low-frequency regime within n2EDM

The two frequency regimes that we just introduced allow for simplifications that yield valuable, analytic expressions for the mercury-induced false EDM. In the low-frequency regime $\omega\tau \ll 1$, we can simply take $\cos(\omega\tau) = 1$ in the general expression (4.25) to automatically integrate the time derivative of the correlation function. This yields the explicitly static expression:

$$d^{\text{false}}_{n\leftarrow\text{Hg}} = -\frac{\hbar\left|\gamma_n\gamma_{\text{Hg}}\right|}{2c^2}\left\langle xb_x + yb_y\right\rangle = -\frac{\hbar\left|\gamma_n\gamma_{\text{Hg}}\right|}{2c^2}\left\langle \rho b_\rho\right\rangle, \tag{4.28}$$

where $b_\rho = b_x\cos\varphi + b_y\cos\varphi$ in cylindrical coordinates (ρ, φ, z), and where $\left\langle xb_x + yb_y\right\rangle = \left\langle \rho b_\rho\right\rangle$ is simply the correlation function evaluated at $\tau = 0$. As we will later show, this initial value is the maximum that this function reaches. This means that the lower the field is, the more problematic the false EDM becomes. From the perspective of the mercury atoms who, as we saw, possess a very short correlation time, the n2EDM holding field of $B_0 = 1\,\mu\text{T}$, is a low field in the sense that $\gamma B_0\tau_c \ll 1$. Because of this, expression (4.28) is a good approximation for the false EDM in n2EDM.

The control of the false EDM then relies on a precise estimate of the $\left\langle \rho b_\rho\right\rangle$ term. The angle brackets indicate an average over all mercury atoms inside the considered precession chamber. But under the assumption that all particles are evenly distributed inside the volume, this statistical average amounts to a volume average. Using the harmonic expansion of the magnetic field it is possible to express the false EDM as a function of the geometrical parameters of the precession chambers. Chapter 5 will deal with this formalism and apply it to several scenarios of geometrical defects.

4.2.2 High-frequency regime and alternative strategies

Although n2EDM is set to operate primarily at $B_0 = 1\,\mu\text{T}$, the behavior of the false EDM at high fields hints at possible ways to correct this effect. To get a high-frequency regime expression for the false EDM, one can integrate (4.25) by parts successively so as to expand the expression in powers of $1/\omega$:

$$\begin{aligned} d^{\text{false}}_{n\leftarrow\text{Hg}}(\omega) &= \frac{\hbar|\gamma_n\gamma_{\text{Hg}}|}{2c^2}\left\{\left[\frac{\sin(\omega\tau)}{\omega}\frac{dC(\tau)}{d\tau}\right]_0^\infty - \int_0^\infty d\tau\frac{\sin(\omega\tau)}{\omega}\frac{d^2C(\tau)}{d\tau^2}\right\} \\ &= \frac{\hbar|\gamma_n\gamma_{\text{Hg}}|}{2c^2}\left\{0 + \left[\frac{\cos(\omega\tau)}{\omega^2}\frac{d^2C(\tau)}{d\tau^2}\right]_0^\infty + o\left(\frac{1}{\omega^4}\right)\right\} \\ &\approx -\frac{\hbar|\gamma_n\gamma_{\text{Hg}}|}{2c^2}\frac{1}{\omega^2}\left.\frac{d^2C(\tau)}{d\tau^2}\right|_{\tau=0}, \end{aligned} \tag{4.29}$$

with $C(\tau) = \left\langle x(\tau)b_x(0) + y(\tau)b_y(0)\right\rangle$. We used the reasonable assumption that not only the correlation function itself but also all its time-derivatives vanish at infinity (Schwartz function). It is clear that only even powers of $1/\omega$ survive the expansion, hence the $\mathcal{O}(1/\omega^2)$ behavior of the false EDM when $\omega \to \infty$.

The sign of the false EDM in this regime is determined by the sign of $\ddot{C}(0)$. One can show from Maxwell's equations and 4.1.3 that

$$d^{\text{false}}_{n\leftarrow\text{Hg}}(\omega) = -\frac{\hbar|\gamma_n\gamma_{\text{Hg}}|}{2c^2}\frac{1}{\omega^2}\left\langle\frac{\partial b_z}{\partial z}\right\rangle\left\langle v_\rho^2\right\rangle, \tag{4.30}$$

where the average horizontal velocity of mercury atoms $\left\langle v_\rho^2\right\rangle = \left\langle \dot{x}^2(0)+\dot{y}^2(0)\right\rangle$ corresponds to their thermal velocity (al., 2022). Comparing the high-frequency false EDM (4.30) to its low-frequency counterpart (4.28), one may crucially observe that the false EDM crosses the horizontal axis if $\langle\partial b_z/\partial z\rangle$ and $\left\langle xb_x + yb_y\right\rangle$ are of opposite signs. The numerical results of chapter 6 will show that this zero-crossing is achieved for all considered magnetic configurations. For now, simply consider a vertical gradient field given by the harmonic expansion $G_{10}\mathbf{\Pi}_{10}(x,y,z)$. From A.2 we have $\mathbf{B} = G_{10}(-x/2,-y/2,z)$, which yields $\left\langle xb_x + yb_y\right\rangle = -G_{10}R^2/4$ and $\langle\partial b_z/\partial z\rangle = G_{10}$. If we let $G_{10} > 0$, the false EDM at $\omega = 0$ is positive but indeed approaches zero from negative values for $\omega \to +\infty$. The existence of this zero-crossing is what justifies a recent approach to control the false EDM, which consists in setting B_0 to the so-called "magic value" B^{mag} that satisfies $d^{\text{false}}_{n\leftarrow\text{Hg}}(\gamma_{\text{Hg}}B^{\text{mag}}) = 0$ for a given magnetic configuration (Pignol, 2019).

4.3 A novel frequency-domain formulation of the false EDM

4.3.1 Power spectral densities and the Wiener-Khinchin theorem

We introduced the false EDM induced by either the neutrons or mercury atoms in (4.25) as a function of the particle's precession frequency. This quantity is in general proportional to the integral of a time-dependent correlation function $C(\tau)$ that describes the correlation between the particle's trajectory and the experienced magnetic field. One may legitimately wonder if rewriting the correlation function in terms of an equivalent frequency domain quantity could yield a more direct expression for the false EDM. It turns out that this alternative formulation is allowed by a theorem attributed to Wiener and Khinchin (Wiener, 1930; Khintchine, 1934), that we will introduce here after an important definition.

Definition 4.3.1. Given two stochastic processes $\{X(t) \mid t \in T\}$ and $\{Y(t) \mid t \in T\}$ for which a Fourier transform exists, we define their **power spectral density** (PSD), as the quantity

$$S_{XY}(\omega) = \lim_{T\to\infty}\frac{1}{2T}\left\langle\left(\int_{-T}^{T} dt_1\, X(t_1)e^{-i\omega t_1}\right)^*\left(\int_{-T}^{T} dt_2\, Y(t_2)e^{-i\omega t_2}\right)\right\rangle. \tag{4.31}$$

The PSD can be interpreted as the frequency distribution of a signal's power density. In fact, the definition above is obtained by applying Parseval's theorem to the average power of a combined signal.

Theorem 4.1: (Wiener-Khinchin)

If $\{X(t) \mid t \in T\}$ and $\{Y(t) \mid t \in T\}$ are two wide-sense stationary processes, then their cross power spectral density is the Fourier transform of their cross-correlation function:

$$S_{XY}(\omega) = \int_{-\infty}^{+\infty} d\tau \, \langle X(0)Y^*(\tau)\rangle \, e^{-i\omega\tau}. \tag{4.32}$$

The proof for the Wiener-Khinchin (WK) theorem relies on the stationarity $\langle X(0)Y(\tau)\rangle = \langle X(t)Y(t+\tau)\rangle$ of the correlation function. An obvious consequence of the WK-theorem is that a correlation function can be written as the inverse Fourier transform of its associated PSD:

$$\langle X(0)Y^*(\tau)\rangle = \frac{1}{2\pi}\int_{-\infty}^{+\infty} d\omega \, S_{XY}(\omega)e^{i\omega\tau} \tag{4.33}$$

Finally, combining the WK theorem with properties of the correlation function 4.1.4 yields another set of identities.

Properties 4.3.1. PSD properties:

(i) $S_{YX}(\omega) = S^*_{XY}(\omega)$, by a change of variable $\tau \to -\tau$ in (4.31) and correlation function reflectivity 4.1.4(i).

(ii) The PSD of a single process $\{X(t) \mid t \in T\}$ is real-valued and positive:

$$S_X(\omega) = \lim_{T\to+\infty} \frac{1}{2T}\left\langle \left| \int_{-T}^{T} dt \, X(t)e^{-i\omega t} \right|^2 \right\rangle \geq 0, \tag{4.34}$$

by definition of the PSD (4.31) and by reflectivity 4.3.0(i).

(iii) If $\{X(t) \mid t \in T\}$, and $\{Y(t) \mid t \in T\}$ are real-valued, then $S_{XY}(-\omega) = S_{YX}(\omega)$, by stationarity of correlation functions 4.1.3(ii).

4.3.2 Power spectral density form of the false EDM

The frequency-domain formulation of correlation functions grants a fresh look on the spin-relaxation equations (4.3), (4.4), and (4.5). We can define the following power spectral densities for the correlation functions involved in these equations (Pignol, 2015):

$$S_z(\omega) = \int_{-\infty}^{+\infty} d\tau \, \langle b_z(0)b_z(\tau)\rangle \, e^{-i\omega\tau}, \tag{4.35}$$

$$S_T(\omega) = \int_{-\infty}^{+\infty} d\tau \, \langle b_T(0)b^*_T(\tau)\rangle \, e^{-i\omega\tau}. \tag{4.36}$$

Because of property 4.3.0(i), we have $S_T(\omega) = S^*_T(\omega)$ and $S_z(\omega) = S^*_z(\omega)$: both spectral densities are real-valued. By property 4.3.0(iii) we have $S_z(\omega) = S_z(-\omega)$, but in general $S_T(\omega) \neq S_T(-\omega)$ because b_T is not necessarily real. One can then try to express from (4.33) the three spin-relaxation quantities as pure functions of frequency. Making use of reflectivity 4.1.4(i), along with changes of variables $\omega \to$

$-\omega$, we get for the transverse relaxation rate (4.3):

$$\frac{1}{T_1}(\omega) = \frac{\gamma^2}{2} S_T(\omega). \tag{4.37}$$

The longitudinal relaxation rate expression is obtained by noticing that, for a real-valued auto-correlation function $\langle X(0)X(\tau)\rangle$,

$$S_X(\omega) = \frac{S_X(\omega) + S_X^*(\omega)}{2} = \int_0^\infty d\tau \cos(\omega\tau) \langle X(0)X(\tau)\rangle . \tag{4.38}$$

This leads to:

$$\frac{1}{T_2}(\omega) = \frac{\gamma^2}{4} [S_T(\omega) + 4S_z(0)] \tag{4.39}$$

The reformulation of the frequency shift (4.5), unfortunately, is not as straightforward. Substituting the inverse Fourier transform of the correlation function in (4.5) we get

$$\begin{aligned}
\int_0^\infty d\tau \langle b_T(0) b_T^*(\tau)\rangle e^{-i\omega_0\tau} &= \frac{1}{2\pi}\int_0^\infty d\tau e^{-i\omega_0 t}\left[\int_{-\infty}^{+\infty} S_T(\omega) e^{i\omega\tau}\right] \\
&= \frac{1}{2\pi}\int_{-\infty}^{+\infty} d\omega S_T(\omega)\int_0^\infty d\tau e^{i(\omega-\omega_0)t} \\
&= \frac{1}{2\pi}\int_{-\infty}^{+\infty} d\omega S_T(\omega)\left[\pi\delta(\omega-\omega_0) + i\,\text{P.V.}\left(\frac{1}{\omega-\omega_0}\right)\right] \\
&= \frac{1}{2}S_T(\omega_0) + \frac{i}{2\pi}\text{P.V.}\int_{-\infty}^{+\infty} d\omega \frac{S_T(\omega)}{\omega-\omega_0},
\end{aligned} \tag{4.40}$$

where we invoked identity (B.19) of appendix B from the second to third line, the Cauchy principal value distribution having been defined in equation (B.14). Note that we recover $1/T_1$ as expected by taking the real part of the last line and recalling that $\text{Im}\{S_T(\omega)\} = 0$. Taking the imaginary part of the expression yields the frequency domain expression of the frequency shift, which is proportional to the Hilbert transform (identity (B.15)) of the transverse magnetic noise PSD:

$$\delta\omega(\omega_0) = -\frac{\gamma^2}{4\pi}\text{P.V.}\int_{-\infty}^{+\infty} d\omega \frac{S_T(\omega)}{\omega-\omega_0}. \tag{4.41}$$

This allows us to derive a frequency domain expression for the false EDM (4.25). Instead of the magnetic field and trajectory correlation $C(\tau) = \langle x(\tau)b_x(0) + y(\tau)b_y(0)\rangle$, this version of the false EDM will involve the cross power spectral density $S(\omega)$ of both processes. The equivalence between the two is given by the WK theorem:

$$S(\omega) = \int_{-\infty}^{+\infty} d\tau e^{-i\omega\tau} C(\tau). \tag{4.42}$$

We know that the false EDM is generated by the E-linear terms $\delta_E(\omega)$ of the total frequency shift $\delta(\omega)$, so naturally we only consider E-linear terms of the spectral density $S_T(\omega)$, labelled $S_{T,E}(\omega)$. The E-linear frequency shift is then

$$\delta\omega_E(\omega_0) = -\frac{\gamma^2}{4\pi}\text{P.V.}\int_{-\infty}^{+\infty} d\omega \frac{S_{T,E}(\omega)}{\omega-\omega_0}. \tag{4.43}$$

To determine $S_{T,E}(\omega)$, we expand equation (4.36) in powers of E and identify the field-position correlation function. This yields

$$S_{T,E} = \frac{-i2E_0}{c^2}\int_{-\infty}^{+\infty} d\tau e^{-i\omega\tau}\frac{d}{d\tau}C(\tau), \tag{4.44}$$

which is consistent with equation (4.22) where $\delta\omega_E(\omega)$ depends on the time-derivative of $C(\tau)$. Integrating equation (4.44) by parts yields an expression for the E-linear PSD that depends explicitly on $S(\omega)$:

$$\begin{aligned} S_{T,E} &= \frac{-2iE_0}{c^2}\left(\left[e^{-i\omega t}C(t)\right]_{-\infty}^{+\infty} - \int_{-\infty}^{+\infty} d\tau(-i\omega)e^{-i\omega\tau}C(\tau)\right) \\ &= \frac{2E_0}{c^2}\omega S(\omega), \end{aligned} \tag{4.45}$$

where we used the fact that $C(\tau)$ vanishes at infinity by property 4.1.4(v) of correlation functions. Substituting the above expression for $S_{T,E}$ into (4.41) gives an expression for the E-odd frequency shift $\delta\omega_E$ depending explicitly on $S(\omega)$. The false EDM being proportional to the E-linear frequency shift difference of $\delta\omega_E - \delta\omega_{-E}$ (equation (4.23)), we follow the same reasoning to arrive at the following frequency domain expression of the false EDM:

$$d^{\text{false}}_{n\leftarrow\text{Hg}}(\omega_0) = -\frac{\hbar|\gamma_n\gamma_{\text{Hg}}|}{4\pi c^2}\text{P.V.}\int_{-\infty}^{+\infty} d\omega\frac{\omega S(\omega)}{\omega-\omega_0}, \tag{4.46}$$

which is proportional to the Hilbert transform of $\omega S(\omega)$.

The above expression along with equation (4.25) embody two complementary approaches to estimate the core systematic effect of the n2EDM experiment. The latter relies on the calculation of a correlation function of the form $C(\tau) = \langle x(\tau)b_x(0) + y(\tau)b_y(0)\rangle$ between two stationary stochastic processes, while the former involves the cross power spectral density of these processes, which by the definition (4.31) is expressed as[6]

$$\begin{aligned} S(\omega) = &\lim_{T\to\infty}\frac{1}{2T}\left\langle\left(\int_{-T}^{T} dt_1\, x(t_1)e^{-i\omega t_1}\right)^*\left(\int_{-T}^{T} dt_2\, b_x(t_2)e^{-i\omega t_2}\right)\right\rangle \\ &+\lim_{T\to\infty}\frac{1}{2T}\left\langle\left(\int_{-T}^{T} dt_1\, y(t_1)e^{-i\omega t_1}\right)^*\left(\int_{-T}^{T} dt_2\, b_y(t_2)e^{-i\omega t_2}\right)\right\rangle. \end{aligned} \tag{4.47}$$

Chapter 6 will be dedicated to the numerical calculation of this correlation function and its PSD in specific field configurations. For now we will turn to an introductory correlation function example and determine its associated PSD.

4.4 Introductory case study: vertical gradient field

So far we have established that the most significant n2EDM systematic effect, the mercury false neutron EDM, is proportional to shifts in the mercury precession frequency, which are generated by the combination of an E-dependent motional field and non-uniform fields. In more specific terms, this E-linear frequency shift depends on the correlation between two stochastic processes: a non-uniform magnetic

[6] Like its time-domain counterpart, the bare notation $S(\omega)$ will always refer to the false EDM generating PSD (4.47) unless stated otherwise.

noise, and the mercury atoms' trajectory. As such it is also intrinsically linked to the cross power spectral density of these two processes. Before we dive into a numerical calculation of the full frequency spectrum of the false EDM (chapter 6), we will examine the hopefully instructive case of a linear gradient field and determine the general shape of the three key quantities: the correlation function $\langle \rho(\tau) B_\rho(0) \rangle$, its associated power spectral density, and of course the false EDM it generates.

Correlation function

Perhaps the most basic non-uniform field configuration we could think of consists of two modes: a uniform vertical field and a vertical linear gradient field. Using harmonic expansion (3.2) this field is expressed as

$$\mathbf{B}(\rho, \varphi, z) = (G_{00} + G_{10} z)\, \mathbf{e}_z + \frac{-G_{10}\rho}{2} \mathbf{e}_\rho, \tag{4.48}$$

in the n2EDM coordinate system taking the center of the double chambers as its origin. We then write the correlation function involved in the false EDM, relating the mercury atoms trajectories with their perceived magnetic field, as[7]

$$\begin{aligned} C(\tau) &= \langle \rho(\tau) B_\rho(0) \rangle \\ &= \frac{-G_{10}}{2} \langle \rho(\tau) \rho(0) \rangle \end{aligned} \tag{4.49}$$

The properties given in section 4.1 already tell us a few important things about the correlation term $\langle \rho(\tau)\rho(0) \rangle$. First, it reaches its maximum $\langle \rho^2 \rangle$ at $\tau = 0$. This maximum can be computed as the volume average in cylindrical coordinates

$$\langle \rho^2 \rangle = \frac{1}{\pi R^2} \int_0^{2\pi} d\varphi \int_0^R d\rho\, \rho^3 = \frac{R^2}{2} \tag{4.50}$$

Second, it vanishes when τ goes to infinity. Third, it is an even function of τ and as such presents a null derivative at the origin $\dot{C}(0) = 0$. Note that although in general it only applies to the restrictive case of auto-correlation functions, the initial condition on the derivative of $C(\tau)$ can be extended to any correlation function involving trajectories. This is because we assume that a particle's position is completely uncorrelated to its velocity at a given time, i.e. $\dot{C}(0) = \langle \rho(0)\dot{\rho}(0) \rangle = 0$. Doing this we have determined the zero and first order terms of the τ expansion of the correlation function around the origin, so let us briefly turn to the second order term. Although it cannot be constrained by any general properties of correlation functions, in the case of trajectories of gas particles it can be (Pignol, 2019). Indeed, evaluating the time derivative of $\langle \rho(t)\rho(t+\tau) \rangle$ at $\tau = 0$, one arrives at an equality that summons the thermal velocity of mercury atoms:

$$\langle \rho(0)\ddot{\rho}(0) \rangle = -\langle \dot{\rho}(0)\dot{\rho}(0) \rangle = -\left\langle v_\rho^2 \right\rangle = -\frac{k_B T}{m_{\mathrm{Hg}}}, \tag{4.51}$$

where k_B is the Boltzmann constant, T is the mercury gas' temperature, here taken at 20°C, and m_{Hg} is the mass of a mercury atom, yielding $\left\langle v_\rho^2 \right\rangle \approx (11\,\mathrm{cm/ms})^2$. With all of this in mind we already have an idea of the small τ behavior of the correlation

[7] When it is clear such as in this case that $b_\rho = B_\rho$, with $B_\rho = B_x \cos\varphi + B_y \sin\varphi$ and $b_\rho = (B_x - \langle B_x \rangle)\cos\varphi + (B_y - \langle B_y \rangle)\sin\varphi$, we retain the upper-case magnetic field notation.

function:

$$\langle \rho(\tau)\rho(0)\rangle = \langle \rho^2 \rangle - \frac{\tau^2}{2}\left\langle v_\rho^2 \right\rangle + o(\tau^4). \tag{4.52}$$

One model that can potentially fulfill all of the criteria we presented, on top of being conveniently rapidly decreasing, involves two decreasing exponentials of opposite signs:

$$C(\tau) = Se^{-s\tau} - Fe^{-f\tau}, \qquad \text{with } f > s > 0. \tag{4.53}$$

This model has consistently been invoked in the literature to describe correlation functions arising in frequency shifts (Lamoreaux and Golub, 2005), although there is no *a priori* indication that the correlation should take this form outside of its asymptotic regions. The exponential decay rates s and f can be understood respectively as a *slow* long-term decay and a *fast* short-term growth. Out of the four independent parameters, two can be constrained thanks to the initial conditions on $C(\tau)$ and its first-order derivative, which yields $F = sC(0)/(f-s)$ and $S = fC(0)/(f-s)$, with $C(0) = -G_{10}R^2/4$. In our example the two-parameter correlation function model is then

$$C(\tau) = \frac{-G_{10}R^2}{4}\frac{1}{f-s}\left(fe^{-s\tau} - se^{-f\tau}\right). \tag{4.54}$$

The dominant term in this expression is the slow exponential term with a fast amplitude. Since it describes the long term decorrelation of the particle trajectories due to random motions, we can already guess that the slow decay rate s is close to the inverse characteristic time $1/\tau_c$, with $\tau_c \approx 5\,\text{ms}$. As for the fast growth f, taking the second order derivative of (4.54) yields $f = (-\ddot{C}(0)/C(0)) \times (1/s)$, with $\ddot{C}(0)$ being given by the remaining initial condition (4.51). Using the thermal velocity given above we have $(\ddot{C}(0)/C(0)) \approx 0.25\,\text{ms}^{-2}$. So by setting $s = 1/\tau_c$ we can propose a tentative drawing of the correlation function in figure 4.2 (topmost plot), with $s = 0.2\,\text{ms}^{-1}$ and $f = 1.25\,\text{ms}^{-1}$.

Power Spectral Density

The associated power spectral density is obtained as always by taking the Fourier transform of the correlation function, which in exponential form (4.54) yields a combination of Lorentzian functions:

$$S(\omega) = \frac{-G_{10}}{2}\int_{-\infty}^{\infty} d\tau\ \langle \rho(\tau)\rho(0)\rangle\, e^{-i\omega\tau} \tag{4.55}$$

$$= \frac{-G_{10}R^2}{4}\frac{2sf(f+s)}{(f^2+\omega^2)(s^2+\omega^2)}. \tag{4.56}$$

Figure 4.2 provides a sketch of the PSD in its bottom plot. One may first notice that expression (4.55) evaluated at $\omega = 0$ corresponds to the definition of the correlation function's correlation time 4.1.4(iii) to a factor $-G_{10}\langle \rho^2 \rangle$. Identifying τ_c in the PSD we obtain

$$S(0) = -G_{10}\langle \rho^2 \rangle \tau_c. \tag{4.57}$$

Let us now compare this to the value given by the model-dependent expression (4.56), evaluated at $S(0) = (-G_{10}R^2/4) \times 2(f+s)/(sf)$. This allows us to define the fitted function's correlation time in terms of the fit parameters s and f as

$$\tau_c^{\text{fit}} = \frac{f+s}{sf}, \tag{4.58}$$

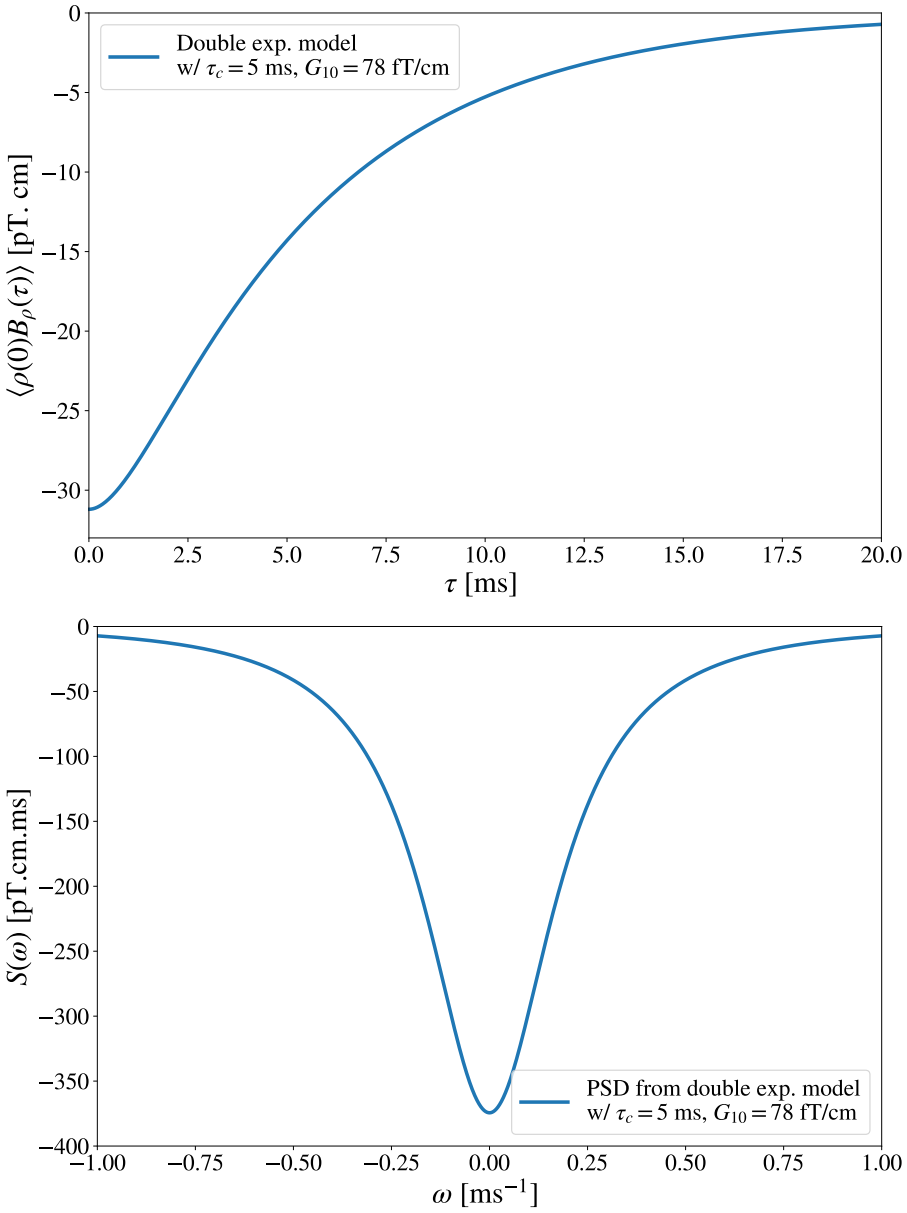

FIGURE 4.2: Example of a double exponential model for the field-position correlation function as a function of the correlation time (top), with associated cross power spectral density as a function of frequency (bottom). The considered field non-uniformity B_ρ arises from a vertical linear gradient $G_{10}\mathbf{\Pi}_{10}$, here with $G_{10} = 78\,\mathrm{fT/cm}$ and $R = 40\,\mathrm{cm}$ for the n2EDM geometry. Taking $\tau_c = 5\,\mathrm{ms}$, we set the exponential decay and growth rates to $s = 0.2\,\mathrm{ms}^{-1}$ and $f = 1.25\,\mathrm{ms}^{-1}$ respectively.

which simplifies to as expected to τ_c in the limit $s/f \to 0$. As for the region $\omega \to \infty$, we note that $S_{\rho\rho}(\omega)$ goes to zero as $\mathcal{O}(1/\omega^4)$. Both asymptotic cases will serve as an important check for the upcoming numerical simulations.

False EDM

Finally, the false EDM can be obtained from the correlation function by plugging the double exponential model (4.54) into the false EDM expression (4.25) and integrating

over τ:

$$\begin{aligned} d^{\text{false}}_{n\leftarrow\text{Hg}}(\omega) &= \frac{\hbar\left|\gamma_n\gamma_{\text{Hg}}\right|}{2c^2}\int_0^\infty d\tau\cos(\omega\tau)\frac{d}{d\tau}\left\langle\rho(\tau)B_\rho(0)\right\rangle \\ &= \frac{\hbar\left|\gamma_n\gamma_{\text{Hg}}\right|}{2c^2}\frac{-G_{10}R^2}{4}\frac{sf(\omega^2-sf)}{(s^2+\omega^2)(f^2+\omega^2)} \end{aligned} \tag{4.59}$$

For consistency we can compare the expression above with those from section 4.2 in the mercury precession frequency limits $\omega \to 0$ and $\omega \to \infty$. At the origin, the false EDM is indeed proportional to the volume-averaged term $\langle\rho B_\rho\rangle$ with $d^{\text{false}}_{n\leftarrow\text{Hg}} = \hbar\left|\gamma_n\gamma_{\text{Hg}}\right|/(2c^2)) \times (G_{10}R^2/4)$. At infinity, it decreases as expected from equation (4.30) in $\mathcal{O}(1/\omega^2)$. Both behaviors can be witnessed in figure 4.3, which shows the false EDM as a function of ω. The value of the vertical gradient coefficient was set at $G_{10} = 78\,\text{fT/cm}$ so as to obtain an absolute $1\times10^{-27}\,e\,\text{cm}$ false EDM at $\omega = 0$.

The striking feature of this quantity is that it crosses the horizontal axis, in this case at a frequency $\omega_0 \approx 0.5\,\text{ms}^{-1}$. Indeed, for a correlation function taking the form of a double exponential, the second order derivative evaluated at the origin $\ddot{C}(0) = -C(0)sf$, which determines the sign of $C(\tau)$ at high frequencies (equation (4.30)), is opposite to the origin value $C(0)$. This is consistent with the prediction we gave at the end of section 4.2 by comparing the high and low frequency regimes of the false EDM. In principle one could then set the holding field to the zero-crossing value $B_0 = \omega_0/\gamma_{\text{Hg}} \approx 10\,\mu\text{T}$ in order to largely suppress the false EDM. This discussion will be starting point of chapter 6.

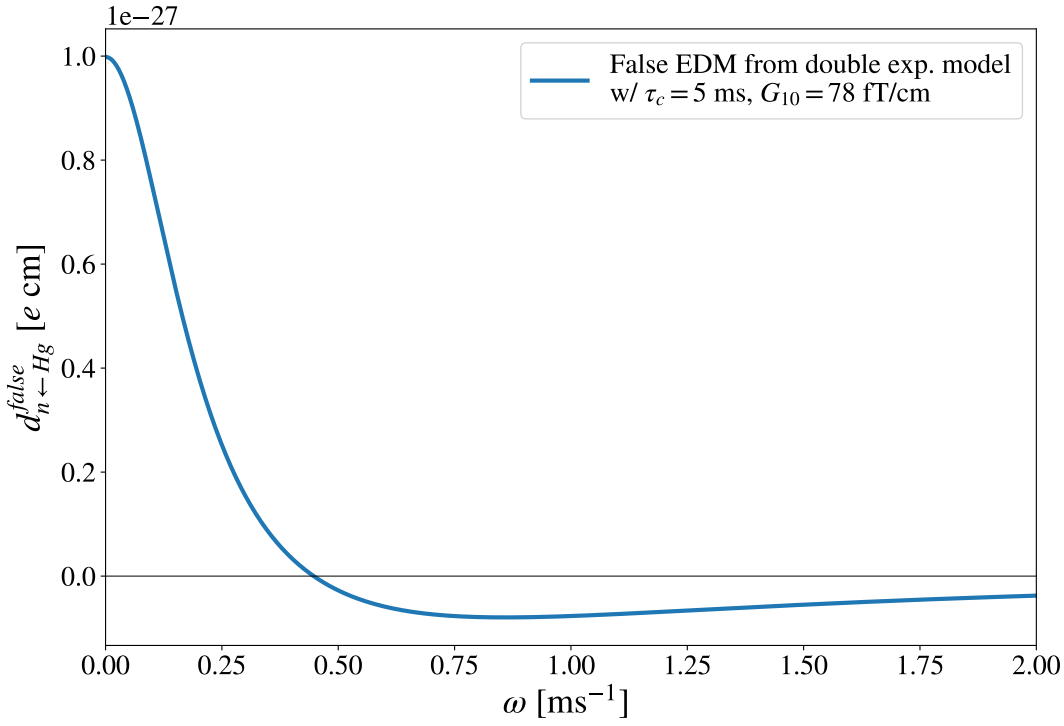

FIGURE 4.3: Mercury-induced false neutron EDM generated by a gradient field $\mathbf{B} = G_{10}\mathbf{\Pi}_{10}$ as a function of the mercury precession frequency. The false EDM is obtained either from the field-position correlation function $C(\tau)$ or its associated PSD $S(\omega)$, which in this case are featured in figure 4.2.

4.5 Conclusion

One of the most concerning systematic effects plaguing the sensitivity of n2EDM is the false EDM. In this chapter, we started from the theoretical description of precession frequency shifts and arrived through two different paths at two equivalent formulations of the false EDM: one well-known and one new.

We began by introducing the precession frequency shift of spin-1/2 particles as a result of spin-relaxation theory. As this quantity involves the auto-correlation of a magnetic noise, which is a *stationary* and *ergodic* stochastic process, we then took some time to define these terms and list their most relevant properties. We then described the transverse magnetic noise of n2EDM as the sum of two contributions: a non-uniform field, and a relativistic field generated by moving particles inside an electric potential. Noticing that the false EDM is proportional to frequency shifts linear in the electric field amplitude E_0, we arrived at the conclusion that this systematic effect is generated by a combination of the two noises. Specifically, it depends on a correlation function $C(\tau)$ which involves the position of the spin 1/2 particle and the magnetic field it experiences.

In n2EDM the main culprits are not the UCNs but the mercury atoms, by virtue of their much shorter interaction time. So what we refer to as *the* false EDM in this experiment is in fact a shorthand for *mercury-induced false neutron EDM*. We finally described the low frequency behavior of the false EDM, valid at the n2EDM standard $B_0 = \omega_0/\gamma_{\mathrm{Hg}} = 1\,\mu\mathrm{T}$, and its high frequency behavior, which hints at a suppression of the effect for high B_0 values.

In the third section, we presented a novel approach to the false EDM, which begins with the frequency-domain formulation of spin-relaxation quantities in terms of so-called *power spectral densities* (PSDs) of stochastic processes. This pivotal link between correlation functions and PSDs is granted by the Wiener-Khinchin theorem. From this result we derived a frequency-domain expression of the false EDM, involving the field-position PSD $S(\omega)$ associated to the field-position correlation function $C(\tau)$. Specifically, we showed that the false EDM is proportional to the Hilbert transform of $\omega S(\omega)$.

We concluded this chapter with the illustrative example of a magnetic field consisting of a single gradient mode $G_{10}\mathbf{\Pi}_{10}$. Assuming that the correlation function can be described by a double exponential model, we determined its explicit expression as a function of the correlation time with reasonable physical assumptions. We then used our previous formulations of the PSD and false EDM in terms of the correlation function to determine a model-dependent expression of both quantities as a function of the precession frequency. Although these are not accurate representations of the more complex experimental reality, they serve as an adequate template for the numerical calculations to come. We expect in particular the false EDM curve to cross the horizontal axis at a frequency (or magnetic field) value proper to the considered magnetic configuration. The determination of these "magic field" values is the main focus of chapter 6.

In the meantime, we will make use of the low-frequency expression of the false EDM to study the impact of geometrical imperfections on its measurement.

Chapter 5

False EDM measurement and imperfect geometries

Contents

This chapter focuses on the low-frequency false EDM, in order to first introduce the so-called *phantom modes* as the most concerning contributions to this systematic effect, and then evaluate the accuracy of this expression in the presence of geometrical defects affecting the precession chambers. We begin by giving symmetrical motivations to the presence of the phantom modes in the false EDM's geometrical average, and arrive at a measurement-ready expression in terms of the phantom gradients (section 5.1). We then move to the study of non-ideal geometrical configurations. We derive a more general geometrical formula for the false EDM through an independent definition of the magnetic frame (section 5.2), before applying it to three realistic scenarios of geometrical defects (section 5.3).

5.1 Geometrical expression of the false EDM and phantom modes

The low frequency formulation of the false EDM correlates the trajectories of mercury atoms inside a precession chamber with the magnetic noise they perceive at a same point in time. Because these atoms uniformly occupy the volume they are injected in, this correlation can be assumed to depend only on the geometry of the precession chambers. Specifically, the magnitude of the false EDM is modulated by a volume averaged quantity $\langle \rho B_\rho \rangle$, which as we will show only involves a combination of harmonic modes that resist the cylindrical symmetry of the n2EDM apparatus.

5.1.1 The false EDM in the cylindrical symmetry of n2EDM

In the double chamber configuration of n2EDM, the false EDM generated over the entire apparatus is simply the average of the false EDM generated by each chamber. A more geometrically explicit version of equation (4.28) is then

$$\begin{aligned} d^{\text{false}}_{n\leftarrow\text{Hg}} &= -\frac{\hbar\left|\gamma_n\gamma_{\text{Hg}}\right|}{4c^2}\Big[\left\langle xB_x + yB_y\right\rangle_{\text{TOP}} + \left\langle xB_x + yB_y\right\rangle_{\text{BOT}}\Big] \\ &= -\frac{\hbar\left|\gamma_n\gamma_{\text{Hg}}\right|}{4c^2}\Big[\left\langle \rho B_\rho\right\rangle_{\text{TOP}} + \left\langle \rho B_\rho\right\rangle_{\text{BOT}}\Big], \end{aligned} \tag{5.1}$$

where the horizontal coordinates correspond to the components of the trajectory of the mercury atom inside either the top or the bottom chamber. That is, $x = \mathbf{r}\cdot\mathbf{e_x}$, $y = \mathbf{r}\cdot\mathbf{e_y}$, and $z = \mathbf{r}\cdot\mathbf{e_z}$, with $(\mathbf{e_x}, \mathbf{e_y}, \mathbf{e_z})$ forming a basis defined such that $\mathbf{e_z}$ points up along the double chamber vertical axis and $\mathbf{e_x}$ points towards the vacuum tubes. Finally, $\mathbf{r} = \overrightarrow{O_T M}$ is the trajectory of an atom at a point M inside the top chamber, respectively $\mathbf{r} = \overrightarrow{O_B M}$ for the bottom chamber, O_T and O_B being the centers of the two chambers pictured in figure 5.1. In both chamber averages, the magnetic field components are expanded in the n2EDM coordinate system, which consists of the canonical $(\mathbf{e_x}, \mathbf{e_y}, \mathbf{e_z})$ basis and a coordinate origin O corresponding to the center of the double chamber system, also shown in figure 5.1. This coordinate system is chosen so that the field evaluated at the origin O is equal to the uniform vertical B_0 field, i.e. $\mathbf{B}(0) = B_0\mathbf{e_z}$. The top $(+)$ and the bottom $(-)$ volume average terms can then be written in polar coordinates as

$$\left\langle \rho B_\rho(\rho,\varphi,z)\right\rangle_{\text{TOP/BOT}} = \frac{1}{\pi R^2 H}\int_{-H/2}^{H/2} dz \int_0^{2\pi} d\varphi \int_0^R d\rho\, \rho^2 B_\rho(\rho,\varphi,z \pm H'/2), \tag{5.2}$$

with $R = 40$cm and $H = 12$cm. Replacing B_ρ with its harmonic expansion (3.2) one can make the following intuitive observations. First, because of the rotational invariance, all non-zero in m, $m \in \mathbb{N}$ functions of the form $\cos(m\varphi)$, $\sin(m\varphi)$ average out to zero for both the top and the bottom chambers. This excludes all $\mathbf{\Pi}_{l,m\neq 0}$ harmonic terms. Second, because of the horizontal planar symmetry enforced by averaging over the two chambers, all z-even terms yield H'-odd that also cancel out. This excludes the remaining $\mathbf{\Pi}_{2k,0}$ terms, $k \in \mathbb{N}$. The geometrical contribution to the false EDM is then a linear combination of $\mathbf{\Pi}_{2k+1,0}$ harmonic modes. However, not all of these asymmetric terms are considered on the same footing when trying to estimate the false EDM.

5.1.2 The odd-degree phantom modes

As alluded to in section 3.2, the field generated by a specific combination of these l-odd, $m = 0$ harmonic modes can be monitored during data-taking thanks to mercury co-magnetometers. This "visible" contribution is referred to as the *top-bottom gradient*, as it is effectively a first order magnetic gradient, defined as

$$\begin{aligned} G_{\text{TB}} &= \frac{\langle B_z\rangle_{\text{TOP}} - \langle B_z\rangle_{\text{BOT}}}{H'} \\ &= G_{10} - L_3^2 G_{30} + L_5^4 G_{50} - \dots \end{aligned} \tag{5.3}$$

where $H' = 40$ cm is the height difference between the centers of the two chambers, and where the second line is obtained by using the harmonic expansion of B_z. The

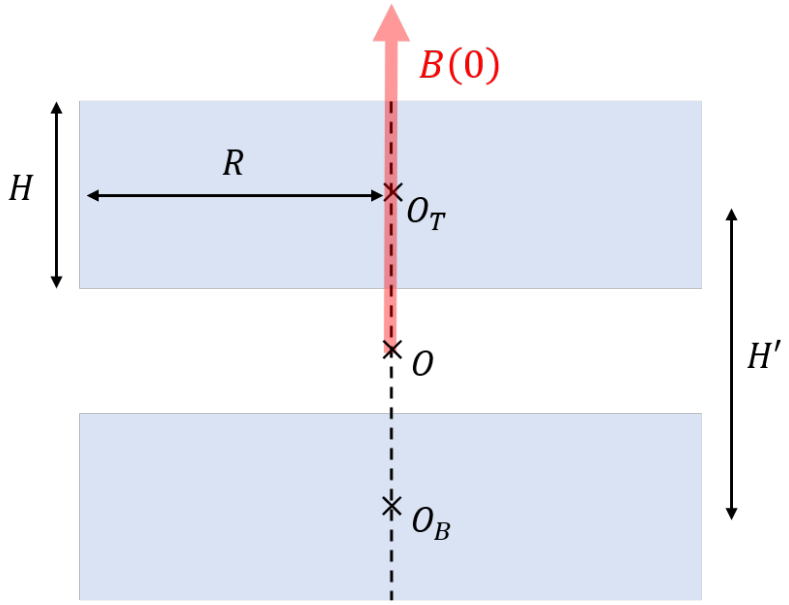

FIGURE 5.1: Double chamber geometry of n2EDM with cylindrical precession chambers. Its center O corresponds to the origin of the harmonic expansion of the magnetic field. The n2EDM coil system is designed so that $\mathbf{B}(0) = B_0\mathbf{e_z}$, with $\mathbf{e_z}$ the vertical element of the geometric frame. The size of the chambers is determined by the three geometrical parameters $R = 40$cm, $H = 12$cm, and $H' = 18$cm.

L_l are geometric coefficients with a unit of distance, derived in appendix section C.2 and given explicitly in table C.3. A field consisting only of these visible modes will produce through (5.1) a false EDM directly proportional to the top-bottom gradient, of the form

$$\begin{aligned} d^{\text{false}}_{n\leftarrow\text{Hg}} &= -\frac{\hbar\left|\gamma_n\gamma_{\text{Hg}}\right|}{2c^2}\left\langle\rho B_\rho\right\rangle \\ &= -\frac{\hbar\left|\gamma_n\gamma_{\text{Hg}}\right|}{2c^2}\left(\frac{-R^2}{4}G_{\text{TB}}\right) \end{aligned} \tag{5.4}$$

for a given precession chamber. Generally however, the top-bottom gradient is not the only contribution to the false EDM's effective first-order gradient $\left\langle\rho B_\rho\right\rangle/(-R^2/4)$. The remaining, "invisible" contribution we say is generated by *phantom modes*. These modes, denoted $\acute{\Pi}_{2k+1}$ as they must also be a combination l-odd, $m = 0$ harmonics, are simply defined as modes that generate a false EDM while satisfying $G_{\text{TB}} = 0$. They are determined by requiring that a field configuration of the form

$$\mathbf{B} = G_{\text{TB}}\mathbf{\Pi}_{10} + \acute{G}_3\acute{\mathbf{\Pi}}_3 + \acute{G}_5\acute{\mathbf{\Pi}}_5 + \ldots, \tag{5.5}$$

generates through equation (5.1) a false EDM

$$d^{\text{false}}_{n\leftarrow\text{Hg}} = \frac{\hbar\left|\gamma_n\gamma_{\text{Hg}}\right|}{8c^2}R^2\left(G_{\text{TB}} + \acute{G}_3 + \acute{G}_5 + \acute{G}_7 + \ldots\right).. \tag{5.6}$$

The explicit form of these modes is derived and given in appendix C.2, according to the concepts first presented in section 4.7 of (al., 2022). Figure 5.2 gives a visual representation of the vertical component of the third and fifth order phantom modes

in the vertical plane. It is clear in equation (5.6) that the phantom gradients $\acute{G}_{2k+1}$ are of the same dimension as the top-bottom gradient, that is, are first order magnetic gradients. Their normalization is given by the *normalizing distances* D^{2k}_{2k+1}, derived in appendix section C.2 and featured in table 5.1, such that

$$\acute{G}_{2k+1} = G_{2k+1,0} D^{2k}_{2k+1}. \tag{5.7}$$

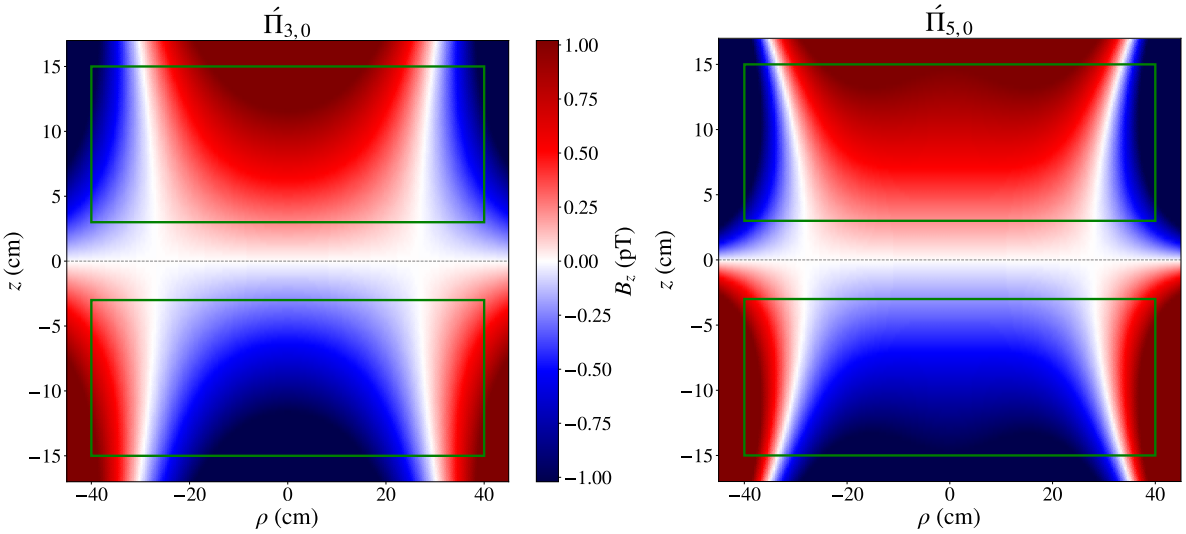

FIGURE 5.2: Vertical component of the magnetic field produced by a third order (left plot) and a fifth order (right plot) phantom mode, in the n2EDM XZ plane. The rectangles represent the vertical cut of the two precession chambers

Framed in this fashion, the magnetic dependency of the false EDM in the n2EDM geometry is contained in a set of effective first order-gradients, shown in parenthesis in equation (5.6). When n2EDM will measure the neutron and mercury precession frequencies at $B_0 = 1\,\mu\text{T}$, the generated false EDM will be estimated through this formula, thanks to the online monitoring of G_{TB}, and previous offline measurements of the $\acute{G}_3$, $\acute{G}_5$, and $\acute{G}_7$. As established in the requirements section 3.2, these should be reproducible and accurately measurable within of 10^{-2} pT/cm (conditions (3.17) and (3.18)).

The control of systematic uncertainties in n2EDM from the offline estimate of the false EDM, through its low-frequency expression (5.1), will be the subject of the third part of this thesis. In the meantime, we explore the legitimacy of this expression by considering realistic scenarios of geometrical defects.

l	1	2	3	4	5	6	7
D_l (cm)	1	18	23.7	−29.1	31.8	39.7	33.8

TABLE 5.1: Normalizing distances up to $l = 7$.

5.2 The necessity of an independent magnetic frame

The validity of the geometrical false EDM formula (4.28), on which the measurement strategy of the false EDM through (5.6) relies, is conditioned by a few key assumptions that must be made explicit. As we have established in the previous section, the magnitude of the applied vertical magnetic field must be low enough to put the mercury atoms in the low-frequency regime. At $B_0 = 1\,\mu\text{T}$, it is. Another assumption, that until now we assumed was always satisfied, concerns the *direction* of this magnetic field. There are in reality two vertical axes in n2EDM. One is the obvious cylindrical vertical axis along which the two precession chambers are aligned. The other, far less intuitive, is the axis that the magnetic perturbation is transverse to. It is aligned with the average field over the precession volume and because of this is proper to each chamber. In the ideal geometry considered up to now, we assumed that the perturbation was along the cylindrical axis. For the study of mechanical imperfections that will follow however, the distinction between the two axes, corresponding to two frames, has to be made:

1. The **geometric frame** is the basis $(\mathbf{e_x}, \mathbf{e_y}, \mathbf{e_z})$ that is attached to the precession chambers[1]. It is defined so that $\mathbf{e_z}$ is along the common vertical axis of the two chambers, pointing in the direction of the top chamber, and $\mathbf{e_x}$ points towards the vacuum tubes in the transverse cylindrical plane.

2. The **magnetic frame** is a basis $(\mathbf{h_x}, \mathbf{h_y}, \mathbf{h_z})$ for which $\mathbf{h_z}$ is aligned with $\langle \mathbf{b} \rangle$, that is,
$$\mathbf{h_z} = \frac{\langle \mathbf{B} \rangle}{|\langle \mathbf{B} \rangle|}. \tag{5.8}$$
This stems from the definition of the magnetic perturbation in section 4.1 as the null-average quantity $\mathbf{b}(t) = \mathbf{B}(t) - \langle \mathbf{B}(t) \rangle$. Here it is implied that its transverse contribution $b_T(t) = \mathbf{b}(t) \cdot (\mathbf{h_x} + i\mathbf{h_y})$ is defined relatively to the vertical, perturbed field $\langle \mathbf{B}(t) \rangle$.

In the ideal n2EDM scenario, the two precession chambers satisfy the cylindrical symmetry of figure 5.1 and a mostly uniform magnetic field is applied mainly along the geometric axis $\mathbf{e_z}$, albeit with small transverse components. On average however this field is along $\mathbf{e_z}$ for both chambers. By the definition above, in this case the geometric frame *is* a magnetic frame. Now in the case of non-ideal, asymmetrical geometries, the magnetic field inside a given chamber could average along an axis slightly tilted from the geometric axis. This would inevitably alter the form of the so-called transverse perturbation and in turn lead to a redefinition of the volume averaged quantity in the false EDM (4.25). We will try to give here a general framework for the calculation of false EDMs in these non-ideal geometries.

Consider a more general chamber geometry that slightly breaks the cylindrical symmetry. In this case the average B_0 field inside a given chamber is mostly vertical in the geometric frame, but also carries a small radial component. We can without loss of generality consider that the radial contribution is along the x axis and write:

$$\langle \mathbf{B} \rangle = \langle B_x \rangle \, \mathbf{e_x} + \langle B_z \rangle \, \mathbf{e_z}, \tag{5.9}$$

where it is implied that the magnetic field components are given relatively to the geometric frame, with $B_x = \mathbf{B} \cdot \mathbf{e_x}$ and $B_z = \mathbf{B} \cdot \mathbf{e_z}$. The magnetic axis $\mathbf{h_z}$ defined

[1] Note that the geometrical frame is defined independently from gravity, so that there is no preferred rotation of the cylindrical chambers with respect to gravity.

by (5.8) can then be expressed in the geometric frame as a slight tilt of $\mathbf{e_z}$ in the $(\mathbf{e_x}, \mathbf{e_z})$ plane. We are free to choose $\mathbf{h_x}$ in the $(\mathbf{e_x}, \mathbf{e_z})$ plane as well so that the entire magnetic frame is rotated. Assuming that $\langle B_x \rangle / \langle B_z \rangle \approx \langle B_x \rangle / B_0 \ll 1$, the magnetic frame can be written as a first-order rotation of the geometric frame

$$\begin{pmatrix} \mathbf{h_x} \\ \mathbf{h_z} \end{pmatrix} = \begin{pmatrix} 1 & -\eta \\ \eta & 1 \end{pmatrix} \begin{pmatrix} \mathbf{e_x} \\ \mathbf{e_z} \end{pmatrix}, \tag{5.10}$$

where

$$\eta \approx \frac{\langle B_x \rangle}{B_0} \tag{5.11}$$

is the tilt angle, from now on referred to as the *magnetic angle*. Figure 5.3 shows one example of a non-zero magnetic angle for the top chamber in the case of a horizontal shift between the two precession chambers.

The transverse perturbation responsible for the precession frequency shift can now be properly expressed in the geometric frame, taking into account a possible mismatch between this frame and its magnetic counterpart. Considering the n2EDM magnetic noise given by (4.20) and consisting of the typical non-uniform field and the additional motional field in the non-ideal geometric configuration, the transverse component of the perturbation, expressed in the geometric frame, takes the form

$$b_T(t) = \left[\mathbf{B}(\mathbf{r}(t)) + \frac{E_0}{c^2} \mathbf{e_z} \times \dot{r}(t) \right] \left[\mathbf{e_x} + i\mathbf{e_y} - \eta \mathbf{e_z} \right]. \tag{5.12}$$

It is clear in this expression that the electric field is attached to the geometric frame, since the electrodes are part of the mechanical structure of the precession chambers. As before, $\mathbf{r}(t)$ refers to the random trajectory of the mercury atom inside the precession volume, which must satisfy $\langle \mathbf{r}(t) \rangle = 0$.

The E_0-odd terms of this newly defined transverse magnetic noise will generate through the initial frequency shift expression (4.5) a slightly shifted false EDM in the considered precession chamber, of the form

$$d^{\text{false}}_{n \leftarrow \text{Hg}} = \frac{\hbar \left| \gamma_n \gamma_{\text{Hg}} \right|}{2c^2} \left[\langle x B_x + y B_y \rangle - \eta \langle x B_z \rangle \right], \tag{5.13}$$

where again the magnetic field and trajectory components are expressed in the geometric frame, and the coordinate origin is the center of the considered volume. Note that in the "ideal geometry" limit $\langle B_x \rangle \to 0$, we have $\eta \to 0$ and recover as expected the initial false EDM expression (4.28). This more general false EDM expression (5.13) is valid even when the magnetic frame and the geometric frame are distinct, which will help us tackle potentially harmful geometric misalignments.

5.3 Application of the revised false EDM formula to geometrical defects

5.3.1 Horizontal shift of a single chamber

The first case we will consider is that of a horizontal shift of one precession chamber with respect to the other. Specifically, we consider that the top chamber is shifted to the right by a distance δ from the double chamber origin O along the geometric axis

$\mathbf{e_x}$, and that the bottom chamber remains in its initial configuration. This could realistically occur because the groove inside the electrodes that the precession chamber sits in is about 1 mm wider than the chamber walls (see the later discussed electrode design 5.5). Such a scenario is illustrated in figure 5.3 for the top chamber. Because the magnetic field is still applied along the geometric vertical axis attached to the double chamber origin O, with $\mathbf{B}(0) = B_0\mathbf{e_z}$, the field in the top chamber will not receive the same contribution from the right and from the left parts of the volume and average in a direction $\mathbf{h_z}$ that is tilted with respect to $\mathbf{e_z}$. The magnetic frame is then distinct from the geometric frame.

The scale of this tilt can be estimated by considering a first order harmonic expansion of the magnetic field sensitive to this asymmetry, in the $(\mathbf{e_x}, \mathbf{e_z})$ plane. Working in the top chamber coordinate system, where (x, y, z) are expressed relatively to O_T, this expansion is written

$$\mathbf{B}(x,z) = \left[-G_{10}\frac{x+\delta}{2} + G_{11}\left(z+\frac{H'}{2}\right) + G_{12}\left(x+\delta\right)\right]\mathbf{e_x} + \left[B_0 + G_{10}\left(z+\frac{H'}{2}\right) + G_{11}\left(x+\delta\right)\right]\mathbf{e_z}. \tag{5.14}$$

The so-called magnetic angle between $\mathbf{e_z}$ and $\mathbf{h_z}$ in the top chamber is given by (5.11):

$$\eta_{\mathrm{TOP}} \approx \frac{\langle B_x\rangle}{B_0} = \frac{G_{11}H'/2 + (G_{12} - G_{10}/2)\delta}{B_0}. \tag{5.15}$$

There are two distinctive contributions to this tilt. The first, proportional to H', is not the result of the horizontal misalignment but of the structural vertical shift of the top chamber with respect to O. It is easy to see that the false EDM generated by this term will inevitably cancel out when averaging over the two chambers, since the equivalent term in η_{BOT} will be proportional to $-H'$. The second term in δ characterizes the considered geometrical defect and because it is asymmetrical will generate additional contributions to the total false EDM.

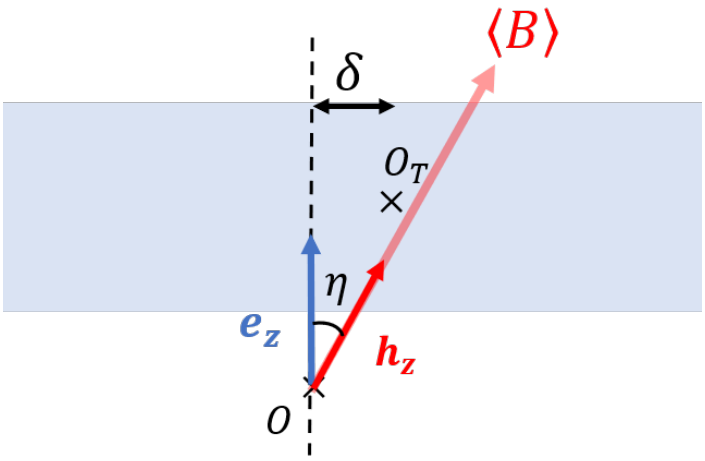

FIGURE 5.3: Vertical cut of the top chamber in the case of a horizontal displacement of the top chamber origin O_T with respect to the double chamber origin O by a distance δ. This induces a tilt η between the vertical axes of the magnetic frame (in red) and the geometric frame (in blue).

Plugging η_{TOP} and the harmonic field expansion (5.14) in the modified false EDM expression (5.13), we obtain for the top chamber:

$$d_{n\leftarrow\mathrm{Hg}}^{\mathrm{false,\,TOP}} = \frac{\hbar\left|\gamma_n\gamma_{\mathrm{Hg}}\right|}{8c^2}R^2\left[G_{10}+\eta_{\mathrm{TOP}}G_{11}\right] \tag{5.16}$$

Similarly, one can express the false EDM in the bottom chamber as a function of $\eta_{\mathrm{BOT}} = \frac{-G_{11}H'/2}{B_0}$. The total false EDM is determined by taking the average of both quantities, which results in

$$\begin{aligned} d_{n\leftarrow\mathrm{Hg}}^{\mathrm{false}} &= \frac{1}{2}\left(d_{n\leftarrow\mathrm{Hg}}^{\mathrm{false,\,TOP}} + d_{n\leftarrow\mathrm{Hg}}^{\mathrm{false,\,BOT}}\right) \\ &= \frac{\hbar\left|\gamma_n\gamma_{\mathrm{Hg}}\right|}{8c^2}R^2\left[G_{10}+\frac{\delta(2G_{12}-G_{10})}{4B_0}G_{11}\right]. \end{aligned} \tag{5.17}$$

Our work is not completely over yet because the expression above is not expressed in a field parametrization that is transparent with respect to what is easily measured, and what is not. We recall from the previous section that only the top-bottom gradient G_{TB} is visible in the online monitoring, so for convenience's sake we should make this contribution explicit. In our shifted chamber scenario, equation (5.3) yields $G_{\mathrm{TB}} = G_{10} + G_{11}\delta/H'$, which yields the working false EDM expression

$$d_{n\leftarrow\mathrm{Hg}}^{\mathrm{false}} = \frac{\hbar\left|\gamma_n\gamma_{\mathrm{Hg}}\right|}{8c^2}R^2\left[G_{\mathrm{TB}}-\frac{\delta}{H'}\left(G_{11}+\frac{H'G_{11}(G_{10}-2G_{12})}{4B_0}\right)\right]. \tag{5.18}$$

We then consider $l = 2$ harmonic gradients to go to second order in δ/H'. Skipping similar calculations we finally arrive at

$$d_{n\leftarrow\mathrm{Hg}}^{\mathrm{false}} = \frac{\hbar\left|\gamma_n\gamma_{\mathrm{Hg}}\right|}{8c^2}R^2\left[G_{\mathrm{TB}}-\frac{\delta}{H'}\left(G_{11}+\frac{H'G_{11}(G_{10}-2G_{12})}{4B_0}\right)+\frac{\delta^2}{H'^2}\left(\frac{H'G_{20}}{2}-H'G_{22}\right)+o\left(\frac{\delta^3}{H'^3}\right)\right]. \tag{5.19}$$

The result above shows us the false EDM generated in a shifted double chamber setup as a sum of effective first-order gradients (inside the square brackets). The first term is the top-bottom gradient, isolated specifically because it is unproblematic. So we are concerned only with the remaining gradients.

Among these, we focus first on the δ/H' terms. Considering a displacement $\delta = 1\,\mathrm{mm}$ and requiring, as for the phantom gradients, that the effective first order gradient stays below $2\times10^{-2}\,\mathrm{pT/cm}$ (conditions (3.17) and (3.18)), this sets a limit on the $l = 1$ terms of $3.6\,\mathrm{pT/cm}$. From the B_0 mapping data featured in appendix D, that we will present in the third part of this thesis, we have in the worst polarity $|G_{11}| < 1\,\mathrm{pT/cm}$, which matches this limit. The remaining term modulated by $H'G_{11}/B_0 \approx 10^{-5}$ will clearly yield completely negligible contributions. As for the $(\delta/H')^2$ terms, the limit imposed by a 1 mm displacement is $648\,\mathrm{pT/cm}$, which clearly is much larger than the effective $l = 2$ gradients of the coil's harmonic spectrum.

We conclude that the limiting contribution is the $(\delta/H')\times G_{11}$ term and that it is deemed unproblematic when confronted to the mapping data. Note that we considered a particular radial displacement that favored the x axis, so in reality this term would involve some combination of G_{11} (pure x displacement) and G_{1-1} (pure y displacement). From the mapping data we have at worst $|G_{1-1}| < 1.4\,\mathrm{pT/cm}$, which also matches the $3.6\,\mathrm{pT/cm}$ limit for a 1 mm displacement. Conversely, we can say that the maximum displacement allowed given the coil mapping data is

$\delta = 2.5\,\text{mm}$.

5.3.2 Vertical tilt of the double chamber system

Another problematic scenario one could reasonably consider is that of a tilt of the vertical axis of a precession chamber with respect to the coil's vertical axis, along which the uniform B_0 field is generated. The tilt of a single chamber is unrealistic because both chambers are attached to the central high-voltage electrode, so we only consider a tilt of the entire double chamber apparatus. In this case the geometric frame rotates along with the two chambers so that the electric field generated by the electrodes remains along its vertical axis $\mathbf{e}_z$. This scenario is illustrated in figure 5.4. Here the magnetic field is not applied along the geometric vertical axis but along the coil's vertical axis. Consequently, the magnetic axis $\mathbf{h}_z$ that the field averages along will again be tilted with respect to $\mathbf{e}_z$. We will see that for a tilt of the order of 1 mrad, the magnetic angle is simply the tilt angle.

We consider again a first order harmonic expansion of the magnetic field in the $(\mathbf{e_x}, \mathbf{e_z})$ plane, in the top chamber coordinate system:

$$\begin{aligned}\mathbf{B}(x,z) = &\left[-G_{10}\frac{x-\varepsilon z}{2} + G_{11}\left(z+\varepsilon x+\frac{H'}{2}\right) + G_{12}(x-\varepsilon z)\right][\mathbf{e_x}-\varepsilon\mathbf{e_z}]\\ &+\left[B_0 + G_{10}\left(z+\varepsilon x+\frac{H'}{2}\right) + G_{11}(x-\varepsilon z)\right][\mathbf{e_z}+\varepsilon\mathbf{e_x}]\,,\end{aligned} \tag{5.20}$$

where it is clear that the vertical axis parallel to the uniform B_0 component is obtained by a first-order rotation of angle ε of the geometric vertical axis. Similarly the x, z top chamber coordinates are a first order rotation of the field expansion coordinates. With $B_x = \mathbf{B}\cdot\mathbf{e}_x$ the magnetic angle between $\mathbf{e_z}$ and $\mathbf{h_z}$ in the top chamber is

$$\eta_{\text{TOP}} = \varepsilon + \frac{G_{11}H'/2}{B_0} + \varepsilon\frac{G_{10}H'/2}{B_0} \approx \varepsilon. \tag{5.21}$$

Here the magnetic angle receives contributions from both the tilt angle and the structural H' odd terms. The latter should as mentioned before cancel out in the double chamber average. However by evaluating the largest of these H' terms with the mapping data to be $\frac{G_{11}H'/2}{B_0} \approx 10^{-5}$, which is completely suppressed by $\varepsilon \approx 10^{-3}$, we can already say that the magnetic angle reduces to the tilt angle.

Plugging $\eta_{\text{TOP}} = \varepsilon$ and the harmonic field expansion (5.20) in the modified false EDM expression (5.13), we obtain for the top chamber:

$$\begin{aligned}d^{\text{false, TOP}}_{n\leftarrow\text{Hg}} &= \frac{\hbar\left|\gamma_n\gamma_{\text{Hg}}\right|}{8c^2}R^2\Big[G_{10}-\varepsilon G_{11}\Big]\\ &= \frac{\hbar\left|\gamma_n\gamma_{\text{Hg}}\right|}{8c^2}R^2 G_{\text{TB}}.\end{aligned} \tag{5.22}$$

Fortuitously, the effect of the tilt is completely absorbed by the top-bottom gradient. One can check that sending $B_z = \mathbf{B}\cdot\mathbf{e}_z$ from equation (5.20) to the top-bottom gradient definition (5.3) indeed yields $G_{\text{TB}} = G_{10} - \varepsilon G_{11}$. This expression does not depend on H' hence will be valid for the bottom chamber as well. Surprisingly still, $l = 2$ harmonic modes do not yield any extra terms, so finally,

$$d^{\text{false}}_{n\leftarrow\text{Hg}} = \frac{\hbar\left|\gamma_n\gamma_{\text{Hg}}\right|}{8c^2}R^2 G_{\text{TB}}. \tag{5.23}$$

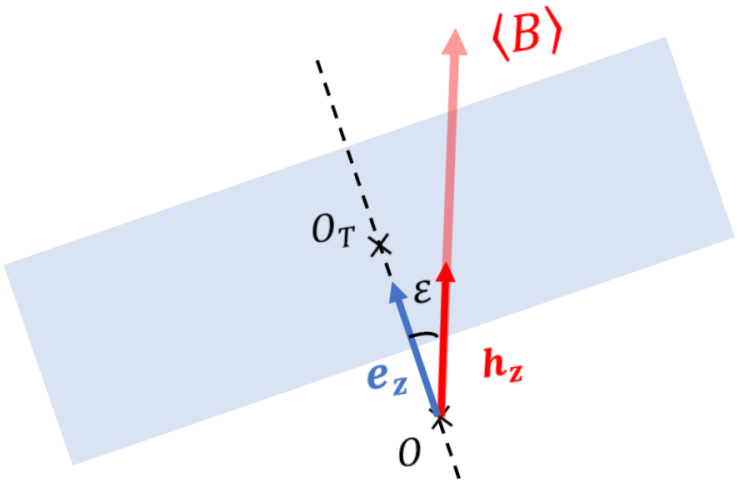

FIGURE 5.4: Vertical cut of the top chamber in the event of a global tilt of the double chamber system by an angle ε in the $(\mathbf{e}_x, \mathbf{e}_z)$ plane. In this case the magnetic angle between the magnetic frame vertical axis (in red) and the geometric frame vertical axis (in blue) reduces to the tilt angle.

At this point one may wonder if pushing this calculation to $l > 2$ harmonic terms could reveal non-G_{TB} contributions. We argue that if these indeed existed they would be completely negligible. The mapping data D.4 shows us that effective first order gradients $D_l^{l-1}G_{lm}$ tend to decrease as the gradient order l rises. At $l = 3$, possible tilt-generated effective false EDM contributions will be of the form $\varepsilon \left| D_3^2 G_{3m} \right| \lesssim \varepsilon \times 1\,\mathrm{pT/cm}$, which for $\varepsilon \approx 10^{-3}$ is still one order of magnitude below our $1 \times 10^{-2}\,\mathrm{pT/cm}$ requirement.

We conclude that the effects of a first-order rotation of the double chamber system in the vertical plane are entirely captured by the online measurement of the false EDM. The problematic, invisible contribution to the false EDM is insensitive to this tilt.

5.3.3 Off-centered cavity in the electrodes

Even if they are ideally positioned, the two precession chambers themselves could present potentially harmful geometrical defects. This is because the precession volume is not exactly cylindrical, as it is assumed to be in the evaluation of the volume average (5.2). We can identify three areas of the electrodes and chamber walls that make them imperfect cylinders. These appear in the two technical designs of figure 5.5. The first is a central cavity located on both ground electrodes that allows the UCNs to enter both precession volumes. These cavities do not break the cylindrical symmetry of the double chamber system thus cannot generate any invisible false EDM terms. A similar argument can be made for the second defect, the groove that runs along the walls of the precession chambers at the intersection with the electrodes. The third defect is an off-centered cavity meant to let in the mercury atoms, which because of the rotational invariance we assume is located on the surface of the ground electrode, at $x_0 = 20$ cm, $z_0 = 6$ cm, with respect to the chamber origin O_T for the top chamber. Unlike the first cavity this one breaks the cylindrical symmetry

and will generate a correction to the false EDM which we will now try to estimate. Figure 5.6 shows a vertical cut of the top chamber where the mercury cavity appears.

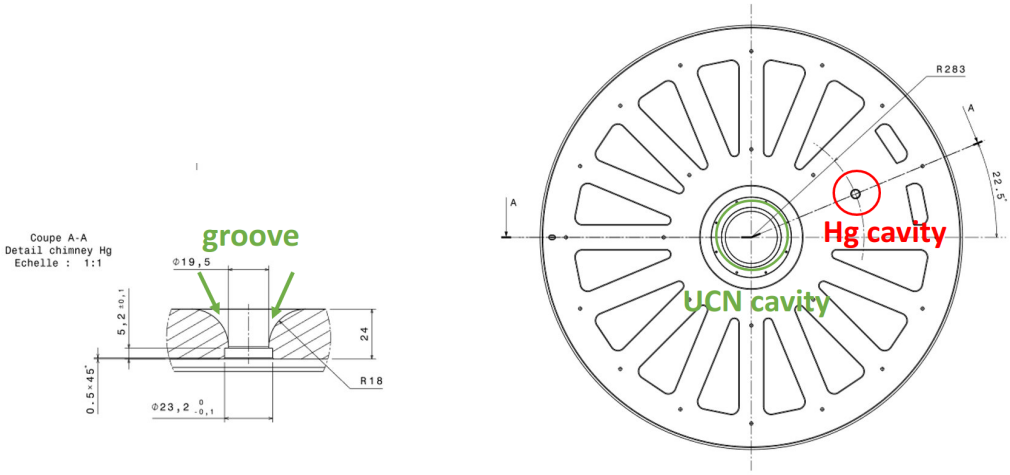

FIGURE 5.5: Vertical (left) and horizontal (right) cuts of the ground electrode. The groove that support the chamber is in reality slightly wider than the walls. Potentially problematic is the presence of an off-centered cavity for mercury gas admission because it violates the cylindrical symmetry of the double chamber system. The groove and UCN cavity are unproblematic.

We write the first-order harmonic expansion in the top chamber coordinate system as we normally would:

$$\mathbf{B}(x,z) = \left[-G_{10}\frac{x}{2} + G_{11}\left(z + \frac{H'}{2}\right) + G_{12}x\right]\mathbf{e_x} + \left[B_0 + G_{10}\left(z + \frac{H'}{2}\right) + G_{11}x\right]\mathbf{e_z}. \tag{5.24}$$

The effect of the off-centered cavity is felt only when evaluating the magnetic angle. Under the assumption that the volume of the cavity V_0 is small compared to the cylindrical precession volume V, the field inside the cavity can be considered constant. This allows the local approximation $\int_{V_0} B_x(x,z)dV \approx V_0 B_x(x_0,z_0)$. Letting $v = V_0/(V+V_0)$ and plugging in B_x from the line above, the sole non-zero contribution to the magnetic angle arises from the volume average over the cavity:

$$\eta_{\text{TOP}} = \frac{\langle B_x\rangle_{V+V_0}}{B_0} \approx \frac{vG_{11}z_0}{B_0}. \tag{5.25}$$

With an estimate of the volume ratio $v \approx 10^{-4}$ the tilt between the magnetic axis and the geometric axis is negligibly small. We can compute the false EDM (5.13) while setting $\eta_{\text{TOP}} = 0$. This explains why only the geometric axes feature on figure 5.6.

Averaging again over the realistic precession volume $V + V_0$ we arrive at a final expression of the false EDM over the two chambers:

$$\begin{aligned} d^{\text{false}}_{n\leftarrow\text{Hg}} &= \frac{\hbar\,|\gamma_n\gamma_{\text{Hg}}|}{8c^2}R^2\left[G_{10}\left(1 - v\frac{2x_0^2}{R^2}\right) - vG_{12}\frac{4x_0^2}{R^2} - vG_{21}\frac{3x_0^3 - 4x_0z_0^2}{R^2} + vG_{23}\frac{4x_0^3}{R^2}\right] \\ &= \frac{\hbar\,|\gamma_n\gamma_{\text{Hg}}|}{8c^2}R^2\left[G_{\text{TB}} - v\left(G_{10}\frac{2x_0^2}{R^2} + G_{12}\frac{4x_0^2}{R^2} + H'G_{21}\left(\frac{3x_0^3 - 4x_0z_0^2}{R^3} - \frac{x_0z_0}{H'^2}\right) - H'G_{23}\frac{4x_0^3}{R^3}\right)\right], \end{aligned} \tag{5.26}$$

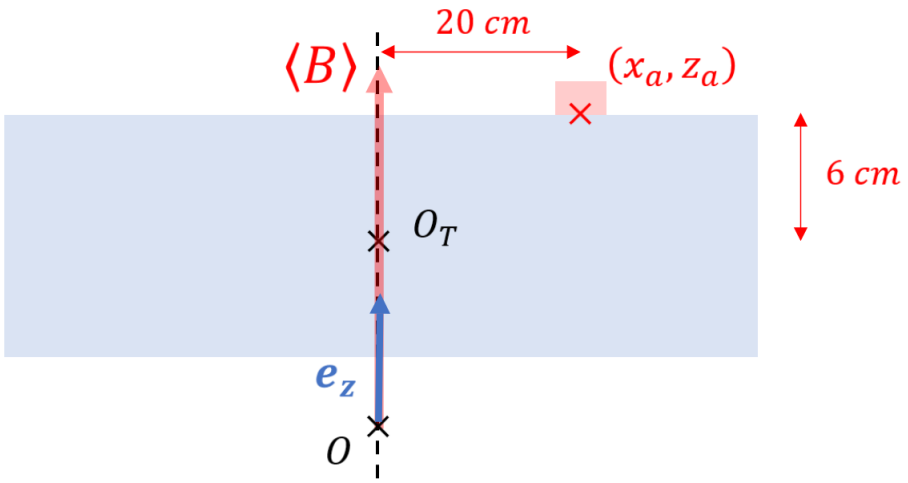

FIGURE 5.6: Vertical cut of the top chamber in presence of an off-centered cavity at (x_a, z_a) w.r.t. the top chamber origin. In this case the tilt of the magnetic frame induced by this defect is completely negligible, so $\mathbf{e}_z = \mathbf{h}_z$.

where we identified as usual part of the effective first order gradient with the computed top-bottom gradient. Aside from the online-monitored G_{TB}, the terms inside the square brackets should not contribute to more than 10^{-2} pT/cm. With a volume ratio $v \approx 10^{-4}$, and referring to the mapping data D.4, we estimate both the $l = 1$ (G_{1m}) and the $l = 1$ ($H'G_{2m}$) effective gradients terms to be at most of the order of 10^{-3} pT/cm. We conclude that the presence of the mercury cavity generates an unproblematic additional false EDM one order of magnitude below our error budget of 10^{-2} pT/cm.

5.4 Conclusion

The false EDM can easily be estimated when n2EDM operates at 1 µT, which puts the mercury atoms in the low-frequency regime. In this chapter we focused on this explicit, low-frequency formulation of the concerning systematic effect.

We began by recalling that, because of the cylindrical symmetry of the precession chambers, the geometrical average involved in the false EDM selects specific modes of the harmonic field expansion. These are l-odd, $m = 0$ gradients $\Pi_{l,m}$. Fortunately, some combination of these selected modes, the top-bottom gradient, is visible in the online field analysis and can be used to accurately estimate part of the generated false EDM. On the other hand, this implies that the remaining contribution to the false EDM is not picked up by the online monitoring. The combinations of harmonic modes that make up this invisible contribution are referred to as *phantom modes*. It is precisely these modes that we will seek to measure in the third part of this thesis, in order to provide an accurate estimate of the false EDM.

We then set out to test the validity of the low-frequency false EDM expression in non-ideal geometrical configurations of the double-chamber system. We began by proposing a more general expression of the systematic effect, based on a redefinition of the axes of the magnetic perturbation. This consisted in defining a *magnetic frame* independent from the cylindrical axes of the two chambers. We then introduced a correction to the false EDM proportional to the angle between the vertical axes of

the two newly-defined frames. We finally applied this formalism to three scenarios of geometrical defects. First, we considered a horizontal shift δ of one chamber with respect to the other. Confronting our calculations with the mapping data (which will be presented in 9), we found that the additional false EDM generated by this shift can be considered unproblematic as long as δ is kept under 2.5 cm. Second, we studied the effect of a global tilt of the double chamber system by an angle ε. In this case we concluded that the additional systematic contribution is not concerning as it is entirely captured by the visible top-bottom gradient. Finally, we examined the presence of holes and grooves inside the electrodes, among which the only potentially harmful defect is an off-centered cavity for the injection of Hg gas. Relying again on measurements of the coil's harmonic spectrum, we concluded that this defect was negligible as it generated an additional false EDM one order of magnitude below our requirement.

We now move to the final chapter concerning the fundamental study of systematic effects, and abandon the low-frequency regime to consider numerical calculations of the false EDM's entire frequency spectrum.

Chapter 6

The magic field solution to the false EDM

Contents

We concluded chapter 4 with a pivotal observation: the false EDM is expected to go to zero for a value of the applied magnetic field B_0 that depends on the chosen magnetic configuration. Yet this claim rests on an *ad hoc* model choice for the correlation function associated with the false EDM, whose parameters can be constrained by physical initial conditions. We will now present a series of numerical calculations that are in agreement with this model for different magnetic configurations.

We will begin by recalling previous efforts on the calculation of correlation functions achieved by a Monte-Carlo simulation tool, in order to present a first numerical fit of the false EDM for a simplified magnetic configuration (section 6.1). In a second section we will present our alternative determination of the false EDM through the Wiener-Khinchin theorem. This will begin with a calculation of the power spectral density of a mercury atom's trajectory, and lead to a direct numerical calculation of the false EDM and its magic value. By applying this new method to a gradient field configuration we will show its consistency with the previous approach (section 6.2). We will then turn to more realistic, higher-order magnetic configurations. From the calculation of false EDMs generated by l-odd polynomial fields, we will in a third section motivate the "magic field" determination strategy for n2EDM which consists in canceling the fifth order phantom mode. We will also comment on the experimental feasibility of operating at such high magnetic fields (section 6.3). In

the final section we will look at dipole fields, which are even higher order structures not efficiently described by a polynomial expansion. By determining a calculation method for dipole-like correlation functions we will show that the false EDM generated by those dipoles is satisfyingly suppressed at the previously chosen magic value (section 6.4).

6.1 Fitting the false EDM in the time domain

Our task is to determine the B_0 field value that cancels the false EDM generated by a given magnetic configuration, a value which we know to exist from chapter 4 on the condition that the correlation function can be described by a double exponential model. Although analytic expressions of the false EDM have been found in the high and low frequency regimes ((4.28) and (4.30)), there are none valid for any frequency value. Previous investigations thus naturally began from the general false EDM formula

$$d^{\text{false}}_{n\leftarrow\text{Hg}}(\omega_0) = \frac{\hbar|\gamma_n\gamma_{\text{Hg}}|}{2c^2}\int_0^\infty d\tau\cos(\omega_0\tau)\frac{dC(\tau)}{d\tau}, \tag{6.1}$$

where $C(\tau) = \langle x(\tau)b_x(0) + y(\tau)b_y(0)\rangle$ is the function describing the correlation between the random trajectory of a mercury atom inside the chamber and the magnetic field seen by that atom. It should be clear from the form of this correlation function that the false EDM is proper to a given magnetic field, as well as a geometry of the precession volume whose effect is felt in the ensemble average. Computing $C(\tau)$ with a choice of magnetic field and geometry is then the key to determining the frequency spectrum of the false EDM. The existing approach consists in fitting the correlation function in the time domain to finally obtain the false EDM in terms of the fit parameters.

6.1.1 Calculation of correlation functions with TOMAt

A 2019 article presented a calculation of such correlation functions along with the generated false EDM (Pignol, 2019), thanks to the dedicated Monte-Carlo simulation tool TOMAt (Trajectory Of Mercury Atoms) [1]. We will briefly recall its operating principle here. TOMAt functions in two modes: the first simulates trajectories of mercury atoms inside a closed volume, the second calculates correlation functions involving polynomial expansions of these trajectories.

In trajectory mode, ballistic trajectories $(x(t), y(t), z(t))$ inside a cylindrical volume are calculated by considering only wall collisions, which is a reasonable assumption for rarefied gases. On collision the mercury atoms undergo diffuse reflection, so their velocities $(v_x(t), v_y(t), v_z(t))$ are randomized at each wall according to the Maxwell-Boltzmann distribution. This yields trajectories such as the ones shown in figure 6.1. Since the magnetic field experienced by a mercury atom at a given time is a function of the atom's position, TOMAt's trajectory mode also indirectly allows us to simulate a magnetic noise. In fact we already displayed both motional and non-uniform magnetic noises generated by this code in chapter 4 with figure 4.1.

Correlation mode makes use of simulated trajectories to calculate polynomial-type correlation functions, of the form $C^{ijk}_{abc}(\tau) = \langle x^a(0)y^b(0)z^c(0)x^i(\tau)y^j(\tau)z^k(\tau)\rangle$.

[1] https://gitlab.in2p3.fr/NEDM/tomat

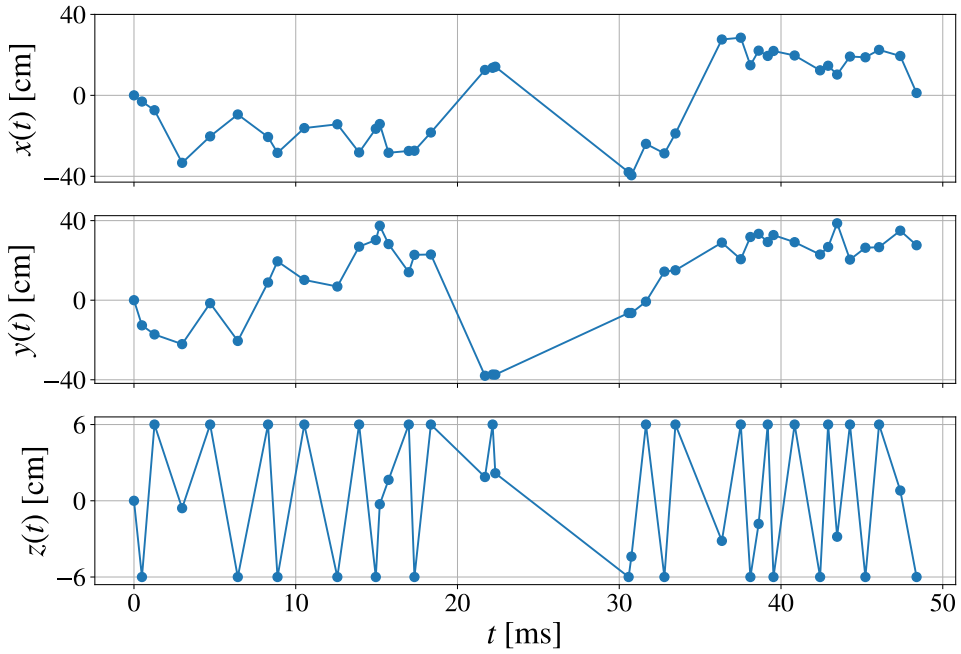

FIGURE 6.1: Trajectories of mercury atoms inside a cylindrical volume obtained with the Monte-Carlo simulation tool TOMAt. Each point corresponds to a wall collision. The chosen geometry, $R = 40\,\text{cm}$ and $H = 12\,\text{cm}$ is that of n2EDM.

The code relies on an assumption of ergodicity:

$$C^{ijk}_{abc}(\tau) = \lim_{T\to\infty} \frac{1}{T} \int_0^T dt\, x^a(t) y^b(t) z^c(t) x^i(t+\tau) y^j(t+\tau) z^k(t+\tau), \tag{6.2}$$

which is indeed a property of the type of stochastic processes considered here, as defined by 4.1.6 in chapter 4. It also benefits from the fact that, between two collisions, the atom's trajectory is a linear function of time. For a given time-difference τ, the integral above can then be efficiently computed by partitioning the time interval $[0, T]$ into smaller intervals $[t_n, t_{n+1}]$ onto which the simulated trajectories $x(t), y(t), z(t)$ as well as their delayed counterparts $x(t+\tau), y(t+\tau), z(t+\tau)$ are all linear in t. Repeating this process for $N_\tau = \tau_{\max}/\Delta\tau$ values of τ yields a time spectrum of the correlation function. This approach will also be at the foundation of our later numerical calculations (sections 6.2 and 6.4). For given cylindrical dimensions, TOMAt is fed three parameters that affect its numerical precision:

- A number of collisions N_c per set of trajectories (that is, per value of τ),
- A maximum time-difference $\tau_{\max}$,
- A time-difference step $\Delta\tau$.

The n2EDM field-position correlation function $C(\tau)$ can then be calculated by plugging the correlation terms C^{ijk}_{abc} into the appropriate harmonic field expansion A.2. Consider for instance a magnetic field consisting of either a first or a third order

harmonic mode. In this case the correlation functions are written[2]:

$$G_{10}\left\langle x(\tau)\Pi_{x,10}(0)+y(\tau)\Pi_{y,10}(0)\right\rangle = \frac{-G_{10}}{2}C^{100}_{100}(\tau)+\frac{-G_{10}}{2}C^{010}_{010}(\tau), \tag{6.3}$$

$$G_{30}\left\langle x(\tau)\Pi_{x,30}(0)+y(\tau)\Pi_{y,30}(0)\right\rangle = \frac{3G_{30}}{8}\left(C^{100}_{300}+C^{100}_{120}-4C^{100}_{102}\right)+\frac{3G_{30}}{8}\left(C^{010}_{030}+C^{010}_{210}-4C^{010}_{012}\right). \tag{6.4}$$

Note that because of the precession chamber's rotational invariance, we can exchange x and y and equivalently compute the x terms twice. The field-position correlation function is finally fitted with the double exponential model presented in section 4.4:

$$C(\tau) = \frac{C_0}{f-s}\left(fe^{-s\tau}-se^{-f\tau}\right). \tag{6.5}$$

This model depends on three parameters introduced earlier: the slow decay rate s, the fast growth rate f, and the initial value $C_0 \equiv C^{ijk}_{abc}(\tau=0)$ which we know *a priori* from the volume average $C^{ijk}_{abc}(0) = \left\langle x^a y^b z^c x^i y^j z^k\right\rangle$ but choose to leave free for the sake of later testing.

The top plot of figure 6.2 displays the results obtained from TOMAt for an elementary correlation term $C^{100}_{100}(\tau) = \langle x(0)x(\tau)\rangle$ inside an n2EDM-sized precession chamber, where we set $N_c = 10^6$, $\tau_{\max} = 100\,\text{ms}$, and $\Delta\tau = 0.1\,\text{ms}$. This choice of parameters will be motivated in the following subsection when evaluating our numerical precision on the magic field value. The double-exponential model, also plotted in figure 6.2, is in excellent agreement with the data produced by TOMAt for $C^{100}_{100}(\tau)$, with a reduced chi-squared statistic $\chi^2/\nu = 0.03$. Furthermore, it is consistent with the physical expectations outlined in 4.4 through the top plot of figure 4.2. The latter depicts the field-position correlation function for a linear gradient field $(-G_{10}/2)\langle\rho(\tau)\rho(0)\rangle = (-G_{10}/2)\langle x(\tau)x(0)+y(\tau)y(0)\rangle$, which we wrote in terms of TOMAt outputs in (6.3). The plot of $C^{100}_{100}(\tau)$ presented here is proportional to this field-position function to a factor $-G_{10} = -78\,\text{fT/cm}$, since we have $\langle x(\tau)x(0)+y(\tau)y(0)\rangle = 2\langle x(\tau)x(0)\rangle$ by the chamber's rotational invariance. Regarding the asymptotic behaviour, we find $C^{100}_{100}(0) = 399.42(60)\,\text{cm}^2$ compared to an expected $\langle x^2\rangle = R^2/4 = 400\,\text{cm}^2$ for a n2EDM precession chamber, and the correlation function goes to zero at an infinite time-difference. The double-exponential fit yields reasonable parameters $s = 0.275(30)\,\text{ms}^{-1}$ and $f = 1.054(26)\,\text{ms}^{-1}$, which are of the order of the inverse correlation time of mercury atoms $1/\tau_c = 0.2\,\text{ms}^{-1}$ for the slow decay rate and of $-\langle v_x^2\rangle/(\tau_c\langle x^2\rangle) = 1.25\,\text{ms}^{-1}$ for the fast growth rate.

Lastly, figure 6.2 also features the position-velocity correlation function, which is proportional to the time-derivative of the field-position correlation function $\dot{C}(\tau)$. Its curve presents a minimum at the inflection point $\tau_I = \ln(s/f)/(s-f) \approx 1.73\,\text{ms}$ of $C^{100}_{100}(\tau)$. The position-velocity function is central to our discussion, as its cosine transform yields the false EDM through equation (6.1). Its plot can be interpreted as follows: at a time difference $\tau = 0$ between the mercury atom's position and its velocity, there is no correlation between the two quantities as the atom could go in any direction. As the time difference increases towards the mean collision time, which is then close to τ_I, the correlation between position and velocity is maximal

[2]While we favored the cylindrical notation in chapter 4's more fundamental discussion, here we retain the Cartesian coordinates which are more practical for Monte-Carlo simulations.

in absolute value as the velocity is re-determined at the collision, and is negative as the atom will bounce back in the opposite direction. The correlation then naturally decreases as the number of collision grows.

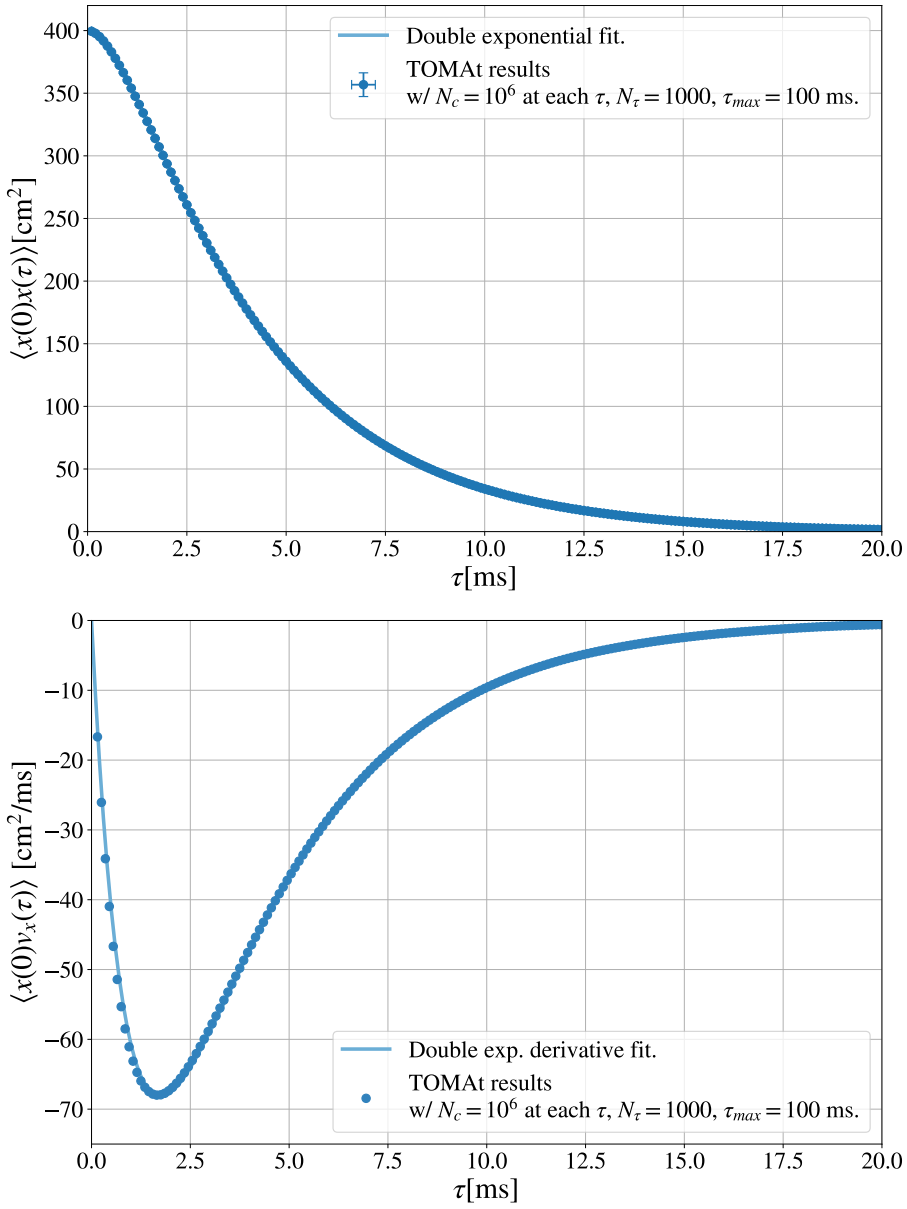

FIGURE 6.2: Correlation between two delayed trajectories as a function of the time delay given by TOMAt in the n2EDM geometry ($H = 12$ cm, $R = 40$ cm). The blue dots give the average of the correlation function over $N = 20$ runs for a choice of numerical parameters. The statistical error bars are smaller than the points. The light-blue curve corresponds to a fit with the double exponential model (6.5). The model and data are in agreement with a reduced chi squared statistic $\chi^2/\nu = 0.03$.

6.1.2 False EDM fitting and magic field

The false EDM generated by a particular magnetic configuration depends on the field-position correlation function $C(\tau)$, which as we discussed can be expressed as

a sum of correlation terms $G_{lm}C^{ijk}_{abc}$ given by the harmonic field expansion. The correlation function fit model yields a model-dependent expression of the false EDM, obtained by replacing $C(\tau)$ by (6.5) in (6.1):

$$d^{\text{false}}_{n\leftarrow\text{Hg}}(\omega_0) = \frac{\hbar\,|\gamma_n\gamma_{\text{Hg}}|}{2c^2}\,\frac{C_0 s f(\omega_0^2 - sf)}{(s^2+\omega_0^2)(f^2+\omega_0^2)}, \tag{6.6}$$

which is just the generalized version of equation (4.25).

In our introductory example of a vertical gradient field $(B_x, B_y, B_z) = G_{10}(-x/2, -y/2, z)$, the field-position correlation responsible for the false EDM is given by equation (6.3). We then have $C_0 = -G_{10}R^2/4$ and the same exponential rates s, f from $C^{100}_{100}(\tau)$. The false EDM for this magnetic configuration is plotted as a function of the applied field $B_0 = \omega_0/\gamma_{\text{Hg}}$ in figure 6.3 (blue curve), where we set $G_{10} = 78\,\text{fT/cm}$. We also included the equivalent false EDM in the smaller nEDM geometry (in green), which allows to check that the size of the precession chamber not only influences the function's value at the origin ($\propto R^2$) but also its relaxation time. Indeed, delayed trajectories decorrelate faster in a smaller volume, which means the cosine term in (6.1) will "cancel out" the correlation function at higher frequencies. So while the false EDM is more potent in n2EDM than in nEDM at the working field value $B_0 = 1\,\mu\text{T}$, it is easier to reach the considerably higher magic field value that suppresses this effect in n2EDM.

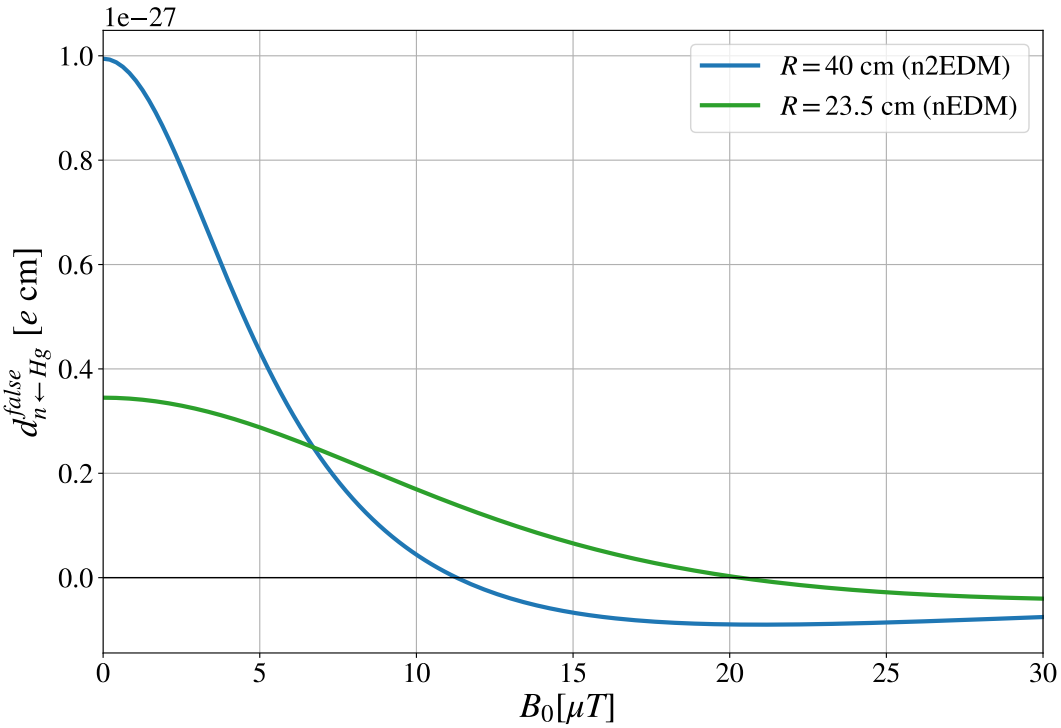

FIGURE 6.3: False EDM obtained from the correlation function fit as a function of the field amplitude $B_0 = \omega_0/\gamma_{\text{Hg}}$, for a vertical gradient magnetic mode. In this magnetic configuration the field-position correlation function is $(-G_{10}/2)\,\langle\rho(0)\rho(\tau)\rangle$, where we set $G_{10} = 78\,\text{fT/cm}$. The blue curve shows this scenario for a precession chamber of n2EDM dimensions and the green curve for nEDM dimensions. The n2EDM curve notably crosses the horizontal axis at a so-called *magic value* $B_1^{\text{mag}} = 11.28(9)\,\mu\text{T}$.

As already observed in the bottom plot of figure 4.2, the false EDM crosses the horizontal axis at a single value of the applied field, which has been referred to in the literature as the *magic field* and denoted B^{mag} (Pignol, 2019). Solving $d^{\mathrm{false}}_{n\leftarrow\mathrm{Hg}}(\gamma_{\mathrm{Hg}}B^{\mathrm{mag}}) = 0$ for B^{mag} with the model-dependent false EDM (6.6) yields

$$B^{\mathrm{mag}} = \frac{\sqrt{sf}}{\gamma_{\mathrm{Hg}}}, \tag{6.7}$$

with $\gamma_{\mathrm{Hg}} = 47.69 \times 10^{-3}\,\mathrm{ms}^{-1}\,\mu\mathrm{T}^{-1}$ (Graner et al., 2016). In the case of a magnetic field consisting only of the vertical gradient mode $\mathbf{\Pi}_{10}$, we obtain $B_1^{\mathrm{mag}} = 11.28(9)\,\mu\mathrm{T}$ over 20 computations of $C_{100}^{100}(\tau)$ with TOMAt, with the same choice of parameters $N_c = 10^6$, $\tau_{\mathrm{max}} = 100\,\mathrm{ms}$, and $\Delta\tau = 0.1\,\mathrm{ms}$. The statistical stability of this value can be evaluated by looking at figure 6.4, where we have computed B_1^{mag} for several independent variations of the three numerical parameters N_c, τ_{max}, and $\Delta\tau$. Clearly, the number of collisions per trajectory dominates the statistical precision on the magic field. This statistical error is approximately divided by 2 for each order of magnitude increase in N_c. For computational efficiency we settle on $N_c = 10^6$ collisions, $\tau_{\mathrm{max}} = 100\,\mathrm{ms}$, and $\Delta\tau = 0.1\,\mathrm{ms}$, which over 20 runs yields B_1^{mag} with a precision of $0.04\,\mu\mathrm{T}$. The accuracy of this magic field value is however undetermined.

In conclusion, the correlation function approach to the false EDM provides a robust calculation of the magic field for a given polynomial field configuration, thanks to an efficient Monte-Carlo simulation of Hg atom trajectories for the calculation of correlation functions. TOMAt allowed us to estimate the magic field that cancels the false EDM generated by a vertical magnetic mode $\mathbf{\Pi}_{10}$ to $B_1^{\mathrm{mag}} = 11.28(9)\,\mu\mathrm{T}$, which we will attempt to verify through an alternative route in section 6.2. We have not yet looked at higher degree polynomial functions which TOMAt is capable of computing, but will do so in section 6.3 when seeking to cancel phantom modes. The limitations of the correlation function approach using TOMAt are twofold. First, it does not provide us with a direct numerical calculation of the false EDM. Rather, it gives us a model-dependent estimate relying on the assumption that the correlation function is a double exponential function. It is therefore very sensitive to parameters that affect the correlation function fit, a fact that is reflected in the expression of the magic field (6.7) which depends explicitly on the fit parameters. Second, TOMAt does not allow the calculation of non-polynomial correlation functions. These are encountered for dipole-like magnetic fields for which a polynomial expansion is impractical, and will be the subject of section 6.4. In the meantime, let us present an alternative approach which does not share the same limitations.

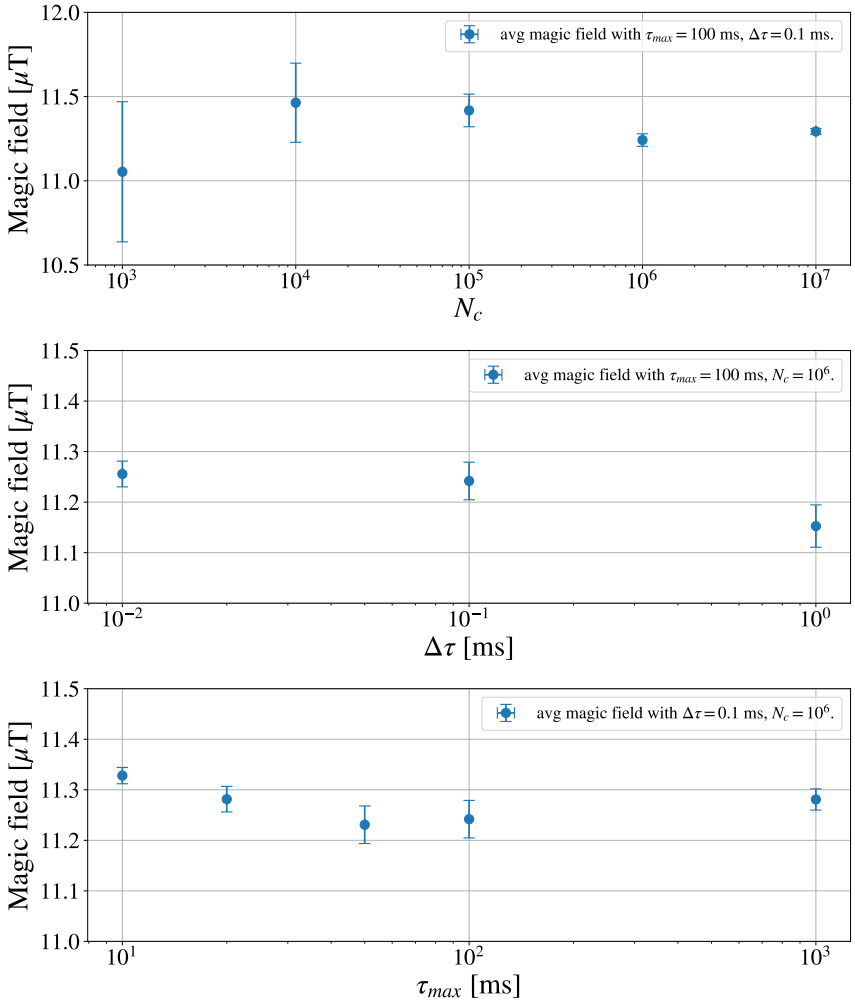

FIGURE 6.4: Magic field value for a gradient field configuration $G_{10}\mathbf{\Pi_{10}}$ in the n2EDM geometry. The blue points with statistical error bars correspond to the average magic field over $N = 20$ TOMAt calculations of $\langle x(0)x(\tau)\rangle$ for an independently varying choice of numerical parameters: number of collisions per time-difference τ (top plot), τ step (middle plot), and maximum τ (bottom plot).

6.2 Calculating the false EDM directly in the frequency domain

Back in chapter 4, we introduced a secondary path to the false EDM that does not rely on the field-position correlation function $C(\tau)$ but on its Fourier transform $S(\omega)$, referred to as the Power Spectral Density (PSD). By invoking the Wiener-Khinchin theorem we determined the frequency domain false EDM to take the form of a Hilbert transform:

$$d^{\text{false}}_{n\leftarrow\text{Hg}}(\omega_0) = -\frac{\hbar|\gamma_n\gamma_{\text{Hg}}|}{4\pi c^2}\text{P.V.}\int_{-\infty}^{+\infty} d\omega \frac{\omega S(\omega)}{\omega - \omega_0}. \tag{6.8}$$

The goal of this section is to present a direct numerical calculation of the quantity above, in order to provide a complementary estimate of the magic field value B_1^{mag}. We will tread cautiously and begin by calculating the PSD alone, as its numerical

estimate can easily be confronted to the correlation function fit model *via* the Wiener-Khinchin theorem. This intermediary step will also allow us to tune our numerical parameters to the most optimal combination of physical accuracy and computational efficiency. We will end with the numerical calculation of (6.8) and of the magic field in our usual gradient field configuration.

6.2.1 Power spectral density calculation

Because $C(\tau)$ describes the correlation between two stationary processes, a trajectory and a magnetic field, its associated PSD $S(\omega)$ can be understood as a power distribution of those same processes. In order to calculate $S(\omega)$ independently from $C(\tau)$ we simply start from its definition (4.47). Taking into account n2EDM's cylindrical symmetry, this expression reduces to

$$S(\omega) = \lim_{T\to\infty} \frac{1}{T} \left\langle \left(\int_0^T dt_1\, x(t_1) e^{-i\omega t_1} \right)^* \left(\int_0^T dt_2\, b_x(t_2) e^{-i\omega t_2} \right) \right\rangle, \tag{6.9}$$

where the angle brackets indicate an ensemble average, and where we have utilized the stationarity of processes $x(t)$ and $b_x(t)$ to shift the integral over positive time values[3]. Our first step would be to build a realistic simulation of the time series $x(t)$ and $b_x(t)$. Fortunately these are already provided to us by TOMAt's trajectory mode, again on the assumption that $b_x(t)$ can be satisfyingly described by a polynomial expansion. What is left to do is to calculate the Fourier transforms inside the angle brackets for lengthy enough trajectories, before averaging these over a large enough trajectory sample. At this point one may already notice that our statistical sensitivity will depend on two parameters:

- The duration of a trajectory T, which is proportional to the number of collisions it contains N_c,
- The number of trajectories considered for the ensemble average, which we will denote N_t.

The Fourier transform of a polynomial noise

We begin by considering the most general Fourier transforms involved in (6.9). Because of the harmonic field expansion, these consist of polynomial terms of the form

$$F_{abc}(\omega) = \int_0^T dt\, e^{-i\omega t} x^a(t) y^b(t) z^c(t). \tag{6.10}$$

Recall that the mercury atom trajectories are supposed ballistic, which means the time series $(x(t), y(t), z(t)$ are simply a set of collision points between which the atom's path is a linear function of time. This prompts us to split, much like in TOMAt's correlation mode, the total time interval $[0, T]$ into $N_c - 1$ "linear" intervals $[t_n, t_{n+1}]$ between collisions n and $n+1$, leading to:

$$F_{abc}(\omega) = \sum_{n=1}^{N_c} \Delta t_n I^{(n)}_{abc}(\omega), \qquad I^{(n)}_{abc}(\omega) = \frac{1}{\Delta t_n} \int_{t_n}^{t_{n+1}} dt\, e^{-i\omega t} x^a(t) y^b(t) z^c(t) \tag{6.11}$$

[3]To be more accurate, the stationarity we invoke here is strict-sense stationarity (definition 4.1.2), which is stronger than our usual wide-sense stationarity and a reasonable assumption for ballistic trajectories

where we let $\Delta t_n = t_{n+1} - t_n$ and defined the elementary integral $I^{(n)}_{abc}$ for every linear interval.

We focus on the calculation of $I^{(n)}_{abc}$. For $t \in [t_n, t_{n+1}]$, we have under the assumption of linearity[4] trajectories of the form $x(t) = \lambda t + \mu$, with $\lambda, \mu \in \mathbb{R}$. With a change to a dimensionless variable $\theta = (t - t_n)/\Delta t_n$ we obtain

$$\begin{aligned} x(\Delta t_n \theta + t_n) &= \lambda \left[(t_{n+1} - t_n)\theta + t_n \right] + \mu \\ &= \left[x(t_{n+1}) - x(t_n) \right] \theta + x(t_n) \\ &= \Delta x_n \theta + x_n, \end{aligned} \tag{6.12}$$

where we denote the collision points $x_n = x(t_n)$, and let $\Delta x_n = x_{n+1} - x_n$. Applying this to (x, y, z) and the change of variable to the elementary integral yields

$$I^{(n)}_{abc} = e^{-i\omega t_n} \int_0^1 d\theta \, e^{-i\omega \Delta t_n \theta} (\Delta x_n \theta + x_n)^a (\Delta y_n \theta + y_n)^b (\Delta z_n \theta + z_n)^c. \tag{6.13}$$

We express $I^{(n)}_{abc}$ itself as a sum of dimensionless integrals J_k:

$$I^{(n)}_{abc} = e^{-i\omega t_n} \sum_{k=0}^{N} c^{(n,k)}_{abc} J_k(\lambda), \tag{6.14}$$

where we let $N = a + b + c$ and the dimensionless variable $\lambda = \omega \Delta t_n$. The N-length dimension coefficients $c^{(n,k)}_{abc}$ are determined by identifying (6.13) with (6.14):

$$c^{(n,0)}_{abc} = x_n^a y_n^b z_n^c, \; c^{(n,1)}_{abc} = \binom{a}{1} \Delta x_n x_n^{a-1} y_n^b z_n^c + \ldots, \; \ldots, \; c^{(n,N)}_{abc} = \Delta x_n^a \Delta y_n^b \Delta z_n^c. \tag{6.15}$$

Or more generally by

$$c^{(n,k)}_{abc} = \sum_{\alpha,\beta,\gamma}^{a,b,c} \delta_{\alpha+\beta+\gamma,k} \binom{a}{\alpha} \binom{b}{\beta} \binom{c}{\gamma} x_n^{a-\alpha} y_n^{b-\beta} z_n^{c-\gamma} \Delta x_n^\alpha \Delta y_n^\beta \Delta z_n^\gamma, \tag{6.16}$$

where $\delta_{\alpha+\beta+\gamma,k}$ is the Kronecker delta, and where the terms in parenthesis are binomial coefficients. In a nutshell, $c^{(n,k)}_{abc}$ is the sum of all permutations that factor θ^k.

Finally, the dimensionless integrals are defined as:

$$J_k(\lambda) = \int_0^1 d\theta \, \theta^k e^{-i\lambda\theta}. \tag{6.17}$$

- In the case $\lambda = 0$, we directly get

$$J_k(0) = \frac{1}{k+1}. \tag{6.18}$$

- In the case $\lambda \in \mathbb{R}^*$, the integrals can be determined recursively. Notice that

$$J_0(\lambda) = i\frac{e^{-i\lambda} - 1}{\lambda}, \qquad J_{k+1}(\lambda) = i\frac{d}{d\lambda} J_k(\lambda). \tag{6.19}$$

[4] The term *linear* is used broadly to include affine functions and not only functions that satisfy $x(\gamma t + t') = \lambda x(t) + x(t'), \lambda \in \mathbb{R}$.

By induction we then have

$$J_k(\lambda) = i^{k+1}\frac{d^k}{d\lambda^k}\left(\frac{e^{-i\lambda}-1}{\lambda}\right), \quad \lambda \in \mathbb{R}^*. \tag{6.20}$$

We conclude that the Fourier transform of polynomial terms of the form $x^a(t)y^b(t)z^c(t)$ involved in equation (6.9) are given by

$$F_{abc}(\omega) = \sum_{n=1}^{N_c}\sum_{k=0}^{N}\Delta t_n c_{abc}^{(n,k)} \times \begin{cases} \dfrac{1}{k+1} & \text{if } \omega = 0, \\ i^{k+1}e^{-i\omega t_n}J_k(\omega\Delta t_n) & \text{if } \omega \in \mathbb{R}^*, \end{cases} \tag{6.21}$$

where $N = a+b+c$, where the $c_{abc}^{(n,k)}$ coefficients are given by (6.16), and the dimensionless integrals J_k by (6.20). The numerical parameter that conditions the statistical precision of this calculation is the number of collisions N_c of the considered trajectories.

The numerical ensemble average

Coming back to the field-position PSD (6.9), our final task is to evaluate an ensemble average involving two Fourier transforms: one of a trajectory $x(t)$, and another of a magnetic field component with harmonic expansion $b_x = G_{lm}\Pi_{x,lm}$. Because of this expansion, $S(\omega)$ is expressed as a sum of ensemble averages of the form

$$\lim_{T\to\infty}\frac{1}{T}\left\langle F_{100}^*(\omega)F_{abc}(\omega)\right\rangle, \tag{6.22}$$

where the Fourier transforms of $x(t)$ (F_{100}) and of polynomial terms of the magnetic expansion (F_{abc}) are given by equation (6.21). In principle, the ensemble average is obtained automatically by iterating the Fourier transform calculation over a large number of trajectories N_t. Alternatively, we choose a more practical approach where we simulate even longer trajectories and split these into N_t equal parts, all of which can be considered standalone trajectories by the strict-sense stationarity of these processes. Considering a total trajectory of duration N_tT, and assuming that all sub-trajectories are of equal duration $T = N_c\Delta T$, with ΔT the average time between two collisions, we then write the numerical version of (6.22) as

$$\frac{1}{\Delta T N_c N_t}\sum_{m=1}^{N_t}F_{100}^{*(m)}(\omega)F_{abc}^{(m)}(\omega). \tag{6.23}$$

The notation $F_{abc}^{(m)}$ implies that (6.21) is summed not from 0 to N_c but from mN_c to $(m+1)N_c$.

Let us summarize. Using TOMAt we simulate trajectories consisting of $N_t \times N_c$ collisions that last a total time $t(N_t \times N_c) = N_tN_c\Delta T = N_tT$. For each sub-trajectory of N_c collisions and of duration T, we calculate the Fourier transforms product $F_{100}^*(\omega)F_{abc}(\omega)$ for the appropriate magnetic configuration. We finally average this result over the N_t sub-trajectories and arrive at a numerical estimate of the field-position PSD. A consequence of this approach is that we cannot maximize N_c and

N_t independently for trajectories of a given length. Instead, we optimize our numerical efficiency by determining the appropriate allocation of statistical power between the two quantities. The example that follows will grant us this opportunity.

Consistency check with correlation function fit

In order to evaluate the consistency of this result with the calculation of associated correlation functions by TOMAt, we finally fit the entire frequency spectrum with the PSD equivalent of a double-exponential. In section 4.1 we already determined this to be a combination of Lorentzian functions. Indeed, by the Wiener-Khinchin theorem we simply take the Fourier transform of the exponential model (6.5) of $C(\tau)$ to obtain

$$S(\omega) = C_0 \frac{2sf(f+s)}{(f^2+\omega^2)(s^2+\omega^2)}, \tag{6.24}$$

which depends as expected on the three parameters C_0, s, f of the correlation function fit.

Example: vertical gradient field

We consider again our false EDM generating correlation function in the case of a vertical gradient field $C(\tau) = -G_{10}\langle x(0)x(\tau)\rangle$. It is an auto-correlation function, which as we know from 4.3.0(ii) yields a real-valued field-position PSD, here of the form

$$S(\omega) = \lim_{T\to\infty} \frac{-G_{10}}{T} \left\langle \left| \int_0^T dt\, x(t) e^{-i\omega t} \right|^2 \right\rangle = \lim_{T\to\infty} \frac{-G_{10}}{T} \left\langle |F_{100}(\omega)|^2 \right\rangle \tag{6.25}$$

with F_{100} given by (6.21) and T the duration of a sub-trajectory. The results of the calculation of the numerical quantity $\left\langle |F_{100}(\omega)|^2 \right\rangle / T$ are shown in figure 6.5, for 500 values of ω in a range $[-5, 5]\,\mathrm{ms}^{-1}$ (zoomed in), and with $N_t = 10^3$ and $N_c = 10^3$. Each blue dot with statistical error bars corresponds to the average PSD at a given frequency value over $N = 20$ total iterations.

Figure 6.5 also shows the fit of the entire frequency spectrum with the Lorentzian model (6.24). It is in very good agreement with the data with a reduced chi-squared $\chi^2/\nu = 0.19$, and matches the expected shape of the field-position PSD $S(\omega)$ of chapter 4's figure 4.2, to a factor $-G_{10}$. We have thus verified the Wiener-Khinchin theorem for an exponential form of the correlation function. In terms of physical expectations, the origin value given by our calculation

$$S(0) = \frac{-G_{10}}{\Delta T N_c N_t} \sum_{m=1}^{N_t} \left| \sum_{n=mNc}^{(m+1)N_c} \Delta t_n \frac{x_{n+1} + x_n}{2} \right|^2 \tag{6.26}$$

should be compared with $S(0) = -G_{10}\langle x^2 \rangle \tau_c$. As explained in section 4.1, this equality arises from the WK theorem result $S(0) = -G_{10}\int_{-\infty}^{+\infty} d\tau \langle x(0)x(\tau)\rangle$, which is proportional to the correlation time given by definition 4.1.4(iii). We obtain from the PSD's numerical estimates $\tau_c = 4.63(9)\,\mathrm{ms}$, compared to a correlation time of mercury atoms that we know to be of the order of 5 ms. Turning now to high frequency values, the Lorentzian model given by (6.24) tells us that the PSD should

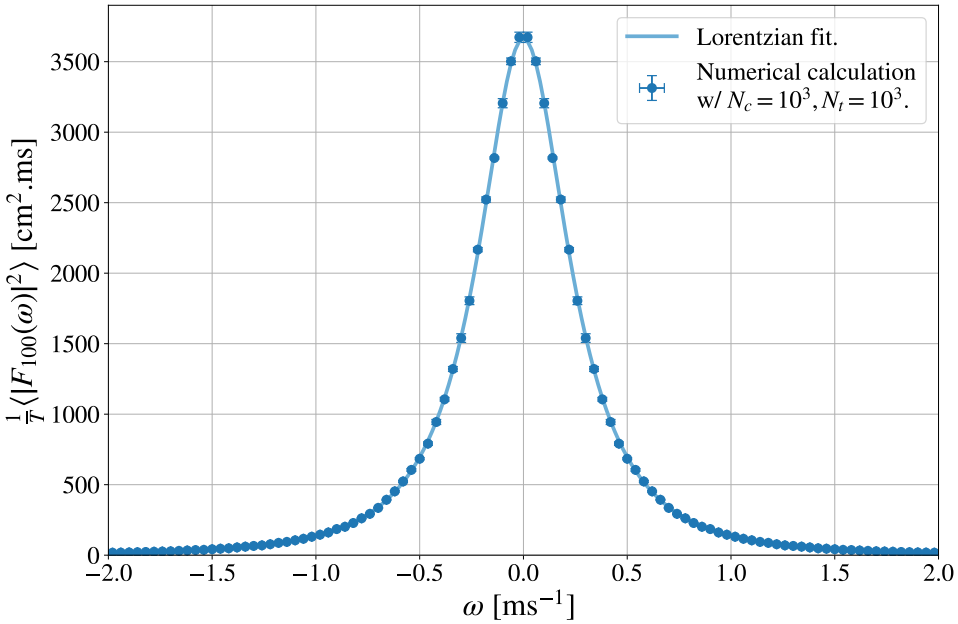

FIGURE 6.5: Results of the power spectral density calculation of a horizontal trajectory $x(t)$ as a function of frequency (in blue). The trajectory is provided by TOMAt, and the calculation is performed $N = 20$ times. The ensemble average concerns N_t trajectories, consisting of each of N_c collisions. The results are fitted with the Lorentzian PSD model (in light-blue), which yield a reduced chi squared $\chi^2/\nu = 0.19$ over a $[-5, 5]$ ms^{-1} frequency range.

go to zero as $\mathcal{O}(1/\omega^4)$. The plot in figure 6.6 gives the PSD's asymptotic behavior for several choices of numerical parameters in a logarithmic scale, which should then decrease as $\ln S(\omega) \sim -4\mathcal{O}(\omega)$. The -4 slope is only reached for $N_c = 10^3$ and above, and tends to settle to -2 at infinity. We will comment on this feature in the next paragraph. The figure's table displays the Root Mean Square Error (RMSE) between our numerical calculation of $S(\omega)$ and its Lorentzian fit, which naturally decreases with the averaging sample size N_t.

Let us now study the impact of the parameters N_t and N_c on our numerical efficiency. For a total number of collision points $N_t \times N_c = 10^6$, which is of the same order of magnitude as the statistics used for the correlation function calculation, we look at different allocations of this fixed statistic to N_c and N_t. Three allocations are featured in both the $d\ln(S(\omega))/d\omega$ plot and the RMSE table of figure 6.6. The role of the number of trajectories N_t is straightforward: it is simply the size of the averaging sample. A higher N_t naturally leads to a more precise calculation of $S(\omega)$. The impact of N_c is less obvious but can be witnessed in the $d\ln(S(\omega))/d\omega$ plot. At high frequencies, the lower-N_c curve exhibits a $-2\mathcal{O}(\omega)$ logarithmic decrease which does not match the expected $-4\mathcal{O}(\omega)$, while for higher-N_c curves the -4 slope is reached before slowly going to -2 as well. We believe this is a numerical feature attributable to the choice of N_c. To see this, consider this simplified expansion of the PSD in powers of $1/\omega$, deduced from the form of F_{100} (6.21):

$$S(\omega) = \frac{-G_{10}}{T}\left\langle|F_{100}(\omega)|^2\right\rangle \propto \frac{-G_{10}}{T}\sum_{n,n'}^{N_c} c_{100}^{(n)}c_{100}^{(n')}\left(\frac{\alpha_{nn'}}{\omega^2}+\frac{\beta_{nn'}}{\omega^3}+\frac{\gamma_{nn'}}{\omega^4}\right), \tag{6.27}$$

where the $\alpha_{nn'}, \beta_{nn'}, \gamma_{nn'}$ are functions of $x_n, x_{n'}, t_n, t_{n'}$. In order for the $1/\omega^4$ term

to dominate at high frequencies as we would expect it to, the coefficients $\alpha_{nn'}$ and $\beta_{nn'}$ should sum out to zero. But the larger the frequency, the more suppressed the $1/\omega^4$ term is, thus the more collisions N_c are needed to cancel the $1/\omega^2$ and $1/\omega^3$ terms at a comparable scale. At low N_c our calculation is then less accurate for high frequencies. In summary, N_t determines the precision of our calculation and N_c its accuracy. Our choice of $N_c = 10^3$ is accurate for frequencies $\omega \lesssim 5\,\text{ms}$, which are largely dominant in the PSD's spectrum. After fixing $N_c = 10^3$ we then set N_t as high as possible.

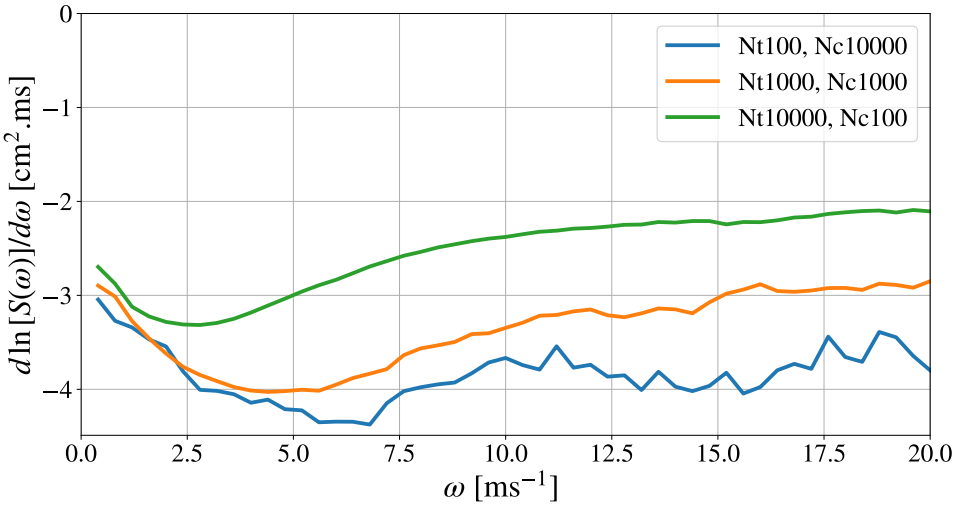

(N_t, N_c)	$(10^2, 10^4)$	$(10^3, 10^3)$	$(10^4, 10^2)$
RMSE$\left[S(\omega) - S^{\text{fit}}(\omega)\right]$ (cm^2 ms)	715	242	155

FIGURE 6.6: An evaluation of the accuracy and precision of the PSD calculation. The plot shows the derivative of the logarithmic PSD as a function of the frequency, for three allocations of the statistic $N_c \times N_t$. The table shows the RMSE between the calculation and the Lorentzian fit for the same statistics.

6.2.2 False EDM calculation and gradient field results

Having validated the consistency of the frequency domain approach to the false EDM with the correlation function approach through the Wiener-Khinchin theorem, we now extend the method presented above to a direct calculation of the false EDM. As opposed to the model-dependent estimate of section 6.1, we do not have to resort to a fit of the PSD. Instead, we use our calculation of $S(\omega)$(6.22) to obtain an explicit expansion of the false EDM. Recall that, because of the harmonic expansion of b_x, $S(\omega)$ is expressed as a sum of polynomial Fourier transforms $\langle F^*_{100} F_{abc} \rangle$. Each of these will generate through equation (6.8) polynomial false EDM terms of the form[5]

[5]Here we only show the case $\omega \neq 0$, which is general enough for the numerical calculation.

$$
\begin{aligned}
d_{abc}(\omega_0) &= -\frac{\hbar|\gamma_n\gamma_{\mathrm{Hg}}|}{4\pi c^2}\frac{G_N}{\Delta T N_c N_t}\sum_{m=1}^{N_t}\mathrm{P.V.}\int_{-\infty}^{+\infty}d\omega\frac{\omega}{\omega-\omega_0}F_{100}^{*(m)}(\omega)F_{abc}^{(m)}(\omega)\\
&= -\frac{\hbar|\gamma_n\gamma_{\mathrm{Hg}}|}{4\pi c^2}\frac{G_N}{\Delta T N_c N_t}\sum_{m=1}^{N_t}\sum_{n,n'=mN_c}^{(m+1)N_c}\sum_{k,k'=0}^{N}(-1)^k i^{k+k'}c_{100}^{(n,k)}c_{abc}^{(n',k')}\\
&\qquad\times\mathrm{P.V.}\int_{-\infty}^{+\infty}d\omega\frac{\omega e^{i\omega(t_n-t'_n)}}{\omega-\omega_0}J_k^*(\omega\Delta t_n)J_{k'}(\omega\Delta t_{n'}),
\end{aligned}
\tag{6.28}
$$

where G_N is a dimensional coefficient corresponding to a magnetic gradient of order $N = a + b + c$.

We will not give the full expansion of the false EDM here. Instead, we observe that the integrals $J_k(\omega\Delta t_n)$ are sums of terms of the form $e^{i\alpha}/\omega^{l\leq k}$. This motivates us to let $d_{abc} = \sum_p a_p K_p/\omega_0^p$, where the K_p are dimensionless Hilbert transforms defined as

$$
K_p(\alpha) = \mathrm{P.V.}\int_{-\infty}^{+\infty}d\nu\frac{e^{i\alpha\nu}}{\nu^p(\nu-1)},
\tag{6.29}
$$

with $\nu = \omega/\omega_0$ and $\alpha \in \mathbb{R}^*$. We will now show that these converge for $p \geq 0$.

Calculation of the K_p Hilbert transforms

The integrals defined by (6.29) can be determined explicitly by integrating in the complex plane and using the residue theorem. We have to consider the cases $p = 0$ and $p = 1$ separately because of the different choices of contour, before we generalize to all $p \geq 0$.

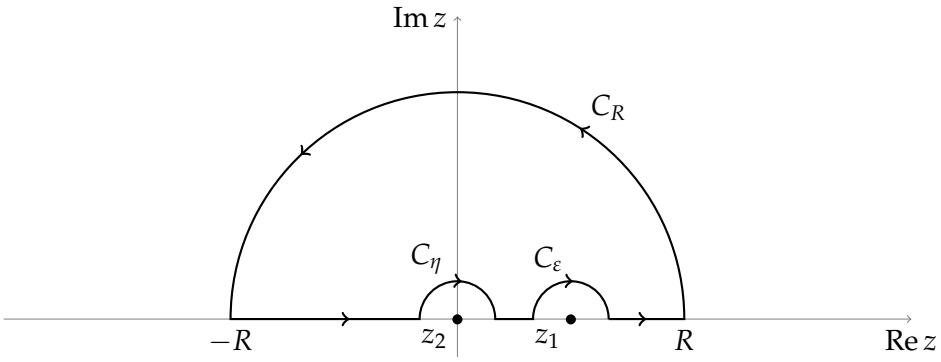

FIGURE 6.7: Contour in the complex plane over which $f(z)$ is integrated. This allows to determine K_p in the limit $R \to +\infty$ and $\varepsilon, \eta \to 0$. For $p = 0$ we only consider the pole $z_1 = 1$, while for $p = 1$ we consider z_1 as well as $z_2 = 0$. The counter-clockwise path chosen for $\alpha > 0$ is shown here.

(i) Case $p = 0$:
We define the complex-valued function on the complex plane

$$f(z) = \frac{e^{i\alpha z}}{z-1}. \tag{6.30}$$

This function is holomorphic on $\mathbb{C} \setminus \{z_1\}$, with a simple pole $z_1 = 1$. Consider the closed contour γ consisting of a half-circle in the positive complex plane and part of the real axis which circles around the simple pole. That is, $\gamma = \Gamma_R \cup \mathcal{C}_R \cup \mathcal{C}_\varepsilon$ with $\Gamma_R = [-R, 1-\varepsilon] \cup [1+\varepsilon, R]$, $\mathcal{C}_R = \{Re^{i\theta} \mid 0 \leq \theta \leq \pi\}$, and $\mathcal{C}_\varepsilon = \{1+\varepsilon e^{i\theta} \mid 0 \leq \theta \leq \pi\}$ with $R, \varepsilon > 0$ (see figure 6.7). In order to ensure that the portion of the integral on $\mathcal{C}_R$ converges, we choose an orientation of γ that depends on the sign of α:

- If $\alpha > 0$, we take γ in the counter-clockwise direction.
- If $\alpha < 0$, we take γ in the clockwise direction.

The purpose of this approach lies in the fact that, in the limit $\varepsilon \to 0$ and $R \to +\infty$, the real line portion of the contour integral goes to K_0:

$$\begin{aligned} K_0(\alpha) &= \lim_{\substack{R\to+\infty,\\ \varepsilon\to 0}} \int_{\Gamma_R} f(z)dz \\ &= \lim_{\substack{R\to+\infty,\\ \varepsilon\to 0}} \left(\oint_\gamma - \int_{\mathcal{C}_R} - \int_{\mathcal{C}_\varepsilon} \right) f(z)dz. \end{aligned} \tag{6.31}$$

We tackle the three integrals in (6.31) one by one. The integral over the entire contour γ is given by the residue theorem. Since we carefully avoided the function's only pole z_1 and given that f is holomorphic outside z_1, we meet the required conditions to apply B.3.1 and get:

$$\oint_\gamma f(z)dz = 0 \tag{6.32}$$

The integral over the outside circle's arc can be shown to go to zero in the large radius R limit. Because f is of the form $f(z) = e^{i\alpha z} g(z)$, with $g(z)$ holomorphic along $\mathcal{C}_R$, Jordans's Lemma (B.3.1) applies:

$$\left| \int_{\mathcal{C}_R} \frac{e^{i\alpha z}}{z-1} dz \right| \leq \frac{\pi}{\alpha R}, \tag{6.33}$$

where we assumed $\alpha > 0$. Clearly this integral vanishes for $R \to \infty$. Note that we would have obtained the same result for $\alpha < 0$ and a contour going in the opposite direction.

The sole contribution to K_0 ultimately comes from the integral over the infinitesimally small half-circle $\mathcal{C}_\varepsilon$ around z_1. This contour is parameterized by $z = 1 + \varepsilon e^{i\theta}$. Integrating over it for γ in the counter-clockwise direction yields

$$\begin{aligned} \int_{\mathcal{C}_\varepsilon} \frac{e^{i\alpha z}}{z-1} dz &= \int_\pi^0 \frac{e^{i\alpha(1+\varepsilon\cos\theta + i\varepsilon\sin\theta)}}{\varepsilon e^{i\theta}} i\varepsilon e^{i\theta} d\theta \\ &= ie^{i\alpha} \int_\pi^0 e^{i\alpha(\varepsilon\cos\theta + i\varepsilon\sin\theta)} d\theta. \end{aligned} \tag{6.34}$$

Taking the limit $\varepsilon \to 0$ leads to $\int_{\mathcal{C}_\varepsilon} f(z)dz = -i\pi e^{i\alpha}$. In the case $\alpha < 0$ we swap the integral bounds to obtain the same result to a -1 factor.

Combining the above in equation (6.31), for $\alpha > 0$ and $\alpha < 0$, we finally obtain

$$K_0(\alpha) = \operatorname{sgn}(\alpha) i\pi e^{i\alpha}, \quad \alpha \in \mathbb{R}^*. \tag{6.35}$$

(ii) Case $p = 1$:
This time the function f is of the form

$$f(z) = \frac{e^{i\alpha z}}{z(z-1)}, \tag{6.36}$$

and is holomorphic on $\mathbb{C} \setminus \{z_1, z_2\}$, with a simple pole $z_1 = 1$ as well as a simple pole $z_2 = 0$. The approach is practically identical to the $p = 0$ case with a slightly modified contour that goes around the extra pole at 0. Here $\gamma = \Gamma_R \cup \mathcal{C}_R \cup \mathcal{C}_\varepsilon \cup \mathcal{C}_\eta$, where $\mathcal{C}_\eta = \{\eta e^{i\theta} \mid 0 \leq \theta \leq \pi\}$ and $\Gamma_R = [-R, -\eta] \cup [\eta, 1-\varepsilon] \cup [1+\varepsilon, R]$ (see figure 6.7). The extra integral along $\mathcal{C}_\eta$, with $z = \eta e^{i\theta}$ and γ going in the counter-clockwise direction, is expressed as

$$\int_{\mathcal{C}_\eta} \frac{e^{i\alpha z}}{z(z-1)} dz = \int_\pi^0 \frac{e^{i\alpha\eta(\cos\theta + i\sin\theta)}}{\eta e^{i\theta}(\eta e^{i\theta} - 1)} i\eta e^{i\theta} d\theta. \tag{6.37}$$

This reduces to $\int_{\mathcal{C}_\eta} f(z)dz = i\pi$ in the limit $\eta \to 0$. We again get the opposite quantity for $\alpha < 0$. Finally,

$$\begin{aligned} K_1(\alpha) &= \lim_{\substack{R\to+\infty,\\ \varepsilon,\eta\to 0}} \int_{\Gamma_R} f(z)dz \\ &= \lim_{\substack{R\to+\infty,\\ \varepsilon,\eta\to 0}} \left(\oint_\gamma - \int_{\mathcal{C}_R} - \int_{\mathcal{C}_\varepsilon} - \int_{\mathcal{C}_\eta} \right) f(z)dz \\ &= \operatorname{sgn}(\alpha) i\pi \left(e^{i\alpha} - 1 \right), \quad \alpha \in \mathbb{R}^*. \end{aligned} \tag{6.38}$$

General case $p \geq 0$:
To determine the higher order integrals, we notice that the following recurrence relation holds for all $p \geq 0$:

$$\begin{aligned} \frac{\partial}{\partial\alpha} K_{p+1}(\alpha) &= \text{P.V.} \int_{-\infty}^{+\infty} d\nu \frac{i e^{i\alpha\nu}}{\nu^p(\nu - 1)} \\ &= i K_p(\alpha). \end{aligned} \tag{6.39}$$

This result is somewhat painful to utilize because $p+1$ order terms are obtained by integrating p order terms, thus can only be determined up to a constant. Fortunately we can evaluate $K_p(\alpha = 0)$ to determine this constant. For instance let us check that we can obtain K_1 from K_0 using this method:

$$\begin{aligned} i \int K_0(\alpha) d\alpha &= i \int \left(i\pi \operatorname{sgn}(\alpha) e^{i\alpha} \right) d\alpha \\ &= i\pi \operatorname{sgn}(\alpha) \left(e^{i\alpha} + C \right), \end{aligned} \tag{6.40}$$

with C a real constant. We then show using the Cauchy principal value definition (B.12) that

$$\begin{aligned} K_1(0) &= \lim_{\varepsilon\to 0}\left(\int_{-\infty}^{-\varepsilon} + \int_{\varepsilon}^{1-\varepsilon}\int_{1+\varepsilon}^{+\infty}\right)\frac{d\nu}{\nu(\nu-1)} \\ &= \lim_{\varepsilon\to 0}\left(\left[\ln\left|\frac{\nu-1}{\nu}\right|\right]_{-\infty}^{-\varepsilon} + \left[\ln\left|\frac{\nu-1}{\nu}\right|\right]_{\varepsilon}^{1-\varepsilon} + \left[\ln\left|\frac{\nu-1}{\nu}\right|\right]_{1+\varepsilon}^{+\infty}\right) \\ &= 0 \end{aligned} \tag{6.41}$$

On the other hand we have $K_1(0) = i\pi\,\mathrm{sgn}(\alpha)(1+C)$, which leads to $C=-1$. We finally recover the $K_1(\alpha) = i\pi\,\mathrm{sgn}(\alpha)\left(e^{i\alpha}-1\right)$ from (6.38). From now on we suppose that $K_p(0)=0$ for $p\geq 1$.

Doing this a few times allows us to guess the pattern that the $K_p(\alpha)$ follow. In fact we claim that, for any $p\geq 0$, these integrals are given by:

$$(P_p) \qquad K_p(\alpha) = i\pi\,\mathrm{sgn}(\alpha)\left(e^{i\alpha} - \sum_{k=0}^{p-1}\frac{(i\alpha)^k}{k!}\right). \tag{6.42}$$

We will prove by induction that (P_p) is true for all $p\geq 1$.

(i) $K_1(\alpha) = \mathrm{sgn}(\alpha) i\pi\left(e^{i\alpha}-1\right) = i\pi\,\mathrm{sgn}(\alpha)\left(e^{i\alpha} - \sum_{k=0}^{1-1}(i\alpha)^k/(k!)\right)$, so (P_1) is true.

(ii) Assume that (P_p) is true. Then by the recurrence relation (6.39),

$$\begin{aligned} K_{p+1}(\alpha) &= i\int d\alpha\left(i\pi\,\mathrm{sgn}(\alpha)\left(e^{i\alpha} - \sum_{k=0}^{p-1}\frac{(i\alpha)^k}{k!}\right)\right) \\ &= i\pi\,\mathrm{sgn}(\alpha)\left(e^{i\alpha} - \sum_{k=0}^{p-1}\frac{(i\alpha)^{k+1}}{(k+1)!} + C\right) \\ &= i\pi\,\mathrm{sgn}(\alpha)\left(e^{i\alpha} - \sum_{k=1}^{p}\frac{(i\alpha)^k}{k!} + C\right) \end{aligned} \tag{6.43}$$

Using $K_{p+1}(0)=0$ yields $C=1$, so finally $K_{p+1}(\alpha) = i\pi\,\mathrm{sgn}(\alpha)\left(e^{i\alpha} - \sum_{k=0}^{p} e(i\alpha)^k/(k!)\right)$. We have shown that if (P_p) is true, then (P_{p+1}) is true.

(iii) From (i) and (ii) we conclude that (P_p) is true for all $p\geq 1$.

Results for a vertical gradient field

We have now all the tools in hand to give a full expansion of the frequency domain false EDM in a given magnetic configuration. As usual we focus on the simple case of a vertical gradient field, which generates a false EDM through the PSD of two noises $x(t)$ and $b_x(t) = -G_{10}x(t)$. In our formalism, this false EDM is simply

$$d^{\mathrm{false}}_{n\leftarrow\mathrm{Hg}}(\omega_0) = \frac{G_{10}}{G_N} d_{100}(\omega_0) \tag{6.44}$$

with d_{100} given by equation (6.28). Using the coefficients $c_{100}^{(n,k)}$ from (6.16) and expanding the J_k terms given by equation (6.20) we give its explicit expansion:

$$
\begin{aligned}
d^{\text{false}}_{n\leftarrow\text{Hg}}(\omega_0) = &-\frac{\hbar|\gamma_n\gamma_{\text{Hg}}|}{4\pi c^2}\frac{G_{10}}{\Delta T N_c N_t}\sum_{m=1}^{N_t}\sum_{k,l=mN_c}^{(m+1)N_c}\times \\
&\left\{\frac{1}{\omega_0}\left[x_{k+1}x_{l+1}K_1(\omega_0\Delta t_{l+1,k+1}) - x_{k+1}x_l K_1(\omega_0\Delta t_{l,k+1}) - x_k x_{l+1}K_1(\omega_0\Delta t_{l+1,k}) + x_k x_l K_1(\omega_0\Delta t_{l,k})\right]\right. \\
&+\frac{i}{\omega_0^2}\left[\left(\frac{\Delta x_l}{\Delta t_l}x_{k+1} - \frac{\Delta x_k}{\Delta t_k}x_{l+1}\right)K_2(\omega_0\Delta t_{l+1,k+1}) - \left(\frac{\Delta x_l}{\Delta t_l}x_{k+1} - \frac{\Delta x_k}{\Delta t_k}x_l\right)K_2(\omega_0\Delta t_{l,k+1})\right] \\
&+\frac{i}{\omega_0^3}\left[\left(\frac{\Delta x_l}{\Delta t_l}x_k - \frac{\Delta x_k}{\Delta t_k}x_{l+1}\right)K_2(\omega_0\Delta t_{l+1,k}) - \left(\frac{\Delta x_l}{\Delta t_l}x_k - \frac{\Delta x_k}{\Delta t_k}x_l\right)K_2(\omega_0\Delta t_{l,k})\right] \\
&\left.+\frac{1}{\omega_0^4}\left[\frac{\Delta x_k\Delta x_l}{\Delta t_k\Delta t_l}\left(K_3(\omega_0\Delta t_{l+1,k+1}) - K_3(\omega_0\Delta t_{l,k+1}) - K_3(\omega_0\Delta t_{l+1,k}) + K_3(\omega_0\Delta t_{l,k})\right)\right]\right\},
\end{aligned}
\tag{6.45}
$$

where we let $\Delta t_{k,l} = t_k - t_l$ and where the dimensionless integrals K_p are given for all $p \geq 0$ by (6.42).

We computed the gradient field false EDM for 100 value of ω_0 in the range $[-3,3]\,\text{ms}^{-1}$, with the PSD's choice of statistics $(N_c, N_t) = (10^3, 10^3)$. Figure 6.8 shows these results (in red) as a function of the magnetic field $B_0 = \omega_0/\gamma_{\text{Hg}}$ in a region of interest, averaged over 20 runs. These are compared with the false EDM obtained from the correlation function fit (in blue) and presented in section 6.1. Both are in very good agreement with a reduced chi-squared $\chi/\nu = 0.61$.

The magic field value B_1^{mag} was determined using a simple zero-crossing search algorithm, wherein we select two points ω_1, ω_2 such that $d^{\text{false}}_{n\leftarrow\text{Hg}}(\omega_1) > 0$ and $d^{\text{false}}_{n\leftarrow\text{Hg}}(\omega_2) < 0$ and calculate the false EDM at $\omega_3 = (\omega_1+\omega_2)/2$. If $d^{\text{false}}_{n\leftarrow\text{Hg}}(\omega_3) > 0$ we reiterate this process with ω_3 and ω_2, if not we reiterate with ω_1 and ω_3. The results are displayed in the table at the bottom of figure 6.8 and compared with those of the $C(\tau)$ fit. With this method we are able to reach within 20 iterations a precision on the magic value comparable to that of the correlation function method, and a compatible magic field value within one sigma.

In conclusion, the PSD approach allows a direct calculation of the false EDM for a given value of the applied field B_0. Using only the results of TOMAt's simulation of mercury atom trajectories, we gave a calculation of a polynomial field-position PSD which we showed was consistent with the field-position correlation function in the case of a vertical field gradient. Doing this we also chose the parameters that optimized both the precision and the accuracy of our numerical estimate. We finally built on this approach to arrive at a frequency-domain false EDM calculation which was also in agreement with its time-domain fit, as was its corresponding magic value B_1^{mag}. The benefit of our approach is that it provides an unbiased estimate of this crucial quantity, as it does not depend on the arbitrary assumption that the field-position correlation of mercury atoms follows a double exponential model. Although both methods boast comparable numerical efficiency, we acquired the much needed confirmation that our estimate of the false EDM was consistent with the correspondence of time and frequency domain expressions of spin-relaxation theory.

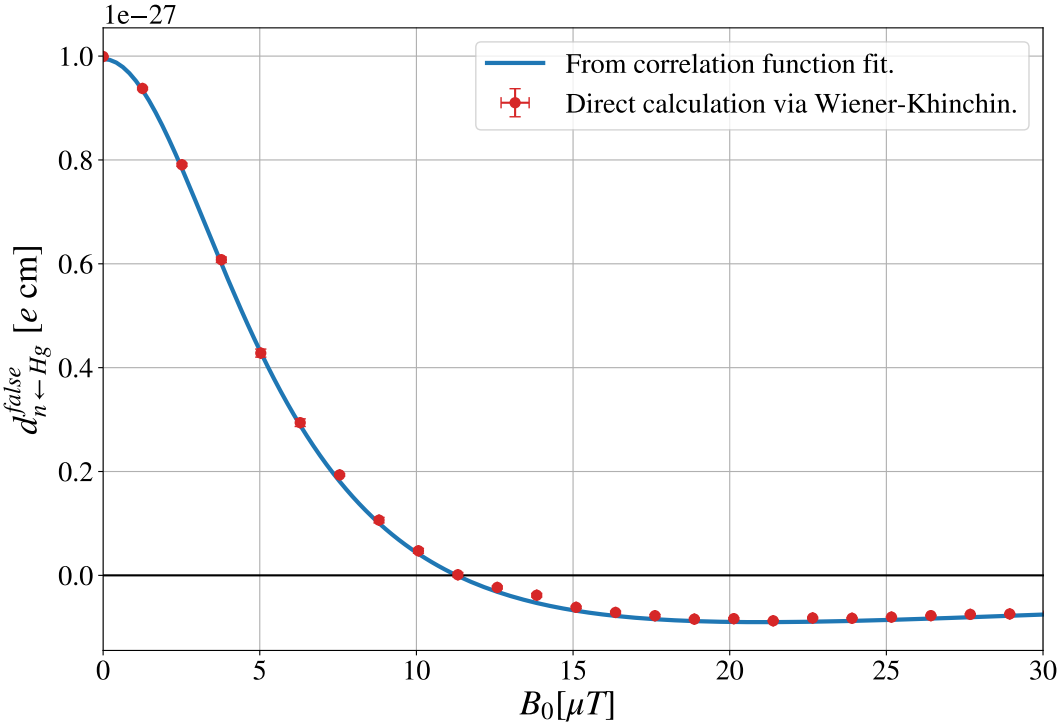

	$C(\tau)$ **fit**	**Direct calc.**
B_1^{mag} (μT)	11.28(9)	11.34(6)

FIGURE 6.8: Comparison of two methods to estimate the false EDM and its magic field in a gradient field configuration. The plot shows the results of the direct false EDM calculation in the frequency domain over $N = 20$ iterations (in red). It is in agreement with the estimate given by the time-domain correlation function fit (in blue), with a reduced chi-squared $\chi/\nu = 0.61$. The table shows the zero crossing, or *magic field*, of both quantities.

6.3 The magic field value for n2EDM

We now turn to the experimental reality of n2EDM. Although the magnetic noise we are concerned with in terms of systematic consists mainly of a vertical gradient, additional contributions arise from more intricate combinations of harmonic modes. We introduced these field combinations in chapter 5 as the phantom modes of odd degree l. Here we present the application of the correlation function calculation to the phantom gradients and subsequently determine the magic field value most appropriate to the magnetic environment of n2EDM. We then show that our field generating instrument, the B_0 coil, is capable of functioning at this much higher value of B_0 in a way that allows us to satisfyingly suppress the false EDM.

6.3.1 Correlation functions of phantom modes and choice of magic value

The realistic non-uniform magnetic field of n2EDM consists as we know from the introductory section of chapter 5 of l-odd, $m = 0$ harmonic modes, that resist the cylindrical symmetry of the apparatus. Some combinations of these in particular are invisible to our online monitoring, i.e. do not generate a measurable top-bottom gradient, and as such are considered problematic. These are the phantom modes

$\acute{G}_{2l+1}\acute{\mathbf{\Pi}}_{2l+1}$. We also know that the false EDM generated by a very general magnetic field configuration is of the form $d^{\text{false}}_{\text{n}\leftarrow\text{Hg}} = \frac{\hbar|\gamma_n\gamma_{\text{Hg}}|}{8\pi c^2}R^2\left(G_{\text{TB}} + \acute{G}_3 + \acute{G}_5 + \acute{G}_7 + \dots\right)$, where the contribution of the phantom gradients is made explicit.

Our goal here is to give the frequency spectrum of the false EDM generated by each of these modes, in order to then determine their respective zero-crossing, or magic value. This has already been carried out and presented in the experiment's design article for phantom modes of order $l = 3$ and $l = 5$ (al., 2022); here we extend it to phantom modes of order $l = 7$. We start again from the general false EDM formula (6.1), valid for any frequency ω, but this time consider correlation functions of the form

$$\begin{aligned} C(\tau) &= \acute{G}_{2l+1}\left\langle x(0)\acute{\Pi}_{x,2l+1}(\tau)\right\rangle + \acute{G}_{2l+1}\left\langle y(0)\acute{\Pi}_{y,2l+1}(\tau)\right\rangle \\ &= \acute{G}_{2l+1}\frac{L^{2k}_{2k+1}}{D^{2k}_{2k+1}}\left[(-1)^k\left\langle x(0)x(\tau)\right\rangle + \frac{1}{L^{2k}_{2k+1}}\left\langle x(0)\Pi_{x,2l+1}(\tau)\right\rangle\right] \\ &+ \acute{G}_{2l+1}\frac{L^{2k}_{2k+1}}{D^{2k}_{2k+1}}\left[(-1)^k\left\langle y(0)y(\tau)\right\rangle + \frac{1}{L^{2k}_{2k+1}}\left\langle y(0)\Pi_{y,2l+1}(\tau)\right\rangle\right], \end{aligned} \tag{6.46}$$

where we have replaced the phantom mode with its harmonic expression, given in appendix (A) by equation (C.13). With the help of the harmonic expansion A.2, we see that $C(\tau)$ is simply a sum of polynomial terms of the form $\left\langle x(0)x^i(\tau)y^j(\tau)z^k(\tau)\right\rangle$ that we can ask TOMAt to compute. Just as in the case of the vertical field gradient, we then fit the simulated correlation function (6.46) with the double exponential model (6.5). All of this is done for $k = 1, 2, 3$ in order to obtain up to order $l = 7$ phantom gradients. The results of these calculations and fits are shown as a function of the applied field $B_0 = \omega/\gamma_{\text{Hg}}$ in figure 6.9, where we set all phantom gradient coefficients to 78 fT/cm.

To each false EDM generated by a specific magnetic configuration corresponds a magic field value, which can be determined from the correlation function's fit parameters through (6.7). Figure 6.10 shows a zoomed in version of the false EDM plot where all zero-crossings are visible. Their values are given in the table below. The magic field strategy of n2EDM will be to set B_0 to a value that completely cancels the false EDM generated by one particularly problematic mode and most suppresses the others. That value is the fifth order phantom mode's magic field $B_5^{\text{mag}} = 10.6\,\mu\text{T}$. The amount of suppression induced by setting B_0 to B_5^{mag} instead of 1 µT is represented by the ratio $\left|d^{\text{false}}_{n\leftarrow\text{Hg}}(B_5^{\text{mag}}/\gamma_{\text{Hg}})/d^{\text{false}}_{n\leftarrow\text{Hg}}(1/\gamma_{\text{Hg}})\right|$, which shows that this choice of magic field suppresses the contributions of all phantom gradients by more than 95%. We will now give a numerical estimate of the false EDM generated at the magic field from the harmonic gradient measurements performed at $B_0 = 10\,\mu\text{T}$.

6.3.2 Experimental viability of the magic field range

Although the analysis of magnetic field measurements is the subject of the third part of this thesis, we present here some data obtained during one of the B_0 coil's mapping campaigns that directly concerns the magic field option to cancel the false EDM. Figure 6.11 shows the harmonic coefficients G_{lm} extracted from a series of B_0 field measurements, for two different values of the current driven through the B_0 coil. The first of these produces the usual $B_0 = 1\,\mu\text{T}$ in which n2EDM will mainly operate, and the second produces a 10 µT field in the range of the values that will cancel the false EDM when implementing the magic field strategy. Both measurements are

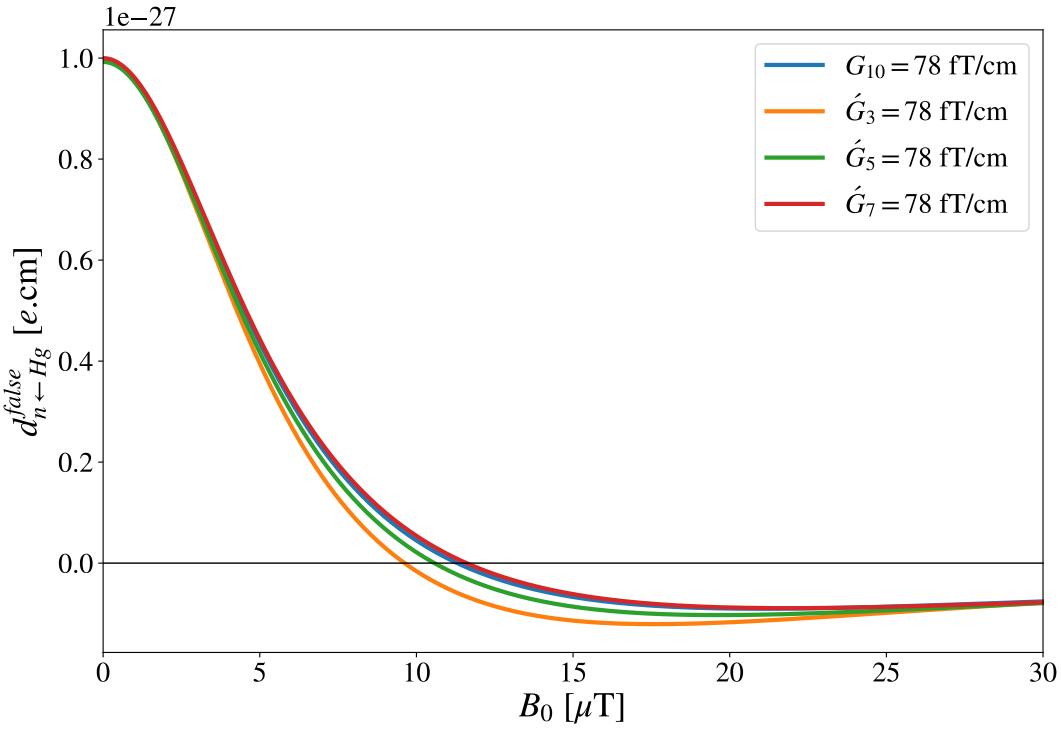

FIGURE 6.9: False EDM generated by a given magnetic setup as a function of the applied field B_0. We show four magnetic configurations: a vertical gradient mode, and phantom modes of order three, five, and seven. The field gradient coefficients are set to 78 fT/cm so that the false EDM at $B_0 = 0$ is $1 \times 10^{-27}\, e$ cm.

compared by scaling the 1 µT measurements up to the magic field measurements to a factor 10. Finally, let us note that these were recorded in a "default" magnetic environment, with full magnetic shielding but without field optimization.

The two scaled spectra are of the same magnitude. This suggests that the harmonic spectrum of the B_0 coil scales linearly with the applied current, at least up to the magic field range. A crucial implication of this linearity is that we can safely extrapolate the 10 µT harmonic spectrum from the much more abundant measurements performed at 1 µT.

Let us now return to our discussion on the suppression of the false EDM when operating at $B_0 = B_5^{\text{magic}}$. We use the measured harmonic gradients, given by figure 6.11 up to $l = 5$, to estimate the false EDM generated by each phantom mode at the chosen magic value, in a realistic n2EDM magnetic environment. The results are shown in figure 6.10 (table's third line). Recalling from 3.2 that our systematical requirement stands at $d^{\text{false}}_{\text{n}\leftarrow\text{Hg}} < 3 \times 10^{-28}\, e$ cm, we conclude that the fifth and seventh order gradients generate a null or negligible false EDM, while the third order modes' false EDM is one order of magnitude above the limit. However these results only apply for a "bare", non-optimized field. As will be thoroughly discussed in chapter 9, there exists a field optimization strategy in which we fine tune the currents running through the trim coil array and gradient coils so as to largely reduce the most problematic harmonic modes. The last line of table 6.10 shows the false EDMs generated at B_5^{magic} with phantom gradients G_{2k+1} extrapolated from the optimized field measurements recorded at 1 µT. In this case the false EDM is completely suppressed for all phantom modes.

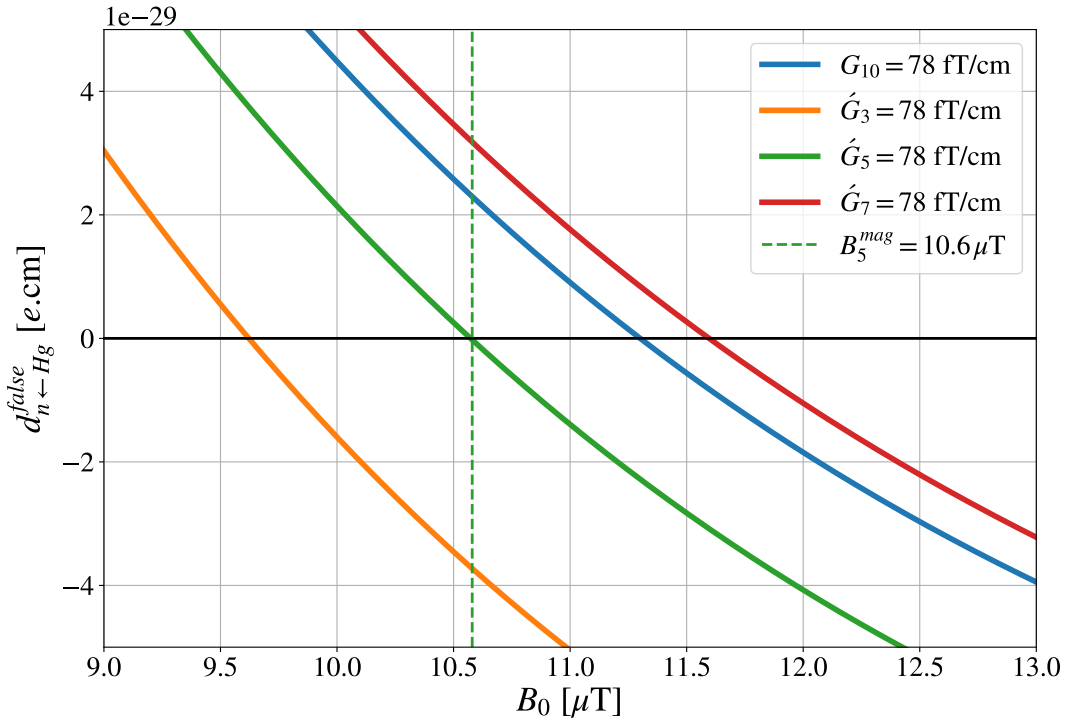

	$\acute{G}_3\acute{I}_3$	$\acute{G}_5\acute{I}_5$	$\acute{G}_7\acute{I}_7$
B^{mag}_{2k+1} [μT]	9.6	10.6	11.6
$\left\lvert \frac{d^{\text{false}}_{n\leftarrow\text{Hg}}(B^{\text{mag}}_5/\gamma_{\text{Hg}})}{d^{\text{false}}_{n\leftarrow\text{Hg}}(1/\gamma_{\text{Hg}})} \right\rvert$	3.7%	0%	3.2%
$d^{\text{false}}_{n\leftarrow\text{Hg}}(B^{\text{mag}}_5/\gamma_{\text{Hg}})$ [$10^{-28}\,e$ cm]	28.4	0	0.1
$d^{\text{false}}_{n\leftarrow\text{Hg}}(B^{\text{mag}}_5/\gamma_{\text{Hg}})$ [$10^{-28}\,e$ cm] (optimized)	0.9	0	< 0.1

FIGURE 6.10: A zoomed in view of figure 6.9 that highlights the zero-crossings - or magic fields - corresponding to each magnetic configuration. The magic field values are given in the attached table, along with the suppression of each false EDM when functioning at the chosen magic value B_5^{magic}. The third line gives the exact false EDM generated by each configuration at the B_5^{magic}, based on the harmonic gradients measurements given by 6.11. The last line gives the same value but in the case where use optimization coils to lower non-uniformities (9). Note that the harmonic gradients values are extrapolated from the optimized 1 μT field measurements.

6.4 Suppression of magnetic dipoles with the magic field approach

We began this chapter by considering simplistic magnetic configurations in order to carefully justify the magic field approach to correcting the false EDM. We then established that it was possible to implement this strategy for more complex magnetic

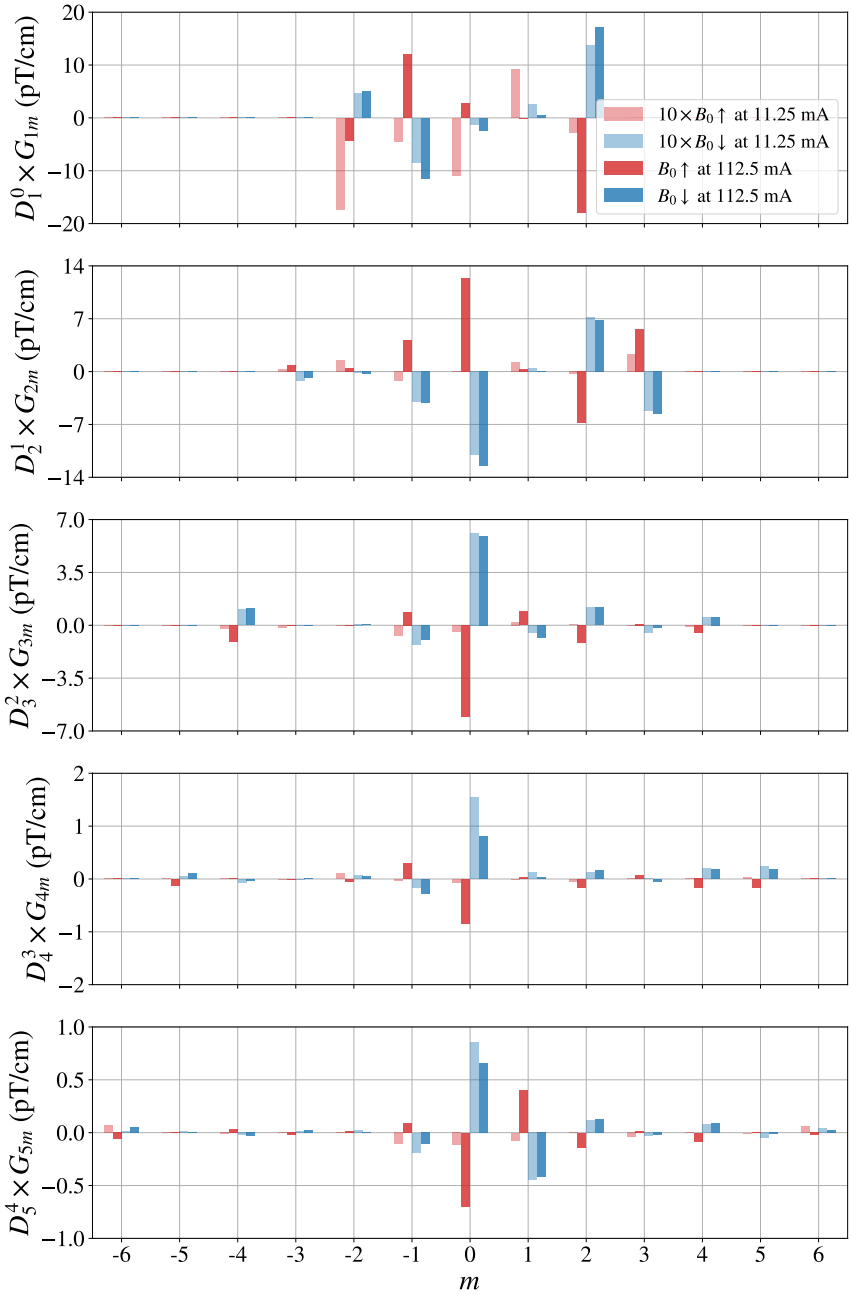

FIGURE 6.11: Harmonic spectrum of the B_0 field extracted from the magnetic mapping data, for two values of the current driven through the B_0 coil. The 11.25 mA current generates the 1 µT uniform field, while the 112.5 mA current generates a field in the region of the magic field value $B_5^{\text{mag}} \approx 10\,\mu\text{T}$. The 1 µT spectrum is scaled up for comparison.

fields that involved up to order $l = 7$ harmonic field expansions. Yet our claims always rested on the assumption that the magnetic field *could* be accurately described by a polynomial expansion. A cause for concern is then the existence of high-order magnetic structures, such as dipole fields, that contribute to the total non-uniformity in a non-negligible way and for which the harmonic expansion is ineffective.

Here we present a method to calculate correlation functions not of polynomial terms but of the form $\langle x(\tau)B_x(0)\rangle$, where B_x takes the form of a dipole field. We

then calculate the associated false EDM with the usual fit method. From our results given in the previous section, we finally estimate the amount of suppression of the dipole-induced false EDM at the chosen magic field B_5^{mag}.

6.4.1 The dipole field correlation function

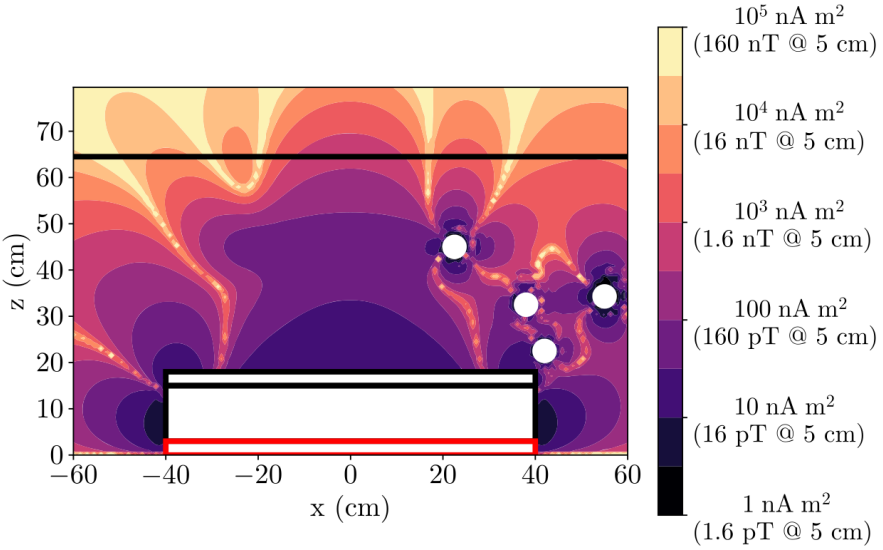

FIGURE 6.12: Top vertical cut of the n2EDM vacuum vessel with top precession chamber visible in white, taken from (al., 2022). The color scale gives the maximum dipole strength allowed by the systematical requirements 3.1 of n2EDM, and is the result of a study by (Pais, 2021). The most critical dipoles are located around the chamber and the cesium magnetometers, represented as white discs.

The area inside the vacuum vessel of n2EDM, depicted in figure 6.12, is likely to contain small ferromagnetic impurities which are especially problematic if they are located near the precession chambers or the cesium magnetometers. It has been estimated that such an impurity, modeled as a spherical iron dust of 20 µm, possesses a magnetic moment $m = 1 \times 10^5\,\text{nA}\,\text{cm}^2$ (Abel et al., 2019). The magnetic field generated by this iron sphere which we assume to be localized at $\mathbf{r}_d$ can be described by the dipole field

$$\begin{aligned}\mathbf{B}(\mathbf{r}) &= \nabla \times \left(\frac{\mu_0}{4\pi} \frac{\mathbf{m} \times (\mathbf{r} - \mathbf{r}_d)}{|\mathbf{r} - \mathbf{r}_d|^3} \right) \\ &= \frac{\mu_0}{4\pi} \left(\frac{3(\mathbf{m} \cdot (\mathbf{r} - \mathbf{r}_d))(\mathbf{r} - \mathbf{r}_d)}{|\mathbf{r} - \mathbf{r}_d|^5} - \frac{\mathbf{m}}{|\mathbf{r} - \mathbf{r}_d|^3} \right),\end{aligned} \tag{6.47}$$

where $\mathbf{m}$ is the dipole's strength. Of course it is always possible to give a polynomial expansion of the dipole field at a point where it is properly defined and differentiable, but the amount of terms needed for this expansion to be accurate goes far beyond our numerical capabilities, which stop at polynomial degree 7. This difficulty increases the closer we are to the singularity $\mathbf{r}_d$, which is a likely scenario when the dipole is located close to the precession volume.

Having ruled out a polynomial form of the field-position correlation function computable by TOMAt, we decide to directly evaluate

$$C(\tau) = \langle x(\tau) B_x(\mathbf{r}(0)) \rangle + \langle y(\tau) B_y(\mathbf{r}(0)) \rangle \,, \tag{6.48}$$

where B_x and B_y are transverse projections of the dipole field (6.47). Here we will only show the calculation of the x contribution of $C(\tau)$, as the method to determine the y contribution is obtained by a simple $x \leftrightarrow y$ substitution. The first steps of our approach follow those presented in the calculation of the polynomial correlation functions and PSDs (see section 6.2), so we will only cover them briefly. We assume the ergodicity of the correlation function in the limit $T \to \infty$ and calculate

$$\langle x(\tau) B_x(\mathbf{r}(0)) \rangle = \frac{1}{T} \int_0^T dt\, x(t+\tau) B_x(\mathbf{r}(t)). \tag{6.49}$$

Partitioning the time integral in intervals on which both $\mathbf{r}(t)$ and $\mathbf{r}(t+\tau)$ are linear functions of t we write:

$$\langle x(\tau) B_x(\mathbf{r}(0)) \rangle = \frac{1}{T} \sum_n \Delta t_n I_n, \qquad I_n = \frac{1}{\Delta t_n} \int_{t_n}^{t_{n+1}} dt\, x(t+\tau) B_x(\mathbf{r}(t)). \tag{6.50}$$

We then apply the change of integration variable $\theta = (t - t_n)/\Delta t_n$, with $\Delta t_n = t_{n+1} - t_n$. Using the linearity (6.12) we have in this case $\mathbf{r}(\Delta t_n \theta + t_n) = \Delta \mathbf{r}_n \theta + \mathbf{r}_n = (\Delta x_n \theta + x_n, \Delta y_n \theta + y_n, \Delta z_n \theta + z_n)$. Rewriting the delayed trajectory as $\tilde{x}(t) \equiv x(t+\tau)$, the elementary integral becomes

$$\begin{aligned}
I_n &= \int_0^1 d\theta\ (\Delta \tilde{x}_n \theta + \tilde{x}_n)\, B_x(\Delta \mathbf{r}_n \theta + \mathbf{r}_n) \\
&= \frac{\mu_0}{4\pi} \int_0^1 d\theta\ (\Delta \tilde{x}_n \theta + \tilde{x}_n) \left(\frac{3(\mathbf{m} \cdot (\Delta \mathbf{r}_n \theta + \mathbf{r}_n - \mathbf{r}_d))(\Delta x_n \theta + x_n - x_d)}{|\Delta \mathbf{r}_n \theta + \mathbf{r}_n - \mathbf{r}_d|^5} - \frac{m_x}{|\Delta \mathbf{r}_n \theta + \mathbf{r}_n - \mathbf{r}_d|^3} \right) \\
&\equiv \frac{\mu_0}{4\pi} \left(\frac{3|\mathbf{m}|}{|\Delta \mathbf{r}_n|^5} \left[b_1^3 J_{23}(\mathbf{u}, \mathbf{v}, \lambda) + b_2^3 J_{22}(\mathbf{u}, \mathbf{v}, \lambda) + b_3^3 J_{21}(\mathbf{u}, \mathbf{v}, \lambda) + b_4^3 J_{20}(\mathbf{u}, \mathbf{v}, \lambda) \right] \right. \\
&\qquad \left. - \frac{|\mathbf{m}|}{|\Delta \mathbf{r}_n|^3} \left[a_1 J_{11}(\mathbf{u}, \mathbf{v}, \lambda) + a_2 J_{10}(\mathbf{u}, \mathbf{v}, \lambda) \right] \right),
\end{aligned} \tag{6.51}$$

where we define the length coefficients a_i, b_i, the unit vectors $\mathbf{u}, \mathbf{v}$, and the dimensionless ratio λ by

$$\begin{cases} a_1 &= m_x \Delta\tilde{x}_n / |\mathbf{m}| \\ a_2 &= m_x \tilde{x}_n / |\mathbf{m}| \end{cases} \tag{6.52}$$

$$\begin{cases} b_1^3 &= \Delta\tilde{x}_n \mathbf{m} \cdot \Delta\mathbf{r}_n \Delta x_n / |\mathbf{m}| \\ b_2^3 &= (\Delta\tilde{x}_n \mathbf{m} \cdot \Delta\mathbf{r}_n (x_n - x_d) + \Delta\tilde{x}_n \mathbf{m} \cdot (\mathbf{r}_n - \mathbf{r}_d)\Delta x_n + \tilde{x}_n \mathbf{m} \cdot \Delta\mathbf{r}_n \Delta x_n)/|\mathbf{m}| \\ b_3^3 &= (\Delta\tilde{x}_n \mathbf{m} \cdot (\mathbf{r}_n - \mathbf{r}_d)(x_n - x_d) + \tilde{x}_n \mathbf{m} \cdot \Delta\mathbf{r}_n (x_n - x_d) + \tilde{x}_n \mathbf{m} \cdot (\mathbf{r}_n - \mathbf{r}_d)\Delta x_n)/|\mathbf{m}| \\ b_4^3 &= \tilde{x}_n \mathbf{m} \cdot (\mathbf{r}_n - \mathbf{r}_d)(x_n - x_d)/|\mathbf{m}| \end{cases} \tag{6.53}$$

$$\begin{cases} \mathbf{u} &= \Delta\mathbf{r}_n / |\Delta\mathbf{r}_n| \\ \mathbf{v} &= (\mathbf{r}_n - \mathbf{r}_d)/|\mathbf{r}_n - \mathbf{r}_d| \\ \lambda &= |\mathbf{r}_n - \mathbf{r}_d| / |\Delta\mathbf{r}_n| \end{cases} \tag{6.54}$$

Finally, we define the dimensionless integrals

$$J_{ij}(\mathbf{u}, \mathbf{v}, \lambda) = \int_0^1 d\theta \, \frac{\theta^j}{|\mathbf{u}\theta + \lambda\mathbf{v}|^{2i+1}}, \tag{6.55}$$

and give their explicit expansion in the next paragraph.

Calculation of the J_{ij} integrals

The integrals $J_{ij}(\mathbf{u}, \mathbf{v}, \lambda)$ converge for integer values of i and j only if $\mathbf{v} \neq 0$. This means that we cannot consider a dipole anywhere inside the integration volume, i.e. inside the precession chamber. In the case where $\mathbf{v} \neq 0$, we consider different configurations of $\mathbf{u}$ and $\mathbf{v}$:

1. If $\mathbf{u} = 0$, which corresponds to $\mathbf{r}_{n+1} = \mathbf{r}_n$ (impossible in principle but a particle locked inside a corner of the chamber goes to this limit), then the denominator does not depend on θ and we simply have

$$\begin{aligned} J_{ij} &= \frac{1}{\lambda^{2i+1}} \int_0^1 d\theta \, \theta^j \\ &= \frac{1}{(j+1)\lambda^{2i+1}}. \end{aligned} \tag{6.56}$$

2. If $\mathbf{u} \neq 0$, then we study the sign of the second degree θ-polynomial $|\mathbf{u}\theta + \lambda\mathbf{v}|^2$. Its determinant is $\Delta = 4\lambda^2 \left([\mathbf{u} \cdot \mathbf{v}]^2 - 1\right)$. By the Cauchy-Schwartz inequality we have $\Delta \leq 0$, and two new cases arise:

   (i) If $\mathbf{u}$ and $\mathbf{v}$ are collinear, i.e. $\mathbf{u} = \mathbf{v}$ since both are unit vectors, then $\Delta = 0$. In this case,

$$\begin{aligned} J_{ij} &= \int_0^1 d\theta \, \frac{\theta^j}{|\theta + \lambda|^{2i+1}} \\ &= \sum_{k=0}^{j} \binom{j}{k} \frac{(-\lambda)^{j-k}}{k - 2i} \left(\frac{1}{(1+\lambda)^{2i-k}} - \frac{1}{\lambda^{2i-k}} \right). \end{aligned} \tag{6.57}$$

(ii) If $\mathbf{u}$ and $\mathbf{v}$ are linearly independent, which is by far the most common case, then $\Delta < 0$. This allows us to complete the square with the substitution $w = \frac{2}{\sqrt{|\Delta|}}(\theta + \lambda \mathbf{u}\cdot\mathbf{v})$:

$$\begin{aligned} J_{ij} &= \int_0^1 d\theta \, \frac{\theta^j}{(\theta^2 + 2\lambda \mathbf{u}\cdot\mathbf{v}\theta + \lambda^2)^{(2i+1)/2}} \\ &= \left(\frac{4}{|\Delta|}\right)^{(2i+1)/2} \int_0^1 d\theta \, \frac{\theta^j}{\left(\frac{4}{|\Delta|}(\theta + \lambda \mathbf{u}\cdot\mathbf{v})^2 + 1\right)^{(2i+1)/2}} \\ &= \left(\frac{4}{|\Delta|}\right)^{i} \int_{w(0)}^{w(1)} dw \, \frac{\left(\frac{\sqrt{|\Delta|}}{2} w - \lambda \mathbf{u}\cdot\mathbf{v}\right)^j}{(w^2+1)^{(2i+1)/2}} \\ &= \left(\frac{4}{|\Delta|}\right)^{i} \sum_{k=0}^{j} \binom{j}{k} (-\lambda \mathbf{u}\cdot\mathbf{v})^{j-k} \left(\frac{\sqrt{|\Delta|}}{2}\right)^k \int_{w(0)}^{w(1)} dw \, \frac{w^k}{(w^2+1)^{(2i+1)/2}} \end{aligned} \tag{6.58}$$

which is just a sum of converging integrals

$$K_{ij} = \int_{w(0)}^{w(1)} dw \, \frac{w^j}{(w^2+1)^{(2i+1)/2}}. \tag{6.59}$$

These are determined thanks to the substitution $\tan z = w$:

$$K_{ij} = \int_{\operatorname{atan} w(0)}^{\operatorname{atan} w(1)} dz \, (\tan z)^j (\cos z)^{2i-1}, \tag{6.60}$$

which for our dipole function (6.51) yields

$$K_{10} = [\sin z]_{w(0)}^{w(1)} = \left[\frac{w}{\sqrt{1+w^2}}\right]_{w(0)}^{w(1)} \tag{6.61}$$

$$K_{11} = -[\cos z]_{w(0)}^{w(1)} = \left[\frac{-1}{\sqrt{1+w^2}}\right]_{w(0)}^{w(1)} \tag{6.62}$$

$$K_{20} = \left[\sin z - \frac{\sin^3 z}{3}\right]_{w(0)}^{w(1)} = \left[\frac{w}{\sqrt{1+w^2}} - \frac{w^3}{3(1+w^2)^{3/2}}\right]_{w(0)}^{w(1)} \tag{6.63}$$

$$K_{21} = \left[\frac{-\cos^3 z}{3}\right]_{w(0)}^{w(1)} = \left[\frac{-1}{3(1+w^2)^{3/2}}\right]_{w(0)}^{w(1)} \tag{6.64}$$

$$K_{22} = \left[\frac{\sin^3 z}{3}\right]_{w(0)}^{w(1)} = \left[\frac{w^3}{3(1+w^2)^{3/2}}\right]_{w(0)}^{w(1)} \tag{6.65}$$

$$K_{23} = \left[\frac{\cos^3 z}{3} - \cos z\right]_{w(0)}^{w(1)} = \left[\frac{1}{3(1+w^2)^{3/2}} - \frac{1}{\sqrt{1+w^2}}\right]_{w(0)}^{w(1)}. \tag{6.66}$$

Results for a dipole on the vertical axis.

We are now able to calculate the dipole correlation function (6.48) of a dipole of arbitrary strength $\mathbf{m}$ and position $\mathbf{r}_d$ outside of the precession volume. Our first application is that of a dipole located on the vertical axis of a cylindrical chamber, with $\mathbf{r}_d = z_d\,\mathbf{e}_z$, and with a vertical magnetic moment $\mathbf{m} = m\,\mathbf{e}_z$. In this case, the dipole field generated at a point $\mathbf{r} = z\,\mathbf{e}_z + \rho\,\mathbf{e}_\rho$ inside the cylindrical volume is expressed in cylindrical coordinates as

$$\mathbf{B}(\mathbf{r}) = \frac{\mu_0 m/(4\pi)}{[\rho^2+(z-z_d)^2]^{3/2}}\left[\frac{3(z-z_d)\rho}{\rho^2+(z-z_d)^2}\mathbf{e}_\rho + \left(\frac{3(z-z_d)^2}{\rho^2+(z-z_d)^2} - 1\right)\mathbf{e}_z\right]. \tag{6.67}$$

The correlation function for this particular magnetic configuration has the advantage of being comparable at $\tau = 0$ to a straightforward geometrical average $\langle xB_x + yB_y\rangle = \langle \rho B_\rho\rangle$. In fact, this quantity is already given to us by a 2012 article investigating precession frequency shifts induced by both large-scale and small-scale magnetic inhomogeneities (Pignol and Roccia, 2012). We recall here its expression in terms of the precession volume's geometry:

$$\begin{aligned}\langle \rho B_\rho\rangle &= \frac{1}{\pi R^2 H} 2\pi \int_{z_d}^{z_d+H} dz \int_0^R d\rho \rho B_\rho \\ &= \frac{\mu_0 m}{2\pi R^2 H}\left(2H + \frac{R^2+2z_d^2}{\sqrt{R^2+z_d^2}} - \frac{R^2+2(z_d+H)^2}{\sqrt{R^2+(z_d+H)^2}}\right).\end{aligned} \tag{6.68}$$

Figure 6.13 shows the results of the dipole-$C(\tau)$ calculation for two dipoles on the vertical axis: one close to the precession chambers at $z_d = 10\,\text{cm}$ above the origin, and another further away at $z_d = 60\,\text{cm}$. These were obtained from TOMAt trajectories of $N_c = 10^6$ collisions. Their values at $\tau = 0$ agree with the analytical

predictions (6.68), plotted as dotted lines on figure 6.13. It is clear that the dipole field that correlates the most with the mercury atom's trajectories is the one closer to the precession volume. Both correlation functions are finally fitted with the double exponential model (6.5), which will now be used to determine the false EDM generated by these dipoles.

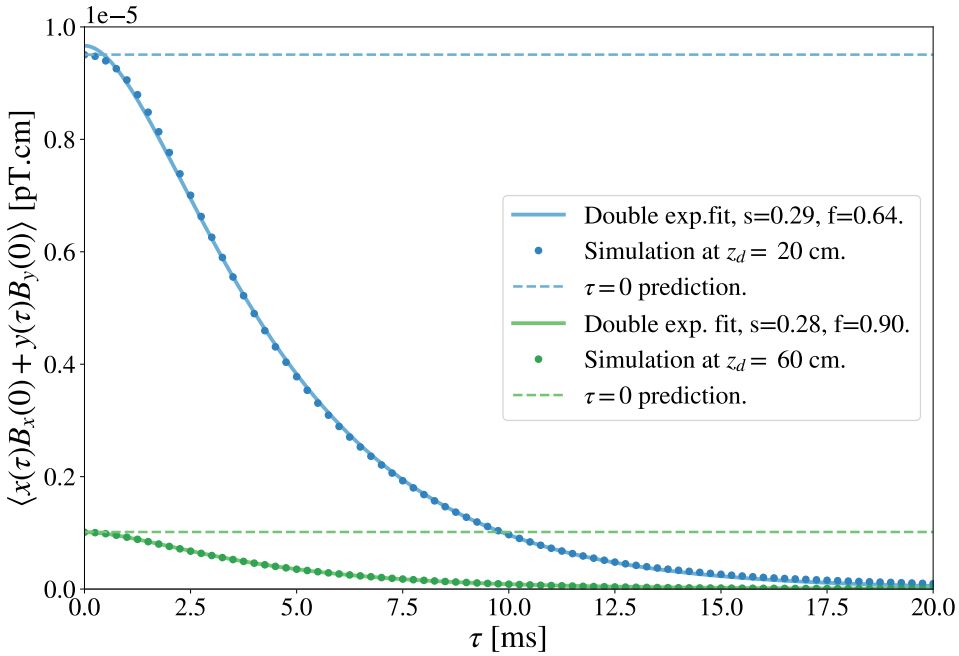

FIGURE 6.13: Field-position correlation function for a dipole field. Two dipole are considered, one placed at $z_d = 60\,\text{cm}$ above the precession chamber's origin on the vertical axis (in blue), another at $z_d = 10\,\text{cm}$ (in green). The number of collisions in the trajectory simulation was $N_c = 10^6$.

6.4.2 The dipole-induced false EDM and its magic field suppression

In the same manner we dealt with polynomial fields, we estimate the false EDM generated by a dipole of arbitrary strength and position through the fitted formula (6.6). Figure 6.14 shows $d^{\text{false}}_{n\leftarrow\text{Hg}}$ as a function of B_0 for several dipole positions, with normalized dipole strengths so that all generate a $1 \times 10^{-27}\, e\,\text{cm}$ systematic effect at $B_0 = 0\,\mu\text{T}$. Two of these are positioned around the precession volume: one at $\rho_d = 0\,\text{cm}, z_d = 6\,\text{cm}$ above the cylindrical chamber's center, which is in the ground electrode along the vertical axis, and another at $\rho_d = 40\,\text{cm}, z_d = 6\,\text{cm}$, at the edge of the ground electrode. A third is located at $\rho_d = 0\,\text{cm}, z_d = 60\,\text{cm}$, around the ceiling of the vacuum vessel. We also plot the false EDM generated by a vertical gradient field $\mathbf{\Pi}_{10}$.

We first notice that the curve for furthermost dipole is the closest of all to the gradient field curve. This is to be expected, as the dipole field resembles a gradient field when evaluated far from the source. We then check that dipoles closer to the precession volume are indeed the most problematic, as they generate a false EDM of the same magnitude as more distant dipoles at a weaker magnetic moment. The values of m considered "problematic" in n2EDM depend on the precise location of these dipoles. A previous PhD student studied the effect of dipole-like impurities on the accuracy of the cesium array's field measurements and determined that, when

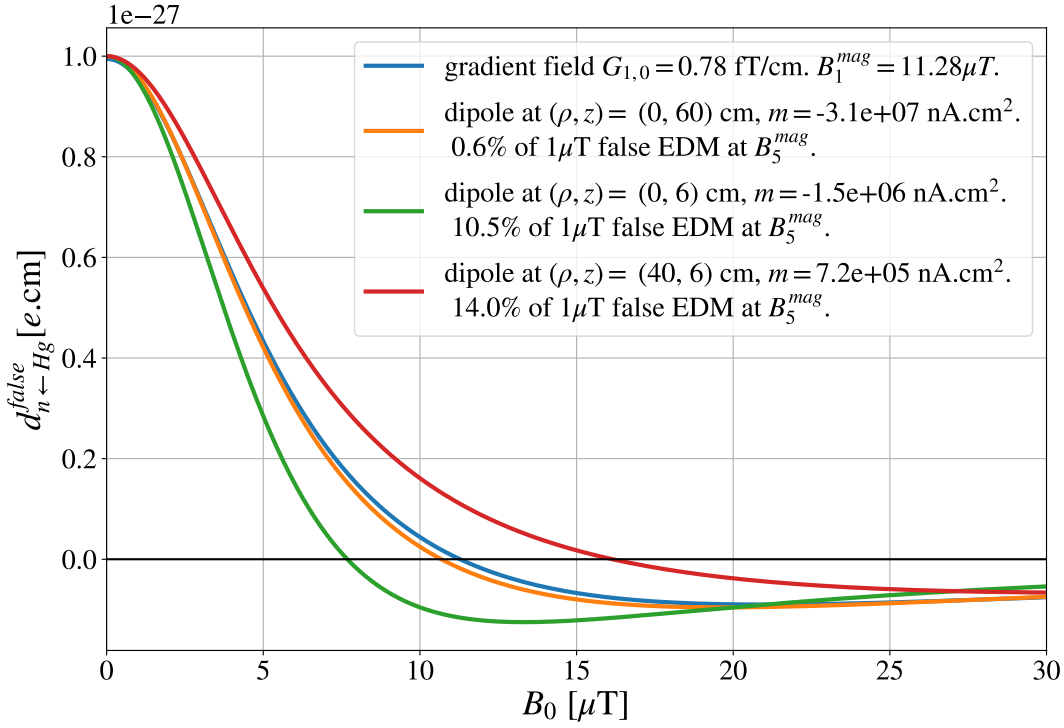

FIGURE 6.14: False EDM generated by a magnetic dipole as a function of the applied field, for different dipole locations and for a vertical gradient field. The magnetic moments are normalized so that all dipoles generate a $1 \times 10^{-27}\, e$ cm false EDM at the origin.

located on the ground electrodes, the maximal allowed dipole field was of the order of $m \approx 1 \times 10^5$ nA cm^2 (Pais, 2021). This result is visible in figure 6.12 (second darkest shade of purple).

In the case where the electrodes do host problematic dipoles, the magic field approach helps us greatly suppress the false EDM these may generate, for a wide range of dipole positions. Figure 6.15 shows two perspectives on this suppression. In both top plots $d^{\text{false}}_{n\leftarrow\text{Hg}}$ is plotted as a function of the radial position of a dipole located either above (up pointing arrows) or below (down pointing arrows) the ground electrode, for vertical (left plot) and transverse (right plot) dipole orientations. In each case the false EDM is evaluated both at $B_0 = 1\,\mu$T (in red) and at the magic field value B_5^{mag} (in green). A second vantage point on the amount of suppression is given by the two bottom plots of figure 6.15, where this time the false EDM at the magic field is given in units of the false EDM at 1 µT, for the same dipole orientations and radial positions. As expected, the inner-electrode dipoles yield the most extreme values. Although the amount of suppression varies with the dipole's radial position and orientation, the dipole false EDM at magic field represents on average just around 10% of the 1 µT false EDM. By comparing the top and bottom plots we see that this suppression only fails to cover a crossing point around the $\rho = 35$ cm mark affecting transverse dipoles, where the two false EDMs are of the same order of magnitude yet are both small compared to other radial positions. Returning to the problematic dipoles of figure 6.12, the magic field approach uniformly relaxes our requirements on dipoles situated on the electrodes by one order of magnitude.

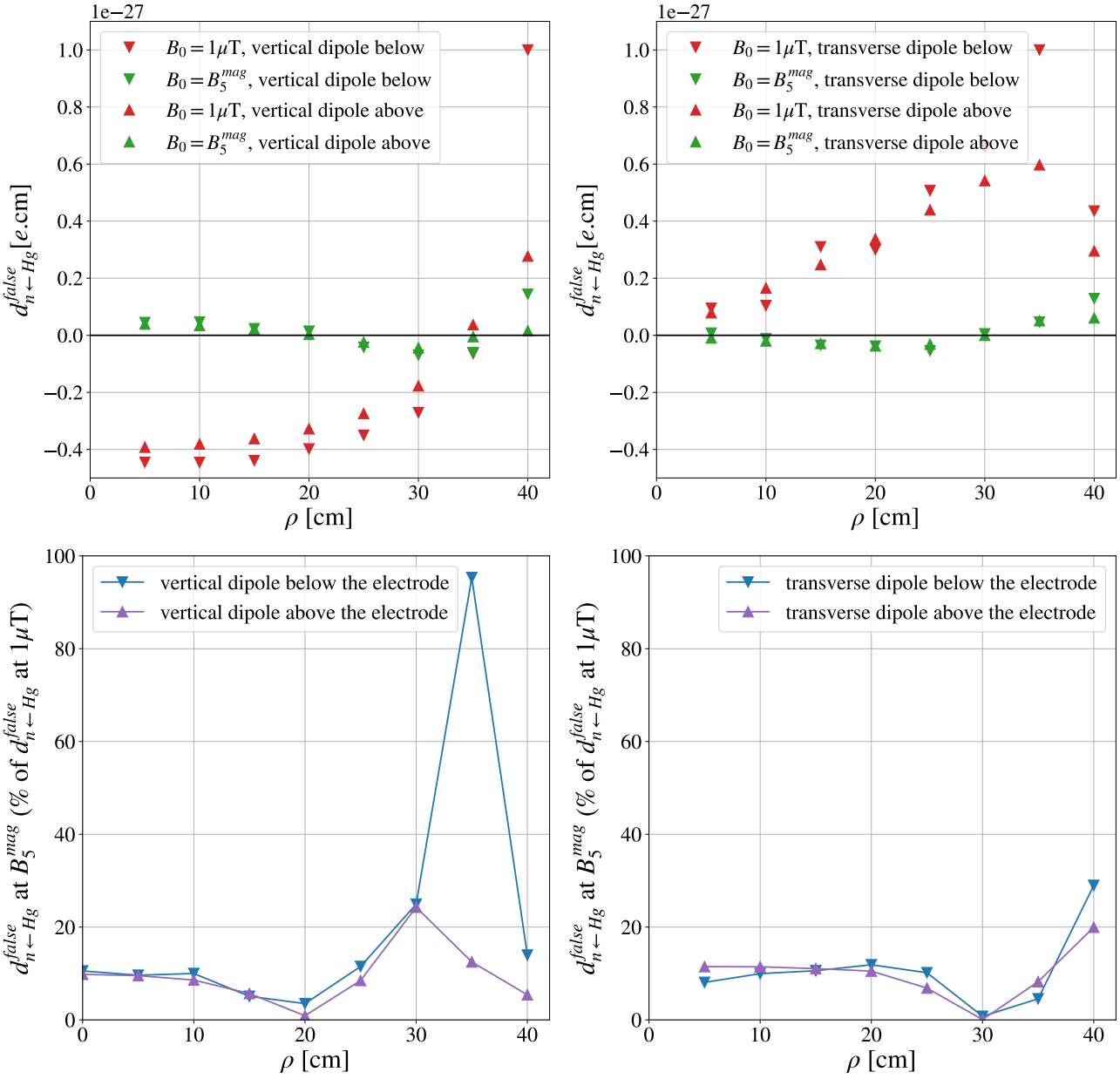

FIGURE 6.15: Top plots: false EDM generated by a dipole with vertical (left) and transverse (right) magnetic moments, as a function of the dipole's radial position. The vertical position of the dipole is either above (up pointing arrows) or below (down pointing arrows) the ground electrode. In red are the false EDM values when operating at the n2EDM standard 1 µT, and in red at the magic field B_5^{mag}. The magnitude of the magnetic moments are normalized so that strongest dipole generates a $1 \times 10^{-27}\, e$ cm false EDM. Bottom plots: false EDM generated by both vertical (left) and transverse (right) dipoles at B_5^{mag}, in units of the false EDM generated at 1 µT.

6.5 Conclusion

This last chapter dedicated to the fundamental study of systematic effects in n2EDM concludes our investigations on the mercury-induced false neutron EDM. Retracing our steps back to the beginning of this second part, we essentially left chapter 4 with

two claims to be tested. (1) The false EDM expressed as a function of the precession frequency ω should cross the horizontal axis at a single "magic" frequency - or field $B_0 = \omega/\gamma_{\mathrm{Hg}}$ - value. Importantly, this claim was based on the assumption that the false EDM could be described by a Lorentzian function, inherited from the *ad hoc* exponential model of the field-position correlation function $C(\tau)$. (2) There exists an alternative calculation of the false EDM in the frequency domain, allowed by the Wiener-Khinchin theorem, that involves the field-position PSD $S(\omega)$. In more specific terms, the false EDM is given by the Hilbert transform of $\omega S(\omega)$. The decisive edge of a direct frequency-domain calculation of this systematic effect over its time-domain counterpart is that it is unbiased by the fit of the correlation function.

The introductory section of this chapter verified the first claim from the existing literature for a vertical magnetic gradient. We used an existing Monte-Carlo simulation tool to calculate the field-position correlation function $C(\tau)$ for this magnetic configuration, and then determined the associated false EDM as a function of ω from the fit parameters of $C(\tau)$. The numerical results were in excellent agreement with both the exponential model and our physical expectations from chapter 4. After optimizing our choice of numerical parameters, we were finally able to precisely estimate the magic field value $B_1^{\mathrm{mag}} = 11.28(9)\,\mu\mathrm{T}$ as a function of the fit parameters and thus verify the first claim.

We then turned to our frequency-domain formulation of the false EDM for a possible model-independent calculation that would not carry the same bias as the time-domain calculation that is currently proposed. Using only the results of TOMAT's simulation of the trajectories of mercury atoms, we first determined a numerical calculation of the field-position PSD $S(\omega)$ based on the partitioning of the Fourier transform over linear trajectories. This allowed us to test the Wiener-Khinchin theorem by verifying that the numerical results of $S(\omega)$ could be fitted with the Fourier transform of the correlation function's fit model. We also determined the optimal allocation of our numerical power between two parameters: the number of trajectories N_t over which the PSD is averaged, which determines our numerical precision, and the number of collisions per trajectory N_c, which determines the faithfulness, or accuracy, of our calculation. We then proposed a novel method for the direct calculation of the false EDM, by proving the convergence of elementary Hilbert transforms of $\omega S(\omega)$, and applied it successfully to the vertical gradient magnetic configuration. We obtained in this scenario a model-independent frequency spectrum of the false EDM which we showed to be in very good agreement with the time-domain fit. This confirmed our second claim. Similarly, we gave an independent calculation of the magic field value $B_1^{\mathrm{mag}} = 11.34(6)\,\mu\mathrm{T}$ which is within one sigma of the time-domain one, granting vital legitimacy to the magic field approach.

In a third section, we studied the experimental viability of the magic field approach. We began by verifying previous false EDM calculations for phantom magnetic configurations $\mathbf{\acute{I}\acute{I}}_3$ and $\mathbf{\acute{I}\acute{I}}_5$, and extended them to $\mathbf{\acute{I}\acute{I}}_7$. The cancellation of such combinations of harmonic modes is the main goal of the magic field approach as these generate a problematic false EDM, invisible to the online field monitoring. From these updated calculations, we confirmed n2EDM's current choice of magic field $B_5^{\mathrm{mag}} = 10.6\,\mu\mathrm{T}$, which cancels the fifth order phantom mode and suppresses phantom modes of order 3 and 7 by more than 95%. We then presented the results of a dedicated mapping of the B_0 coil in the 10 µT range which confirms that the coil's harmonic spectrum grows linearly with the current driven through it. Extrapolating the 1 µT field measurements, we concluded that the optimized B_0 field, discussed in more detail in chapter 9, generates an acceptable false EDM when functioning at the magic field value B_5^{mag}.

The final section was dedicated to the study of dipole fields, which have the troublesome particularity of not being effectively described by an order $l = 7$ harmonic field expansion. We first determined a non-polynomial calculation of the field-position correlation function for dipole fields, valid for a dipole of arbitrary position and magnetic moment outside the precession volume. The numerical results of this calculation were in agreement at $\tau = 0$ with theoretical predictions. We finally fitted these functions to determine the false EDM generated by problematic dipoles, situated above and below the surface of the ground electrodes, of both transverse and vertical magnetic moments. We concluded that, at B_5^{mag}, these dipole-induced false EDMs were either suppressed by around 90% or negligible. This relaxes n2EDM's requirement regarding dipole-like contamination by one order of magnitude when functioning at the magic field.

The magic field approach has been legitimized and expanded to more complex, higher-order magnetic fields. We now turn to the last part of this thesis, which will confront our analysis of the mapping data to the requirements of n2EDM regarding the false EDM.

PART III

Magnetic field mapping and non-uniformities

Chapter 7

The n2EDM mapper and its accuracy

Contents

We reach the third part of this thesis equipped with an understanding of the main systematic effect generated by magnetic non-uniformities, and an awareness of the requirements that the n2EDM magnetic field should satisfy in order to minimize this effect. The remaining three chapters are dedicated to the characterization of the n2EDM magnetic environment through the confrontation of field mapping data to the systematical requirements. In chapter 7, we introduce the robotic "mapper" which the experiment relies on for magnetic field measurements. The first section provides a brief description of the apparatus, recalls the harmonic gradient extraction method, and presents the n2EDM mapping strategy through which we obtain the data presented in the next chapters (section 7.1). We then evaluate the mapper's inherent accuracy through a study of several mechanical defects (section 7.2).

7.1 Introduction to magnetic field mapping

7.1.1 The mapper

In n2EDM, the offline mapping of the magnetic field is performed using an automated field mapper. The mapper consists of a three-axis low-noise Bartington MAG13 fluxgate (n.d.[c]), mounted on a motorized system that allows it to explore a cylindrical volume of 78 cm radius and 82 cm height. Figure 7.1 shows the mapper arm inside the otherwise empty vacuum vessel and gives the main properties of the fluxgate. The fluxgate resides inside a cart travelling along the radial axis on the arm, which itself rotates around and moves up and down the vertical axis, in order to achieve the full cylindrical volume coverage. The cart can also be rotated along the radial axis for the purpose of calibrating the fluxgate. The apparatus discussed here

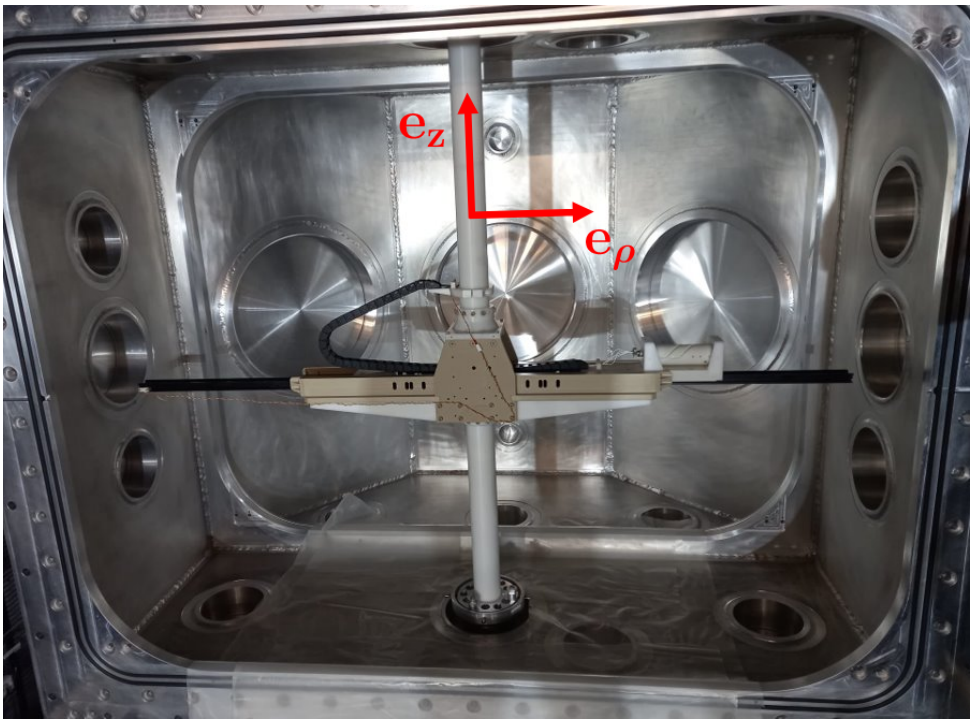

Fluxgate properties	
Measuring range	$\pm\,[70, 1000]$ µT
Bandwidth	≤ 3 kHz
Noise level	$\leq 6\,\mathrm{pT\,Hz^{0.5}}$

FIGURE 7.1: Top: the n2EDM mapper inside the empty vacuum vessel. The fluxgate is inserted in a cart mounted on the mapper arm, which can rotate around as well as move up and down the vertical axis. The cart travels on the arm along the radial axis and can rotate along this axis as well. Bottom: properties of the Bartington MAG13 fluxgate (n.d.[c]).

is an adaptation of the nEDM mapper, described thoroughly in a previous PhD's student thesis dedicated to magnetic field mapping (Ferraris-Bouchez, 2020).

The purpose of the mapper is to obtain an accurate offline measurement of the magnetic field that complements the online measurement. Let us briefly justify this. We know from section 5.1 that the magnetic modes responsible for the false EDM can be split between the top-bottom gradient G_{TB}, deemed unproblematic as it can be monitored during data-taking, and the invisible thus problematic phantom modes $\acute{G}_3, \acute{G}_5, \acute{G}_7$. This is illustrated by equation (3.16) and gives rise to our systematical requirement on the phantom measurement accuracy (3.18), which we recall here:

$$\delta\acute{G}_3 < 20\,\mathrm{fT/cm}, \qquad \delta\acute{G}_5 < 20\,\mathrm{fT/cm}, \qquad \delta\acute{G}_7 < 20\,\mathrm{fT/cm}. \tag{7.1}$$

Meeting these conditions ensures that the accuracy on the false EDM satisfies $\delta d^{\mathrm{false}}_{n\leftarrow\mathrm{Hg}} < 3\times10^{-28}\,e\,\mathrm{cm}$. As the phantom modes are simply a linear combination of harmonic modes, the magnetic field measurement process relies on the extraction of the harmonic gradient spectrum, which we will soon recall.

In n2EDM, the field's harmonic spectrum can be extracted both online thanks to

the cesium magnetometers, and offline with the mapper. This redundancy ensures that the critical systematic parameters are well under control. Furthermore, the online and offline systems are designed to target different modes of the harmonic spectrum. With its 121 magnetometers positioned around the precession chambers, the cesium array offers more limited statistics than the mapper's fluxgate who can continually record the magnetic field at any point of the cylindrical volume. Since the magnetometers are static, it is also impossible to determine their respective offsets. The n2EDM strategy is to trust the cesium array for the extraction of the usually dominant third-order phantom gradient in real-time, while the mapper should provide a measurement of the rest of the harmonic spectrum, in particular of the fifth and seventh order phantom gradients. While it offers greater statistics, the mapper's design comes at the cost of not being operable around the precession chambers. The measurement is then performed offline, and on the condition that it is reproducible enough, provides an estimate of the false EDM that remains valid during data-taking. This last caveat is what we formalized as the reproducibility condition (3.17), which we also recall here:

$$\sigma(\acute{G}_3) < 20\,\mathrm{fT/cm}, \qquad \sigma(\acute{G}_5) < 20\,\mathrm{fT/cm}, \qquad \sigma(\acute{G}_7) < 20\,\mathrm{fT/cm}. \tag{7.2}$$

Let us now briefly explain how the harmonic gradient extraction is performed in n2EDM.

7.1.2 Extracting the harmonic spectrum from a map

The main command executed by the mapper is the recording of a map, which consists in a series of rings in φ performed at a given (ρ, z) and covering the entire cylindrical volume. A plot of the vertical field projection of a B_0 coil map is shown in figure 7.2. The characterization of the magnetic field consists in the extraction of the harmonic spectrum $\{G_{lm}\}_{l\leq 7}$, where $-l-1 \leq m \leq l+1$, of the polynomial expansion (3.2), from a map. This analysis was first developed for the nEDM experiment and presented in a 2022 article (Abel et al., 2022). One implementation of the analysis was the subject of a PhD thesis (Ferraris-Bouchez, 2020). We will briefly recall it here.

The harmonic extraction is performed by first fitting all map rings (ρ_i, z_i) with a Fourier series in φ. The z probe for instance is fitted with

$$B_z(\rho_i, \varphi, z_i) = \sum_{m=0}^{l_{\max}+1} a_m^{(z)}(\rho_i, z_i)\cos(m\varphi) + b_m^{(z)}(\rho_i, z_i)\sin(m\varphi). \tag{7.3}$$

We thus obtain a set of Fourier coefficients $(a_m^{(z)}(\rho_i, z_i), b_m^{(z)}(\rho_i, z_i))$ which are themselves fitted in ρ and z with the harmonic field expansion. For instance,

$$a_m^{(z)} = \sum_{l=0}^{l_{\max}} G_{lm}\tilde{\Pi}_{z,lm}(\rho, z), \tag{7.4}$$

which involves the reduced harmonic polynomials functions $\tilde{\Pi}_{z,lm}(\rho, z)$, defined such that

$$\Pi_{z,lm}(\rho, \varphi, z) = \begin{cases} \tilde{\Pi}_{z,lm}(\rho, z)\cos(m\varphi), & \text{if } m \geq 0, \\ \tilde{\Pi}_{z,lm}(\rho, z)\sin(m\varphi), & \text{if } m < 0. \end{cases} \tag{7.5}$$

The final fit parameters are thus the set of generalized gradients $\{G_{lm}\}_{l\leq l_{\max}}$, with in our case $l_{\max} = 7$. This entire process is explained much more thoroughly in

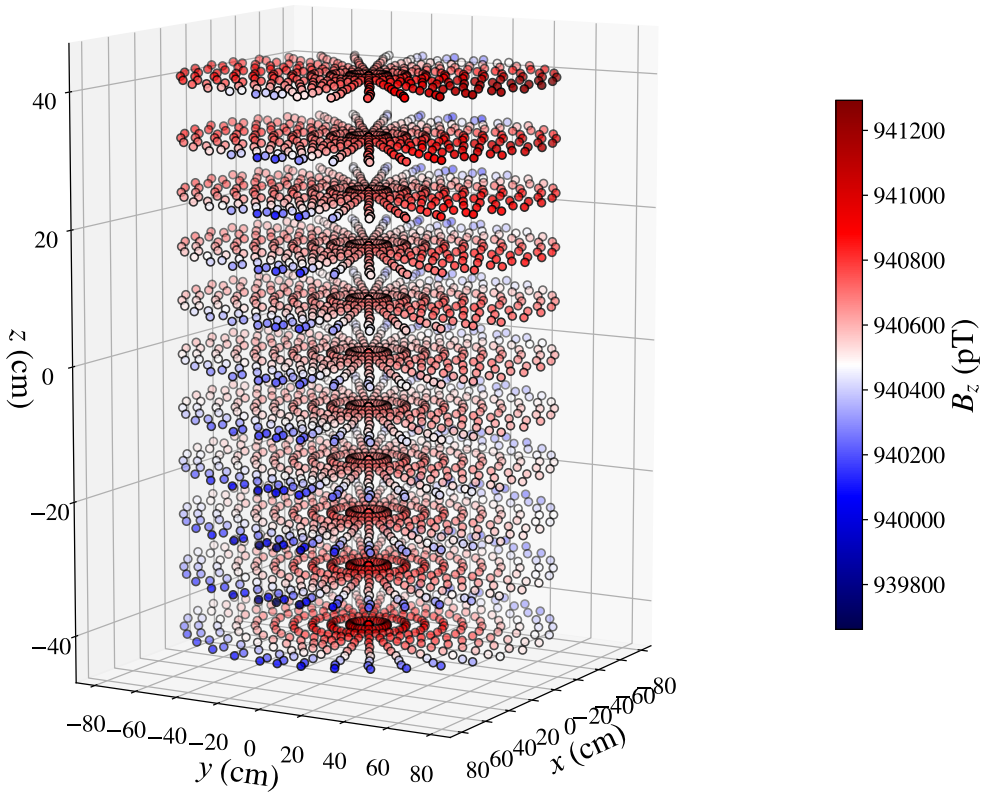

FIGURE 7.2: Each point in this plot corresponds to the average value of the vertical magnetic field projection around a point of cylindrical coordinates (ρ, φ, z), with a φ averaging step of 10°. The plot represents a typical n2EDM map consisting of 121 rings uniformly distributed in a volume $\{(\rho, \varphi, z) \mid \rho \leq 78\,\text{cm}, 0 \leq \varphi \leq 2\pi, |z| \leq 41\,\text{cm}\}$.

(Ferraris-Bouchez, 2020). Lastly, note that an important step of the analysis is the determination of the fluxgate's offset, without which it is impossible to determine the uniform gradients G_{0m} of the three magnetic field directions. To this end each map must contain a ring at the origin $(\rho = 0, z = 0)$ in both up and down orientation of the B_z probe, whose difference allows the extraction of the B_z offset. As for the B_ρ and B_φ offsets, they are extracted from the zero-order Fourier coefficient of any $(\rho = 0, z)$ rings. The main goal of our analysis code is to perform the harmonic spectrum extraction, but it also includes additional features which allows us to easily implement simulations on the mapping data [1].

The harmonic fit method must then be applied to data acquired from a carefully planned mapping strategy.

7.1.3 The n2EDM mapping strategy

Maps of the magnetic field are taken according to a measurement plan whose goal is to determine not only the individual average values of the harmonic spectrum $\mu(G_{lm})$ but more importantly:

[1] https://github.com/bouillaud/n2edm_mapping

- Their **repeatability** $\tau(G_{lm})$, defined as the standard deviation of measurements performed successively without altering the magnetic environment. The field's repeatability is influenced mainly by the precision of the mapping apparatus.
- Their **reproducibility** $\sigma(G_{lm})$, defined as the standard deviation of measurements separated by a full reset of the magnetic environment. Generally, this implies that the field-generating coil is turned off and on again and that MSR is fully demagnetized, or *degaussed*, between each of these measurements. The intention is to emulate the variations of the magnetic field over the time-scale that separates a mapping campaign from physical data-taking.

We will now go over the strategies behind the two mapping campaigns which produced the data presented in chapters 7, 8, and 9 of this thesis. These results are collected in appendix D. For both campaigns we adopted the following conventions:

- A **cycle** refers to a single file where mapper data may be stored.
- A **run** refers to a set of successive cycles.

First mapping campaign

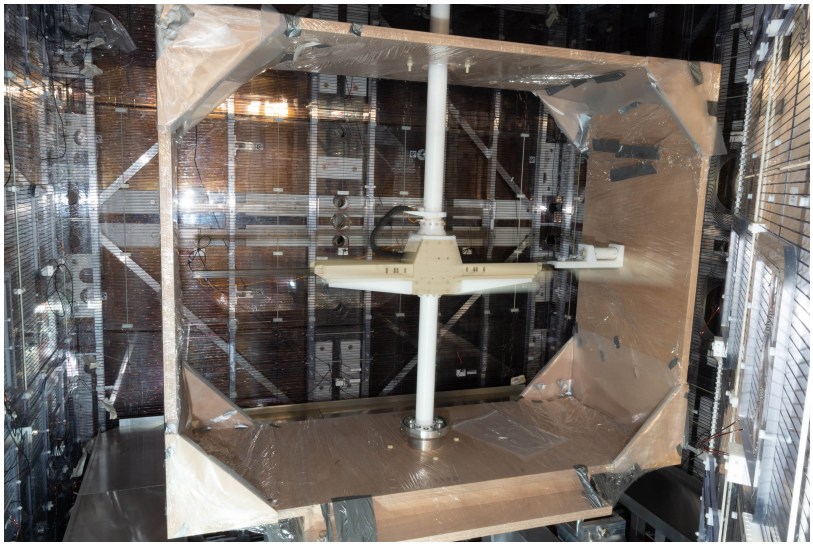

FIGURE 7.3: The mapper inside the empty MSR.

The first mapping campaign took place from January to May 2022, after mounting the B_0 coil and before installing the vacuum vessel, in the state of the MSR shown in figure 7.3. It consisted in a series of preliminary measurements aimed not at determining the full harmonic spectrum, but at giving a basic characterization of the B_0 coil. Specifically, we wished to check the alignment of the coil with the MSR and evaluate the performance of the B_0 coil with respect to the top-bottom resonance matching condition (3.12). We performed magnetic field measurements in sequences of simple vertical scans, where:

- A z**-scan** is a mapping cycle where the mapper is moved from $z = 0$ cm, to $z = 39$ cm, to $z = -39$ cm and back to $z = 0$ cm, at a radial position $\rho = 0$ cm. The back and forth motion is there so that possible fluxgate backlashes are cancelled when fitting the entire scan.

- A z**-scan run** is a set of z-scans performed successively in the same magnetic configuration. In this campaign each sequence contained 20 z-scans.
- A z**-scan sequence** is a set of z-scan runs performed successively according to a specific MSR degaussing pattern. The typical pattern used in this mapping campaign is referred to as **AABB**, where we:

  (1) Degauss layers 5 and 6S (using straight coils) of the MSR (**A**).
  (2) Do a z-scan run.
  (3) Degauss layers 5 and 6S of the MSR (**A**).
  (4) Do a z-scan run.
  (5) Degauss layers 5 and 6C (using crossed coils) of the MSR (**B**).
  (6) Do a z-scan run.
  (7) Degauss layers 5 and 6C of the MSR (**B**).
  (8) Do a z-scan run.

The goal of these sequences is to extract the $m = 0$ generalized gradients, specifically G_{10}, while canceling possible contributions of a poor degaussing. Indeed, the harmonic expansion gives us the vertical field projection over the cylindrical axis as

$$B_z(z, \rho = 0) = \sum_{l \geq 0} G_{l0} z^l, \tag{7.6}$$

which allows us to easily determine the G_{l0} from a z-scan without requiring a full cylindrical map.

Second mapping campaign

The second mapping campaign of n2EDM began after installing the vacuum vessel inside the MSR (visible in 7.1) and took place from September 2022 to January 2023. It occurred in two phases: the first sought to characterize the residual field before turning on the B_0 coil, and the second was after the main challenge: the characterization of the B_0 coil. This time the measurements consisted of high-resolution cylindrical maps from which the harmonic spectrum of the magnetic field could be extracted.

- A **ring** is a mapping cycle where the fluxgate is moved from $\varphi = 0°$, to $\varphi = 360°$, and back to $\varphi = 0°$, at a given (ρ, z) position. The back and forth motion is there so that possible fluxgate backlashes are cancelled when fitting the entire scan.
- A **map** is a set of rings that cover the volume of a cylinder. The maps shown here follow the following pattern:

  (1) Calibrate the B_z sensor. This is done as such:
    (i) Do a ring at $(\rho = 0, z = 0)$ with the B_z sensor pointing up.
    (ii) Do a ring at $(\rho = 0, z = 0)$ with the B_z sensor pointing down.

  The B_z offset is obtained by taking the half sum of the zero order Fourier coefficients of these two rings.

(2) Do all 121 rings in $\rho = \{0, 8, 16, \ldots, 72, 78\} \times z = \{-41, -32, -24, -16, \ldots, 16, 24, 32, 41\}$, starting from the lowest z, and for each z from the lowest ρ. The offsets of the B_ρ and B_φ sensors can be determined from any of the $\rho = 0$ rings by taking the zero order Fourier coefficients of these rings for their respective probes.

(3) Calibrate the B_z sensor.

A plot of B_z over a map is shown in figure 7.2. The standard deviation between successive maps gives their repeatability.

- A mapping **sequence** is a set of maps performed successively according to a specific pattern. One of two different patterns is followed.

  Residual field pattern (B_0 coil is turned off):

  (1) Degauss all 6 layers of the MSR.

  (2) Do N cylindrical maps successively.

  B_0 **field pattern**:

  (1) Set $I = 11.25$ mA and degauss layer 6 of the MSR.

  (2) Do a map (with $B_0 \uparrow$).

  (3) Set $I = -11.25$ mA and degauss layer 6 of the MSR.

  (4) Do a map (with $B_0 \downarrow$).

  The standard deviation between maps taken from different sequences (of the same polarity in the case of B_0 maps) gives the harmonic spectrum's reproducibility.

Chapters 8 and 9 will go over the characterization of the vacuum vessel and of the B_0 coil according to this mapping strategy. But before we can trust our analysis of the mapping data, we wish to evaluate the mapper's inherent ability to accurately determine the harmonic spectrum, through dedicated measurements of its mechanical imperfections.

7.2 Mechanical sources of mapping inaccuracy

The goal of this section is to study the effect of realistic mechanical defects affecting the mapper on the accuracy of the harmonic gradients extraction. We consider three problematic scenarios:

(1) A displacement of the **mapper's origin** O.

(2) A **non-orthogonality** of the mapper's $\mathbf{e}_\rho$ and $\mathbf{e}_z$ axes.

(3) A **roll** α or **pitch** β of the fluxgate[2] (drawn in figure 7.4).

Our approach is simple. We consider two mapping datasets that associate a field (B_ρ, B_φ, B_z) to a position in space (ρ, φ, z): one consisting of the original fluxgate measurements, another consisting of data transformed in a way that simulates the

[2] A yaw may in principle also exist but because of the mapper's geometry is insignificant compared to the other two angles.

considered effect. We then apply the analysis algorithm to both datasets and consider the inaccuracy generated by that effect to be the difference between the two harmonic spectra. Scenario (1) was tested with the use of n2EDM's gradient coils, while for scenarios (2) and (3) we compared laser measurements of the fluxgate's position over ρ-scans and z-scans with the intended orthogonal trajectories. We now present the simulations before discussing the results of the phantom gradient extraction.

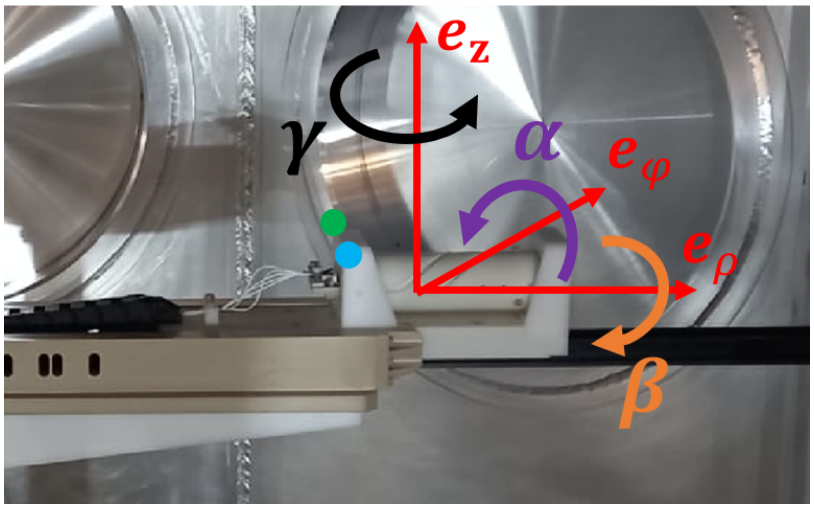

FIGURE 7.4: The purple, orange, and black arrows correspond respectively to the roll, pitch, and yaw angles of the fluxgate. The blue and green dots represent the markers 1 and 2 used for laser-tracking.

7.2.1 Simulations of mechanical defects

Displacement of the mapper origin

One concerning source of mapping inaccuracy would be a displacement of the geometrical center O of the coil with respect to the origin O' of the mapper. We recall that the n2EDM coordinate system consists of the origin O of the coil system and the geometrical basis $(\mathbf{e}_x, \mathbf{e}_y, \mathbf{e}_z)$. The point O is defined as the position at which the field generated by three gradient coils G_{11}, G_{10}, and G_{1-1}, which produce vertical field components linear in x, y, and z respectively, is equal to zero. Note that, additionally, the vertical axis $\mathbf{e}_z$ is defined by the B_0 coil such that the field produced at the coil origin O is along this axis[3]. As for the point O', it is simply the coordinate origin of the fluxgate. If $\overrightarrow{O'O} \neq 0$, then fitting the coil generated-field with a harmonic field expansion in the mapper coordinate system will naturally lead to a biased estimate of the generalized gradients G_{lm}^{map}. Our goal is to calculate the measurement error on the phantom gradients $\delta\acute{G}_{2l+1} \equiv \acute{G}_{2l+1}^{\text{map}} - \acute{G}_{2l+1}$ in the event of such a displacement, and confront it to the systematical requirement (7.1).

(i) Measurement of the displacement

Fortunately, the origin of the coil system can be measured in the mapper's coordinate system by using a dedicated set of gradient coils. As mentioned in section 2.6,

[3]Until now the n2EDM coordinate system has been defined geometrically, such that O is the center of double chamber system, and $\mathbf{e}_z$ is along the vertical cylindrical axis. As discussed here, the absolute reference is in reality the coil system.

the coil system consists not only of the coil responsible for the $B_0 \equiv G_{00}$ field, but also of 56 trim coils and 7 gradient coils. The latter are meant to generate individual modes of the expansion G_{0-1}, G_{01}, G_{1-1}, G_{10}, G_{11}, G_{20}, and G_{30}. In our case, the linear gradient field coils G_{1-1}, G_{10}, G_{11} are particularly useful. For a current I running through each of these coils, we write the generated vertical field component according to table A.2 as, respectively,

$$B_z(I) = B_z^{\text{res}} + \alpha_{1-1} I y', \tag{7.7}$$
$$B_z(I) = B_z^{\text{res}} + \alpha_{10} I z', \tag{7.8}$$
$$B_z(I) = B_z^{\text{res}} + \alpha_{11} I x', \tag{7.9}$$

where the α_{lm} are **coil constants**, defined such that we measure $G_{lm} = \alpha_{lm} I$ for a given current I. B_z^{res} corresponds to the residual field present at zero current. Finally, $\mathbf{r}' = x'\mathbf{e}_x + y'\mathbf{e}_y + z'\mathbf{e}_z$ locates the fluxgate with respect to the mapper origin O', while $\mathbf{r} = x\mathbf{e}_x + y\mathbf{e}_y + z\mathbf{e}_z$ locates the fluxgate with respect to the coil origin O. The origin displacement $\delta\mathbf{r} = \mathbf{r} - \mathbf{r}' = \delta x\mathbf{e}_x + \delta y\mathbf{e}_y + \delta z\mathbf{e}_z$ is then determined by measuring B_z in opposite polarities along the axis aligned with the magnetic gradient. We briefly illustrate this process for the G_{10} coil with figure 7.5. A scan is performed along the $\mathbf{e}_z$ axis with the G_{10} coil plugged in at $I = 10\,\text{mA}$, and then at $I = -10\,\text{mA}$. The zero-crossing of $\Delta B_z = (B_z(I) - B_z(-I))/2 = \alpha_{10} I z'$, independent from the residual field, is then equal to δz. Repeating a similar process for the two other coils, we determine the origin displacement to be $(\delta x, \delta y, \delta z) = (0.2, 0.2, 1.2)\,\text{cm}$. We now propose two alternative methods of calculating the measurement error generated by this displacement.

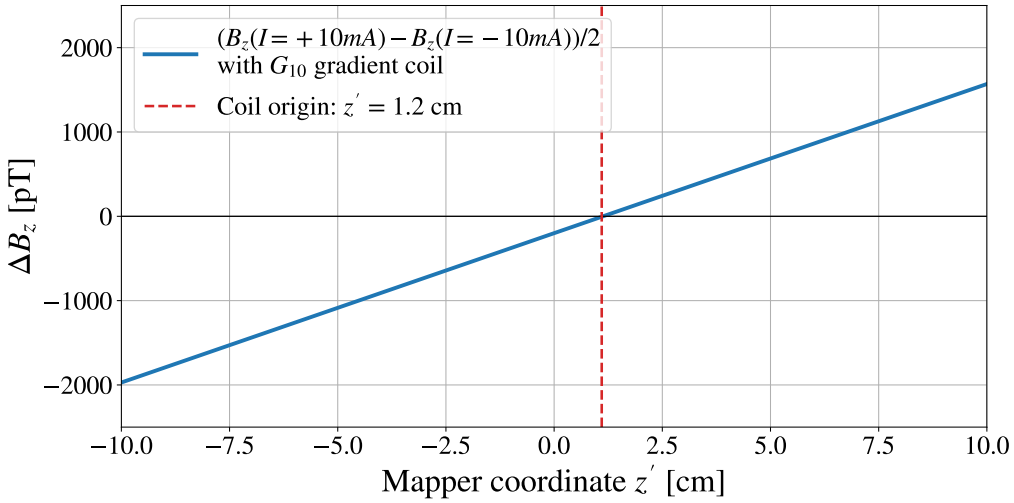

FIGURE 7.5: Difference of the vertical field projection measured in positive and negative polarities of the G_{10} coil, which generates a linear gradient field, over a vertical scan. The curve should cross the horizontal axis at the mapper position $z' = 0$ if the mapper origin O' corresponds to the center of the coil system O. In this case the coil origin is 1.2 cm above the mapper origin.

(ii) Error prediction

We first estimate the error on the harmonic gradients $\delta\acute{G}_{2l+1}$ by determining which extra modes of the harmonic expansion G_{lm} "picks up" from the origin displacement, at first order in the displacement.

Let $\mathbf{r} = \overrightarrow{OM}$ be a vector giving the coordinates of a point M in the coil frame of origin O, and $\mathbf{r}' = \overrightarrow{O'M}$ in the mapper frame of shifted origin O'. Let $\delta\mathbf{r} = \overrightarrow{O'O}$ such that $\mathbf{r}' = \mathbf{r} + \delta\mathbf{r}$. We define two magnetic fields $\mathbf{B}$ and $\mathbf{B}'$ with expansions taking their origins at O and O' respectively. Then,

$$\mathbf{B}(\mathbf{r}) = \mathbf{B}'(\mathbf{r}'). \tag{7.10}$$

Consider the harmonic expansion of the vertical component of the field along the vertical axis

$$B_z(\mathbf{r}) = \sum_{k=0}^{\infty} G_{k0} z^k, \tag{7.11}$$

with (x, y, z) the geometrical coordinates of $\mathbf{r}$. This is a polynomial expansion with coefficients given by

$$G_{k0} = \frac{1}{k!} \left. \frac{\partial^k B_z(\mathbf{r})}{\partial z^k} \right|_{\mathbf{r}=0} \tag{7.12}$$

Using a first order Taylor expansion of the vertical field component in the mapper frame

$$B'_z(\mathbf{r} + \delta\mathbf{r}) = B'_z(\mathbf{r}) + \delta\mathbf{r} \cdot \boldsymbol{\nabla} B'_z(\mathbf{r}) + o(\delta\mathbf{r}^2), \tag{7.13}$$

we can express the coil coefficients G_{lm} in terms of the mapper coefficients G'_{lm}, by substituting (7.13) into (7.12):

$$G_{k0} = G'_{k0} + (k+1)\left(\delta x\, G'_{k+1,1} + \delta y\, G'_{k+1,-1} + \delta z\, G'_{k+1,0}\right). \tag{7.14}$$

Table 7.1 gives the errors $\delta\acute{G}_k = D_k^{k-1}(G'_{k0} - G_{k0})$ computed using equation (7.14) and the mapping data D.4, for a displacement $(\delta x, \delta y, \delta z) = (0.2, 0.2, 1.2)$ cm.

(iii) Error simulation

The same errors $\delta\acute{G}_k$ can be simulated simply by extracting the harmonic spectrum from a map of the B_0 coil with transformed coordinates $\mathbf{r} \to \mathbf{r}' = \mathbf{r} + \delta\mathbf{r}$, and comparing them to the original spectrum. The simulated results for the measured displacement are presented in the last line of table 7.1 and compare well with the first order prediction. They are also featured along other mechanical defects as the red bars in figure 7.8, which we will later discuss.

	$\delta\acute{G}_3$	$\delta\acute{G}_5$	$\delta\acute{G}_7$	Requirement
Predicted (fT/cm)	8.2	5.6		< 20
Simulated (fT/cm)	10.6	6.6	0.1	< 20

TABLE 7.1: Predicted accuracy on phantom modes given by equation (7.14), and simulated accuracy with coordinate transformation (7.15), using a constant displacement $\delta r = (0.2, 0.2, 1.2)$ cm.

Non-orthogonality of the mapper axes

The orthogonality of the $\mathbf{e}_\rho$ and $\mathbf{e}_z$ axes of the mapper was assessed by laser-tracking of the fluxgate's position during both radial and vertical scans. The tracked points are placed on top of the fluxgate, at equal radial and vertical distance from the mapper arm, and separated by a distance $d = 5$ cm (in blue and green on figure 7.4).

Results of the laser measurement during a z-scan (top plot of figure 7.6) and a ρ-scan (bottom plot of figure 7.6) tell us that the angle between the mapper's $\mathbf{e}_\rho$ and $\mathbf{e}_z$ cylindrical axes are indeed not perfectly orthogonal. From the top plot we see that the angle between the two axes exceeds 90° during a z-scan at $\rho = 0$ by a constant value of approximately 0.30°, as well as during a ρ-scan at $z = 0$, peaking at around 0.15°. Furthermore, the varying vertical distance between the two markers during the ρ-scan, and the cart's inclination during both scans, indicates that the fluxgate's pitch and roll angles are also modified. This will be the subject of a dedicated discussion.

This non-orthogonality of the mapper axes biases our estimate of the mapper's position in the coil's frame, and in turn generates an error in the extraction of the magnetic field's harmonic spectrum. This error can be simulated by transforming the mapper's position at every point of a given cycle according to a change of coordinates extrapolated from the fluxgate's trajectories. Specifically, let $\mathbf{r} = (x, y, z)$ be the position of the mapper cart with respect to the mapper origin assuming orthogonality, and let $\mathbf{r}' = (x', y', z')$ be its actual position. We then write the transformation as

$$\begin{cases} x' &= x + F_{12}(y) + F_{13}(z) \\ y' &= F_{21}(x) + y + F_{23}(z) \\ z' &= F_{31}(x) + F_{32}(y) + z \end{cases} \tag{7.15}$$

where the F_{ij} are polynomial functions of x, y, or z obtained by fitting the trajectory of fluxgate marker 2 over ρ and z scans[4]. The polynomial fits appear in figure 7.6. For instance, the bottom's plot blue curve corresponds to $F_{31}(x)$ when $\varphi = 0$. After applying the change of coordinates $\mathbf{r} \to \mathbf{r}'$ to all cycles of a B_0 coil map, we extract its harmonic spectrum and compare it to the original to obtain the results shown in figure 7.8 (blue bars).

Roll and pitch of the fluxgate axes

As the axes along which the fluxgate travels are not orthogonal, we can further assume that its three probes rotate in the geometrical frame during those movements. During a vertical scan for instance, the fluxgate should exhibit a non-zero pitch, equal at first order to the slope of the linear trajectory pictured in the top plot of figure 7.6. This particular pitch angle is plotted in the top figure of 7.7. Similarly, the ρ-scan trajectory plotted in figure 7.6 should generate a varying pitch equal to the slope of the tangent of the green curve, as well as a varying roll equal to the vertical distance between the green and blue curves over d. Both of these effects are represented in the middle and bot plots of figure 7.7.

To simulate the inaccuracies on the phantom modes generated by such tilts of the fluxgate axes, we consider that the field projections measured by the fluxgate $(B'_\rho, B'_\varphi, B'_z)$ can be obtained by a first-order rotation of the actual field projections (B_ρ, B_φ, B_z):

$$\begin{pmatrix} B'_\rho \\ B'_\varphi \\ B'_z \end{pmatrix} = \begin{pmatrix} 1 & \gamma & -\beta \\ -\gamma & 1 & \alpha \\ \beta & -\alpha & 1 \end{pmatrix} \begin{pmatrix} B_\rho \\ B_\varphi \\ B_z \end{pmatrix} \tag{7.16}$$

[4] We choose marker 2 over marker 1 to consider the worst-case non-orthogonality.

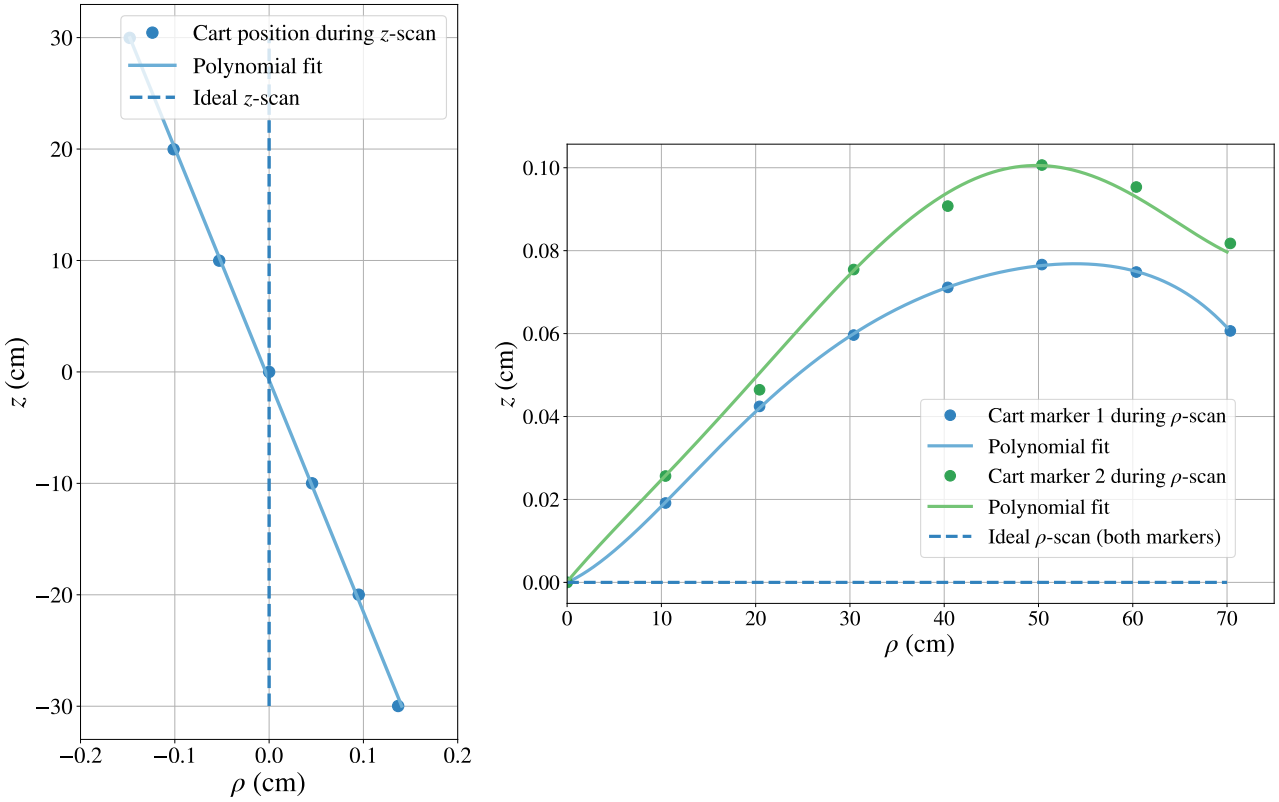

FIGURE 7.6: Trajectories of the mapper cart carrying the fluxgate in the (ρ, z) plane while performing (1) a scan along the z axis (op plot), and (2) a scan along the ρ axis (bottom plot). The dots on the bottom-most plots represent the trajectories of two markers placed on top of the cart, at the same radial distance from the mapper's vertical axis, and separated by a horizontal distance $d = 5\,\text{cm}$. Their positions were obtained by laser-tracking. The topmost plot only shows the trajectory of one of the two markers, as the two overlap. The full lines correspond to polynomial fits of these trajectories.

By plugging the appropriate roll or pitch angles α, β from figure 7.7 into equation (7.16) at each ring of a B_0 map and setting the yaw γ to zero, we obtain a map simulating the mechanical defect and from which the harmonic spectrum is again extracted. The associated errors on the phantom modes are shown in figure 7.8 (orange and purple).

7.2.2 Results and mapping accuracy

Figure 7.8 shows the difference between the phantom gradients extracted from a standard B_0 coil map and the spectrum extracted from a map simulating a mechanical defect for the three scenarios presented above. We conclude that none of the considered defects generate an inaccuracy on the phantom gradient measurement larger than our statistical requirement of 20 fT/cm. Still, the largest of these effects, the displacement of the mapper origin, was largely corrected by moving the vertical mapping coordinate by 1.2 cm in the mapper software. We also note that the effect of the fluxgate pitch is very suppressed compared to the other effects, likely because its main contribution at larger rings is constant (top plot of 7.7) and cannot mimic the behavior of an l-gradient mode. Finally, the effects of the remaining mechanical issues are most strongly felt for the third order phantom gradient, which will

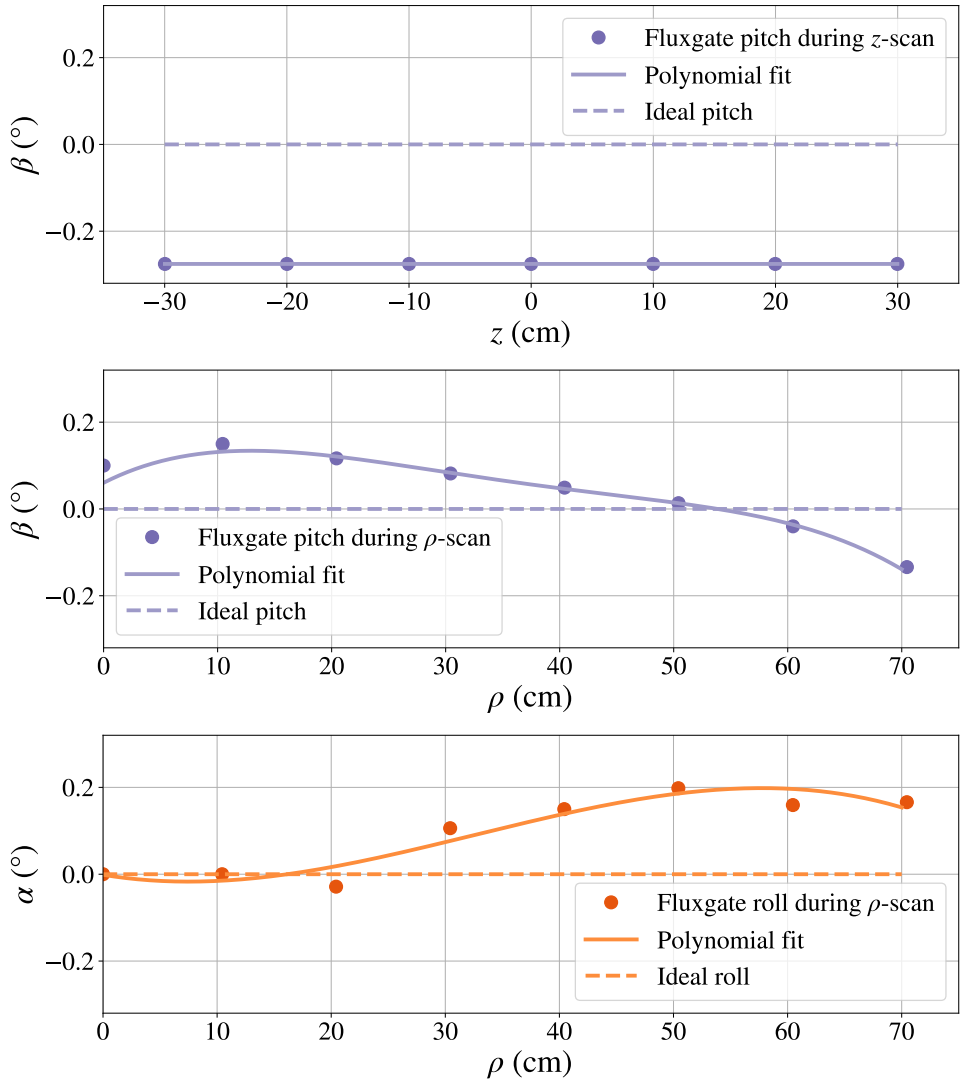

FIGURE 7.7: The top and middle plots show the evolution of the fluxgate pitch angle during a z-scan and a ρ-scan respectively, while the bottom plot shows the evolution of the roll angle during a ρ-scan.

anyways be complemented by the online measurements provided by the cesium magnetometers.

7.3 Conclusion

In this first chapter dedicated to magnetic field mapping, we presented the n2EDM mapping apparatus and evaluated its accuracy. We began by introducing the "mapper" as a robotized fluxgate capable of covering a large cylindrical volume inside the vacuum vessel and exceeding the volume of the two precession chambers. We then recalled the numerical method to extract the harmonic field spectrum of a map recorded by this system, widely used in the previous experiment. Returning to n2EDM, we presented the new experiment's mapping strategy to evaluate both the measurement accuracy and the reproducibility of the generated B_0 field, which will lead to the mapping results discussed in the following chapters.

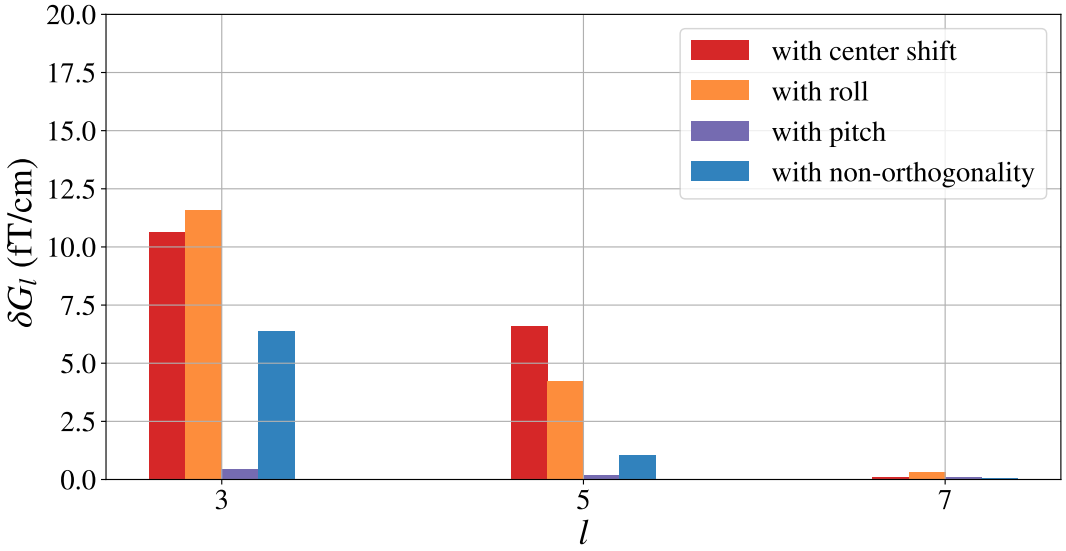

FIGURE 7.8: Errors on the phantom modes generated by several mechanical defects. The colored bars give the absolute difference between the phantom spectrum obtained when simulating the mechanical defects and without the defects. All errors are under the 20 fT/cm requirement.

After this introductory section, we studied the impact of several mechanical defects on the ability of the mapper to accurately determine the phantom gradients $\acute{G}_{2l+1}$, which must satisfy stringent statistical requirements. Focusing on three mechanical sources of inaccuracy, we first presented a measurement of the defect before simulating it in our harmonic gradient extraction code. By comparing the harmonic gradients extracted from the modified map with the original we finally determined a measurement error $\delta\acute{G}_{2l+1}$. The first scenario was of a displacement of the mapper origin, measured using a dedicated set of linear gradient coils, whose error was easily both predicted and simulated. We then showed through laser-tracking of the fluxgate during a radial and a vertical scan that the mapper's $\mathbf{e}_\rho$ and $\mathbf{e}_z$ axes were not perfectly orthogonal, and simulated the defect by extrapolating a global change of coordinates in a map of the coil from the fluxgate's trajectories. We finally considered a third defect wherein the inclination of the fluxgate varies slightly as it travels along the paths shown earlier, which leads to a rotation of its three axes in the geometrical frame. Fortunately, in all three scenarios the resulting inaccuracy on the phantom gradient extraction matched the statistical requirement, with $\delta\acute{G}_{2l+1} < 20\,\mathrm{fT/cm}$.

Having ensured that the inherent accuracy of the n2EDM mapper allows it to satisfy the experimental requirements on magnetic field uniformity, we now turn to the measurements it provides in order to characterize the n2EDM magnetic field.

Chapter 8

Characterization of the residual field inside the vacuum vessel

Contents

The task of the mapper is to characterize the magnetic environment of n2EDM before physical data-taking takes place. The latter can be thought of as the superposition of two fields: one generated by the n2EDM coil system, and a residual field, defined simply as the difference between the total field and the generated field. This chapter focuses on the study of the residual field.

In n2EDM, the magnetically shielding room is given the task of suppressing the ambient magnetic field to minimal levels. Measuring the residual field then amounts to mapping the inside of the functioning MSR with the B_0 coil turned off. This characterization of the MSR has already been performed using a Bartington MAG03 fluxgate (n.d.[c]), installed in a Plexiglas tube running along the vertical axis of the MSR, and led to a 2022 article (Ayres et al., 2022). One of its main results is that the residual field in the central $1\,\mathrm{m}^3$ is of the order 100 pT for the three field components. However the residual field story does not end here, as subsequent mapping of the MSR after installing the aluminum vacuum vessel led to the surprising discovery of a much larger magnetic pattern.

We show in the first section of this chapter that the n2EDM vacuum vessel hosts an unstable residual field which varies in amplitude within the cylindrical volume and is strongly correlated to temperature gradients existing inside the MSR. As such we attribute the residual pattern to a thermo-electric Seebeck effect (section 8.1). Having defined a sufficiently stable thermal state of the MSR, we then confront the residual field to the experimental requirements. We first look at the field mapping data to both establish the reproducibility of the harmonic-fitted field and to rule out any unruly systematic contribution from the harmonic field residuals. We then briefly turn to the online analysis to investigate a potential bias of the cesium magnetometers induced by the residual field pattern (section 8.2).

8.1 The issue of thermal stress on the vacuum vessel

8.1.1 Qualification of the vacuum vessel pattern

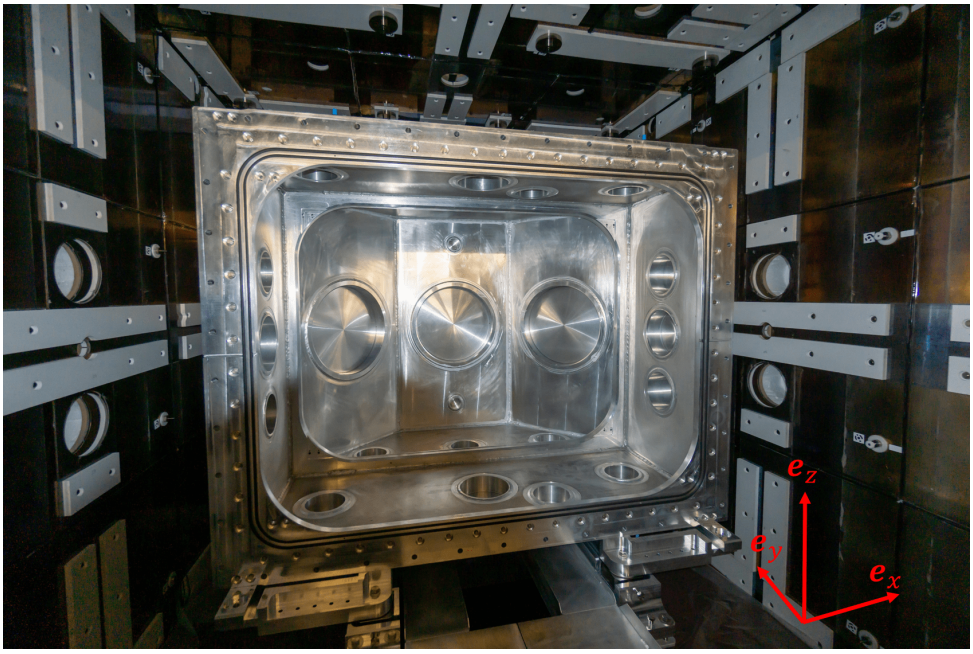

FIGURE 8.1: Back lid of the vacuum vessel inside the magnetic shielding room. The vacuum vessel is 160 cm wide in the $\mathbf{e}_x$ and $\mathbf{e}_y$ directions, and 120 cm tall in the $\mathbf{e}_z$ direction.

The two 2022 mapping campaigns of n2EDM introduced the use of the mapper for magnetic field measurements, and sought to confirm the initial residual field characterization of the MSR before evaluating the B_0-coil generated field. The first mapping campaign of n2EDM was hindered by mechanical issues affecting the movement of the mapper, which had the consequence of only allowing vertical scans inside the MSR. The installation of the vacuum vessel was then delayed and the goal of the campaign became a primitive characterization of the B_0 coil using only $m = 0$ generalized gradients. Full-scale mapping of the MSR equipped with the vacuum vessel (as shown in figure 8.1), with extraction of the entire harmonic spectrum, began with the second mapping campaign of n2EDM in late 2022. Its initial task was merely to verify that the field residuals once the vacuum vessel had been introduced were as negligible as they were during the empty MSR characterization discussed above, before turning to the main challenge in the mapping of the B_0 coil. However, after the first few maps an unexpected hurdle appeared in the form of the "vacuum vessel pattern", a large high-order magnetic signal visible especially in rings close to the walls of the vacuum vessel. The increased performance of the n2EDM magnetic shielding which had allowed us to drastically reduce the residual field inside the MSR had in fact revealed structures that were previously concealed by the higher noise level.

A plot of the pattern is featured at the top of figure 8.2. The green and orange points show the vertical field projection measured by the mapper's fluxgate when performing a ring at respectively $(\rho, z) = (40, -41)$ cm and $(\rho, z) = (78, -41)$ cm. Only rings on the bottom plane are shown as this is where the pattern is the most striking. Clearly, the effect increases with the proximity to the walls of the vacuum

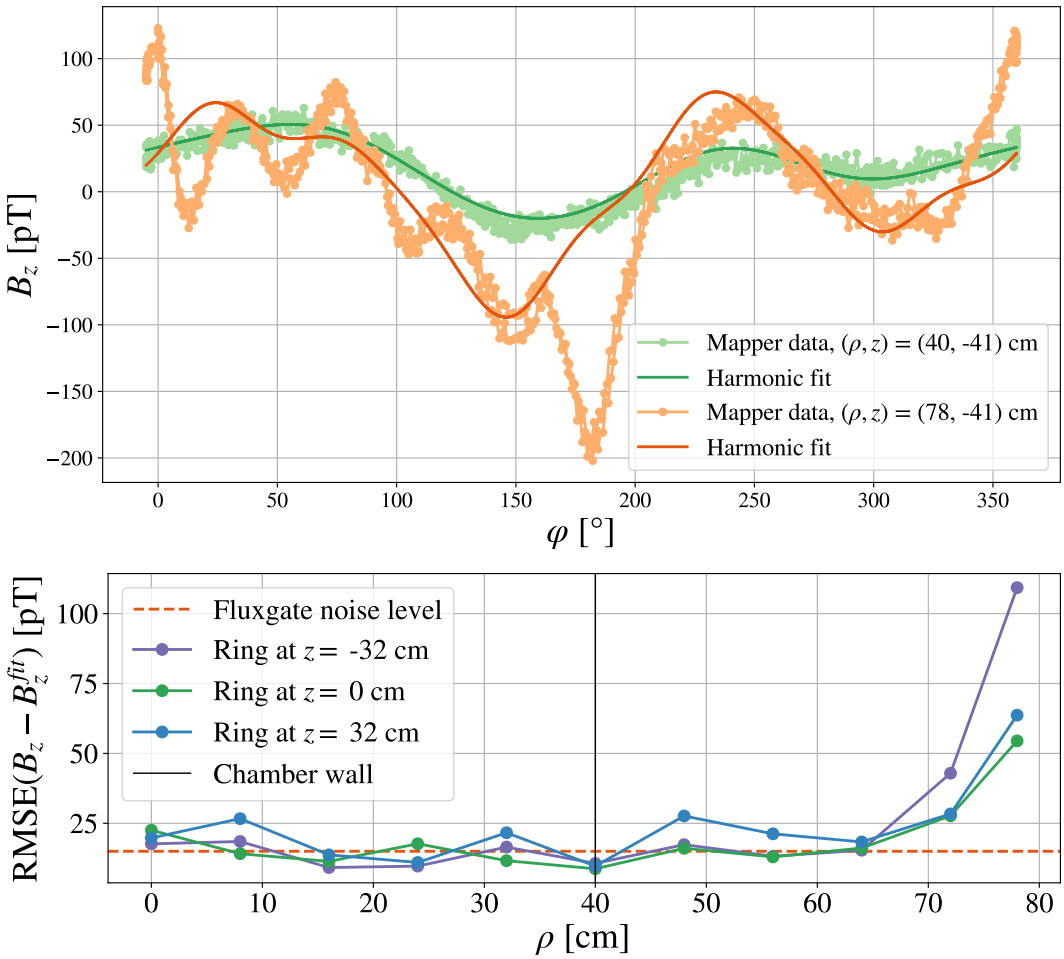

FIGURE 8.2: The top plot shows in light green and orange the data recorded by the fluxgate, for the B_z probe, over two rings of a cylindrical map. While mapping, the MSR contained only the vacuum vessel and the B_0 coil was turned off. The darker green and orange full lines correspond to the harmonic fit of the entire map evaluated over the two rings. The bottom plot shows the root-mean-square error between the harmonic fit and the mapping data for all map values of ρ (x-axis) and for 3 map values of z. The dotted red line represents the measurement deviations attributable to the noise of the Bartington fluxgate. The continuous black line indicates where the precession chamber walls would stand.

vessel, which are barely $\approx 5\,$cm away from the fluxgate for the closest point of the ring-scan at $(\rho, z) = (78, -41)\,$cm. The pattern is considered problematic chiefly because it is not successfully captured by the harmonic fit up to order $l = 7$. To see this we look again at figure 8.2, whose top plot also shows the harmonic fit of the *entire* map (121 rings), evaluated over the two rings. While the ring at mid-radial distance is well described by the fit, the outermost ring exhibits high-order structures that are not captured by the fit. The figure's bottom plot provides the root-mean-square error (RMSE) between the harmonic fit and the mapping data of the vertical field, for several rings indexed by ρ (x-axis) and z (three different values are shown). While rings $\rho \leq 64\,$cm yield acceptable RMSEs of the order of the fluxgate's noise level (dotted red line at 15 pT), which are therefore not attributable to the fit, rings towards the edges of the vacuum vessel spike up well above 50 pT. The problematic

character of these residuals will be the subject of a dedicated discussion in section 8.2.

While investigating the response of the pattern to several stimuli of the magnetic environment, the amplitude of the field was found to be strongly correlated to temperature gradients existing inside the MSR. This was observed after installing nine temperature sensors around the vacuum vessel, whose positions are shown in the bottom drawing of figure 8.3. Several dedicated tests were performed, such as modifying the air flow inside the MSR or locally heating and cooling the exterior of the MSR. Most significant was the observation that the degaussing of the MSR itself injects heat inside the vacuum vessel. Contrarily to all other heat sources which could be eliminated or controlled, degaussing is of course an essential procedure that allows the MSR to greatly suppress the external magnetic environment. The core principle of degaussing is to erase the magnetic "memory" of a material by applying strong sinusoidal magnetic fields of alternating polarity that slowly decay to zero through dedicated magnetic coils. In n2EDM, doing this for the 6 layers of the MSR using a well-studied coil layout achieves the $\sim 100\,\mathrm{pT}$ field at the center of the MSR, yet generates heat through the degaussing coils. Recent reviews of degaussing for magnetic shielding rooms can be found in (Thiel et al., 2007; Voigt et al., 2013; Altarev et al., 2015).

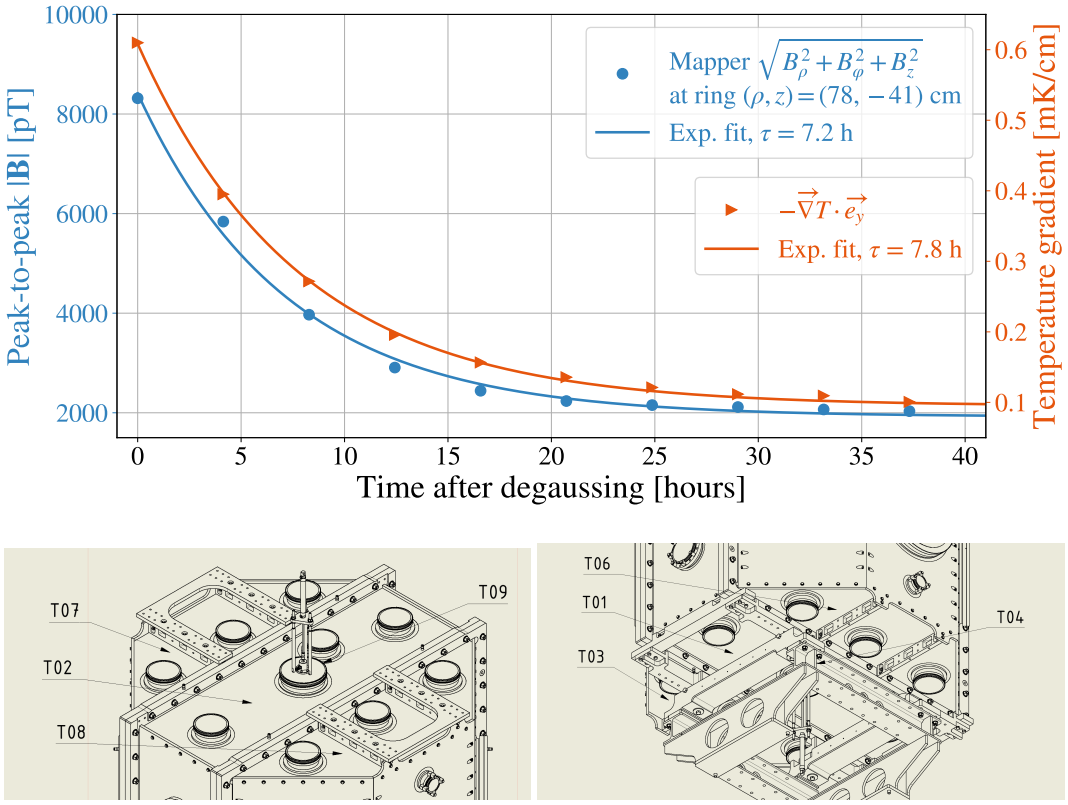

FIGURE 8.3: The top plot shows both the total field amplitude recorded by the mapper and the temperature gradients measured by the sensors over a series of maps performed after a full degaussing of the MSR. The horizontal temperature gradient aligned with $\mathbf{e_y}$ was obtained from sensors T01 and T03, shown in the bottom two figures. The Pearson correlation coefficient between the two data sets is $\rho_{T,B} = 0.99$.

The top plot of figure 8.3 illustrates the impact of degaussing on the thermal

environment of the MSR. The blue points correspond to the quadratic sum of the three field amplitudes over the ring closest to the lower edge of the vacuum vessel, extracted from maps performed in succession after a full degaussing of the MSR. The orange points correspond to the average temperature gradient along the n2EDM $\mathbf{e_y}$ axis over each of these maps, obtained from sensors T01 and T03. The correlation between the temperature gradient and the field amplitude is striking, with a similar exponential decay and a Pearson correlation coefficient $\rho_{\mathrm{T,B}} = 0.99$. The scale of the effect is also surprising. Figure 8.3 tells us that, in the relaxed state of the vacuum vessel, a 1 mK/cm horizontal temperature gradient should generate an about 20 nT increase in the total field amplitude (12 nT increase for B_z only). In more intuitive proportions, a 1 mK temperature difference across the entire 160 cm width of the vacuum vessel should generate a 125 pT field increase (75 pT for B_z only).

8.1.2 An explanation in the thermo-electric Seebeck effect

The physical grounds for this phenomenon lie likely in the *Seebeck effect*, where the presence of a temperature gradient inside a heat-conductive material generates a current density through it. In the case of our aluminum vacuum vessel, the Seebeck current density can be expressed as

$$\mathbf{j} = -\sigma_{\mathrm{Al}} S_{\mathrm{Al}} \boldsymbol{\nabla} T, \tag{8.1}$$

where $\sigma_{\mathrm{Al}} = 3.77 \times 10^5\,\Omega^{-1}\,\mathrm{cm}^{-1}$ is the conductivity of aluminum, and $S_{\mathrm{Al}} = -2.2 \times 10^{-9}\,\mathrm{V\,mK}^{-1}$ is its *Seebeck coefficient*. Considering a temperature gradient of the order of $|\boldsymbol{\nabla} T| = 0.1\,\mathrm{mK\,cm}^{-1}$, we expect a current density of magnitude

$$|\mathbf{j}| \approx 83 \times 10^{-4}\,\mathrm{A\,cm}^{-2} \tag{8.2}$$

A thermo-electric current of this magnitude could potentially induce a magnetic field such as the one witnessed in the vacuum vessel pattern.

We will try to estimate the field produced by a current flowing through the floor of the vacuum vessel, where the strongest temperature gradients arise. Consider an idealistic scenario of a strictly horizontal temperature gradient occurring along an infinite sheet of aluminum of thickness h. Then from equation (8.1) the current flows along the temperature gradient, and for a gradient in the $\mathbf{e_y}$ direction its density is written $\mathbf{j} = -\sigma_{\mathrm{Al}} S_{\mathrm{Al}} (\partial T/\partial y)\mathbf{e_y}$. We apply Ampere's Law by considering the current going through a rectangular surface of height h and length L in the $(\mathbf{e}_x, \mathbf{e}_z)$ plane, perpendicular to the aluminum sheet:

$$\oint \mathbf{B} \cdot \mathbf{dl} = \mu_0 \int_0^h dz \int_0^L dx\, \mathbf{j} \cdot \mathbf{e_y}. \tag{8.3}$$

Since the surface current flows in the $\mathbf{e_y}$ direction, we know from symmetry reasons that the magnetic field at any point above the aluminum sheet will be strictly in the $\mathbf{e}_x$ direction, so only the top and bottom parts of the contour integral contribute. This leads to

$$2B_x L = -\mu_0 \sigma_{\mathrm{Al}} S_{\mathrm{Al}} h L \frac{\partial T}{\partial y}. \tag{8.4}$$

The magnetic field generated by the temperature gradient is then of the form

$$\mathbf{B} = -\mu_0 \sigma_{\mathrm{Al}} S_{\mathrm{Al}} \frac{h}{2} \frac{\partial T}{\partial y} \mathbf{e_y}. \tag{8.5}$$

For a width of the vacuum vessel floor $h \approx 1\,\mathrm{cm}$ and given $\mu_0 = 1.25 \times 10^{-4}\,\mathrm{T\,cm\,A^{-1}}$, we expect an induced field of magnitude

$$|\mathbf{B}| \approx \frac{50\,\mathrm{nT}}{\mathrm{mK/cm}} \times \frac{\partial T}{\partial y}. \tag{8.6}$$

Confronted with the data shown in figure 8.3, this result provides a reasonable order-of-magnitude estimate of the amplitude of the vacuum vessel pattern, which we can extrapolate to 20 nT for a 1 mK/cm horizontal temperature gradient. The Seebeck effect is a plausible explanation for the witnessed magnetic pattern.

What is problematic in regards of the n2EDM experimental requirements is not so much the existence of thermal gradients in itself but the fact that these evolve through time. If left unchecked, the fluctuating magnetic pattern induced by such thermo-electric currents would lead to a poor reproducibility of the total magnetic field that jeopardizes the n2EDM sensitivity through condition (7.2). This issue was addressed first-hand by a meticulous thermal insulation of the MSR that blocks out all air flow through the vacuum vessel. As for the heat deposited by the degaussing, one should simply wait long enough for the pattern to relax to its initial state. The time scale of this relaxation is provided by figure 8.3. Both the temperature gradients and the total field amplitude were fitted with an exponential decay $Ae^{-t/\tau} + B$, $A, B, \tau \in \mathbb{R}$, which gives us comparable decay rates for the two quantities of about $\tau = 8\,\mathrm{hours}$. Waiting $2\tau = 16\,\mathrm{hours}$ after degaussing will suppress the vacuum vessel pattern brought by the degaussing by just under 90%. In the eyes of the offline analysis, observing a 2τ rest-time allows us to achieve a sufficiently stable magnetic state. Subsequent cylindrical mappings of the residual field which aimed at evaluating its reproducibility were performed in this state. We will now discuss the results of these measurements.

8.2 Matching the systematical requirements for a stabilized field

The effect of the vacuum vessel pattern may not only be felt in the offline mapping but also in the online field measurements performed by the cesium magnetometers, so we divide our approach accordingly. We first use the mapping data to check that the residual field satisfies the n2EDM systematical requirements, and then simulate the ability of the cesium array to accurately extract harmonic modes in the presence of the vacuum vessel pattern.

8.2.1 Offline analysis of the vacuum vessel pattern

The goal of the offline analysis is to accurately extract the harmonic spectrum of the total magnetic field and ensure that it is reproducible. As we just have observed, the presence of the high-order structure due to the vacuum vessel challenges this approach because the pattern is not successfully described by the harmonic fit up to $l = 7$. It is then not enough to check that the requirements on the phantom modes are met in order to satisfy the core systematical requirement

$$d^{\mathrm{false}}_{n\leftarrow\mathrm{Hg}} < 3 \times 10^{-28}\,e\,\mathrm{cm}. \tag{8.7}$$

Our new approach is straightforward. We proceed in two steps by considering the residual magnetic field as the sum of two contributions:

1. The **harmonic fit**, for which we need to satisfy (7.1) and (7.2),
2. The **residuals** of the harmonic fit, for which we need to satisfy more generally (8.7).

Reproducibility of the fitted field

After characterizing the thermo-electric effect, systematic mapping of the residual field proceeded according to the second mapping campaign's strategy detailed in 7.1. Since the B_0 coil was turned off at this point, the mapping sequence consisted only of cylindrical maps taken in succession after one full degaussing. In order to evaluate the reproducibility of the *stabilized* magnetic field, a 16 hours relaxation time after degaussing was observed when comparing data obtained from different mapping sequences.

	$\acute{G}_3$	$\acute{G}_5$	$\acute{G}_7$	**Requirement**
Average μ (fT/cm)	−7.2	1.0	2.3	
Repeatability τ (fT/cm)	7.8	2.9	0.9	< 20
Reproducibility σ (fT/cm)	6.2	1.7	0.2	< 20

TABLE 8.1: Average values, repeatability, and reproducibility of phantom modes obtained during the second mapping campaign of n2EDM before turning on the B_0 coil. The measurements consisted of 6 mapping sequences of each 5 to 8 high-resolution cylindrical maps, performed according to the strategy defined in 7.1. A rest-time of about 16 hours was observed after degaussing. The repeatability corresponds to the standard deviation of maps within a sequence, and the reproducibility to the standard deviation between the averages of each sequence.

The results of the harmonic spectrum $\{G_{lm}\}_{l\leq 7}$ extraction from these sequences are condensed in table 8.1, where we provide only the problematic odd-degree phantom modes $\acute{G}_{2k+1} = D^{2k}_{2k+1} G_{2k+1,0}$. The entire spectrum is given in appendix D under the "bare" field columns. The results featured in the mapper repeatability line, which all fall under the 20 fT/cm requirement, tell us that the mapper is able to extract the phantom modes precisely enough for us to estimate the false EDM under its limit. More importantly, the reproducibility results also satisfy their systematical requirement, which allows the offline estimate of the false EDM to remain valid during data-taking within an acceptable margin. Under the condition that enough time elapses after degaussing of the MSR, we conclude that the non-reproducibility of the total field attributable to the vacuum vessel pattern is not concerning with respect to the n2EDM systematical requirements.

False EDM generated by field residuals

There are two ways of addressing the issue of the harmonic fit residuals. The first is to notice in figure 8.2 that the field over the double chamber precession volume $\{(\rho, z) \mid |z| \leq 12, \rho \leq 40\}$ *is* successfully described by the harmonic field expansion. Indeed, below the black line in the bottom plot corresponding to the vertical chamber walls, the field RMSE is comparable to the inherent measurement error due to the fluxgate noise. The effectiveness of the fit is also noticeable in the top plot of

the same figure over the $(\rho = 40, z = -41)$ cm ring. With that in mind one should not worry about strong residuals outside of the precession volume. The second approach, more cautious, is to consider that even these far-residuals may contribute to the false EDM in a way that escapes the harmonic field description. Therefore we must directly calculate the low-frequency false EDM generated by these residuals and ensure that it satisfies (8.7).

Unfortunately, any direct numerical estimate of $\langle \rho B_\rho \rangle$ inside the precession chambers volume is dominated by the fluctuations of the fluxgate offset. To understand this, recall that because of the chamber's cylindrical symmetry the φ-average cancels out all $m \neq 0$ modes in the Fourier expansion of B_ρ over a map's ring (given by (7.3)):

$$\langle \rho B_\rho(\rho, \varphi, z) \rangle = \left\langle \rho \sum_{m=0}^{l_{\max}+1} a_m^{(\rho)}(\rho_i, z_i) \cos(m\varphi) + b_m^{(\rho)}(\rho_i, z_i) \sin(m\varphi) \right\rangle \tag{8.8}$$

$$= \left\langle \rho\, a_0^{(\rho)}(\rho_i, z_i) \right\rangle . \tag{8.9}$$

Therefore the only modes that contribute to the false EDM are extracted from the zeroth order Fourier coefficients of every ring (ρ_i, z_i), which are recorded at different times and therefore vary with the uncompensated part of the B_ρ fluxgate offset. As expected, the result of the residual effective gradient $(4/R^2)\left\langle \rho \left(B_\rho - B_\rho^{\text{fit}} \right) \right\rangle = 246(241)$ fT/cm is inconclusive.

Alternatively, we chose to model the field residuals with a dipole field and calculate the false EDM generated by that dipole. This approach seems appropriate given that the residuals consist of high-order magnetic structures for near dipoles. The dipole field fit is performed by considering the field generated at $\mathbf{r}$ by a dipole located at $\mathbf{r_d}$ as a linear transformation of its magnetic moment $\mathbf{m}$:

$$\mathbf{B}^{\text{dip}}(\mathbf{r}) = M(\mathbf{r} - \mathbf{r_d})\mathbf{m}, \tag{8.10}$$

where $M(\mathbf{r}')$, with here $\mathbf{r}' = \mathbf{r} - \mathbf{r_d}$ is obtained by identifying (6.47) with the above:

$$M(\mathbf{r}') = \frac{\mu_0}{4\pi} \begin{pmatrix} \frac{x'^2}{|\mathbf{r}'|^5} - \frac{1}{|\mathbf{r}'|^3} & \frac{x'y'}{|\mathbf{r}'|^5} & \frac{x'z'}{|\mathbf{r}'|^5} \\ \frac{y'x'}{|\mathbf{r}'|^5} & \frac{y'^2}{|\mathbf{r}'|^5} - \frac{1}{|\mathbf{r}'|^3} & \frac{y'z'}{|\mathbf{r}'|^5} \\ \frac{z'x'}{|\mathbf{r}'|^5} & \frac{z'y'}{|\mathbf{r}'|^5} & \frac{z'^2}{|\mathbf{r}'|^5} - \frac{1}{|\mathbf{r}'|^3} \end{pmatrix}. \tag{8.11}$$

The minimization of the chi-squared function

$$\chi^2 = \frac{1}{\sigma^2} \sum_i \left(\mathbf{B_i} - \mathbf{B}^{\text{dip}}(\mathbf{r_i}) \right)^2, \tag{8.12}$$

where $\mathbf{B_i}, \mathbf{r_i}$ are the fields and position data points of a given scan, is then a linear problem. We readily obtain the magnetic moment vector through

$$\boldsymbol{\nabla}_{\mathbf{m}}(\chi^2) = \mathbf{0} \;\Leftrightarrow\; \mathbf{m} = \left(\sum_i M^2(\mathbf{r_i}, \mathbf{r_d}) \right)^{-1} \left(\sum_i M(\mathbf{r_i}, \mathbf{r_d}) \mathbf{B_i} \right) \tag{8.13}$$

Figure 8.4 shows the residuals of the harmonic fit for the B_z probe over the three outermost rings at the lowest scan height. These residuals were fitted for the magnetic moment $\mathbf{m}$ with (8.12) using the data from all three probes and for several

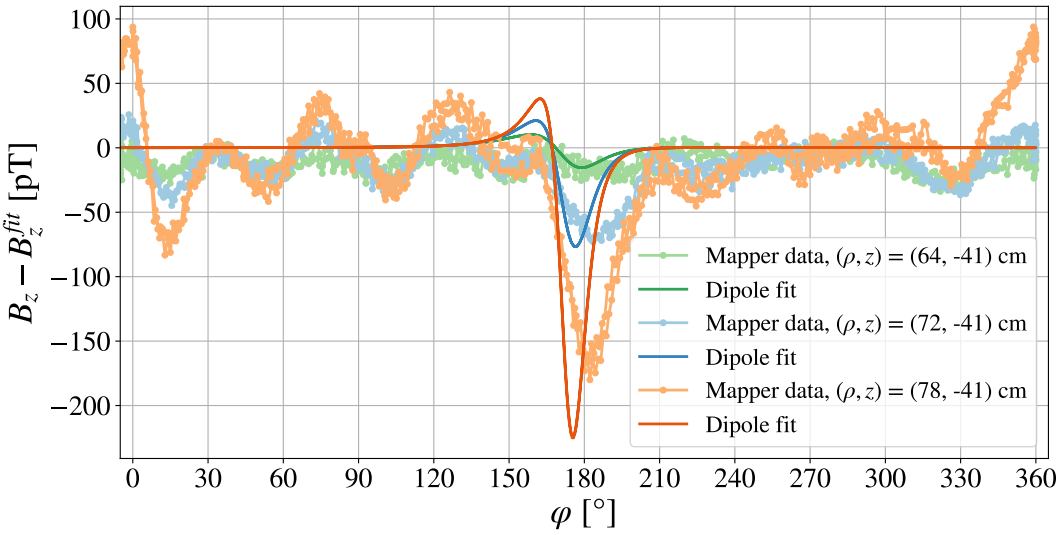

FIGURE 8.4: Vertical field projection of the harmonic fit residuals, plotted for three rings of a cylindrical map with B_0 off. The best dipole fit shown here considers a dipole located at $(x_d, y_d, z_d) = (85, 0, -30)$ cm and returns a magnetic moment $(m_x, m_y, m_z) = (1.18, -5.11, -4.12) \times 10^7$ nA cm^2.

reasonable dipole positions $\mathbf{r}_d$. The fit shown in 8.4 figure assumes a dipole located on the lower end of the vacuum vessel wall, at the closest position to the $\varphi = 180°$ scan points (in the $\mathbf{e_y}$ direction) where the largest unfitted structure appears. We finally evaluate the false EDM generated by this supposed dipole field:

$$-\frac{\hbar\left|\gamma_n\gamma_{\mathrm{Hg}}\right|}{2\pi c^2}\left\langle \rho\, B_\rho^{\mathrm{dip}}\right\rangle \approx 1.8\times 10^{-28}\, e\,\mathrm{cm}, \tag{8.14}$$

which satisfies the core systematical requirement (8.7). This estimate is still quite conservative as the dipole field is constantly larger in magnitude than the residuals over rings inside the chamber volume. Therefore we do not consider the harmonic field residuals to contribute significantly to the false EDM; evaluating the false EDM contribution of harmonic modes $l \leq 7$ is enough to qualify the remnant field.

8.2.2 Effect of the vacuum vessel pattern on cesium array accuracy

The vacuum vessel pattern could also be particularly harmful to the cesium magnetometers, who are responsible for the extraction of the harmonic field spectrum during data-taking thanks to their wide coverage of the area around the precession chambers. Compared to the mapper however, their lower measurement statistics (112 magnetometers) do not allow them to perform such a high-order fit. Their task is to provide an accurate measurement of the $l = 3$ phantom gradient. However this attempt could be thwarted by the presence of a high-order structure such as the vacuum vessel pattern, which could dangerously bias the cesium's harmonic fit. Our goal is to estimate the scale of this bias and ensure that it satisfies a requirement similar to (7.1):

$$\left|\acute{G}_3 - \acute{G}_3^{\mathrm{CS}}\right| < 20\,\mathrm{fT/cm}. \tag{8.15}$$

To this end we simulate the extraction of $\acute{G}_3^{\mathrm{CS}}$ by the cesium array using the

harmonic fitted field from the maps presented earlier. Our Monte Carlo simulation draws at every position of the 112 cesium magnetometers a value of the CS-measured field from a normal distribution, whose mean is given by the $l = 7$ harmonic fit of the mapper-measured field and standard deviation is the residual of this fit. The simulated CS-measured field is then fitted with a $l = 3$ harmonic expansion from which we obtain $\acute{G}_3^{\mathrm{CS}}$. The distribution of $\acute{G}_3^{\mathrm{CS}}$ over 1000 iterations of the simulation is shown in figure 8.5 and tells us two things. First, the difference between the distribution's average third order mode and the mapper's third order mode corresponds to the inaccuracy of the cesium magnetometers attributable to modes $3 < l \leq 7$ of the vacuum vessel pattern. Second, the width of the distribution determines the cesium array's precision and is attributable to the field residuals. In numbers,

$$\mu\left(\acute{G}_3 - \acute{G}_3^{\mathrm{CS}}\right) = 0.3\,\mathrm{fT/cm}, \tag{8.16}$$

$$\sigma\left(\acute{G}_3 - \acute{G}_3^{\mathrm{CS}}\right) = 31.8\,\mathrm{fT/cm}. \tag{8.17}$$

Among these, (8.16) comfortably satisfies the cesium accuracy requirement (8.15). From (8.17), we remark that after 10 successive field measurements performed by the cesium magnetometers, their precision reaches $\sigma\left(\acute{G}_3 - \acute{G}_3^{\mathrm{CS}}\right)/\sqrt{10} \approx 10.1\,\mathrm{fT/cm}$, which is half of the systematical limit. We can safely conclude that the vacuum vessel pattern does not significantly bias the extraction of the third order phantom mode by the cesium magnetometers.

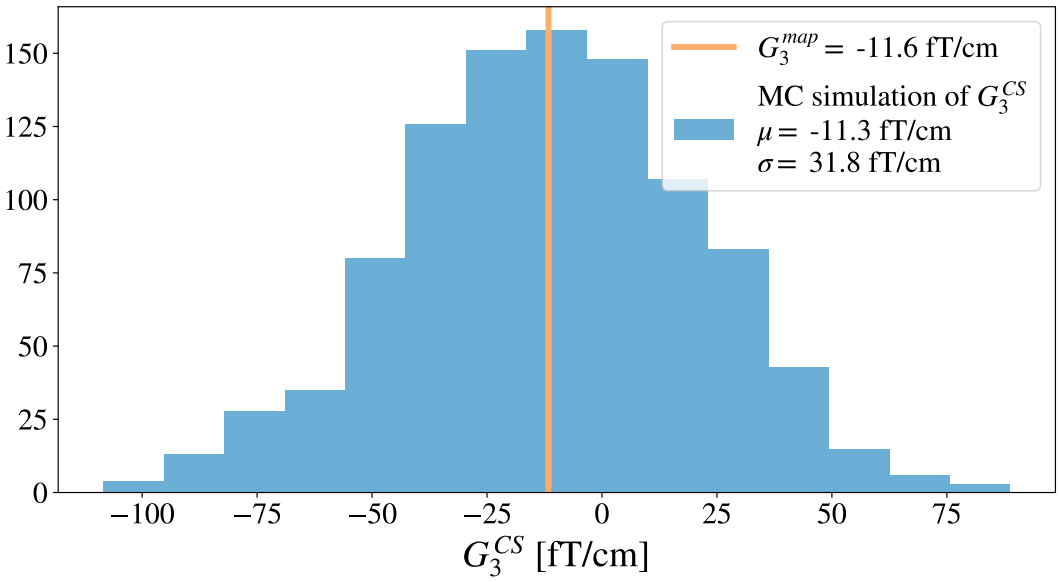

FIGURE 8.5: Distribution of the third order phantom gradients obtained from a MC simulation of the magnetic field measured by the cesium magnetometers. At every point of a cylindrical map, the simulated field is drawn from a normally distributed random variable whose mean is the mapper's harmonic fit to order $l = 7$ and standard deviation is the harmonic fit's residuals. The blue distribution is obtained for $N = 1000$ iterations. The orange bar corresponds to the third order gradient given by the mapper's harmonic fit.

8.3 Conclusion

This chapter provided the first step in the characterization of the magnetic environment of n2EDM by studying the residual field present before turning on the B_0 coil. Although the field inside the empty MSR after demagnetization had already been established to be incredibly small ($\sim 100\,\mathrm{pT}$), the introduction of the aluminum vacuum vessel came with the appearance of a fluctuating magnetic pattern of several nanotesla which could harm the reproducibility of the residual field.

We began with the characterization of the "vacuum vessel pattern", which we attributed to the presence of thermo-electric *Seebeck currents* running around the walls of the vacuum vessel. We confirmed the plausibility of the Seebeck effect by applying Ampere's Law to an idealized version of the vacuum vessel floor and found that the thermo-electric currents could generate a magnetic field comparable to the measured field. Additionally, the decay constants of horizontal temperature gradients inside the vacuum vessel and of the total field amplitude were found to be in excellent agreement. The most concerning source of thermal currents being the degaussing of the MSR layers, we defined a stable-enough thermal state of the vacuum vessel at 16 hours after degaussing, corresponding to two decay constants of the pattern. Having characterized the thermo-electric effect, we concluded that the issue with the vacuum vessel pattern was twofold. (1) It possesses high-order structures not captured by the harmonic fit and therefore not adapted to the formalism of our systematical requirements. (2) It is unstable in time due to the changing thermal environment of n2EDM, which could lead to a poor field reproducibility.

Both issues were addressed in the section that followed. Although the high-order structure generated by thermo-electric currents inside the vacuum vessel is not successfully captured by the harmonic fit towards the edges of the volume, we showed that neither the fitted field *nor* its residuals were concerning with respect to the core systematic requirement $d^{\mathrm{false}}_{\mathrm{n}\leftarrow\mathrm{Hg}} < 3 \times 10^{-28}\,\mathrm{e.cm}$. We found the fitted part of the measured field to be reproducible under this limit, and argued using a dipole field model that the residuals of the harmonic fit produced a false EDM smaller than this limit. We finally extended our analysis to the cesium magnetometers by evaluating the impact of the vacuum vessel pattern on the accuracy of real-time magnetic field measurements. Through a Monte Carlo simulation of the third-order phantom gradient extraction by the cesium array using the offline mapping data, we established that the difference between the cesium-measured and mapper-measured gradients was around two orders of magnitude below the accuracy requirement for the false EDM.

We conclude that the vacuum vessel pattern is unproblematic with respect to the systematical requirements of n2EDM, both regarding the online and the offline magnetic field measurements. We are now ready to superimpose the coil generated field to the residual noise.

Chapter 9

Characterization of the B_0 field

Contents

We finally come to the end of the discussion opened in chapter 3 on the issue of magnetic field uniformity, where we suggested that the field generated by the B_0 coil of n2EDM was in reality not entirely uniform. The characterization of the B_0 field is the subject of this chapter, and the last step in demonstrating that the entire magnetic environment of n2EDM satisfies the experimental requirements set in section 3.2.

The design of the coil system of n2EDM and optimization of its simulated harmonic spectrum was the subject of a 2019 PhD thesis (Flaux, 2019). The coil was then assembled at PSI in 2021 before the first mapping campaign of 2022. The work presented here relies on the results of the two mapping campaigns that followed. We begin by revisiting the group-theoretical considerations of chapter 3 in order to link specific modes of the harmonic spectrum, which we will later measure, to a symmetry-breaking of the coil system (section 9.1). The second section discusses the field mapping results. We first show that, after a minute vertical displacement of the B_0 the coil, the generated field satisfies the statistical requirements of n2EDM with a remarkable achievement in field uniformity. We then demonstrate our ability to measure a reproducible false EDM and thereby match our systematical requirements (section 9.2). Finally, we implement a field optimization strategy, allowed by auxiliary coils of the n2EDM coil system, to produce an even more uniform field for the n2EDM experiment (section 9.3).

9.1 Symmetries of non-ideal coil geometries

In chapter 3 we considered the ideal geometry of the coil system and showed that a specific subset of modes $\{\mathbf{\Pi}_{2k,4n}\}_{k,n\in\mathbb{N}}$ of the field generated by this coil are allowed by its symmetry. Specifically, these modes belong to a subspace of modes

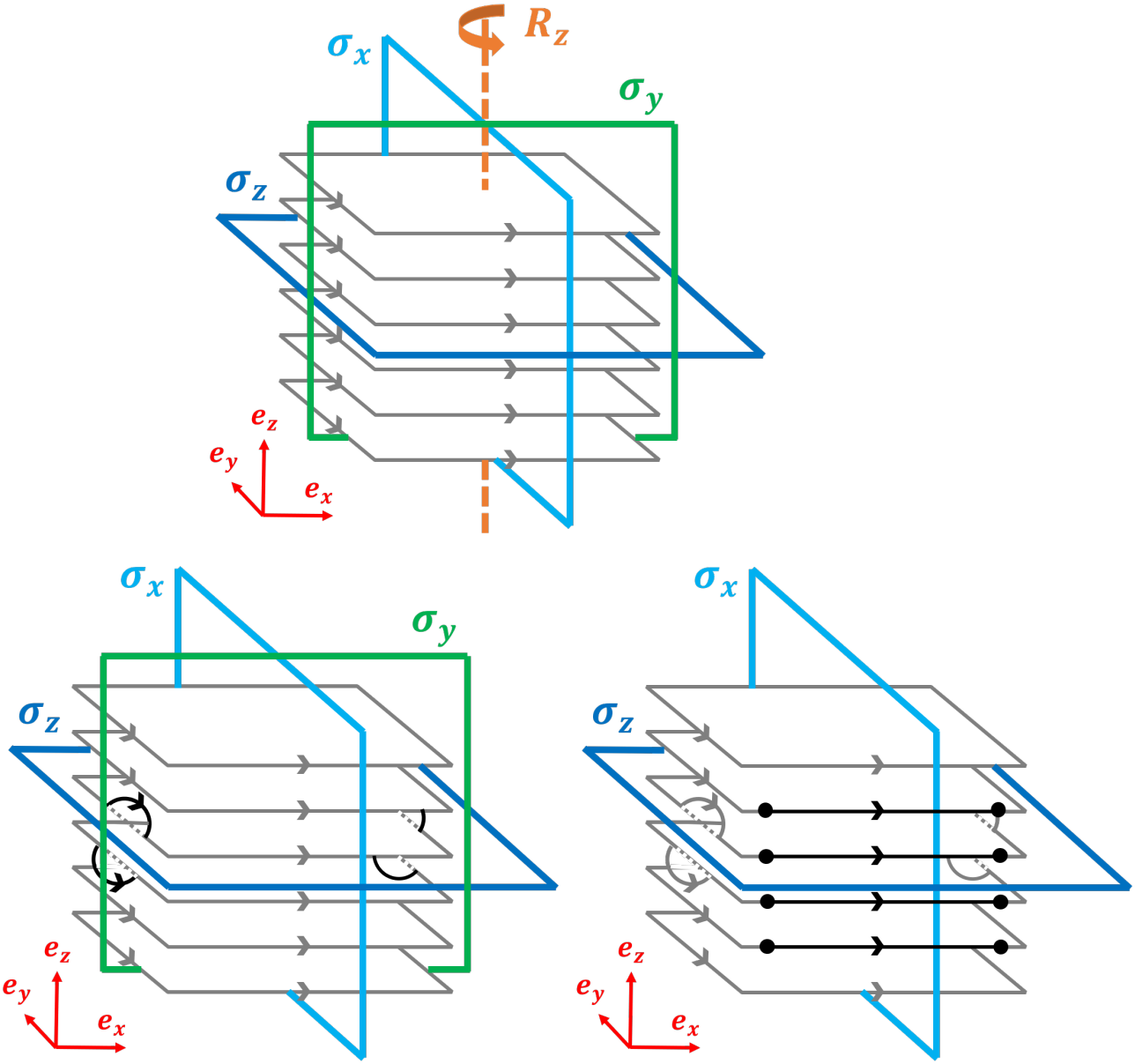

FIGURE 9.1: Schematic drawing of the B_0 coil in its ideal (top plot) and symmetry-broken (bottom plots) geometries. The ideal coil is invariant with respect to the 3 plane reflections and the $\pi/2$ rotation around the z axis. The tube-broken coil (left) loses the rotation, while the door-broken coil loses both the rotation and the reflection w.r.t. the $y = 0$ plane (right).

that is affected by an irreducible representation (irrep) ρ_{00} of the ideal coil symmetry group $\mathcal{D}_{4h}$. A significant consequence of this observation is that one should expect the harmonic spectrum of the coil-generated field to not only consist of the intended G_{00} gradient but also of potentially problematic non-uniform gradients $(G_{20}, G_{40}, G_{44}, \ldots)$.

The goal of this section is to find *which* harmonic gradients we expect to appear in the coil's spectrum given a non-ideal geometrical configuration of the coil. We do this by considering subgroups of $\mathcal{D}_{4h}$ that describe a symmetry-broken configuration of the coil and determine the modes allowed by the new, less restrictive, symmetry.

9.1.1 Symmetry breaking 1: vacuum tubes and UCN guides

We consider the non-ideal geometries already anticipated in the coil design and drawn in figure 3.1 from Pierrick Flaux's thesis (Flaux, 2019). The green boxes indicate regions where the current loops have been adapted to the presence UCN guides and vacuum tubes running from outside of the MSR all the way to the precession chambers and thus crossing the coil walls. We will later see that the coil's simulated spectrum, although optimized to suppress non-uniform modes, exhibits a certain pattern of modes arising from this geometrical defect. Here we predict what these modes are.

The presence of holes in the coil's walls along the y axis breaks the ideal-coil symmetry described by the $\mathcal{D}_{4h}$ group (3.19), by removing the $\pi/2$ rotation around the z axis R_z. This is represented schematically in the left plot of figure 9.1. The symmetry-broken coil is now invariant under transformation of a subgroup of $\mathcal{D}_{4h}$, consisting of the set

$$\mathcal{D}_{2h} = \{I, P, \sigma_x, \sigma_y, \sigma_z, R_x^2, R_y^2, R_z^2\}, \tag{9.1}$$

and matrix multiplication $\times$. It is easy to check that the set above is stable under $\times$ and satisfies all the other group axioms. We can also show that all of the elements of $\mathcal{D}_{2h}$ can be obtained by combining only three of them, as $\langle \sigma_x, \sigma_y, \sigma_z \rangle = \mathcal{D}_{2h}$. This implies that $\sigma_x, \sigma_y, \sigma_z$ are generators of $\mathcal{D}_{2h}$ (B.1.3). Just like the symmetry of the ideal coil was given by the character of the current representation ρ_c of $\mathcal{D}_{4h}$ in table 3.3, the symmetry of the tubes-broken coil is given by the character of the current representation ρ_c^{tubes} of $\mathcal{D}_{2h}$, featured in table 9.1.

irrep	$Cl(I)$	$Cl(P)$	$Cl(\sigma_x)$	$Cl(\sigma_y)$	$Cl(\sigma_z)$	$Cl(R_x^2)$	$Cl(R_y^2)$	$Cl(R_z^2)$
ρ_c^{tubes}	1	1	-1	-1	1	-1	-1	1

TABLE 9.1: Character table of $\mathcal{D}_{2h}$ for the current representation. With the disappearance of R_z, all elements become their own conjugacy classes.

The symmetries of this coil are conserved in the magnetic field it generates. When taking into account the harmonic expansion, the transformations of $\mathcal{D}_{2h}$ on the set of generalized gradients are described by the harmonic representation ρ_h^{tubes}. Back in 3.3, we showed that the harmonic representation ρ_h of the ideal coil symmetry group was reducible, such that all of its irreducible components ρ_{lm} acted on smaller sets of generalized gradients, some of dimension 2, some of dimension 1. The actions of the 8 inequivalent irreps on targeted gradients for the 3 generators were described in table 3.3, which is enough to obtain the action of all possible irreps acting on all possible gradients. Similarly we determine the representation elements $\rho_{lm}^{\text{tubes}}(M)$, for $M = \sigma_x, \sigma_y, \sigma_z$ from equation (3.39), and store them in table 9.2. Here all irreps are of dimension 1. We observe that irrep ρ_{00}^{tubes} (green table line) shares the same character as ρ_c^{tubes}, and conclude that gradients $G_{2k,2n}$ affected by equivalent irreps, share the same symmetries as the coil. These gradients, represented in green in the drawing of figure 9.2, are then allowed by the tube-broken coil symmetry. We now expect gradients such as G_{22} to appear alongside G_{20} in the coil's harmonic spectrum, on a scale that depends on the amount symmetry-breaking caused by the holes inside the coil walls. We also note that:

1. There are still $2^3 = 8$ group elements determined by the minimal number of generators.

2. The dimension-2 irreps of $\mathcal{D}_{4h}$ affecting m-odd modes break down into two dimension-1 irreps when losing the R_z symmetry. This phenomenon is understood by looking at table 3.4, which shows that only R_z mixes harmonic modes of different m. Meanwhile the $0+4n$ and $2+4n$ irreps combine into one $2n$ irrep.

irrep	l	m	$Cl(\sigma_x)$	$Cl(\sigma_y)$	$Cl(\sigma_z)$
$\rho^{\text{tubes}}_{0,0}$	$2k$	$0+2n$	-1	-1	1
$\rho^{\text{tubes}}_{0,1}$	$2k$	$1+2n$	1	-1	-1
$\rho^{\text{tubes}}_{0,-1}$	$2k$	$-1-2n$	-1	1	-1
$\rho^{\text{tubes}}_{0,-2}$	$2k$	$-2-2n$	1	1	1
$\rho^{\text{tubes}}_{1,0}$	$2k+1$	$0+2n$	-1	-1	-1
$\rho^{\text{tubes}}_{1,1}$	$2k+1$	$1+2n$	1	-1	1
$\rho^{\text{tubes}}_{1,-1}$	$2k+1$	$-1-2n$	-1	1	1
$\rho^{\text{tubes}}_{1,-2}$	$2k+1$	$-2-2n$	1	1	-1

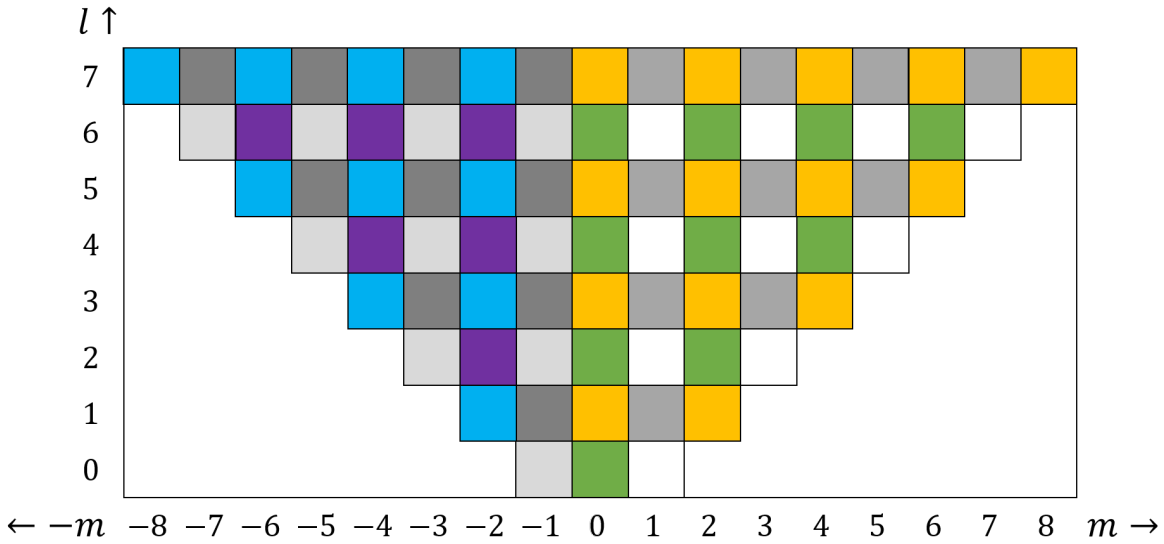

FIGURE 9.2: Top: character table of the 3 group generators of the $\mathcal{D}_{2h}$ group for the 8 inequivalent harmonic irreps. Each line corresponds to equivalent irreps that affects different harmonic modes of indices l and m (second and third columns), for values of $k, n \in \mathbb{N}$. Each of the three last columns gives the elements of that representation for the conjugacy class of a group generator, with $Cl(\sigma_x) = \{\sigma_x\}$, $Cl(\sigma_y) = \{\sigma_y\}$, and $Cl(\sigma_z) = \{\sigma_z\}$. Bottom: visual decomposition of the harmonic modes on the 8 subspaces of $\mathbb{R}^n$ acted on by the 8 harmonic irreps.

9.1.2 Symmetry breaking 2: coil door

We apply the same reasoning when including a further geometrical feature of the B_0 coil: the door represented in blue in figure 3.1. This removes both the R_z and σ_y symmetries from $\mathcal{D}_{4h}$, as shown in the right plot of figure 9.1. The largest subgroup

that we can construct without this element is then

$$\mathcal{C}_{2v} = \{I, \sigma_x, \sigma_z, R_y^2\}, \tag{9.2}$$

together with matrix multiplication. There are now 2 generators, σ_x and σ_z. The coil symmetry is given by the current character ρ_c^{door} in table 9.2.

irrep	$Cl(I)$	$Cl(\sigma_x)$	$Cl(\sigma_z)$	$Cl(R_y^2)$
ρ_c^{door}	1	-1	1	-1

TABLE 9.2: Character table of $\mathcal{C}_{2v}$ for the current representation.

The character of all harmonic ρ_m^{door} irreps is given by table 9.3, where we find 4 inequivalent irreps. The subset of gradients affected by ρ_0^{door} and its equivalent irreps is yet again enlarged, to now include all modes of the form $G_{2k,2n}$ *and* $G_{2k+1,-1-2n}$, with $k, n \in \mathbb{N}$. These are highlighted in green in the table and drawing of figure 9.3. Most notably, we now also expect $G_{1,-1}$ to appear in the spectrum of the coil-generated field. Note that none of the inequivalent irreps discriminate between even and odd l anymore.

irrep	l	m	$Cl(\sigma_x)$	$Cl(\sigma_z)$
ρ_0^{door}	$2k, 2k+1$	$0+2n, -1-2n$	-1	1
ρ_1^{door}	$2k, 2k+1$	$1+2n, -2-2n$	1	-1
ρ_{-1}^{door}	$2k, 2k+1$	$-1-2n, 0+2n$	-1	-1
ρ_{-2}^{door}	$2k, 2k+1$	$-2-2n, 1+2n$	1	1

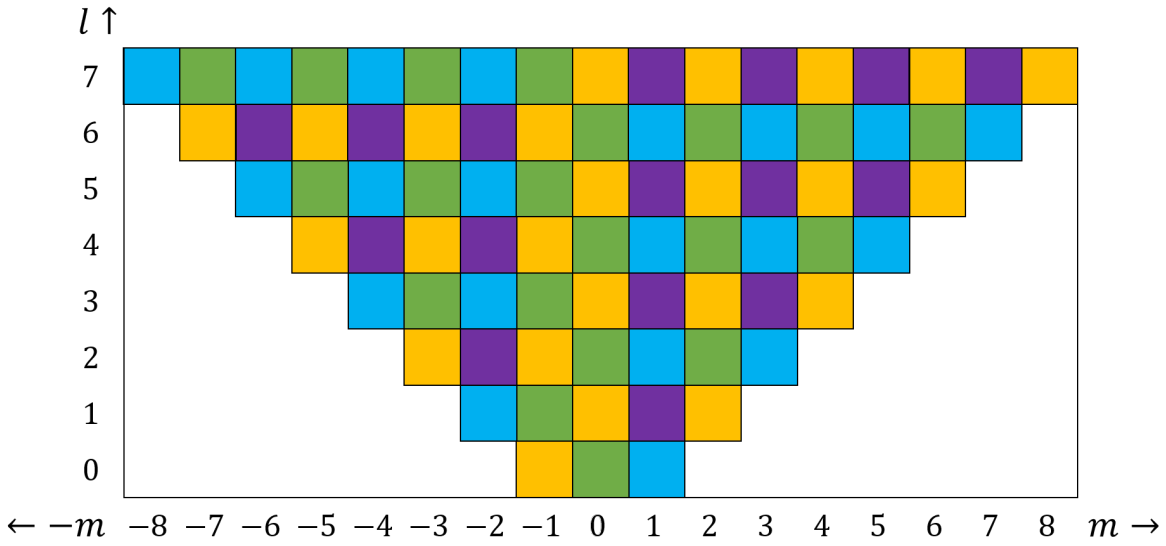

FIGURE 9.3: Top: character table of the 3 group generators of the $\mathcal{C}_{2v}$ group for the 4 inequivalent harmonic irreps. Each line corresponds to equivalent irreps that affects harmonic modes of indices l and m, for values of $k, n \in \mathbb{N}$. Each of the three last columns gives the elements of that representation for the conjugacy class of a group generator. Bottom: visual decomposition of the harmonic modes in the 4 subspaces of $\mathbb{R}^n$ acted on by the 4 harmonic irreps.

We see that the less restrictive the coil symmetry is, the more harmonic modes are

allowed by it. Our knowledge of the relationship between targeted modes of the B_0 harmonic spectrum and types of symmetry-breaking will prove crucial when evaluating later measurements. To this end, table 9.3 indicates which harmonic modes are allowed by different likely symmetry breaking of the ideal coil symmetry, while figure 9.4 provides a visualization of said modes up to $l = 2$.

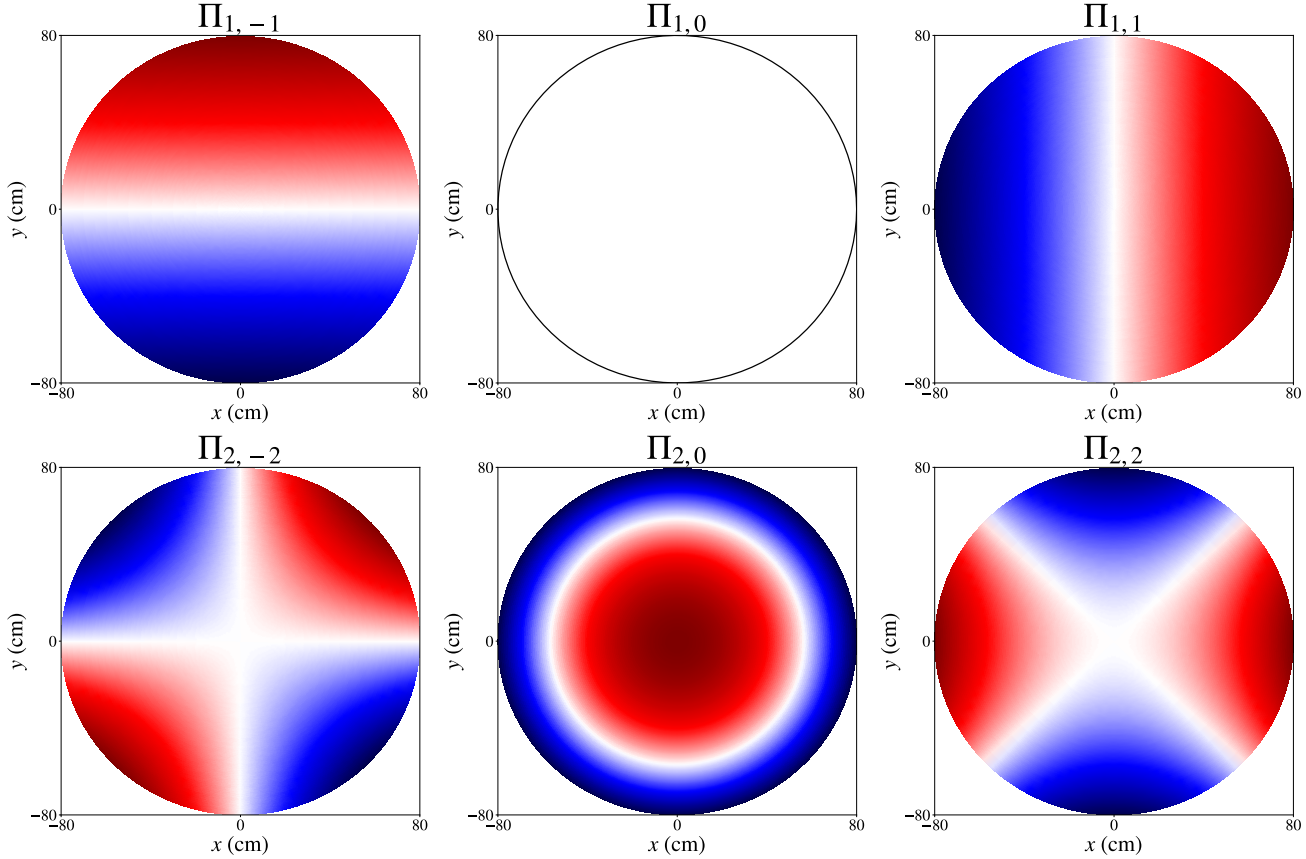

FIGURE 9.4: Horizontal cut at $z = 0$ of harmonic modes $\mathbf{\Pi}_{z,lm}$ allowed by breaking some reflection symmetry of the ideal coil geometry

Broken symmetries	**Subgroup of $\mathcal{D}_{4h}$**	**Allowed modes $\{\mathbf{\Pi}_{lm}\}$**
	$\mathcal{D}_{4h}$	$\{\mathbf{\Pi}_{2k,4n}\}$
R_z	$\mathcal{D}_{2h}$	$\{\mathbf{\Pi}_{2k,2n}\}$
R_z, σ_x	$\mathcal{C}_{2v}$	$\{\mathbf{\Pi}_{2k,2n}\} \cup \{\mathbf{\Pi}_{2k+1,1+2n}\}$
R_z, σ_y	$\mathcal{C}_{2v}$	$\{\mathbf{\Pi}_{2k,2n}\} \cup \{\mathbf{\Pi}_{2k+1,-1-2n}\}$
R_z, σ_z	$\mathcal{C}_{2v}$	$\{\mathbf{\Pi}_{2k,2n}\} \cup \{\mathbf{\Pi}_{2k+1,2n}\}$

TABLE 9.3: Harmonic modes allowed by several symmetry breaking of the ideal coil geometry and their corresponding symmetry groups, with $k, n \in \mathbb{N}$.

9.2 Matching the experimental requirements on the B_0 field

This section will follow the chronology of the two mapping campaigns on n2EDM and aim to show that the field generated by the B_0 coil alone, pictured in figure 9.5, satisfies the statistical and systematical requirements summarized in table 3.1.

9.2.1 Coil displacement and top-bottom gradient

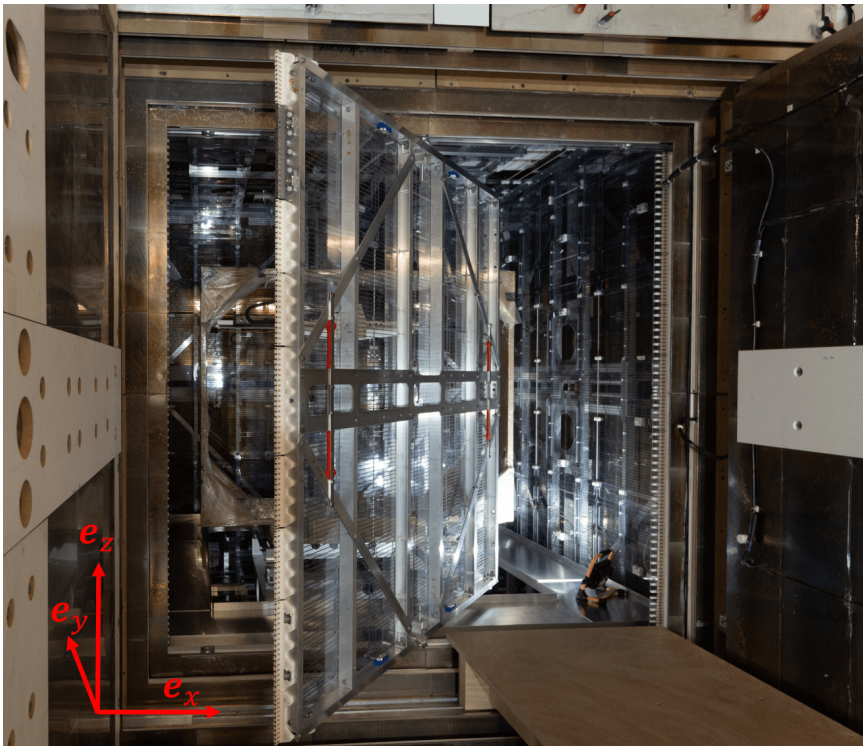

FIGURE 9.5: Opened B_0 coil inside the MSR during the first mapping campaign of n2EDM. The mapper is mounted inside the wooden case and can perform vertical scans along $\mathbf{e}_z$.

The first measurements of the B_0 field were obtained during the first mapping campaign, which because of mechanical limitations consisted solely of vertical scans along the central axis of the MSR, performed according to the measurement strategy detailed in section 7.1. Nevertheless this allowed the extraction of the vertical gradient G_{10}, which is constrained by our first statistical requirement: the top-bottom resonance matching condition (3.12).

The gradient values extracted from the vertical scans of both B_0 coil polarities, plotted on figure 9.6 as the rightmost red and blue points, were far above the 0.6 pT/cm limit. COMSOL simulations performed by Pierrick Flaux indicated that a vertical displacement of the coil with respect to the MSR origin would generate a vertical gradient proportional to the displacement δz, with $G_{10}/\delta z = 6.45\,(\mathrm{pT/cm})/\mathrm{mm}$ (Flaux, 2019). This can be intuited by considering that a vertical coil displacement breaks the reflection symmetry w.r.t. the transverse plane σ_z, which allows a further set of modes that includes G_{10} (second to last line of table 9.3).

It was therefore decided to move the coil down, by first 1 mm, in order to test this claim. Data recorded after this displacement yielded the middle set of points shown in figure 9.6 and confirmed our prediction, as the slope of the linear fit (in purple) matched the one provided by the simulation. The coil was moved again by 2 mm in

order to reach the satisfactory values shown as the leftmost set of points in figure 9.6. A more thorough mapping of the coil in its final geometrical configuration, including estimates of reproducibility with respect to degaussing between scan sequences, led to the values given in the first line of table 9.5. We conclude that the B_0 coil satisfies without optimization the top-bottom resonance matching condition (3.12).

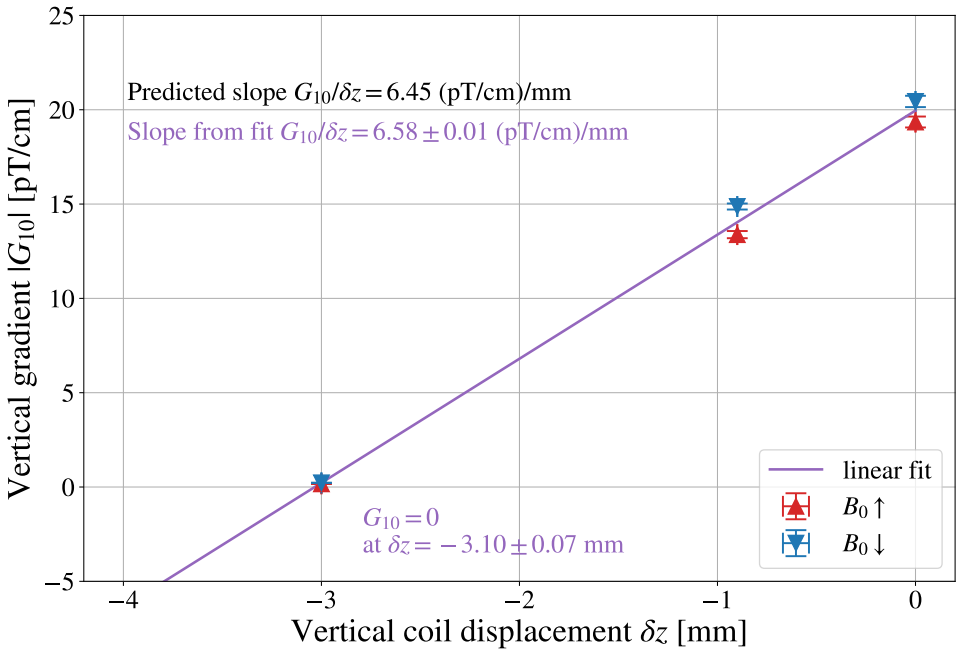

FIGURE 9.6: Linear vertical gradient as a function of the vertical displacement of the B_0 coil with respect to its initial position. The three measurements were performed from right to left during the first mapping campaign of n2EDM. The slope of the linear fit matches the simulated value from (Flaux, 2019).

9.2.2 A remarkable field uniformity

The remaining statistical requirement on the uniformity of the vertical field (3.13) could only be evaluated after mapping the entire cylindrical volume accessible by the mapper with the B_0 coil turned on. This occurred in the second mapping campaign of n2EDM, after the characterization of the residual field presented in chapter 8. The harmonic spectrum extracted from these maps is recorded in appendix D.

A depiction of the vertical component of the measured B_0 field in the $z = 0$ plane, for a positive coil parity, appears in the bottom-left plot of figure 9.7. The top plot of this figure shows the same quantity for the simulated data. The scale of these non-uniformities in a $\rho < 78$ cm disc is comparable: they are situated in a 300 pT range for the simulated field and in a 500 pT range for the measured field. Over the mapped cylindrical volume of radius 78 cm and height 82 cm, the measured values are in a 1600 pT range. Regarding the statistical requirements, our numerical estimate of the vertical non-uniformity of the measured field

$$\sigma(B_z) = 49\,\mathrm{pT} < 170\,\mathrm{pT} \tag{9.3}$$

comfortably satisfies condition (3.13).

We also note that the gradient extraction of the B_0 field map, plotted up to $l = 2$ in figure 9.8, is consistent with this estimate. As expected and simulated, the dominant

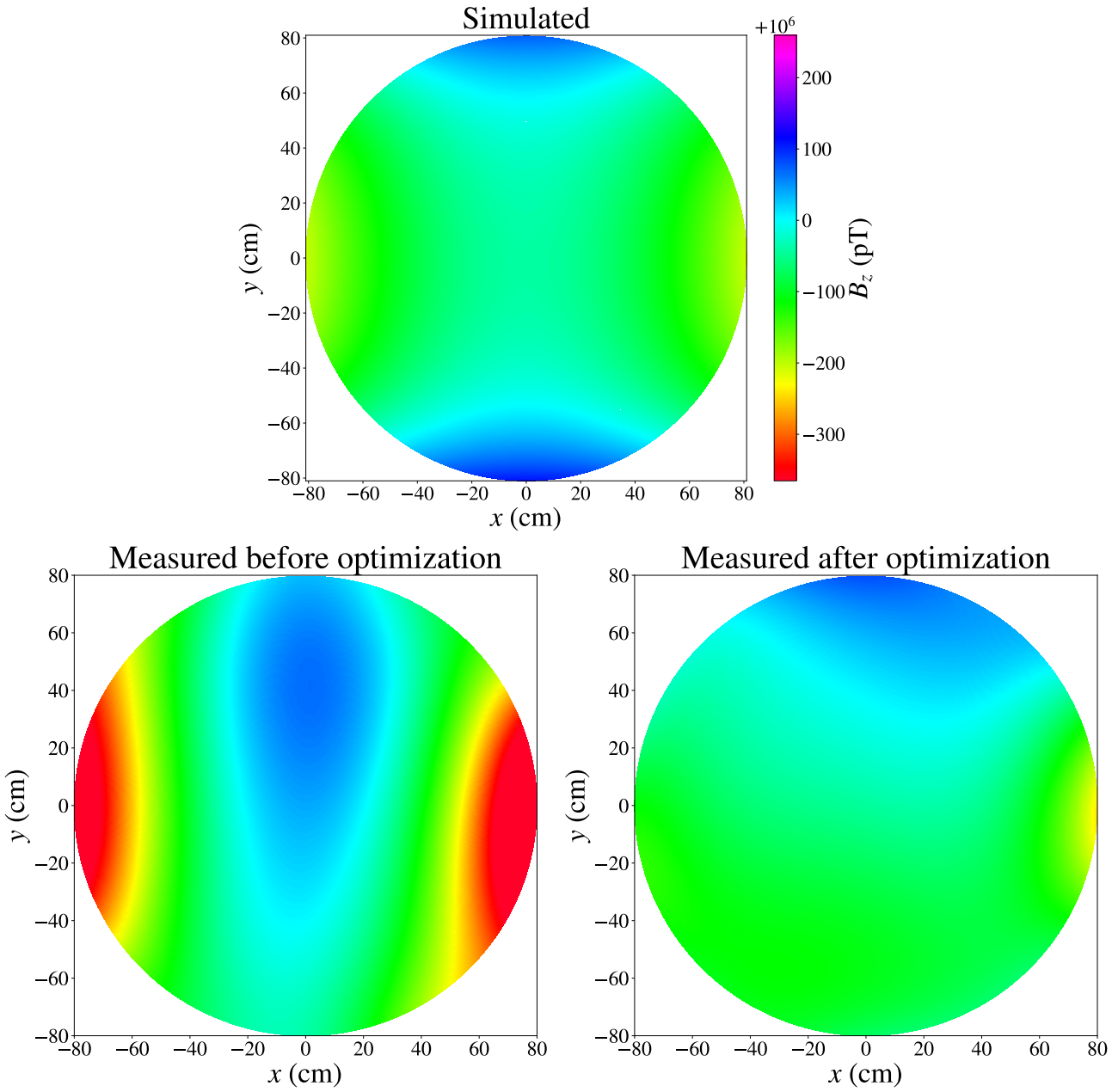

FIGURE 9.7: Horizontal cut at $z = 0$ of the vertical field projection of the B_0 field, in the positive coil polarity. The simulated values from (Flaux, 2019) are compared to the 2022 measurements before and after optimization with trim coils and gradient coils. The latter successfully cancels the main contributions of the $\mathbf{\Pi}_{20}$ and $\mathbf{\Pi}_{22}$ modes.

contributions to $\sigma(Bz)$ are $\mathbf{\Pi}_{20}$, who is allowed by the ideal coil symmetry $\mathcal{D}_{4h}$, and $\mathbf{\Pi}_{22}$, who is allowed by the less restrictive symmetry $\mathcal{D}_{2h}$ without the $\pi/2$ rotation around the z axis. The presence of the $\mathbf{\Pi}_{22}$ in particular confirms the presence of holes around the vacuum tubes and UCN guides in the coil wiring. Inserting the measured generalized gradients into the polynomial expansion (3.2), we obtain

$$\sigma(G_{20}\Pi_{z,20}) = 21\,\text{pT}, \qquad \sigma(G_{22}\Pi_{z,22}) = 28\,\text{pT}. \tag{9.4}$$

The orthogonality of the trigonometric functions of $m\varphi$ (appendix equation (A.7))

enforces that modes of different m-index add up quadratically inside $\sigma(B_z)$. This is detailed more thoroughly in appendix C.3. Both modes then participate to 35 pT of the total non-uniformity, which is consistent with our numerical estimate (9.3).

The dominance of the $\mathbf{\Pi}_{20}$ and $\mathbf{\Pi}_{22}$ modes in the measured harmonic spectrum is a significant and expected feature of the B_0 field. Let us evaluate their weight in the transverse plane plots of figure 9.7. Considering only these two modes in the polynomial expansion 3.2, we write the vertical field component as $B_z = -(G_{20}/2 - G_{22})x^2 - (G_{20}/2 + G_{22})y^2$. For the measured field, the harmonic spectrum of figure 9.8 gives $G_{20} > -2G_{22} > 0$. This leads to a negative parabola along the y axis and to a sharper negative parabola along the x axis. In the case of the simulated field, we have $2G_{22} < G_{20} < -2G_{22}$, so the vertical field projection follows a negative parabola along the x axis but a positive parabola along the y axis. These features are confirmed in the two first plots of figure 9.7, which can be thought of as two different linear combinations of $\mathbf{\Pi}_{20}$ and $\mathbf{\Pi}_{22}$, drawn in the $z = 0$ plane in figure 9.4.

As for the y-odd structure that appears only in the measured fields, this can be attributed to the presence of l-odd harmonic modes, especially of $\mathbf{\Pi}_{1,-1}$ (also plotted in figure 9.4). The vertical field consisting only of this mode writes $B_z = G_{1,-1}y$. The measured $G_{1,-1} > 0$ explains the shift of the parabolic curve on the y axis. This presence of the $\mathbf{\Pi}_{1,-1}$ mode indicates a breaking of the reflection symmetry w.r.t. the $y = 0$ plane, which can be attributed to the presence of the MSR door in this same plane and is described by the $\mathcal{C}_{2v}$ symmetry. Figure 9.8 shows that this feature had been taken into account in the simulation, but that its measured magnitude is much larger than expected.

We conclude that the field generated by the B_0 coil is consistent with a non-ideal coil symmetry where the presence of the neutron guides, vacuum tubes, and MSR door has been taken into account. More importantly, its vertical component comfortably satisfies the n2EDM requirements on field uniformity.

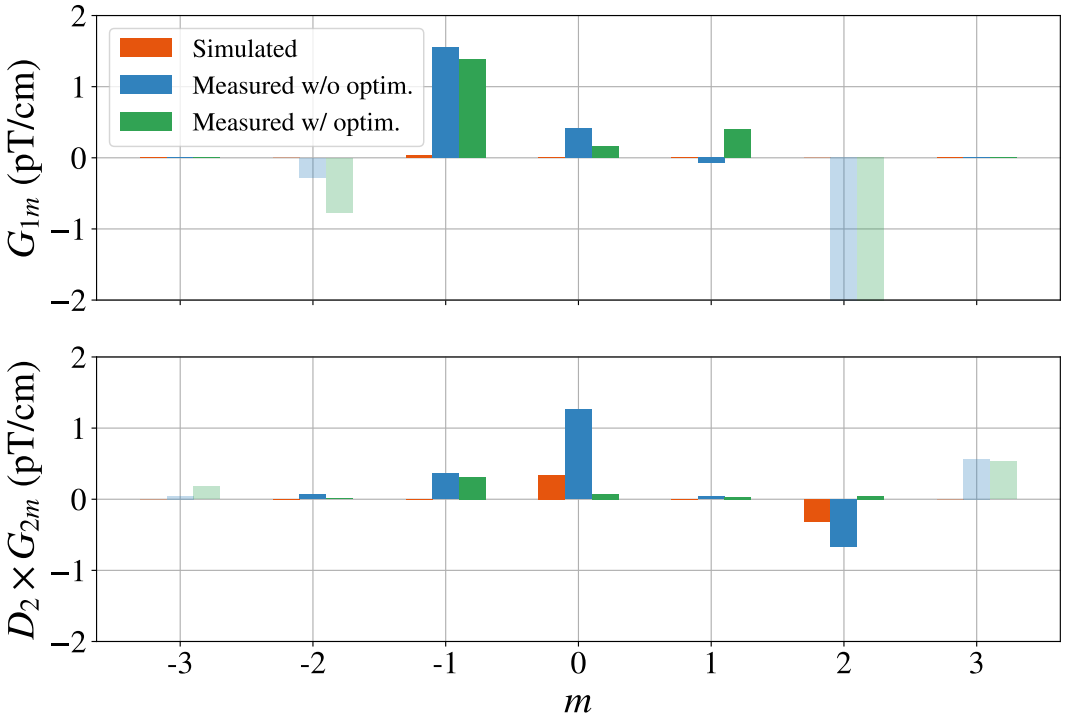

FIGURE 9.8: Harmonic spectra of the B_0 coil in the positive polarity, simulated in (Flaux, 2019), and measured during the second mapping campaign, before and after optimization with trim coils and gradient coils. The transparent bars refer to purely transverse harmonic modes.

9.2.3 A reproducible estimate of the false EDM

We finally turn to the systematical requirements and evaluate the reproducibility of the false EDM generated by the B_0 coil.

The harmonic spectra of the B_0 field extracted during the second mapping campaign allow us to determine the reproducibility of the problematic phantom modes of orders three, five and seven. We first check that variations on the values of these modes are indeed dominated by the non-reproducibility of the field rather than our lack of mapping precision reflected by the repeatability. For the least consistent phantom mode $\acute{G}_3$ we recorded a repeatability of 7.4 fT/cm, which is about a third of its reproducibility of 22.2 fT/cm (results in appendix D). One may also notice that these reproducibility values are practically identical to those measured *without* the B_0 coil, shown in table 8.1 of the previous chapter, which means that the vacuum vessel pattern is the main contributor to the non-reproducibility of the phantom modes. We then verify that the reproducibility of the false EDM generated by each phantom mode is small enough to allow an estimate of the false EDM below $3 \times 10^{-28}\, e\,$cm. This is confirmed by figure 9.9, which shows the false EDMs generated by the three phantom modes for both polarities of the B_0 coil, and their reproducibility as errorbars. The blue values for the measured field without optimization indeed match the reproducibility condition but the generated false EDM is still above the requirement. n2EDM can still function in this coil configuration simply by measuring the false EDM.

We conclude that the total n2EDM magnetic field matches the requirements on

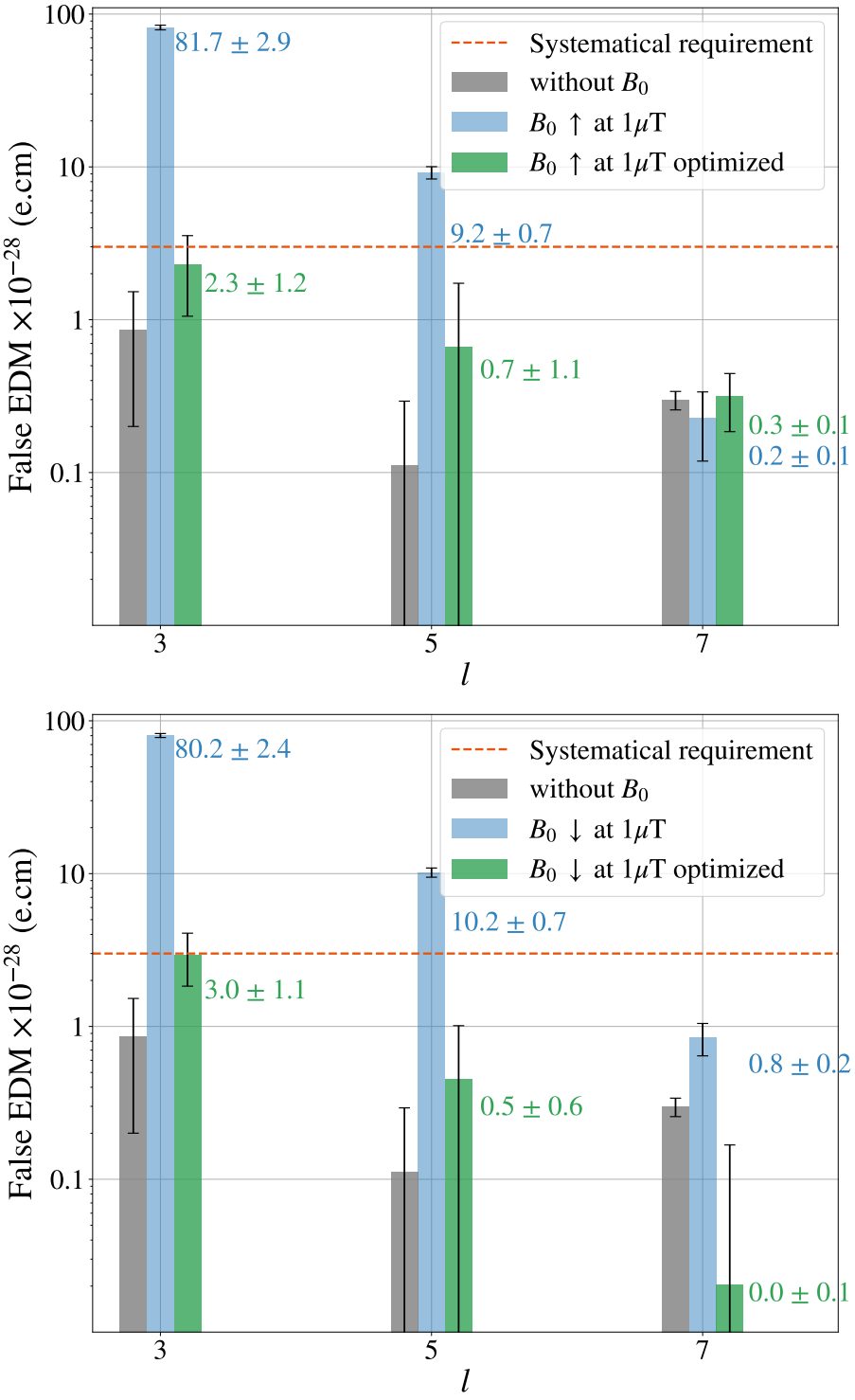

FIGURE 9.9: False EDM generated by phantom modes of orders three, five, and seven, in three different field configurations: residual field (B_0 coil is turned off), B_0 coil turned on in on of two polarities, and B_0 coil turned on along with a combination of trim coils and gradient coils meant to reduce the total non-uniformity. The optimized field satisfies the statistical requirement (red dotted line). The error bars are determined by the magnetic field's reproducibility.

field uniformity w.r.t. both statistical errors and systematical errors. In particular, offline measurements show that problematic phantom modes are reproducible enough to either (1) allow for an estimate of the generated false EDM through the low-frequency expression (3.16), or (2) cancel these modes so as to bring the systematic effect below the sensitivity requirement $d^{\text{false}}_{n\to\text{Hg}} < 3\times10^{-28}\,e\,\text{cm}$. We will now show how the second option, referred to as field optimization, is made possible through specific combinations of the trim coils and gradient coils of the n2EDM coil system.

9.3 Field optimization for an even greater uniformity

The second mapping campaign concluded with a last effort to not only make the false EDM measurable but to also strongly suppress it, *via* the use of coils dedicated to the generation of specific modes of the harmonic spectrum. The optimization strategy is in essence straightforward. Prior individual mapping of the 56 trim coils and 7 gradient coils, visible in figure 2.9, determined their respective coil coefficients. These correspond to the ratio between the current driven through the coil and the amplitude G_{lm} of the generated harmonic modes, for all modes of the spectrum. One may then use this information to determine the coil currents that cancel particularly problematic modes of the measured harmonic spectrum.

While the gradient coils can only perform one task, which is to produce one specific mode G_{0-1}, G_{01}, G_{1-1}, G_{10}, G_{11}, G_{20}, or G_{30}, the trim coils are only operable in conjunction with one another within a very large number of combinations. Our previous considerations on the symmetries of the B_0 coil considerably ease this choice of combinations, as one can simply match the symmetries of a targeted harmonic mode with the geometry of the trim coil array. Figure 9.10 shows a flattened representation of the cubic coil array, where each colored box represents a single square coil with a current running around its edges. The color code is chosen so that coils of a same color are *invariant* with respect to all symmetries of the ideal coil system, meaning that applying any transformation of $\mathcal{D}_{4h}$ to a trim coil of a color yields a trim coil of the same color (appendix definition B.1.8). There are 6 distinct invariant sets of coils under the ideal coil symmetry, and 1 non-invariant set of coils. Among the 6 invariant sets, 1 is unused because their coil constants were not completely determined (in grey).

By applying a current in either the clockwise or counter-clockwise direction around each of the trim coils, each of these invariant sets can be made to form a set of currents that matches the character of a harmonic mode irrep from table 3.3. Here we skip the group-theoretical determination of the current sets as they can be intuited from figure 9.10. Table 9.4 shows the character of all signed current combinations of coils within an invariant colored set and their matching harmonic irrep. The harmonic modes affected by that irrep can then be generated by a set of coils that exhibit the same symmetries with a particular current configuration. We notice that some modes are easier to generate than other. For instance the light green modes of figure 3.3 such as $\mathbf{\Pi}_{0,2}$ can only be generated by a trim coil set capable of producing currents with the same character as $\rho_{0,2}$, which means these currents must be anti-symmetric with respect to σ_x and R_z and symmetric with respect to σ_z. From 9.10 we see that only the orange coils are capable of generating that particular set of gradients.

After the current signs have been decided in order to produce a specific harmonic mode, we determine the amplitude that cancels the measured gradient. This is done

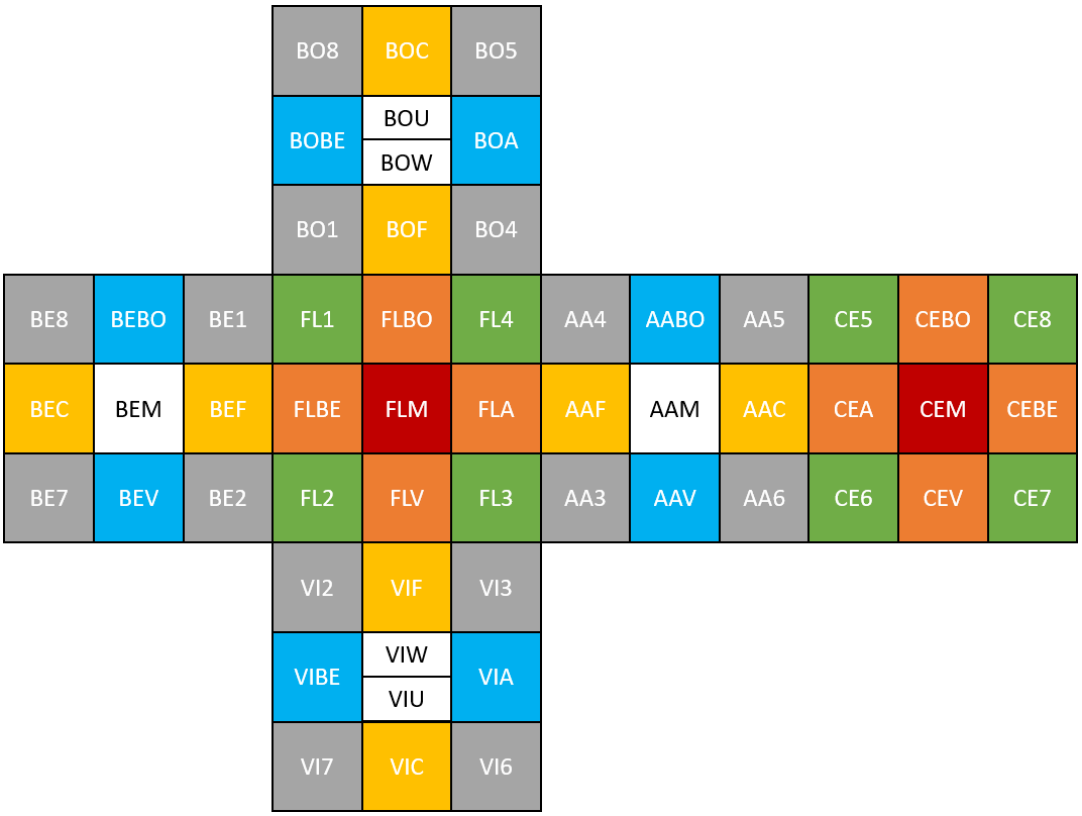

FIGURE 9.10: Flattened representation of the trim coil array. Each color corresponds to an invariant set of coils under the ideal coil symmetries. Only the white coils are not invariant. Around each colored coil, a current flows in either the clockwise or counter-clockwise direction. Note that the grey coils have not been entirely mapped and are therefore not used in the analysis.

by inverting a linear application consisting of coil constants, that maps a set of currents to a set of harmonic gradients. We denote this currents-to-gradients transition matrix T_G and its inverse T_I. The components of a vector $\mathbf{G}$ consisting of harmonic gradients we wish to cancel are then written in terms of those of the current vector $\mathbf{I}$ driven through the trim coils as

$$G_{ik} = [T_G]_{ij} I_{jk}. \tag{9.5}$$

Inverting T_G then yields the currents that cancels the given gradients through

$$I_{ik} = [T_G^{-1}]_{ij} G_{jk} = [T_I]_{ij} G_{jk}. \tag{9.6}$$

Let us apply this cancellation strategy to the "red" magnetic modes ($G_{10}, G_{30}, G_{34}, \ldots$) of the ideal coil symmetry, represented in figure 3.3. For the symmetry reasons given in table 9.4, these modes can be generated by all 5 invariant sets of coils. We can then choose 5 gradients to cancel simultaneously. The currents-to-gradients map is then

a 5×5 matrix of the form

$$T_{G_{10}} = \begin{pmatrix} G_{10}/I_{\text{red}} & G_{10}/I_{\text{gre}} & G_{10}/I_{\text{ora}} & G_{10}/I_{\text{yel}} & G_{10}/I_{\text{blu}} \\ G_{30}/I_{\text{red}} & G_{30}/I_{\text{gre}} & G_{30}/I_{\text{ora}} & G_{30}/I_{\text{yel}} & G_{30}/I_{\text{blu}} \\ G_{34}/I_{\text{red}} & G_{34}/I_{\text{gre}} & G_{34}/I_{\text{ora}} & G_{34}/I_{\text{yel}} & G_{34}/I_{\text{blu}} \\ G_{50}/I_{\text{red}} & G_{50}/I_{\text{gre}} & G_{50}/I_{\text{ora}} & G_{50}/I_{\text{yel}} & G_{50}/I_{\text{blu}} \\ G_{54}/I_{\text{red}} & G_{54}/I_{\text{gre}} & G_{54}/I_{\text{ora}} & G_{54}/I_{\text{yel}} & G_{54}/I_{\text{blu}} \end{pmatrix}, \tag{9.7}$$

with entries given by the appropriate coil constants. The gradient-to-currents matrix $T_{I_{10}} = T_{G_{10}}^{-1}$ finally provides in each row the currents we should drive through the 5 invariant coil sets in order to produce a given red mode $G_{2k+1,4n}$. With the appropriate linear combination of trim coil currents we are then able to cancel several problematic gradients.

The optimization strategy of n2EDM is to use the gradient coils to cancel G_{20} and part of G_{30}, for which we also need the trim coils because of current limitations of the gradient coil, and trim coils to cancel modes G_{22}, G_{50}, and the rest of G_{30}. Our intent is to cancel both phantom modes and dominant modes of the B_0 spectrum allowed by the realistic coil symmetry. Measurements of the optimized B_0 field are featured in figures 9.7, 9.8, and 9.9. The exact coil current values that cancel these modes are given in appendix D.2. The major accomplishment of the B_0 optimization is shown in figure 9.9: we see that the phantom modes of the optimized field all generate a false EDM below the systematical requirement materialized by the dotted red line, for both coil polarities. In addition, the suppression of the $\mathbf{\Pi}_{20}$ and $\mathbf{\Pi}_{22}$ modes, as

Trim coil irrep	$Cl(\sigma_x)$	$Cl(\sigma_z)$	$Cl(R_z)$	Harmonic irrep	$\mathbf{\Pi}_{lm}$
Red coils	-1	1	1	ρ_{00}	$\mathbf{\Pi}_{2k,0+2n}$
	-1	-1	1	ρ_{10}	$\mathbf{\Pi}_{2k+1,0+4n}$
Green coils	-1	1	1	ρ_{00}	$\mathbf{\Pi}_{2k,0+4n}$
	-1	-1	1	ρ_{10}	$\mathbf{\Pi}_{2k+1,0+4n}$
	1	-1	-1	$\rho_{1,-2}$	$\mathbf{\Pi}_{2k+1,-2-4n}$
	1	1	-1	$\rho_{0,-2}$	$\mathbf{\Pi}_{2k,-2-4n}$
Orange coils	-1	1	1	ρ_{00}	$\mathbf{\Pi}_{2k,0+4n}$
	-1	-1	1	ρ_{10}	$\mathbf{\Pi}_{2k+1,0+4n}$
	-1	-1	-1	ρ_{12}	$\mathbf{\Pi}_{2k+1,2+4n}$
	-1	1	-1	ρ_{02}	$\mathbf{\Pi}_{2k,2+4n}$
Yellow coils	1	-1	1	$\rho_{1,-4}$	$\mathbf{\Pi}_{2k+1,-4-4n}$
	-1	-1	1	ρ_{10}	$\mathbf{\Pi}_{2k+1,0+4n}$
	-1	-1	-1	ρ_{12}	$\mathbf{\Pi}_{2k+1,2+4n}$
Blue coils	1	-1	1	$\rho_{1,-4}$	$\mathbf{\Pi}_{2k+1,-4-4n}$
	-1	-1	1	ρ_{10}	$\mathbf{\Pi}_{2k+1,0+4n}$
	1	-1	-1	$\rho_{1,-2}$	$\mathbf{\Pi}_{2k+1,-2-4n}$

TABLE 9.4: Character table of the 3 group generators of the $\mathcal{D}_{4h}$ group for the trim coil irreps. Each color corresponds to a set of coils invariant under the symmetries of $\mathcal{D}_{4h}$. Each line corresponds to the character of a trim coil irrep for a possible combination of current signs (the exact signs are omitted). These are matched with harmonic irreps.

shown by the harmonic spectrum plot 9.8, reduces the vertical non-uniformity to

$$\sigma(B_z) = 35\,\mathrm{pT}, \tag{9.8}$$

nearly one order of magnitude below the statistical requirement. The last plot of figure 9.7, depicting the vertical field component of the optimized field, confirms that it is indeed the suppression of the parabolic modes $\mathbf{\Pi}_{20}$ and $\mathbf{\Pi}_{22}$ that lowers the non-uniformity.

In conclusion, we are not only able to match the reproducibility requirements for the control of the false EDM, but also to largely suppress it. Furthermore, the optimized B_0 vertical field is nearly one order of magnitude more uniform than the design requirement. All experimental requirements discussed in this section and confronted with the B_0 field data are summarized in table 9.5.

	Required	$B_0 \uparrow$ **alone**	$B_0 \uparrow$ **optim.**	$B_0 \downarrow$ **alone**	$B_0 \downarrow$ **optim.**
Statistical requirements					
Vertical uniformity $\sigma(B_z)$ (pT)	< 170	49.1 ± 1.5	34.7 ± 1.5	42.4 ± 1.1	25.5 ± 1.5
Top-bottom condition $\lvert G_{10}\rvert$ (pT/cm)	< 0.6	0.35 ± 0.25	0.16 ± 0.21	-0.21 ± 0.31	-0.14 ± 0.22
Systematical requirements					
$d^{\mathrm{false}}_{\mathrm{n}\leftarrow\mathrm{Hg}}(\acute{G}_3\acute{I}_3)$ ($10^{-28}\,e\,$cm)	< 3	81.7 ± 2.9	2.3 ± 1.2	80.2 ± 2.4	3.0 ± 1.1
$d^{\mathrm{false}}_{\mathrm{n}\leftarrow\mathrm{Hg}}(\acute{G}_5\acute{I}_5)$ ($10^{-28}\,e\,$cm)	< 3	9.2 ± 0.7	0.7 ± 1.1	10.2 ± 0.7	0.5 ± 0.6
$d^{\mathrm{false}}_{\mathrm{n}\leftarrow\mathrm{Hg}}(\acute{G}_7\acute{I}_7)$ ($10^{-28}\,e\,$cm)	< 3	0.3 ± 0.1	0.2 ± 0.1	0.3 ± 0.1	0.0 ± 0.1

TABLE 9.5: Table of the n2EDM requirements on magnetic field generation for statistical and systematical errors, and their measured values with associated reproducibility. Both the field produced by the B_0 coil alone, and the optimized field produced by the B_0 coil and a well-chosen combination of trim coils and gradient coils, are presented. The systematical requirements concern both the measured false EDM values and their reproducibility.

9.4 Conclusion

The magnetic environment of n2EDM is now fully characterized. In this chapter, we approached the coil-generated field by first revisiting chapter 3's discussion on the symmetries of the B_0 coil, in order to predict the presence of specific modes in the measured harmonic spectrum of the coil. Two realistic geometries of the B_0 coil were considered. In both cases, a breaking of the ideal coil symmetry group occurs such that the realistic coil satisfies a less restrictive symmetry which allows more harmonic modes in its spectrum. First, we consider the presence of holes inside the coil walls meant for the vacuum tubes and UCN guides. We confront this particular coil symmetry group with its representations on all harmonic modes, to show that a larger set of modes $\{\mathbf{\Pi}_{2k,2n}\}_{k,n\in\mathbb{N}}$ is now allowed in the coil's spectrum. Second, we study the impact of the coil's door in the $y = 0$ plane, and similarly show that an even larger set of modes $\{\mathbf{\Pi}_{2k,2n}\}_{k,n\in\mathbb{N}} \cup \{\mathbf{\Pi}_{2k+1,-1-2n}\}_{k,n\in\mathbb{N}}$ is allowed by this smaller symmetry group.

With these tools in hand we turn to the B_0 field data provided by the two mapping campaigns of n2EDM. During the first campaign we noticed a strong vertical gradient caused by a breaking of the reflection symmetry w.r.t. the transverse plane. This was resolved by adjusting the height of the coil according to the results of prior simulations. We concluded that the displaced coil satisfies the top-bottom resonance matching condition (3.12) on the vertical gradient. The second mapping campaign consisting of high-resolution maps allowed the extraction of the complete B_0 field spectrum. We confirmed that the generated field comfortably satisfies the uniformity requirement, and that its harmonic spectrum is dominated by $\mathbf{\Pi}_{20}$ and $\mathbf{\Pi}_{22}$ modes, which are indicative of the expected coil geometry. We finally determined the false EDM generated by each phantom mode of the B_0 field spectrum along with their typical reproducibility. We concluded that, while the magnetic field generated by the B_0 coil alone produces a non-negligible false EDM, the field is reproducible enough for us to measure the systematic effect below our requirement (2.11).

In the final section of this chapter we implemented an optimization strategy meant to cancel the false EDM with the use of gradient and trim coils, a task that is made possible by the good reproducibility of the magnetic field. To this end we invoked once again the ideal symmetry group of the coil system, which also applies to the trim coil array. We showed that there existed 5 invariant sets of trim coils that can be tuned independently in order to cancel harmonic modes affected by matching symmetries. Taking advantage of the trim coil sets and the dedicated gradient coils, we were able to cancel both the problematic $\acute{\mathbf{\Pi}}_3$ and $\acute{\mathbf{\Pi}}_5$ phantom modes as well as the dominant $\mathbf{\Pi}_{20}$ and $\mathbf{\Pi}_{22}$ modes. The resulting optimized field produces a false EDM below our statistical requirement, in addition to achieving an unprecedented uniformity with an RMSE of 35 pT over the precession chamber volume.

Conclusion

The search for the neutron EDM is a formidable endeavour for particle physicists in that it possesses incredible theoretical reach and, to that end, causes tantalizing and often unexpected experimental challenges. The theoretical motivation was laid out succinctly in chapter 1. After noticing that the dynamics of fermion EDMs violated time-reversal symmetry, we saw that the need for CP-violating interactions was of cosmological origin and formed one of Sakharov's conditions for baryogenesis. We went on to recall that the Standard Model did not contain enough of these and described the neutron EDM as a BSM CP-violating coupling which probes new physics at the 10^6 TeV scale. The stage was then set for n2EDM (chapter 2), the ultimate successor to half a century of experimental endeavours which aims to measure the neutron EDM d_n with a sensitivity of $10^{-27}\,e\,\text{cm}$. This upgraded version of nEDM combines many technological advances, such as the use of Ultra-Cold neutrons in a large volume for high statistical sensitivity, world-leading magnetic shielding, and mercury co-magnetometry in order to compensate time-fluctuations of the applied magnetic field. However, the latter is not without significant systematical drawbacks. This naturally led us to the theme of magnetic field uniformity in chapter 3, where we presented the requirements that keep under control the unwanted systematic effect brought by the Hg co-magnetometer as well as maximize the experiment's statistical sensitivity. We concluded this introductory part with a novel group-theoretical investigation that allows us determine modes of the harmonic spectrum that preserve the symmetries of the B_0 coil.

The common thread of the second and third parts of this thesis is the control of the false neutron EDM induced by the mercury atoms $d^{\text{false}}_{n\leftarrow\text{Hg}}$. We introduced the latter in chapter 4 as a systematical error on d_n generated by the combined motion of mercury atoms inside an electric field and the presence of a non-uniform magnetic field. As a function of the precession frequency of mercury atoms, the false EDM possesses a known analytical form for high and low frequencies (or fields), but only numerical estimates for arbitrary frequencies that rely on the calculation of a field-position correlation function. Alternatively, we proposed a new frequency-domain expression of the false EDM as the Hilbert transform of the field-position power spectral density. We then tested the validity of the low-frequency false EDM expression, which depends on the problematic phantom modes, and showed that considering slightly rotated or displaced precession chambers brought only a negligible correction to this quantity (chapter 5). We finally tackled in chapter 6 the recent magic field strategy, which consists in setting the B_0 field to a value that completely cancels the systematic effect. We showed from a direct numerical calculation of the false EDM in the frequency domain that the obtained magic field value for first-order gradients was compatible with its time-domain equivalent, without the bias of the correlation function fit. We then expanded on the n2EDM magic field strategy that targets phantom modes and addressed higher-order magnetic configurations by calculating the field-position correlation function of a dipole field. We concluded that at $B_0 = 10.6\,\mu\text{T}$, the false EDM generated by $l = 3, 5, 7$ harmonic modes was suppressed by more than 95% and the dipole-generated false EDM by around 90%.

We finally turned to magnetic field mapping for estimates of the false EDM in the low-frequency regime. In chapter 7 we introduced the mapping apparatus and measurement strategy, tailored for the extraction of phantom modes and their reproducibility. We also showed that the inherent mechanical defects of the mapper and fluxgate, whose axes are not perfectly orthogonal, do not significantly hinder the mapper's accuracy on the extraction of the phantom modes. The n2EDM magnetic field was then approached in two steps. First, we measured the residual field (chapter 8) and observed an unexpected fluctuating pattern which we showed to be attributable to a thermo-electric Seebeck effect affecting the walls of the vacuum vessel. We ultimately demonstrated that the controlled "vacuum vessel pattern" did not significantly decrease the reproducibility of the phantom modes of order 3, 5, and 7 extracted by the mapper nor the accuracy of the cesium magnetometers on the extraction of the third-order phantom mode. Second, we measured the field generated by the B_0 coil superimposed to the residual field (chapter 9). We invoked again the symmetries of the coil and matched the presence of specific harmonic modes to symmetry-breaking features in the coil's design. These features were confirmed in the measured harmonic spectrum but did not spoil the vertical uniformity of the generated field. Furthermore, the generated phantom modes were showed to be reproducible enough to allow for a successful optimization involving a dedicated set of auxiliary coils. The optimized field, achieved by targeting both phantom modes and symmetrically-allowed modes with the so-called trim and gradient coils, boasts impressive uniformity and generates negligible phantom gradients.

This final result allows the following *offline* estimate of the total false EDM in the low-frequency regime, which condenses both phantom modes and dipole-like contributions:

$$\begin{aligned} d^{\text{false}}_{n\leftarrow\text{Hg}}(1\,\mu\text{T}) &= \frac{\hbar\left|\gamma_n\gamma_{\text{Hg}}\right|R^2}{8c^2}\left[\acute{G}_3+\acute{G}_5+\acute{G}_7+\frac{\left\langle\rho B^{\text{dip}}_\rho\right\rangle}{-R^2/4}\right] \\ &= [(2.3\pm1.2)+(0.7\pm1.1)+(0.2\pm0.1)+1]\times10^{-28}\,e\,\text{cm}. \end{aligned} \tag{9.9}$$

In the expression above, $\mathbf{B}^{\text{dip}}$ corresponds to the field induced by a vertical dipole of strength $m = 1.6\times10^5\,\text{nA}\,\text{cm}^2$ located on a ground electrode. This particular dipole generates a field at the center of the precession chamber of the same amplitude as the average 15 pT harmonic fit residual inside the precession volume, and describes a worse-case scenario where the fluxgate noise completely masks a problematic field. The four false EDM contributions quadratically add up to approximately $3\times10^{-28}\,e\,\text{cm}$. This already allows n2EDM to reach its $10^{-27}\,e\,\text{cm}$ sensitivity goal. Let us now consider the false EDM generated at the ten-times stronger magic field. Extrapolating the phantom gradients values from the 1 µT maps and considering a 90% suppression of the dipole field, we obtain

$$d^{\text{false}}_{n\leftarrow\text{Hg}}(10.6\,\mu\text{T}) = [(0.8\pm0.4)+0+(0.06\pm0.03)+0.1]\times10^{-28}\,e\,\text{cm}. \tag{9.10}$$

In the magic field scenario, the four false EDM contributions add up to only $0.8\times10^{-28}\,e\,\text{cm}$. Even more impressive is the fact that the clearly dominant contribution is the third order phantom mode, measurable online by the cesium magnetometers. After online correction, we predict a false EDM at magic field of the order of $1\times10^{-29}\,e\,\text{cm}$, two orders of magnitude below the n2EDM target sensitivity.

We close our discussion with the far more tangible view of the n2EDM magnetic environment proposed by figure 9.11. Over an equivalent precession volume, the

magnetic field in n2EDM is two orders of magnitude more uniform than it was in nEDM. Thanks to the foresight and coordinated efforts of its collaboration members, the n2EDM experiment is magnetically prepared to reach its desired sensitivity.

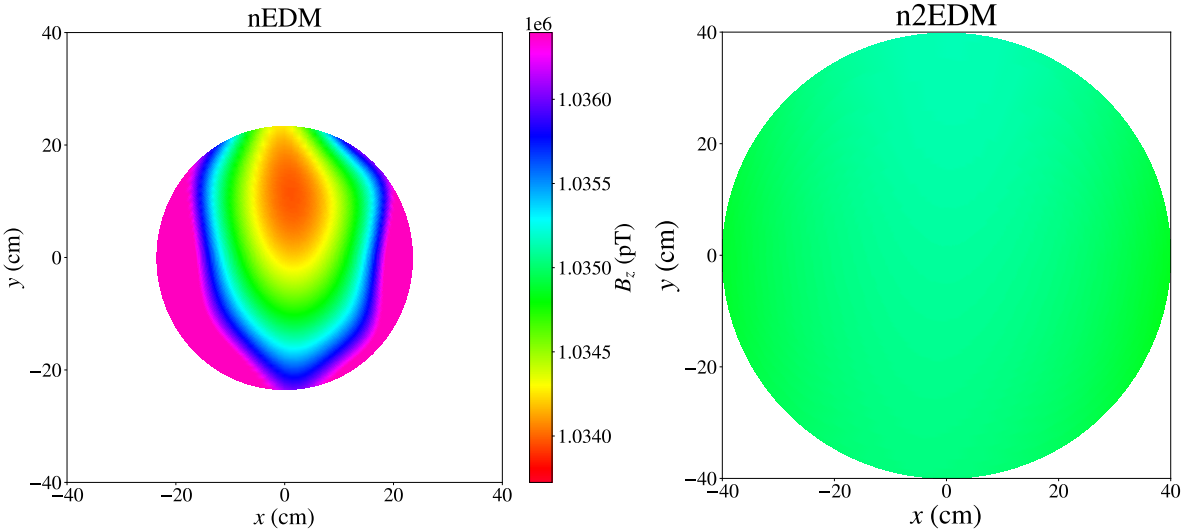

FIGURE 9.11: Vertical component of the n2EDM magnetic field in the positive coil polarity, over the precession volume of nEDM (left) and n2EDM (right).

Appendix A

Modes of the harmonic expansion

Here we provide explicit expressions for modes of the harmonic field expansion defined in section 3.1. These are given in Cartesian coordinates by

$$\Pi_{x,l,m} = \partial_x V_{l+1,m}, \qquad \Pi_{y,l,m} = \partial_y V_{l+1,m}, \qquad \Pi_{z,l,m} = \partial_z V_{l+1,m}, \tag{A.1}$$

where V is the magnetic potential defined by $\mathbf{B} = \boldsymbol{\nabla} V$, with elements V_{lm} of the spherical harmonic basis given by

$$V_{lm}(\rho,\theta,\varphi) = \frac{(l-1)!(-2)^{|m|}}{(l+|m|)!}\rho^l P_l^{|m|}(\cos(\theta)) \times \begin{cases} \cos(|m|\varphi) & \text{if } m \geq 0 \\ \sin(|m|\varphi) & \text{if } m < 0. \end{cases} \tag{A.2}$$

The Legendre polynomials P_l^m are given explicitly in table A.1 up to order $l = 6$. Table A.2 gives the explicit harmonic modes $\mathbf{\Pi}_{l,m}$ in Cartesian coordinates up to order $l = 7$, with $-l-1 \leq m \leq l+1$.

The harmonic functions in cylindrical coordinates (ρ, φ, z) are found by letting

$$\Pi_{\rho,l,m} = \cos\varphi \Pi_{x,l,m} + \sin\varphi \Pi_{y,l,m}, \quad \Pi_{\varphi,l,m} = -\sin\varphi \Pi_{x,l,m} + \cos\varphi \Pi_{y,l,m}. \tag{A.3}$$

For the purpose of field mapping it is often useful to separate the angular and polynomial parts of harmonic functions. This is done by defining **reduced harmonic functions** $\tilde{\Pi}_{z,lm}(\rho,z)$, which satisfy

$$\Pi_{\rho,lm}(\rho,\varphi,z) = \begin{cases} \tilde{\Pi}_{\rho,lm}(\rho,z)\cos(m\varphi), & \text{if } m \geq 0, \\ \tilde{\Pi}_{\rho,lm}(\rho,z)\sin(m\varphi), & \text{if } m < 0, \end{cases} \tag{A.4}$$

$$\Pi_{\varphi,lm}(\rho,\varphi,z) = \begin{cases} \tilde{\Pi}_{\varphi,lm}(\rho,z)\sin(m\varphi), & \text{if } m \geq 0, \\ \tilde{\Pi}_{\varphi,lm}(\rho,z)\cos(m\varphi), & \text{if } m < 0, \end{cases} \tag{A.5}$$

$$\Pi_{z,lm}(\rho,\varphi,z) = \begin{cases} \tilde{\Pi}_{z,lm}(\rho,z)\cos(m\varphi), & \text{if } m \geq 0, \\ \tilde{\Pi}_{z,lm}(\rho,z)\sin(m\varphi), & \text{if } m < 0. \end{cases} \tag{A.6}$$

In particular, note that the angular modes of the harmonic basis are orthogonal:

$$\langle \mathbf{\Pi}_{lm}(\rho,\varphi,z)\mathbf{\Pi}_{kn}(\rho,\varphi,z)\rangle = \delta_{mn}\left\langle \tilde{\mathbf{\Pi}}_{lm}(\rho,z)\tilde{\mathbf{\Pi}}_{kn}(\rho,z)\right\rangle. \tag{A.7}$$

The harmonic functions in cylindrical coordinates are provided by tables A.3 and A.4 up to order $l = 7$, which is the maximum order of the offline magnetic field fit.

TABLE A.1: Associated Legendre polynomials up to order $l = 6$.

l	m	$P_m^l(\cos\theta)$
1	0	$\cos\theta$
1	1	$-\sin\theta$
2	0	$\frac{1}{2}\left(3\cos^2\theta - 1\right)$
2	1	$-3\cos\theta\sin\theta$
2	2	$3\sin^2\theta$
3	0	$\frac{1}{2}\cos\theta\left(5\cos^2\theta - 3\right)$
3	1	$-\frac{3}{2}\left(5\cos^2\theta - 1\right)\sin\theta$
3	2	$15\cos\theta\sin^2\theta$
3	3	$-15\sin^3\theta$
4	0	$\frac{1}{8}\left(35\cos^4\theta - 30\cos^2\theta + 3\right)$
4	1	$-\frac{5}{2}\cos\theta\left(7\cos^2\theta - 3\right)\sin\theta$
4	2	$\frac{15}{2}\left(7\cos^2\theta - 1\right)\sin^2\theta$
4	3	$-105\cos\theta\sin^3\theta$
4	4	$105\sin^4\theta$
5	0	$\frac{1}{8}\cos\theta\left(63\cos^4\theta - 70\cos^2\theta + 15\right)$
5	1	$-\frac{15}{8}\left(21\cos^4\theta - 14\cos^2\theta + 1\right)\sin\theta$
5	2	$\frac{105}{2}\cos\theta\left(3\cos^2\theta - 1\right)\sin^2\theta$
5	3	$-\frac{105}{2}\left(9\cos^2\theta - 1\right)\sin^3\theta$
5	4	$945\cos\theta\sin^4\theta$
5	5	$-945\sin^5\theta$
6	0	$\frac{1}{16}\cos\theta\left(231\cos^6\theta - 315\cos^4\theta + 105\cos^2\theta - 5\right)$
6	1	$-\frac{21}{8}\cos\theta\left(33\cos^4\theta - 30\cos^2\theta + 5\right)\sin\theta$
6	2	$\frac{105}{8}\left(33\cos^4\theta - 18\cos^2\theta + 1\right)\sin^2\theta$
6	3	$-\frac{315}{2}\cos\theta\left(11\cos^2\theta - 3\right)\sin^3\theta$
6	4	$\frac{945}{2}\left(11\cos^2\theta - 1\right)\sin^4\theta$
6	5	$-10395\cos\theta\sin^5\theta$
6	6	$10395\sin^6\theta$

TABLE A.2: The basis of harmonic polynomials in Cartesian coordinates up to degree $l = 3$.

l	m	Π_x	Π_y	Π_z
0	-1	0	1	0
0	0	0	0	1
0	1	1	0	0
1	-2	y	x	0
1	-1	0	z	y
1	0	$-\frac{1}{2}x$	$-\frac{1}{2}y$	z
1	1	z	0	x
1	2	x	$-y$	0

TABLE A.2: The basis of harmonic polynomials in Cartesian coordinates up to degree $l = 3$.

l	m	Π_x	Π_y	Π_z
2	-3	$2xy$	$x^2 - y^2$	0
2	-2	$2yz$	$2xz$	$2xy$
2	-1	$-\frac{1}{2}xy$	$-\frac{1}{4}\left(x^2 + 3y^2 - 4z^2\right)$	$2yz$
2	0	$-xz$	$-yz$	$z^2 - \frac{1}{2}(x^2 + y^2)$
2	1	$-\frac{1}{4}\left(3x^2 + y^2 - 4z^2\right)$	$-\frac{1}{2}xy$	$2xz$
2	2	$2xz$	$-2yz$	$x^2 - y^2$
2	3	$x^2 - y^2$	$-2xy$	0
3	-4	$3x^2y - y^3$	$x^3 - 3xy^2$	0
3	-3	$6xyz$	$3(x^2z - y^2z)$	$3x^2y - y^3$
3	-2	$-\frac{1}{2}(3x^2y + y^3 - 6yz^2)$	$-\frac{1}{2}(x^3 + 3xy^2 - 6xz^2)$	$6xyz$
3	-1	$-\frac{3}{2}xyz$	$-\frac{1}{4}(3x^2z + 9y^2z - 4z^3)$	$3yz^2 - \frac{3}{4}(x^2y + y^3)$
3	0	$\frac{3}{8}(x^3 + xy^2 - 4xz^2)$	$\frac{3}{8}(x^2y + y^3 - 4yz^2)$	$z^3 - \frac{3}{2}z(x^2 + y^2)$
3	1	$-\frac{1}{4}(9x^2z + 3y^2z - 4z^3)$	$-\frac{3}{2}xyz$	$3xz^2 - \frac{3}{4}(x^3 + xy^2)$
3	2	$-x^3 + 3xz^2$	$-3yz^2 + y^3$	$3(x^2z - y^2z)$
3	3	$3(x^2z - y^2z)$	$-6xyz$	$x^3 - 3xy^2$
3	4	$x^3 - 3xy^2$	$-3x^2y + y^3$	0

TABLE A.3: The basis of harmonic polynomials in cylindrical coordinates up to degree $l = 7$.

l	m	Π_ρ	Π_φ	Π_z
0	-1	$\sin\varphi$	$\cos\varphi$	0
0	0	0	0	1
0	1	$\cos\varphi$	$-\sin\varphi$	0
1	-2	$\rho\sin 2\varphi$	$\rho\cos 2\varphi$	0
1	-1	$z\sin\varphi$	$z\cos\varphi$	$\rho\sin\varphi$
1	0	$-\frac{1}{2}\rho$	0	z
1	1	$z\cos\varphi$	$-z\sin\varphi$	$\rho\cos\varphi$
1	2	$\rho\cos 2\varphi$	$-\rho\sin 2\varphi$	0
2	-3	$\rho^2\sin 3\varphi$	$\rho^2\cos 3\varphi$	0
2	-2	$2\rho z\sin 2\varphi$	$2\rho z\cos 2\varphi$	$\rho^2\sin 2\varphi$
2	-1	$\frac{1}{4}\left(4z^2 - 3\rho^2\right)\sin\varphi$	$\frac{1}{4}\left(4z^2 - \rho^2\right)\cos\varphi$	$2\rho z\sin\varphi$
2	0	$-\rho z$	0	$-\frac{1}{2}\rho^2 + z^2$
2	1	$\frac{1}{4}\left(4z^2 - 3\rho^2\right)\cos\varphi$	$\frac{1}{4}\left(\rho^2 - 4z^2\right)\sin\varphi$	$2\rho z\cos\varphi$
2	2	$2\rho z\cos 2\varphi$	$-2\rho z\sin 2\varphi$	$\rho^2\cos 2\varphi$
2	3	$\rho^2\cos 3\varphi$	$-\rho^2\sin 3\varphi$	0
3	-4	$\rho^3\sin 4\varphi$	$\rho^3\cos 4\varphi$	0
3	-3	$3\rho^2 z\sin 3\varphi$	$3\rho^2 z\cos 3\varphi$	$\rho^3\sin 3\varphi$
3	-2	$\rho\left(3z^2 - \rho^2\right)\sin 2\varphi$	$\frac{1}{2}\rho\left(6z^2 - \rho^2\right)\cos 2\varphi$	$3\rho^2 z\sin 2\varphi$

TABLE A.3: The basis of harmonic polynomials in cylindrical coordinates up to degree $l = 7$.

l	m	Π_ρ	Π_φ	Π_z
3	-1	$\frac{1}{4}z\left(4z^2-9\rho^2\right)\sin\varphi$	$\frac{1}{4}z\left(4z^2-3\rho^2\right)\cos\varphi$	$\rho\left(3z^2-\frac{3}{4}\rho^2\right)\sin\varphi$
3	0	$\frac{3}{8}\rho\left(\rho^2-4z^2\right)$	0	$\frac{1}{2}z\left(2z^2-3\rho^2\right)$
3	1	$\frac{1}{4}z\left(4z^2-9\rho^2\right)\cos\varphi$	$\frac{1}{4}z\left(3\rho^2-4z^2\right)\sin\varphi$	$\rho\left(3z^2-\frac{3}{4}\rho^2\right)\cos\varphi$
3	2	$\rho\left(3z^2-\rho^2\right)\cos 2\varphi$	$\frac{1}{2}\rho\left(\rho^2-6z^2\right)\sin 2\varphi$	$3\rho^2 z\cos 2\varphi$
3	3	$3\rho^2 z\cos 3\varphi$	$-3\rho^2 z\sin 3\varphi$	$\rho^3\cos 3\varphi$
3	4	$\rho^3\cos 4\varphi$	$-\rho^3\sin 4\varphi$	0
4	-5	$\rho^4\sin 5\varphi$	$\rho^4\cos 5\varphi$	0
4	-4	$4\rho^3 z\sin 4\varphi$	$4\rho^3 z\cos 4\varphi$	$\rho^4\sin 4\varphi$
4	-3	$\frac{1}{4}\left(24\rho^2z^2-5\rho^4\right)\sin 3\varphi$	$\frac{3}{4}\left(8\rho^2z^2-\rho^4\right)\cos 3\varphi$	$4\rho^3 z\sin 3\varphi$
4	-2	$4\left(\rho z^3-\rho^3 z\right)\sin 2\varphi$	$2\left(2\rho z^3-\rho^3 z\right)\cos 2\varphi$	$\left(6\rho^2z^2-\rho^4\right)\sin 2\varphi$
4	-1	$\frac{1}{8}\left(8z^4-36\rho^2z^2+5\rho^4\right)\sin\varphi$	$\frac{1}{8}\left(8z^4-12\rho^2z^2+\rho^4\right)\cos\varphi$	$\left(4\rho z^3-3\rho^3 z\right)\sin\varphi$
4	0	$\frac{1}{2}\left(3\rho^3 z-4\rho z^3\right)$	0	$\frac{1}{8}\left(8z^4-24\rho^2z^2+3\rho^4\right)$
4	1	$\frac{1}{8}\left(8z^4-36\rho^2z^2+5\rho^4\right)\cos\varphi$	$-\frac{1}{8}\left(8z^4-12\rho^2z^2+\rho^4\right)\sin\varphi$	$\left(4\rho z^3-3\rho^3 z\right)\cos\varphi$
4	2	$4\left(\rho z^3-\rho^3 z\right)\cos 2\varphi$	$-2\left(2\rho z^3-\rho^3 z\right)\sin 2\varphi$	$\left(6\rho^2z^2-\rho^4\right)\cos 2\varphi$
4	3	$\frac{1}{4}\left(24\rho^2z^2-5\rho^4\right)\cos 3\varphi$	$-\frac{3}{4}\left(8\rho^2z^2-\rho^4\right)\sin 3\varphi$	$4\rho^3 z\cos 3\varphi$
4	4	$4\rho^3 z\cos 4\varphi$	$-4\rho^3 z\sin 4\varphi$	$\rho^4\cos 4\varphi$
4	5	$\rho^4\cos 5\varphi$	$-\rho^4\sin 5\varphi$	0

TABLE A.4: The basis of harmonic polynomials in cylindrical coordinates up to degree $l = 4$, with $-l-1 \le m \le l+1$

l	m	Π_ρ	Π_φ	Π_z
5	-6	$\rho^5\sin 6\varphi$	$\rho^5\cos 6\varphi$	0
5	-5	$5\rho^4 z\sin 5\varphi$	$5\rho^4 z\cos 5\varphi$	$\rho^5\sin 5\varphi$
5	-4	$\frac{1}{2}\left(20\rho^3z^2-3\rho^5\right)\sin 4\varphi$	$\rho^3\left(10z^2-\rho^2\right)\cos 4\varphi$	$5\rho^4 z\sin 4\varphi$
5	-3	$\frac{5}{4}\left(8\rho^2z^3-5\rho^4 z\right)\sin 3\varphi$	$\frac{5}{4}\left(8\rho^2z^3-3\rho^4 z\right)\cos 3\varphi$	$\frac{5}{4}\left(8\rho^3z^2-\rho^5\right)\sin 3\varphi$
5	-2	$\frac{5}{16}\left(16\rho z^4-32\rho^3z^2+3\rho^5\right)\sin 2\varphi$	$\frac{5}{16}\left(16\rho z^4-16\rho^3z^2+\rho^5\right)\cos 2\varphi$	$5\left(2\rho^2z^3-\rho^4 z\right)\sin 2\varphi$
5	-1	$\frac{1}{8}\left(8z^5-60\rho^2z^3+25\rho^4 z\right)\sin\varphi$	$\frac{1}{z}\left(8z^5-20\rho^2z^3+5\rho^4 z\right)\cos\varphi$	$\frac{5}{8}\left(8\rho z^4-12\rho^3z^2+\rho^5\right)\sin\varphi$
5	0	$\frac{5}{16}\left(-8\rho z^4+12\rho^3z^2-\rho^5\right)$	0	$\frac{1}{8}\left(8z^5-40\rho^2z^3+15\rho^4 z\right)$
5	1	$\frac{1}{8}\left(8z^5-60\rho^2z^3+25\rho^4 z\right)\cos\varphi$	$-\frac{1}{8}\left(8z^5-20\rho^2z^3+5\rho^4 z\right)\sin\varphi$	$\frac{5}{8}\left(8\rho z^4-12\rho^3z^2+\rho^5\right)\cos\varphi$
5	2	$\frac{5}{16}\left(16\rho z^4-32\rho^3z^2+3\rho^5\right)\cos 2\varphi$	$-\frac{5}{16}\left(16\rho z^4-16\rho^3z^2+\rho^5\right)\sin 2\varphi$	$5\left(2\rho^2z^3-\rho^4 z\right)\cos 2\varphi$
5	3	$\frac{5}{4}\left(8\rho^2z^3-5\rho^4 z\right)\cos 3\varphi$	$-\frac{5}{4}\left(8\rho^2z^3-3\rho^4 z\right)\sin 3\varphi$	$\frac{5}{4}\left(8\rho^3z^2-\rho^5\right)\cos 3\varphi$
5	4	$\frac{1}{2}\left(20\rho^3z^2-3\rho^5\right)\cos 4\varphi$	$-\rho^3\left(10z^2-\rho^2\right)\sin 4\varphi$	$5\rho^4\cos 4\varphi z$
5	5	$5\rho^4 z\cos 5\varphi$	$-5\rho^4 z\sin 5\varphi$	$\rho^5\cos 5\varphi$
5	6	$\rho^5\cos 6\varphi$	$-\rho^5\sin 6\varphi$	0
6	-7	$\rho^6\sin 7\varphi$	$\rho^6\cos 7\varphi$	0
6	-6	$6\rho^5 z\sin 6\varphi$	$6\rho^5 z\cos 6\varphi$	$\rho^6\sin 6\varphi$
6	-5	$\frac{1}{4}\rho^4\left(60z^2-7\rho^2\right)\sin 5\varphi$	$\frac{5}{4}\rho^4\left(12z^2-\rho^2\right)\cos 5\varphi$	$6\rho^5 z\sin 5\varphi$
6	-4	$\rho^3 z\left(20z^2-9\rho^2\right)\cos 4\varphi$	$2\rho^3 z\left(10z^2-3\rho^2\right)\cos 4\varphi$	$\frac{3}{2}\rho^4\left(10z^2-\rho^2\right)\sin 4\varphi$
6	-3	$\frac{3}{16}\rho^2\left(80z^4-100\rho^2z^2+7\rho^4\right)\cos 3\varphi$	$\frac{3}{16}\rho^2\left(80z^4-60\rho^2z^2+3\rho^4\right)\cos 3\varphi$	$\frac{5}{2}\rho^3 z\left(8z^2-3\rho^2\right)\sin 3\varphi$
6	-2	$\frac{1}{8}\rho z\left(48z^4-160\rho^2z^2+45\rho^4\right)\cos 2\varphi$	$\frac{1}{8}\rho z\left(48z^4-80\rho^2z^2+15\rho^4\right)\cos 2\varphi$	$\frac{15}{16}\rho^2\left(16z^4-16\rho^2z^2+\rho^4\right)\sin 2\varphi$
6	-1	$\frac{1}{64}\left(64z^6-720\rho^2z^4+600\rho^4z^2-35\rho^6\right)\cos\varphi$	$\frac{1}{64}\left(64z^6-240\rho^2z^4+120\rho^4z^2-5\rho^6\right)\cos\varphi$	$\frac{3}{4}\rho z\left(8z^4-20\rho^2z^2+5\rho^4\right)\sin\varphi$
6	0	$\frac{3}{8}\rho\left(-8z^5+20\rho^2z^3-5\rho^4 z\right)$	0	$\frac{1}{16}\left(16z^6-120\rho^2z^4+90\rho^4z^2-5\rho^6\right)$
6	1	$\frac{1}{64}\left(64z^6-720\rho^2z^4+600\rho^4z^2-35\rho^6\right)\sin\varphi$	$-\frac{1}{64}\left(64z^6-240\rho^2z^4+120\rho^4z^2-5\rho^6\right)\sin\varphi$	$\frac{3}{4}\rho z\left(8z^4-20\rho^2z^2+5\rho^4\right)\cos\varphi$
6	2	$\frac{1}{8}\rho z\left(48z^4-160\rho^2z^2+45\rho^4\right)\sin 2\varphi$	$-\frac{1}{8}\rho z\left(48z^4-80\rho^2z^2+15\rho^4\right)\sin 2\varphi$	$\frac{15}{16}\rho^2\left(16z^4-16\rho^2z^2+\rho^4\right)\cos 2\varphi$
6	3	$\frac{3}{16}\rho^2\left(80z^4-100\rho^2z^2+7\rho^4\right)\sin 3\varphi$	$-\frac{3}{16}\rho^2\left(80z^4-60\rho^2z^2+3\rho^4\right)\sin 3\varphi$	$\frac{5}{2}\rho^3 z\left(8z^2-3\rho^2\right)\cos 3\varphi$
6	4	$\rho^3 z\left(20z^2-9\rho^2\right)\sin 4\varphi$	$-2\rho^3 z\left(10z^2-3\rho^2\right)\sin 4\varphi$	$\frac{3}{2}\rho^4\left(10z^2-\rho^2\right)\cos 4\varphi$

TABLE A.4: The basis of harmonic polynomials in cylindrical coordinates up to degree $l = 4$, with $-l - 1 \leq m \leq l + 1$

l	m	Π_ρ	Π_φ	Π_z
6	5	$\frac{1}{4}\rho^4\left(60z^2 - 7\rho^2\right)\cos 5\varphi$	$-\frac{5}{4}\rho^4\left(12z^2 - \rho^2\right)\sin 5\varphi$	$6\rho^5 z\cos 5\varphi$
6	6	$6\rho^5 z\cos 6\varphi$	$-6\rho^5 z\sin 6\varphi$	$\rho^6\cos 6\varphi$
6	7	$\rho^6\cos 7\varphi$	$-\rho^6\sin 7\varphi$	0
7	-8	$\rho^7\sin 8\varphi$	$\rho^7\cos 8\varphi$	0
7	-7	$7\rho^6 z\sin 7\varphi$	$7\rho^6 z\cos 7\varphi$	$\rho^7\sin 7\varphi$
7	-6	$\rho^5\left(21z^2 - 2\rho^2\right)\sin 6\varphi$	$\frac{3}{2}\rho^5\left(14z^2 - \rho^2\right)\cos 6\varphi$	$7\rho^6 z\sin 6\varphi$
7	-5	$\frac{7}{4}\rho^1 z\left(20z^2 - 7\rho^2\right)\sin 5\psi$	$\frac{35}{4}\rho^4 z\left(4z^2 - \rho^2\right)\cos 5\varphi$	$\frac{7}{4}\rho^5\left(12z^2 - \rho^2\right)\sin 5\varphi$
7	-4	$\frac{7}{4}\rho^3\left(20z^4 - 18\rho^2 z^2 + \rho^4\right)\sin 4\varphi$	$\frac{7}{7}\rho^3\left(40z^4 - 24\rho^2 z^2 + 3\rho^4\right)\cos 4\varphi$	$\frac{7}{2}\rho^4 z\left(10z^2 - 3\rho^2\right)\sin 4\varphi$
7	-3	$\frac{7}{16}\rho^2 z\left(48z^4 - 100\rho^2 z^2 + 21\rho^4\right)\sin 3\varphi$	$\frac{21}{16}\rho^2 z\left(16z^4 - 20\rho^2 z^2 + 3\rho^4\right)\cos 3\varphi$	$\frac{7}{16}\rho^3\left(80z^4 - 60\rho^2 z^2 + 3\rho^4\right)\sin 3\varphi$
7	-2	$\frac{7}{16}\rho\left(16z^6 - 80\rho^2 z^4 + 45\rho^4 z^2 - 2\rho^6\right)\sin 2\varphi$	$\frac{7}{32}\rho\left(32z^6 - 80\rho^2 z^4 + 30\rho^4 z^2 - \rho^6\right)\cos 2\varphi$	$\frac{7}{16}\rho^2 z\left(48z^4 - 80\rho^2 z^2 + 15\rho^4\right)\sin 2\varphi$
7	-1	$\frac{1}{64}z\left(64z^6 - 1008\rho^2 z^4 + 1400\rho^4 z^2 - 245\rho^6\right)\sin\varphi$	$\frac{1}{64}z\left(64z^6 - 336\rho^2 z^4 + 280\rho^4 z^2 - 35\rho^6\right)\cos\varphi$	$\frac{7}{64}\rho\left(64z^6 - 240\rho^2 z^4 + 120\rho^4 z^2 - 5\rho^6\right)\sin\varphi$
7	0	$\frac{7}{122}\rho\left(-64z^6 + 240\rho^2 z^4 - 120\rho^4 z^2 + 5\rho^6\right)$	0	$\frac{1}{16}z\left(16z^6 - 168\rho^2 z^4 + 210\rho^4 z^2 - 35\rho^6\right)$
7	1	$\frac{1}{4}z\left(64z^6 - 1008\rho^2 z^4 + 1400\rho^4 z^2 - 245\rho^6\right)\cos\varphi$	$-\frac{1}{64}z\left(64z^6 - 336\rho^2 z^4 + 280\rho^4 z^2 - 35\rho^6\right)\sin\varphi$	$\frac{7}{64}\rho\left(64z^6 - 240\rho^2 z^4 + 120\rho^4 z^2 - 5\rho^6\right)\cos\varphi$
7	2	$\frac{7}{16}\rho\left(16z^6 - 80\rho^2 z^4 + 45\rho^4 z^2 - 2\rho^6\right)\cos 2\varphi$	$-\frac{7}{5}\rho\left(32z^6 - 80\rho^2 z^4 + 30\rho^4 z^2 - \rho^6\right)\sin 2\varphi$	$\frac{7}{16}\rho^2 z\left(48z^4 - 80\rho^2 z^2 + 15\rho^4\right)\cos 2\varphi$
7	3	$\frac{7}{16}\rho^2 z\left(48z^4 - 100\rho^2 z^2 + 21\rho^4\right)\cos 3\varphi$	$-\frac{21}{16}\rho^2 z\left(16z^4 - 20\rho^2 z^2 + 3\rho^4\right)\sin 3\varphi$	$\frac{7}{16}\rho^3\left(80z^4 - 60\rho^2 z^2 + 3\rho^4\right)\cos 3\varphi$
7	4	$\frac{7}{4}\rho^3\left(20z^4 - 18\rho^2 z^2 + \rho^4\right)\cos 4\varphi$	$-\frac{7}{8}\rho^3\left(40z^4 - 24\rho^2 z^2 + 3\rho^4\right)\sin 4\varphi$	$\frac{7}{2}\rho^4 z\left(10z^2 - 3\rho^2\right)\cos 4\varphi$
7	5	$\frac{7}{4}\rho^4 z\left(20z^2 - 7\rho^2\right)\cos 5\psi$	$-\frac{35}{4}\rho^4 z\left(4z^2 - \rho^2\right)\sin 5\varphi$	$\frac{7}{4}\rho^5\left(12z^2 - \rho^2\right)\cos 5\varphi$
7	6	$\rho^5\left(21z^2 - 2\rho^2\right)\cos 6\varphi$	$-\frac{3}{2}\rho^5\left(14z^2 - \rho^2\right)\sin 6\varphi$	$7\rho^6 z\cos 6\varphi$
7	7	$7\rho^6 z\cos 7\varphi$	$-7\rho^6 z\sin 7\varphi$	$\rho^7\cos 7\varphi$
7	8	$\rho^7\cos 8\varphi$	$-\rho^7\sin 8\varphi$	0

Appendix B

Useful definitions and identities

Contents

B.1 Notes on groups and representations

We recall here a few key definitions to supplement chapter 3 and 9's discussions on representations of the B_0 coil symmetry groups.

B.1.1 Groups

Definition B.1.1. A **group** is a set G together with a binary operation $\star$, denoted $(G, \star)$, that satisfies the following axioms:

(i) G is closed under $\star$: $\forall x, y \in G,\ x \star y \in G$.

(ii) $\star$ is associative: $\forall x, y, z \in G,\ (x \star y) \star z = x \star (y \star z)$.

(iii) G contains a neutral element: $\exists e \in G,\ \forall x \in G,\ x \star e = e \star x = x$.

(iv) G contains an inverse of each of its elements: $\forall x \in G,\ \exists y \in G,\ x \star y = y \star x = e$. The inverse y of x is usually denoted x^{-1}.

If the operation $\star$ is commutative, then we say that the group is *abelian*.

Definition B.1.2. Given a group $(G, \star)$, the set H together with the same binary operation $\star$ is said to be a **subgroup** of $(G, \star)$ iff $H \subset G$ and $(H, \star)$ is a group.

Definition B.1.3. Given a group $(G, \star)$ and a subset $S \subset G$, we define the **subgroup generated by** S, denoted $\langle S \rangle$, as the smallest subgroup of $(G, \star)$ containing every element in S.

If $\langle S \rangle = G$, then we say that the elements of S are **generators** of the group $(G, \star)$.

Definition B.1.4. Two elements x and y of a group G are said to be **conjugate** if there exists an element $g \in G$ such that $y = gxg^{-1}$. We call the **conjugacy class** of an element $x \in G$ the set of all conjugates of x, defined as

$$Cl(x) = \{gxg^{-1} \mid g \in G\}. \tag{B.1}$$

B.1.2 Representations of groups

Definition B.1.5. Given two groups $(G, \star)$ and $(H, \cdot)$, a **group homomorphism** from $(G, \star)$ to $(H, \cdot)$ is a map $f : G \to H$ such that

$$\forall x, y \in G, \quad f(x \star y) = f(x) \cdot f(y). \tag{B.2}$$

Proposition B.1.1. Given a vector space V over a field F, the set of all bijective linear maps $V \to V$ (*automorphisms* of V), together with the map composition $\circ$, is a group. This group is referred to as the **General Linear group** and denoted $GL(V)$.

For instance, given a coordinate vector space $\mathbb{C}^n$, the set of all $n \times n$ invertible matrices with complex coefficients are bijective linear maps on $\mathbb{C}^n$, which together with matrix multiplication form the general linear group denoted $GL(\mathbb{C}^n)$.

Definition B.1.6. A **representation** of a group G[1] on a vector space V, denoted (ρ, V), is a group homomorphism from G to $GL(V)$. In other words, it is a map $\rho : G \to GL(V)$ such that

$$\forall x, y \in G, \quad \rho(xy) = \rho(x)\rho(y). \tag{B.3}$$

Definition B.1.7. Two representations (ρ, V) and (σ, W) of a group G are said to be **equivalent** if there exists a bijective linear map $T : V \to W$ such that

$$\forall x \in G, \quad \rho(x) = T\sigma(x)T^{-1}. \tag{B.4}$$

Definition B.1.8. Given a representation (ρ, V) of a group G, a subspace $W \subset V$ is said to be **invariant** if

$$\forall \mathbf{u} \in W, \forall x \in G, \quad \rho(x)\mathbf{u} \in W. \tag{B.5}$$

The fact that the null-space $\{0\}$ and V itself are always invariant subspaces of V motivates the following definition.

Definition B.1.9. A representation (ρ, V) of a group G is said to be **irreducible** if there are no non-trivial invariant subspaces of V, i.e. if the only invariant subspaces of V are $\{0\}$ and V itself. The representation is said to be **reducible** if it is not irreducible.

Definition B.1.10. Let (ρ_1, V_1) and (ρ_2, V_2) be two representations of a group G. We define their **direct sum** as the representation $(\rho_1 \oplus \rho_2, V_1 + V_2)$, where given $x \in G$ and $\mathbf{v_1} \in V_1$, $\mathbf{v_2} \in V_2$,

$$(\rho_1 \oplus \rho_2)(x)(\mathbf{v_1} + \mathbf{v_2}) = \rho_1(x)\mathbf{v_1} + \rho_2(x)\mathbf{v_2}. \tag{B.6}$$

For finite-dimensional representations, the matrix $(\rho_1 \oplus \rho_2)(x)$ is block-diagonal:

$$(\rho_1 \oplus \rho_2)(x) = \begin{pmatrix} \rho_1(x) & 0 \\ 0 & \rho_2(x) \end{pmatrix}. \tag{B.7}$$

Property B.1.1. A finite-dimensional representation (ρ, V) of a group G which can be written in block-diagonal form is reducible. By "can be written", we mean that there exists an equivalent representation (ρ', V'), obtained by the bijective linear map $T : V \to V'$, which is a direct sum of representations:

$$\forall x \in G, \quad T\rho(x)T^{-1} = \rho'(x) = \rho'_1(x) \oplus \rho'_2(x) \oplus \ldots \oplus \rho'_n(x). \tag{B.8}$$

[1] From now on we use G interchangeably for the set G and the group $(G, \star)$ when no confusion is possible.

Furthermore, if the representations $\rho_{k\leq n}$ are irreducible, the representation (ρ, V) is said to be *completely reducible*.

Definition B.1.11. Given a representation (ρ, V) of a group G, we define the **character** of ρ as the function $\chi_\rho : G \to \mathbb{C}$ given by

$$\chi_\rho(g) = \mathrm{Tr}\{\rho(g)\}. \tag{B.9}$$

Theorem B.1.1 (Orthogonality theorem). If (ρ_i, V_i) and (ρ_j, V_j) are two irreducible representations of a group G, then

$$\frac{1}{|G|}\sum_{g\in G}\chi_{\rho_i}(g)\chi_{\rho_j}(g^{-1}) = 0, \tag{B.10}$$

where $|G|$ is the cardinality of the group and $\chi_{\rho_i}(g)$ and $\chi_{\rho_j}(g)$ are the characters of the two representations.
If (ρ, V) is an irreducible representation of G, then

$$\frac{1}{|G|}\sum_{g\in G}\chi_{\rho}(g)\chi_{\rho}(g^{-1}) = 1. \tag{B.11}$$

B.2 Notes on Hilbert transforms

B.2.1 Definitions

Definition B.2.1. Let f be a real-valued function singular in $c \in \mathbb{R}$, and let $a, b \in \mathbb{R}$. Then the **principal value** (PV) of the integral of f over the real interval $[a, b]$ is defined as

$$\text{P.V.}\int_a^b dx\, f(x) = \lim_{\varepsilon\to 0}\left(\int_a^{c-\varepsilon} dx\, f(x) + \int_{c+\varepsilon}^b dx\, f(x)\right), \tag{B.12}$$

when the limit exists.

This allows the definition of a distribution

$$\text{P.V.}\frac{1}{x} : \gamma_c^\infty(\mathbb{R}) \longrightarrow \mathbb{C}, \tag{B.13}$$

with $\gamma_c^\infty(\mathbb{R})$ the set of smooth functions with compact support on the real line, such that for $f \in \gamma_c^\infty(\mathbb{R})$,

$$\left\langle \text{P.V.}\frac{1}{x}, f\right\rangle = \text{P.V.}\int_a^b dy\,\frac{f(y)}{y} = \lim_{\varepsilon\to 0}\left(\int_a^{-\varepsilon} dy\,\frac{f(y)}{y} + \int_\varepsilon^b dy\,\frac{f(y)}{y}\right). \tag{B.14}$$

Definition B.2.2. The convolution of P.V.$\frac{1}{\pi x}$ with f

$$\text{P.V.}\frac{1}{\pi x} * f = \frac{1}{\pi}\text{P.V.}\int_{-\infty}^{+\infty} dy\,\frac{f(y)}{x-y} \tag{B.15}$$

is known as the **Hilbert transform** of f.

B.2.2 Identities

A Dirac distribution equivalent:

$$\lim_{\varepsilon\to 0}\frac{1}{\pi}\frac{1}{x^2+\varepsilon^2}=\delta(x). \tag{B.16}$$

We can use this form of the Dirac distribution to show that

$$\lim_{\varepsilon\to 0}\int_a^b dx\frac{f(x)}{x\pm i\varepsilon}=\text{P.V.}\int_a^b dx\frac{f(x)}{x}\mp i\pi\int_a^b dx f(x)\delta(x), \tag{B.17}$$

which in terms of distributions means

$$\lim_{\varepsilon\to 0}\frac{1}{x\pm i\varepsilon}=\text{P.V.}\left(\frac{1}{x}\right)\mp i\pi\delta(x). \tag{B.18}$$

Another useful application of this identity is the evaluation of an integral of a complex exponential on half of the real line:

$$\begin{aligned}\int_0^\infty dt\, e^{i\omega t}&=\lim_{\varepsilon\to 0^+}\int_0^\infty dt\, e^{i(\omega+i\varepsilon)t}\\&=\lim_{\varepsilon\to 0^+}\frac{i}{\omega+i\varepsilon}\\&=\pi\delta(\omega)+i\,\text{P.V.}\left(\frac{1}{\omega}\right).\end{aligned} \tag{B.19}$$

Recurring Hilbert transforms:

- Hilbert transform of a Lorentzian:

$$\text{P.V.}\int_{-\infty}^{+\infty}d\omega\left(\frac{1}{\omega_0-\omega}\right)\left(\frac{1}{\omega^2+\omega_1^2}\right)=\frac{-\pi(\omega_0/\omega_1)}{\omega_0^2+\omega_1^2}. \tag{B.20}$$

- Hilbert transform of a $\omega\times$ Lorentzian:

$$\text{P.V.}\int_{-\infty}^{+\infty}d\omega\left(\frac{1}{\omega_0-\omega}\right)\left(\frac{\omega}{\omega^2+\omega_1^2}\right)=\frac{\pi\omega_1}{\omega_0^2+\omega_1^2}. \tag{B.21}$$

B.3 Notes on complex analysis

Definition B.3.1. Given an open subset $U\subset\mathbb{C}$, a function $f: U\mapsto\mathbb{C}$ is said to be **holomorphic** on U if it is complex differentiable at every point $z_0\in U$. By complex differentiable we mean that the limit

$$\lim_{z\to z_0}\frac{f(z)-f(z_0)}{z-z_0} \tag{B.22}$$

exists.

One important consequence is that a holomorphic function is equal to its Taylor expansion at every point it is defined on.

Definition B.3.2. (Cauchy-Riemann conditions) Let $x,y\in\mathbb{R}$ such that $z=x+iy$, and let u,v be two real valued functions of $\mathbb{R}^2$ such that $f(x+iy)=u(x,y)+iv(x,y)$.

Then f is holomorphic in $z_0 = x_0 + iy_0$ if and only if

$$\left.\frac{\partial u(x,y)}{\partial x}\right|_{x=x_0} = \left.\frac{\partial v(x,y)}{\partial y}\right|_{y=y_0}. \tag{B.23}$$

For the following, let U be a simply connected open subset of the complex plane $\mathbb{C}$, let $\{z_1, z_2, \ldots, z_n\}$ a set of points in U, and f a function defined and holomorphic on $U \setminus \{z_1, z_2, \ldots, z_n\}$.

Definition B.3.3. We say that $f(z)$ has **pole** of order r at $z_0 \in \{z_1, z_2, \ldots, z_n\}$ if it can be written as

$$f(z) = \frac{g(z)}{(z - z_0)^r}, \tag{B.24}$$

such that $g(z)$ is holomorphic in a neighborhood $U_0 \subset U$ of z_0 and $g(z_0) \neq 0$.

Property B.3.1. For each of the points $z_0 \in \{z_1, z_2, \ldots, z_n\}$, there exists a neighborhood $U_0 \subset U$ of z_0 onto which f is holomorphic. Furthermore f can be written as the Laurent expansion on U_0

$$f(z) = \sum_{n=-\infty}^{+\infty} a_n (z - z_0)^n. \tag{B.25}$$

This implies that if the Laurent expansion of f around z_0 goes down to order $n = -r$, $r > 0$, then z_0 is a pole of order r of f. We also note the following:

Definition B.3.4. The coefficient a_{-1} of the Laurent expansion is referred to as the **residue** of f at z_0.

Property B.3.2. If f possesses a pole of order r at z_0, then the residue of f at z_0 can be obtained by the following formula:

$$\mathrm{Res}(f, z_0) = \frac{1}{(n-1)!} \lim_{z \to z_0} \frac{d^{n-1}}{dz^{n-1}} \left[(z - z_0)^n f(z) \right]. \tag{B.26}$$

We can finally introduce this famous theorem, valid in our present definition of f and U:

Theorem B.3.1. (Residue theorem) Let γ be a closed rectifiable curve in U (i.e. does not encounter any singular points) with a winding number around $z_k \in \{z_1, z_2, \ldots, z_n\}$ denoted $I(\gamma, z_k)$. Then

$$\oint_\gamma f(z) dz = 2\pi i \sum_{k=1}^{n} I(\gamma, z_k) \,\mathrm{Res}(f, z_k). \tag{B.27}$$

Note that the complex line integral over a differentiable curve $\gamma : [a, b] \to U$ can be written

$$\int_\gamma f(z) dz = \int_a^b f(\gamma(t)) \dot{\gamma}(t) dt. \tag{B.28}$$

A few simple results from the residue theorem:

- If f is holomorphic in z_0, then $\mathrm{Res}(f, z_0) = 0$. Now if γ does not include any poles of f (f is holomorphic inside γ), then

$$\oint_\gamma f(z) dz = 0. \tag{B.29}$$

- For $f(z) = a/z$ (holomorphic on $\gamma \setminus \{0\}$), we let $\gamma = e^{it}$ (closed unity circle around first order pole at $z_0 = 0$) to find

$$\oint_\gamma f(z)dz = 2ia\pi. \tag{B.30}$$

We end with a powerful tool for contour integration:

Lemma B.3.1. (Jordan's Lemma) Define the semi-circular contour $\gamma = \{Re^{i\theta} \mid 0 \leq \theta \leq \pi\}$ of radius $R > 0$. If f can be written as

$$f(z) = e^{iaz}g(z), \tag{B.31}$$

for a real number $a > 0$ and a function g holomorphic along γ, then

$$\left| \int_0^\pi f(z)dz \right| \leq \frac{\pi}{a} \max_{0 \leq \theta \leq \pi} \left| g\left(Re^{i\theta}\right) \right|. \tag{B.32}$$

A few remarks:

- The caveat $a > 0$ directly conditions the absolute convergence of this integral through a $\left|e^{iaRe^{i\theta}}\right|$ bound factor in the integral on the semi-circle arc. In a situation where $a < 0$ one should choose a counter-clockwise contour $\gamma = \{Re^{-i\theta} \mid 0 \leq \theta \leq \pi\}$ to achieve the same convergence. Remember that this leads to $I(\gamma, z_0) = -1$.
- When integrating over the real line, we work in the limit $R \to +\infty$ with functions that usually satisfy $\lim_{R\to+\infty} g(Re^{i\theta}) = 0$. Therefore the integral of $f(z)$ over the semi-circle goes to zero.

Appendix C

Tools for the low-frequency false EDM

Contents

C.1 Volume averages

We derive here the explicit volume averages of harmonic polynomial terms taking their origin in the middle of the two precession chambers chambers (point O in 5.1). Working in Cartesian coordinates, the lack of correlation between horizontal and vertical trajectories leads to the important identity

$$\left\langle x^n y^m z^k \right\rangle = \left\langle x^n y^m \right\rangle \left\langle z^k \right\rangle . \tag{C.1}$$

We then compute vertical and horizontal averages separately.

Vertical averages

The vertical averages are given by

$$\left\langle z^n \right\rangle = \frac{\left\langle \left(z + \frac{H'}{2}\right)^n \right\rangle_{\text{TOP}} + \left\langle \left(z - \frac{H'}{2}\right)^n \right\rangle_{\text{BOT}}}{2}, \tag{C.2}$$

where the vertical averages over the top $(+)$ or bottom $(-)$ chamber are defined as

$$\begin{aligned} \left\langle \left(z \pm \frac{H'}{2}\right)^n \right\rangle &= \frac{1}{H} \int_{-H/2}^{H/2} dz \left(z \pm \frac{H'}{2}\right)^n \\ &= (\pm 1)^n \frac{1}{2^n} \sum_{2p \leq n} \binom{n}{2p} \frac{H'^{n-2p} H^{2p}}{2p+1}. \end{aligned} \tag{C.3}$$

These terms are given explicitly up to $n = 8$ in table C.1.

Horizontal averages

Horizontal averages of the form $\langle x^n y^m \rangle$ are obtained by switching to polar coordinates, wherein

$$\left\langle x^n y^m \right\rangle = \left\langle \rho^{n+m} \cos^n(\varphi) \sin^m(\varphi) \right\rangle . \tag{C.4}$$

The radial part reduces to

$$\langle \rho^n \rangle = \frac{1}{R^2/2} \int_0^R d\rho\, \rho^{n+1} = \frac{2}{n+2} R^n. \tag{C.5}$$

The angular part is solved by using the fact that $\int_0^{2\pi} d\theta \cos^{2n}\theta = \int_0^{2\pi} d\theta \sin^{2n}\theta$, which finally yields

$$\langle x^n y^m \rangle = \frac{R^{n+m}}{n+m+2} \frac{1}{\pi} \int_0^{2\pi} d\varphi \cos^n(\varphi) \sin^m(\varphi). \tag{C.6}$$

Note that the cylindrical symmetry of the double chamber imposes that:

- $\langle x^n y^m \rangle \neq 0$ only if both n and m are even,
- $\langle x^n y^m \rangle = \langle x^m y^n \rangle$.

The horizontal averages are given explicitly up to $m+n=8$ by table C.2.

C.2 Phantom modes and normalization of generalized gradients

The phantom modes $\acute{\Pi}_{2k+1}$ are defined as l-odd, $m=0$ terms that generate a non-zero false EDM through equation (4.28) while satisfying $G_{\mathrm{TB}}=0$ in equation (5.3). Here we propose a derivation of their explicit form based on what is presented in the design article (al., 2022).

Recall that the harmonic expansion of the false EDM generating field is given by

$$\mathbf{B} = G_{10}\mathbf{\Pi}_{10} + G_{30}\mathbf{\Pi}_{30} + G_{50}\mathbf{\Pi}_{50} + \dots. \tag{C.7}$$

n	$\left\langle \left(z \pm \frac{H'}{2} \right)^n \right\rangle$
1	$\pm\frac{H'}{2}$
2	$\frac{3H'^2+H^2}{12}$
3	$\pm\frac{H'^3+H'H^2}{8}$
4	$\frac{5H'^4+10H'^2H^2+H^4}{80}$
5	$\pm\frac{3H'^5+10H'^3H^2+3H'H^4}{96}$
6	$\frac{7H'^6+35H'^4H^2+21H'^2H^4+H^6}{448}$
7	$\pm\frac{H'^7+7H'^5H^2+7H'^3H^4+H'H^6}{128}$
8	$\frac{9H'^8+84H'^6H^2+126H'^4H^4+36H'^2H^6+H^8}{2304}$

TABLE C.1: Vertical averages over the top $(+)$ or bottom $(-)$ chamber.

and that the top-bottom gradient generated by this configuration is

$$G_{\rm TB} = G_{10} - L_3^2 G_{30} + L_5^4 G_{50} - \dots . \tag{C.8}$$

The phantom modes are made to appear explicitly in this expansion by isolating the $G_{\rm TB}$ generating term:

$$\mathbf{B} = G_{\rm TB}\mathbf{\Pi}_{10} + \acute{G}_3\acute{\mathbf{\Pi}}_3 + \acute{G}_5\acute{\mathbf{\Pi}}_5 + \dots , \tag{C.9}$$

where we let

$$\acute{G}_3\acute{\mathbf{\Pi}}_3 = G_{30}L_3^2\left[\mathbf{\Pi}_{10} + \frac{1}{L_3^2}\mathbf{\Pi}_{30}\right], \qquad \acute{G}_5\acute{\mathbf{\Pi}}_5 = G_{50}L_5^4\left[-\mathbf{\Pi}_{10} + \frac{1}{L_5^4}\mathbf{\Pi}_{50}\right], \tag{C.10}$$

and more generally

$$\acute{G}_{2k+1}\acute{\mathbf{\Pi}}_{2k+1} = G_{2k+1,0}L_{2k+1}^{2k}\left[(-1)^k\mathbf{\Pi}_{10} + \frac{1}{L_{2k+1}^{2k}}\mathbf{\Pi}_{2k+1,0}\right], \tag{C.11}$$

for all modes of odd degree $2k+1$. The normalization of the phantom modes is obtained by requiring that a field configuration of the form (C.9) generates a false EDM

$$d^{\rm false}_{n\leftarrow{\rm Hg}} = \frac{\hbar\left|\gamma_n\gamma_{\rm Hg}\right|}{2c^2}\left\langle\rho B_\rho\right\rangle = \frac{\hbar\left|\gamma_n\gamma_{\rm Hg}\right|}{2c^2}\frac{-R^2}{4}\left(G_{\rm TB} + \acute{G}_3 + \acute{G}_5 + \dots\right). \tag{C.12}$$

This amounts to imposing $\left\langle\rho\acute{\mathbf{\Pi}}^{(\rho)}_{2k+1}\right\rangle = (-R^2/4)$ for all odd modes. Then, letting

$$\acute{\mathbf{\Pi}}_{2k+1} = \frac{L_{2k+1}^{2k}}{D_{2k+1}^{2k}}\left[\mathbf{\Pi}_{10} - \frac{(-1)^k}{L_{2k+1}^{2k}}\mathbf{\Pi}_{2k+1,0}\right], \tag{C.13}$$

n	m	$\langle x^n y^m\rangle$
0	2	$\frac{R^2}{4}$
0	4	$\frac{R^4}{8}$
2	2	$\frac{R^4}{24}$
0	6	$\frac{5R^6}{64}$
2	4	$\frac{R^6}{64}$
0	8	$\frac{7R^8}{128}$
2	6	$\frac{R^8}{128}$
4	4	$\frac{3R^8}{640}$

TABLE C.2: Horizontal averages over the top or bottom chambers.

with D_{2k+1} a normalization coefficient with a unit of distance and where one may check that (C.13) satisfies indeed $G_{\mathrm{TB}} = 0$, we obtain

$$D_{2k+1}^{2k} = \left[L_{2k+1}^{2k} - (-1)^k \frac{\left\langle \rho \Pi_{2k+1,0}^{(\rho)} \right\rangle}{-R^2/4} \right]. \tag{C.14}$$

These coefficients serve as a normalizing factor between generalized gradients and first-order gradients such as the phantom gradients, with

$$\acute{G}_{2k+1} = G_{2k+1,0} D_{2k+1}^{2k}, \tag{C.15}$$

so we will refer to them as the **normalizing distances**. Their numerical values in the n2EDM geometry are given in table 5.1.

This also allows us to define a more general, convenient normalization valid for any harmonic gradient. All $G_{2k+1,m}$ gradients can be normalized by simply applying the D_{2k+1}^{2k} factor. Furthermore, all $G_{2k,m}$ gradients, which do not generate a false EDM in the double chamber configuration, can be normalized by considering the false EDM produced in the top chamber alone. We thus define the l-even normalizing distances D_{2k}^{2k-1} as

$$D_{2k}^{2k-1} = \frac{\left\langle \rho \Pi_{2k,0}^{(\rho)} \right\rangle_{\mathrm{TOP}}}{-R^2/4}. \tag{C.16}$$

They satisfy

$$\acute{G}_{2k,0} = G_{2k,0} D_{2k}^{2k-1}. \tag{C.17}$$

These distances also figure in table 5.1. Their values are obtained from the geometric coefficients featured in tables C.3 and C.4.

Coef.	Expression	Value
L_3^2	$\frac{3R^2}{4} - \frac{H^2 + H'^2}{4}$	$(32.9\,\mathrm{cm})^2$
L_5^4	$\frac{5R^4}{8} - \frac{5R^2(H^2 + H'^2)}{8} + \frac{3H^4 + 10H^2H'^2 + 3H'^4}{48}$	$(32.7\,\mathrm{cm})^4$
L_7^6	$\frac{1}{16}\left(\frac{35R^6}{4} - \frac{70R^4(H^2 + H'^2)}{3} + \frac{21R^2(3H^4 + 10H^2H'^2 + 3H'^4)}{12} - \frac{H^6 + 7H^4H'^2 + 7H^2H'^4 + H'^6}{4}\right)$	$(32.5\,\mathrm{cm})^2$

TABLE C.3: Geometrical coefficient L_{2k+1}^{2k} for each $2k+1$ term of the top-bottom gradient expansion (5.3), up to order $2k+1 = 7$.

C.3 Addition of harmonic modes

We provide here a tool to estimate the vertical non-uniformity $\sigma(B_z)$ from dominant modes of the harmonic spectrum. First we define the non-uniform vertical field as $b_z = B_z - \langle B_z \rangle$ and parameterize it in terms of non-uniform harmonic basis elements $\pi_{lm} = \Pi_{lm} - \langle \Pi_{lm} \rangle$, such that

$$b_z(\rho, \varphi, z) = \sum_{l \geq 0} \sum_{m=-l-1}^{l+1} G_{lm} \pi_{lm}(\rho, \varphi, z). \tag{C.18}$$

These inherit the inner product orthogonality (A.7) from the old harmonic basis elements Π_{lm}:

$$\langle \pi_{lm}(\rho,\varphi,z)\pi_{kn}(\rho,\varphi,z)\rangle = \delta_{mn}\langle \tilde{\pi}_{lm}(\rho,z)\tilde{\pi}_{kn}(\rho,z)\rangle \tag{C.19}$$

Using the above we can then set an upper bound on the non-uniformity generated by the sum of all $G_{lm}\pi_{lm}$ modes, expressed in terms of non-uniformities $\sigma\left(G_{lm}\Pi_{lm}\right)$ generated by individual modes:

$$\begin{aligned}
\sigma^2\left(\sum_{l,m} G_{lm}\Pi_{lm}\right) &= \left\langle \left(\sum_{l,m} G_{lm}\pi_{lm}\right)^2 \right\rangle \\
&= \sum_{k,l,m} G_{lm}G_{km}\langle \tilde{\pi}_{lm}\tilde{\pi}_{km}\rangle \\
&\leq \sum_{k,l,m} |G_{lm}||G_{km}| \left\langle \pi_{lm}^2\right\rangle^{\frac{1}{2}} \left\langle \pi_{km}^2\right\rangle^{\frac{1}{2}} \\
&\leq \sum_{m}\left(\sum_{l}\sigma\left(G_{lm}\Pi_{lm}\right)\right)^2,
\end{aligned} \tag{C.20}$$

where we used the Cauchy-Schwartz inequality in the second to third line. Therefore for the most general field configuration B_z we always have:

$$\sigma\left(B_z\right) \leq \sqrt{\sum_{m}\left[\sum_{l}\sigma\left(G_{lm}\Pi_{lm}\right)\right]^2}. \tag{C.21}$$

l-order	$\frac{\left\langle \rho\Pi_{lm}^{(\rho)}\right\rangle_{\text{TOP}}}{-R^2/4}$
1	1
2	H'
3	$\frac{-R^2}{2}+\frac{H^2+3H'^2}{4}$
4	$-R^2H'+\frac{H^2H'+H'^3}{2}$
5	$\frac{5R^4}{16}-\frac{5R^2(H^2+3H'^2)}{12}+\frac{H^4+10H^2H'^2+5H'^4}{16}$
6	$\frac{5R^4H'}{2}-\frac{5R^2(H'H^2+H'^3)}{4}+\frac{3H^4H'+10H'^2H^3+3H'^5)}{16}$
7	$-\frac{7R^6}{32}+\frac{70R^4(H^2+3H'^2)}{128}-\frac{7R^2(H^4+10H^2H'^2+5H'^4)}{32}+\frac{H^6+21H^4H'^2+35H^2H'^4+7H'^6}{64}$

TABLE C.4: Geometrical coefficients for generalized gradients normalization (C.15) and (C.17), up to order $l=7$.

Appendix D

Magnetic field mapping results

Contents

D.1 B_0 field

We display in this section the results of the B_0 coil maps for both polarities, as well as remnant field maps. For these three sets the average μ and reproducibility σ were obtained by comparing the averages of each mapping sequence, while the repeatability τ was taken as the average standard deviation of each mapping sequence. The maps used for the averages gradient values were recorded in January 2023 after applying an optimized degaussing procedure. The reproducibility and repeatability of these gradients account for maps recorded during the entire second mapping campaign of n2EDM, which started in September 2022.

TABLE D.1: Uniform modes of the generalized gradient spectrum, given in pT, for the two B_0 coil polarities ($\uparrow$ for $I = 11.25\,\text{mA}$ and $\downarrow$ for $I = -11.25\,\text{mA}$) and without the B_0 coil (bare). In each configuration we give the average value over all sequences μ, the average repeatability inside a sequence τ, and the reproducibility between sequences σ.

(pT)	$\uparrow \mu$	$\uparrow \tau$	$\uparrow \sigma$	$\downarrow \mu$	$\downarrow \tau$	$\downarrow \sigma$	bare μ	bare τ	bare σ
$G_{0,-1}$	1603.8	3.8	3.3	-1556.2	3.2	10.0	5.7	6.3	18.2
$G_{0,0}$	940526.8	6.9	708.9	-940516.7	29.0	575.4	22.8	6.8	6.9
$G_{0,1}$	-86.4	11.2	12.8	217.9	1.6	8.3	-57.1	11.3	44.5

TABLE D.2: $l > 0$ modes of the generalized gradients spectrum, for the two B_0 coil polarities ($\uparrow$ for $I = 11.25\,\mathrm{mA}$ and $\downarrow$ for $I = -11.25\,\mathrm{mA}$) and without the B_0 coil. These are normalized to first order gradients $\acute{G}_{lm} = D_l^{l-1} G_{lm}$ with the distances given in table 5.1, and given in units of fT/cm. In each configuration we give the average value over all sequences μ, the average repeatability inside a sequence τ, and the reproducibility between sequences σ.

(fT/cm)	$\uparrow \mu$	$\uparrow \tau$	$\uparrow \sigma$	$\downarrow \mu$	$\downarrow \tau$	$\downarrow \sigma$	bare μ	bare τ	bare σ
$\acute{G}_{1,-2}$	-769.0	199.9	573.3	249.6	135.2	470.6	-2395.0	248.6	990.5
$\acute{G}_{1,-1}$	1539.1	99.3	122.9	-813.3	72.7	139.5	-240.0	53.8	82.3
$\acute{G}_{1,0}$	346.6	79.2	254.8	-208.1	106.1	319.4	-646.1	140.6	252.6
$\acute{G}_{1,1}$	32.9	64.5	218.8	324.6	39.1	410.7	700.6	82.2	294.2
$\acute{G}_{1,2}$	-2292.4	56.7	232.9	1539.4	129.5	217.6	0.3	52.3	262.1
$\acute{G}_{2,-3}$	81.1	18.3	44.8	-116.7	17.3	45.8	44.4	12.8	36.4
$\acute{G}_{2,-2}$	95.1	14.7	42.6	25.9	16.4	53.2	90.8	11.1	17.6
$\acute{G}_{2,-1}$	370.8	19.2	24.4	-433.5	18.1	26.6	-109.0	9.5	43.2
$\acute{G}_{2,0}$	1265.9	26.4	50.9	-1151.7	23.6	146.4	-71.2	22.6	24.8
$\acute{G}_{2,1}$	36.2	7.3	37.2	41.9	14.0	18.2	72.8	7.4	45.8
$\acute{G}_{2,2}$	-672.7	9.5	12.9	692.9	5.3	15.2	-79.5	6.0	39.6
$\acute{G}_{2,3}$	570.2	13.9	53.2	-533.7	11.6	47.6	1.3	5.4	46.8
$\acute{G}_{3,-4}$	-123.7	2.4	11.7	104.0	3.6	10.9	-54.9	3.3	15.9
$\acute{G}_{3,-3}$	-5.6	1.7	3.2	-5.6	1.0	3.5	-12.9	1.5	5.6
$\acute{G}_{3,-2}$	-1.9	1.9	3.0	4.6	0.9	4.6	-9.9	2.4	10.5
$\acute{G}_{3,-1}$	51.8	4.3	11.8	-120.5	3.7	13.5	-18.6	3.8	5.9
$\acute{G}_{3,0}$	-633.6	7.4	22.2	594.2	17.1	18.5	-7.2	7.8	6.2
$\acute{G}_{3,1}$	77.0	3.0	10.8	-51.0	2.0	11.5	32.9	4.6	5.8
$\acute{G}_{3,2}$	-119.6	1.3	4.2	120.4	2.3	3.4	-0.6	1.0	4.5
$\acute{G}_{3,3}$	-23.3	4.0	7.0	-50.9	3.5	4.8	-2.3	3.4	5.8
$\acute{G}_{3,4}$	-34.5	2.9	13.8	56.7	4.3	9.9	15.3	3.0	9.9
$\acute{G}_{4,-5}$	-17.2	0.9	2.6	8.8	1.2	2.4	10.4	1.2	5.9
$\acute{G}_{4,-4}$	-2.3	0.6	0.8	-6.6	0.7	1.6	-0.5	0.7	1.2
$\acute{G}_{4,-3}$	-1.1	0.3	0.7	-1.1	0.2	0.5	-0.7	0.3	1.3
$\acute{G}_{4,-2}$	-0.3	0.6	1.7	9.2	0.8	3.0	10.8	1.0	3.6
$\acute{G}_{4,-1}$	20.8	1.7	6.8	-23.1	1.5	4.0	-19.7	2.6	4.7
$\acute{G}_{4,0}$	-122.5	6.5	18.2	141.9	7.2	21.2	0.2	4.7	2.8
$\acute{G}_{4,1}$	-2.7	2.2	6.2	10.0	1.3	5.3	-15.3	1.4	5.2
$\acute{G}_{4,2}$	-14.4	1.1	2.1	11.4	0.9	2.3	-4.4	0.3	1.4
$\acute{G}_{4,3}$	10.6	1.2	2.6	-0.3	1.0	3.0	-9.5	0.8	3.5
$\acute{G}_{4,4}$	-18.1	0.8	0.6	19.2	0.5	0.9	-1.5	0.2	0.3
$\acute{G}_{4,5}$	-12.2	1.3	2.5	23.1	1.3	2.9	-2.9	0.7	6.3
$\acute{G}_{5,-6}$	-8.3	1.0	2.1	3.7	0.8	2.0	10.7	1.4	6.3
$\acute{G}_{5,-5}$	0.8	0.1	0.1	1.7	0.1	0.1	1.0	0.1	0.2
$\acute{G}_{5,-4}$	3.4	0.1	0.4	-2.1	0.1	0.4	0.4	0.1	0.2

TABLE D.2: $l > 0$ modes of the generalized gradients spectrum, for the two B_0 coil polarities ($\uparrow$ for $I = 11.25\,\text{mA}$ and $\downarrow$ for $I = -11.25\,\text{mA}$) and without the B_0 coil. These are normalized to first order gradients $\acute{G}_{lm} = D_l^{l-1} G_{lm}$ with the distances given in table 5.1, and given in units of fT/cm. In each configuration we give the average value over all sequences μ, the average repeatability inside a sequence τ, and the reproducibility between sequences σ.

(fT/cm)	$\uparrow \mu$	$\uparrow \tau$	$\uparrow \sigma$	$\downarrow \mu$	$\downarrow \tau$	$\downarrow \sigma$	bare μ	bare τ	bare σ
$\acute{G}_{5,-3}$	-2.4	0.2	0.6	1.8	0.2	0.7	-2.3	0.2	0.9
$\acute{G}_{5,-2}$	4.3	0.3	1.0	2.1	0.2	1.4	-0.4	0.4	0.2
$\acute{G}_{5,-1}$	0.0	1.1	3.1	-16.7	0.6	5.3	2.0	1.2	2.2
$\acute{G}_{5,0}$	-74.8	3.0	6.5	77.0	6.0	5.4	1.0	2.9	1.7
$\acute{G}_{5,1}$	16.8	1.3	4.5	-48.7	1.2	3.4	-7.1	1.2	1.6
$\acute{G}_{5,2}$	-15.4	0.7	0.9	13.3	0.4	1.2	0.5	0.3	1.0
$\acute{G}_{5,3}$	0.0	0.4	0.5	-3.6	0.3	0.4	0.9	0.4	0.5
$\acute{G}_{5,4}$	-8.2	0.3	0.2	8.8	0.1	0.1	0.2	0.1	0.2
$\acute{G}_{5,5}$	-3.8	0.2	0.2	-4.8	0.1	0.2	-3.8	0.1	0.3
$\acute{G}_{5,6}$	-2.4	0.3	1.2	4.7	0.3	0.8	4.2	0.6	2.5
$\acute{G}_{6,-7}$	-8.6	0.4	0.9	5.7	0.5	1.2	5.7	0.7	3.0
$\acute{G}_{6,-6}$	-1.3	0.2	0.6	-4.9	0.2	0.8	-3.3	0.3	0.5
$\acute{G}_{6,-5}$	-1.6	0.1	0.1	0.6	0.0	0.1	-0.7	0.1	0.1
$\acute{G}_{6,-4}$	0.2	0.3	0.4	-0.4	0.2	0.3	1.4	0.2	0.5
$\acute{G}_{6,-3}$	0.6	0.2	0.2	2.9	0.2	0.3	2.4	0.2	0.6
$\acute{G}_{6,-2}$	-5.6	1.4	2.2	0.4	1.3	2.2	4.9	1.5	2.5
$\acute{G}_{6,-1}$	0.9	0.9	2.3	-5.3	0.7	1.6	-6.9	1.2	1.6
$\acute{G}_{6,0}$	-87.4	5.7	4.2	101.9	4.5	16.1	-9.9	4.1	1.3
$\acute{G}_{6,1}$	15.9	1.2	1.8	4.3	0.7	2.1	2.2	0.8	2.0
$\acute{G}_{6,2}$	10.3	0.8	0.8	-12.3	0.4	1.1	-3.9	0.2	0.5
$\acute{G}_{6,3}$	-1.5	0.3	0.9	-2.6	0.2	1.1	-4.4	0.2	0.7
$\acute{G}_{6,4}$	-0.5	0.3	0.3	1.7	0.2	0.1	1.6	0.1	0.3
$\acute{G}_{6,5}$	2.0	0.1	0.3	-0.2	0.1	0.3	0.0	0.1	0.1
$\acute{G}_{6,6}$	-6.4	0.2	0.4	6.5	0.2	0.4	0.7	0.2	0.4
$\acute{G}_{6,7}$	-4.4	0.7	1.9	1.5	0.3	0.9	-4.6	0.6	2.1
$\acute{G}_{7,-8}$	-2.7	0.1	0.3	-0.4	0.0	0.2	-2.0	0.1	0.1
$\acute{G}_{7,-7}$	0.1	0.0	0.0	0.3	0.0	0.0	0.4	0.0	0.1
$\acute{G}_{7,-6}$	0.1	0.0	0.1	0.0	0.0	0.1	-0.2	0.0	0.1
$\acute{G}_{7,-5}$	-0.1	0.0	0.0	-0.1	0.0	0.0	-0.1	0.0	0.0
$\acute{G}_{7,-4}$	0.4	0.0	0.1	0.3	0.0	0.1	0.7	0.0	0.2
$\acute{G}_{7,-3}$	-0.1	0.0	0.0	0.3	0.0	0.1	0.0	0.0	0.1
$\acute{G}_{7,-2}$	0.4	0.1	0.4	0.1	0.1	0.4	-1.0	0.1	0.2
$\acute{G}_{7,-1}$	0.4	0.1	0.4	-2.5	0.1	0.8	0.2	0.2	0.4
$\acute{G}_{7,0}$	-2.8	0.5	0.8	4.0	1.1	1.6	2.3	0.9	0.2
$\acute{G}_{7,1}$	2.9	0.1	0.4	-4.7	0.3	0.8	-0.9	0.1	0.1

TABLE D.2: $l > 0$ modes of the generalized gradients spectrum, for the two B_0 coil polarities ($\uparrow$ for $I = 11.25\,\mathrm{mA}$ and $\downarrow$ for $I = -11.25\,\mathrm{mA}$) and without the B_0 coil. These are normalized to first order gradients $\acute{G}_{lm} = D_l^{l-1} G_{lm}$ with the distances given in table 5.1, and given in units of fT/cm. In each configuration we give the average value over all sequences μ, the average repeatability inside a sequence τ, and the reproducibility between sequences σ.

(fT/cm)	$\uparrow \mu$	$\uparrow \tau$	$\uparrow \sigma$	$\downarrow \mu$	$\downarrow \tau$	$\downarrow \sigma$	bare μ	bare τ	bare σ
$\acute{G}_{7,2}$	-1.6	0.1	0.2	0.0	0.2	0.1	-0.5	0.1	0.1
$\acute{G}_{7,3}$	0.0	0.1	0.1	-0.8	0.1	0.2	-0.4	0.1	0.1
$\acute{G}_{7,4}$	-0.1	0.0	0.1	0.7	0.1	0.1	0.4	0.0	0.1
$\acute{G}_{7,5}$	0.1	0.0	0.0	0.2	0.0	0.0	0.2	0.0	0.0
$\acute{G}_{7,6}$	-0.1	0.0	0.0	0.1	0.0	0.0	-0.0	0.0	0.0
$\acute{G}_{7,7}$	-0.2	0.0	0.1	-0.5	0.0	0.1	-0.5	0.1	0.1
$\acute{G}_{7,8}$	-0.8	0.1	0.2	0.9	0.0	0.1	-0.2	0.0	0.1

FIGURE D.1: Harmonic spectrum of the n2EDM magnetic field, for two polarities of the B_0 coil ($I = \pm 11.25\,\mathrm{mA}$).

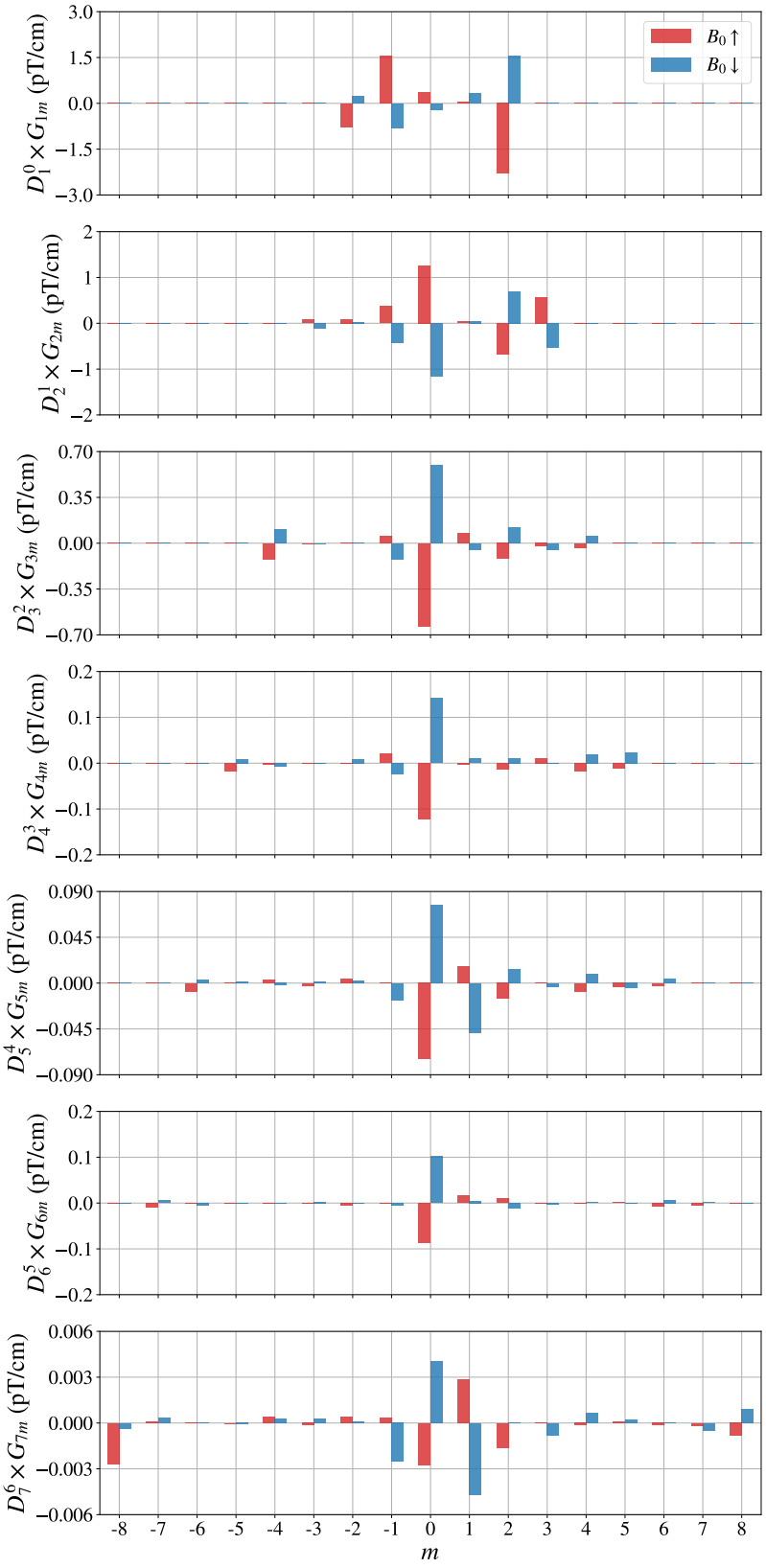

D.2 Optimized B_0 field

The mapping results of the optimized B_0 field, also recorded in January 2023, are presented in the following tables. The optimized coil configuration was obtained by setting all coil currents to the values given in figure D.3.

TABLE D.3: Uniform modes of the optimized generalized gradient spectrum, given in pT, for the two B_0 coil polarities ($\uparrow$ for $I = 11.25\,\text{mA}$ and $\downarrow$ for $I = -11.25\,\text{mA}$) and without the B_0 coil (bare). In this optimized setup, the trim coils and gradient coils are turned on in addition to the B_0 coil, with currents specified in figure D.3. In each configuration we give the average value over all sequences μ, the average repeatability inside a sequence τ, and the reproducibility between sequences σ.

(pT)	$\uparrow \mu$	$\uparrow \tau$	$\uparrow \sigma$	$\downarrow \mu$	$\downarrow \tau$	$\downarrow \sigma$	bare μ	bare τ	bare σ
$G_{0,-1}$	1539.4	7.4	7.3	-1504.4	7.2	17.0	10.1	6.9	18.6
$G_{0,0}$	939941.1	22.2	700.1	-939886.7	28.7	700.0	22.8	7.0	7.9
$G_{0,1}$	-135.2	12.6	53.5	264.6	11.1	40.8	-72.9	9.3	43.5

TABLE D.4: $l > 0$ modes of the optimized generalized gradients spectrum, for the two B_0 coil polarities ($\uparrow$ for $I = 11.25\,\text{mA}$ and $\downarrow$ for $I = -11.25\,\text{mA}$) and without the B_0 coil. These are normalized to first order gradients $\acute{G}_{lm} = D_l^{l-1} G_{lm}$ with the distances given in table 5.1, and given in units of fT/cm. In this optimized setup, the trim coils and gradient coils are turned on in addition to the B_0 coil, with currents specified in figure D.3. In each configuration we give the average value over all sequences μ, the average repeatability inside a sequence τ, and the reproducibility between sequences σ.

(fT/cm)	$\uparrow \mu$	$\uparrow \tau$	$\uparrow \sigma$	$\downarrow \mu$	$\downarrow \tau$	$\downarrow \sigma$	bare μ	bare τ	bare σ
$G_{1,-2}$	-709.2	199.9	573.3	874.1	135.2	470.6	-2395.0	248.6	990.5
$G_{1,-1}$	1326.2	99.3	122.9	-695.9	72.7	139.5	-240.0	53.8	82.3
$G_{1,0}$	49.4	79.2	254.8	-142.3	106.1	319.4	-646.1	140.6	252.6
$G_{1,1}$	353.4	64.5	218.8	86.1	39.1	410.7	700.6	82.2	294.2
$G_{1,2}$	-3051.4	56.7	232.9	1931.7	129.5	217.6	0.3	52.3	262.1
$G_{2,-3}$	185.3	18.3	44.8	-224.9	17.3	45.8	44.4	12.8	36.4
$G_{2,-2}$	10.8	14.7	42.6	102.4	16.4	53.2	90.8	11.1	17.6
$G_{2,-1}$	310.6	19.2	24.4	-356.5	18.1	26.6	-109.0	9.5	43.2
$G_{2,0}$	85.7	26.4	50.9	38.1	23.6	146.4	-71.2	22.6	24.8
$G_{2,1}$	32.1	7.3	37.2	47.2	14.0	18.2	72.8	7.4	45.8
$G_{2,2}$	47.8	9.5	12.9	-12.5	5.3	15.2	-79.5	6.0	39.6
$G_{2,3}$	533.8	13.9	53.2	-479.5	11.6	47.6	1.3	5.4	46.8
$G_{3,-4}$	-125.2	2.4	11.7	109.9	3.6	10.9	-54.9	3.3	15.9
$G_{3,-3}$	-7.6	1.7	3.2	0.7	1.0	3.5	-12.9	1.5	5.6
$G_{3,-2}$	-5.8	1.9	3.0	8.9	0.9	4.6	-9.9	2.4	10.5
$G_{3,-1}$	51.2	4.3	11.8	-126.7	3.7	13.5	-18.6	3.8	5.9
$G_{3,0}$	-17.7	7.4	22.2	-22.7	17.1	18.5	-7.2	7.8	6.2

TABLE D.4: $l > 0$ modes of the optimized generalized gradients spectrum, for the two B_0 coil polarities ($\uparrow$ for $I = 11.25\,\text{mA}$ and $\downarrow$ for $I = -11.25\,\text{mA}$) and without the B_0 coil. These are normalized to first order gradients $\acute{G}_{lm} = D_l^{l-1} G_{lm}$ with the distances given in table 5.1, and given in units of fT/cm. In this optimized setup, the trim coils and gradient coils are turned on in addition to the B_0 coil, with currents specified in figure D.3. In each configuration we give the average value over all sequences μ, the average repeatability inside a sequence τ, and the reproducibility between sequences σ.

(fT/cm)	$\uparrow \mu$	$\uparrow \tau$	$\uparrow \sigma$	$\downarrow \mu$	$\downarrow \tau$	$\downarrow \sigma$	bare μ	bare τ	bare σ
$G_{3,1}$	63.6	3.0	10.8	-55.0	2.0	11.5	32.9	4.6	5.8
$G_{3,2}$	-140.8	1.3	4.2	135.9	2.3	3.4	-0.6	1.0	4.5
$G_{3,3}$	-37.9	4.0	7.0	-55.7	3.5	4.8	-2.3	3.4	5.8
$G_{3,4}$	-19.6	2.9	13.8	36.4	4.3	9.9	15.3	3.0	9.9
$G_{4,-5}$	-18.6	0.9	2.6	5.5	1.2	2.4	10.4	1.2	5.9
$G_{4,-4}$	-1.8	0.6	0.8	-8.8	0.7	1.6	-0.5	0.7	1.2
$G_{4,-3}$	4.9	0.3	0.7	-8.4	0.2	0.5	-0.7	0.3	1.3
$G_{4,-2}$	-8.4	0.6	1.7	18.9	0.8	3.0	10.8	1.0	3.6
$G_{4,-1}$	36.5	1.7	6.8	-29.5	1.5	4.0	-19.7	2.6	4.7
$G_{4,0}$	-82.0	6.5	18.2	85.7	7.2	21.2	0.2	4.7	2.8
$G_{4,1}$	-1.6	2.2	6.2	23.9	1.3	5.3	-15.3	1.4	5.2
$G_{4,2}$	94.4	1.1	2.1	-95.8	0.9	2.3	-4.4	0.3	1.4
$G_{4,3}$	10.0	1.2	2.6	6.7	1.0	3.0	-9.5	0.8	3.5
$G_{4,4}$	-13.3	0.8	0.6	17.0	0.5	0.9	-1.5	0.2	0.3
$G_{4,5}$	-15.2	1.3	2.5	30.2	1.3	2.9	-2.9	0.7	6.3
$G_{5,-6}$	-5.4	1.0	2.1	-2.3	0.8	2.0	10.7	1.4	6.3
$G_{5,-5}$	2.0	0.1	0.1	0.9	0.1	0.1	1.0	0.1	0.2
$G_{5,-4}$	3.2	0.1	0.4	-1.2	0.1	0.4	0.4	0.1	0.2
$G_{5,-3}$	-2.4	0.2	0.6	2.0	0.2	0.7	-2.3	0.2	0.9
$G_{5,-2}$	3.2	0.3	1.0	5.6	0.2	1.4	-0.4	0.4	0.2
$G_{5,-1}$	0.4	1.1	3.1	-19.9	0.6	5.3	2.0	1.2	2.2
$G_{5,0}$	5.1	3.0	6.5	3.5	6.0	5.4	1.0	2.9	1.7
$G_{5,1}$	12.2	1.3	4.5	-47.4	1.2	3.4	-7.1	1.2	1.6
$G_{5,2}$	-12.3	0.7	0.9	9.2	0.4	1.2	0.5	0.3	1.0
$G_{5,3}$	-2.2	0.4	0.5	-5.1	0.3	0.4	0.9	0.4	0.5
$G_{5,4}$	-6.9	0.3	0.2	7.3	0.1	0.1	0.2	0.1	0.2
$G_{5,5}$	-3.7	0.2	0.2	-4.4	0.1	0.2	-3.8	0.1	0.3
$G_{5,6}$	-3.3	0.3	1.2	5.4	0.3	0.8	4.2	0.6	2.5
$G_{6,-7}$	-6.2	0.4	0.9	1.2	0.5	1.2	5.7	0.7	3.0
$G_{6,-6}$	-1.6	0.2	0.6	-3.9	0.2	0.8	-3.3	0.3	0.5
$G_{6,-5}$	-2.2	0.1	0.1	1.9	0.0	0.1	-0.7	0.1	0.1
$G_{6,-4}$	-0.1	0.3	0.4	-1.3	0.2	0.3	1.4	0.2	0.5
$G_{6,-3}$	-0.5	0.2	0.2	3.1	0.2	0.3	2.4	0.2	0.6
$G_{6,-2}$	-7.1	1.4	2.2	-4.2	1.3	2.2	4.9	1.5	2.5

TABLE D.4: $l > 0$ modes of the optimized generalized gradients spectrum, for the two B_0 coil polarities ($\uparrow$ for $I = 11.25\,\mathrm{mA}$ and $\downarrow$ for $I = -11.25\,\mathrm{mA}$) and without the B_0 coil. These are normalized to first order gradients $\acute{G}_{lm} = D_l^{l-1} G_{lm}$ with the distances given in table 5.1, and given in units of fT/cm. In this optimized setup, the trim coils and gradient coils are turned on in addition to the B_0 coil, with currents specified in figure D.3. In each configuration we give the average value over all sequences μ, the average repeatability inside a sequence τ, and the reproducibility between sequences σ.

(fT/cm)	$\uparrow \mu$	$\uparrow \tau$	$\uparrow \sigma$	$\downarrow \mu$	$\downarrow \tau$	$\downarrow \sigma$	bare μ	bare τ	bare σ
$G_{6,-1}$	1.2	0.9	2.3	-0.8	0.7	1.6	-6.9	1.2	1.6
$G_{6,0}$	-55.2	5.7	4.2	70.5	4.5	16.1	-9.9	4.1	1.3
$G_{6,1}$	16.0	1.2	1.8	6.1	0.7	2.1	2.2	0.8	2.0
$G_{6,2}$	27.0	0.8	0.8	-27.2	0.4	1.1	-3.9	0.2	0.5
$G_{6,3}$	-1.3	0.3	0.9	-1.3	0.2	1.1	-4.4	0.2	0.7
$G_{6,4}$	0.1	0.3	0.3	0.4	0.2	0.1	1.6	0.1	0.3
$G_{6,5}$	1.3	0.1	0.3	0.4	0.1	0.3	0.0	0.1	0.1
$G_{6,6}$	-4.9	0.2	0.4	5.3	0.2	0.4	0.7	0.2	0.4
$G_{6,7}$	-2.7	0.7	1.9	3.9	0.3	0.9	-4.6	0.6	2.1
$G_{7,-8}$	-2.3	0.1	0.3	-0.5	0.0	0.2	-2.0	0.1	0.1
$G_{7,-7}$	0.1	0.0	0.0	0.4	0.0	0.0	0.4	0.0	0.1
$G_{7,-6}$	0.1	0.0	0.1	0.1	0.0	0.1	-0.2	0.0	0.1
$G_{7,-5}$	-0.0	0.0	0.0	-0.1	0.0	0.0	-0.1	0.0	0.0
$G_{7,-4}$	0.3	0.0	0.1	0.2	0.0	0.1	0.7	0.0	0.2
$G_{7,-3}$	-0.0	0.0	0.0	0.2	0.0	0.1	0.0	0.0	0.1
$G_{7,-2}$	0.1	0.1	0.4	1.0	0.1	0.4	-1.0	0.1	0.2
$G_{7,-1}$	0.6	0.1	0.4	-3.3	0.1	0.8	0.2	0.2	0.4
$G_{7,0}$	2.4	0.5	0.8	0.2	1.1	1.6	2.3	0.9	0.2
$G_{7,1}$	2.8	0.1	0.4	-3.6	0.3	0.8	-0.9	0.1	0.1
$G_{7,2}$	-1.5	0.1	0.2	-0.3	0.2	0.1	-0.5	0.1	0.1
$G_{7,3}$	-0.3	0.1	0.1	-0.7	0.1	0.2	-0.4	0.1	0.1
$G_{7,4}$	0.1	0.0	0.1	0.4	0.1	0.1	0.4	0.0	0.1
$G_{7,5}$	0.1	0.0	0.0	0.2	0.0	0.0	0.2	0.0	0.0
$G_{7,6}$	-0.2	0.0	0.0	0.2	0.0	0.0	-0.0	0.0	0.0
$G_{7,7}$	-0.2	0.0	0.1	-0.2	0.0	0.1	-0.5	0.1	0.1
$G_{7,8}$	-1.3	0.1	0.2	1.5	0.0	0.1	-0.2	0.0	0.1

FIGURE D.2: Harmonic spectrum of the optimized n2EDM magnetic field. In this case the B_0 coil as well as the trim coils and gradient coils are turned on, for the two coil polarities ($I = 11.25\,\mathrm{mA}$). The optimizing coil currents used to achieve this field are given in figure D.3.

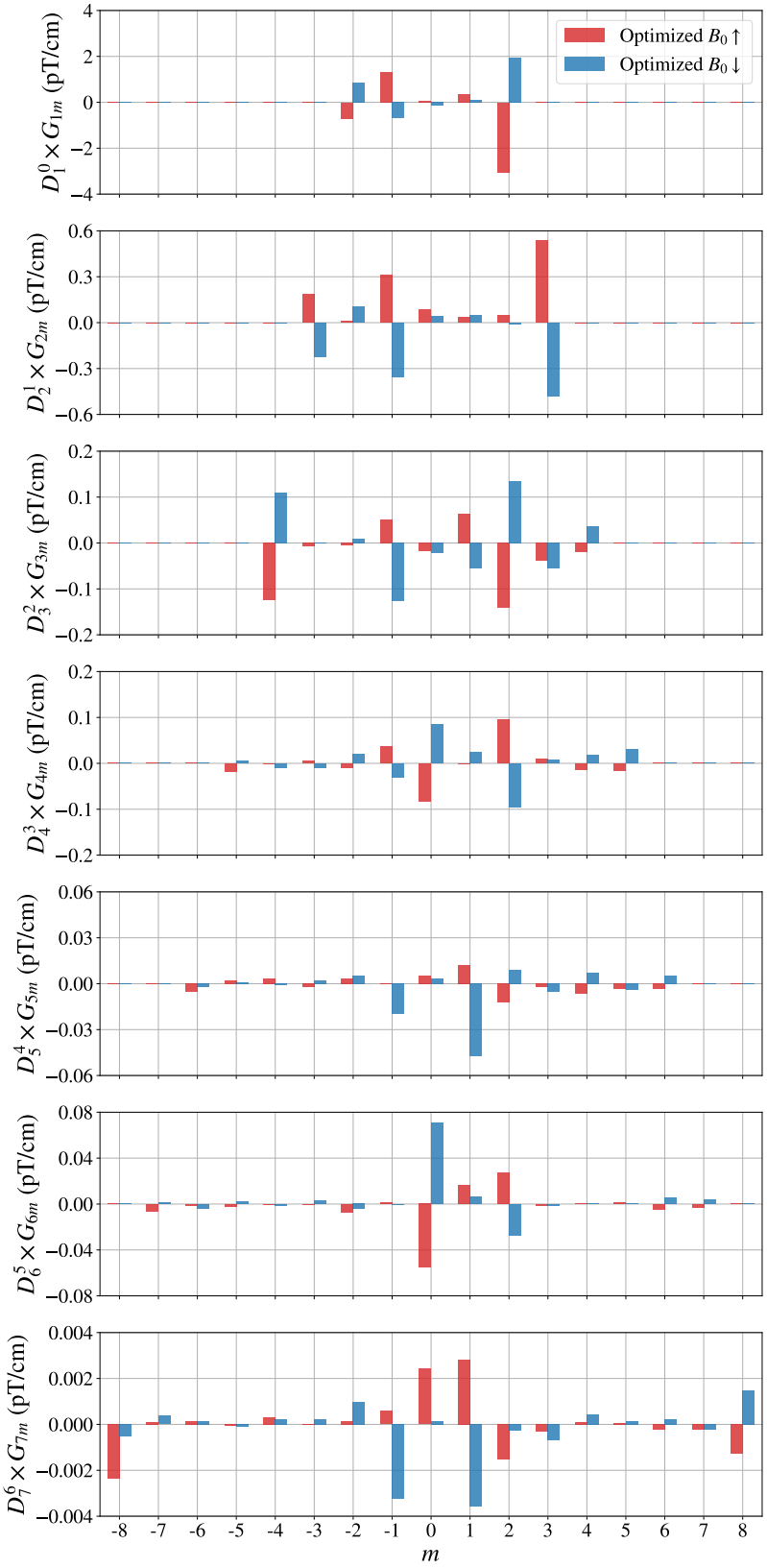

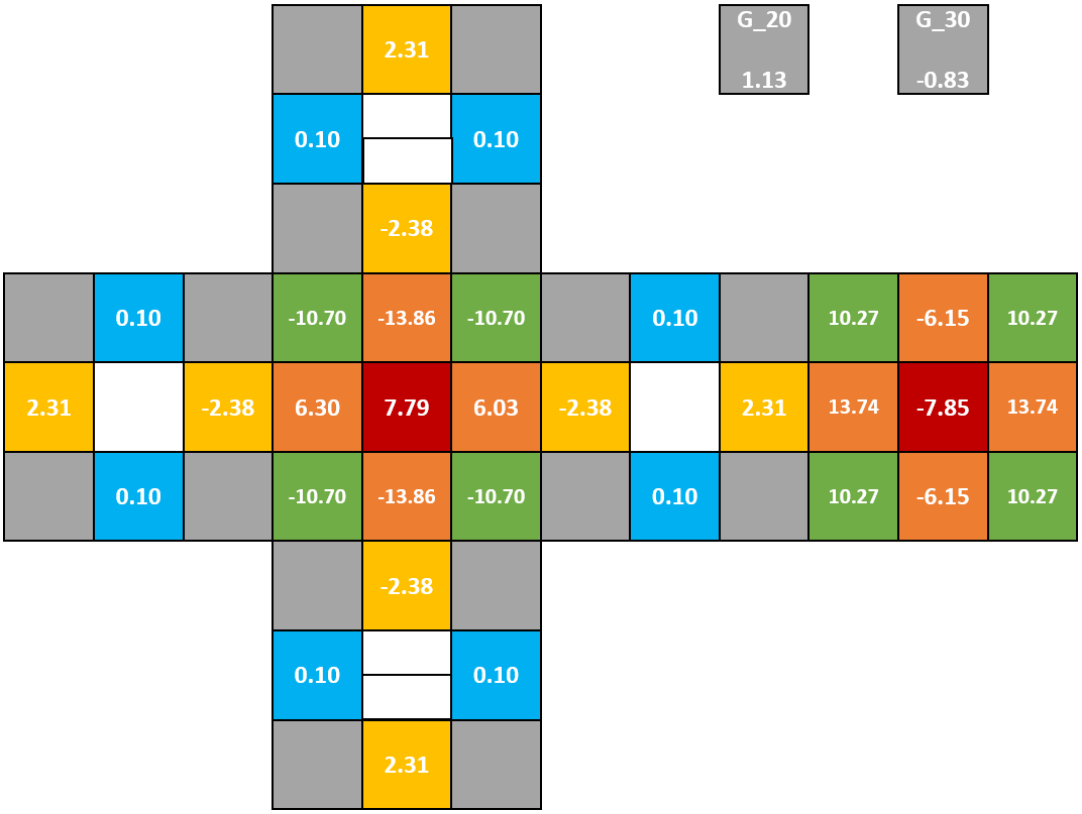

FIGURE D.3: Currents (in mA) applied to the trim coils and gradient coils in order to cancel harmonic gradients $G_{20}, G_{22}, G_{30}, G_{50}$ of the B_0 field spectrum in the negative polarity. Currents for the positive B_0 polarity can be obtained by reversing the signs of these currents.

Bibliography

(N.d.[b]). URL: https://gitlab.in2p3.fr/NEDM/tomat.

(N.d.[c]). Bartington Instruments Ltd, Thorney Leys Park Witney OX28 4GE, United Kingdom.

(N.d.[d]). URL: https://github.com/bouillaud/n2edm_mapping.

Abel, C. et al. (Apr. 2019). "Magnetic-field uniformity in neutron electric-dipole-moment experiments". In: *Phys. Rev. A* 99 (4), p. 042112. DOI: 10.1103/PhysRevA.99.042112. URL: https://link.aps.org/doi/10.1103/PhysRevA.99.042112.

Abel, C. et al. (Feb. 2020). "Measurement of the Permanent Electric Dipole Moment of the Neutron". In: *Phys. Rev. Lett.* 124 (8), p. 081803. DOI: 10.1103/PhysRevLett.124.081803. URL: https://link.aps.org/doi/10.1103/PhysRevLett.124.081803.

Abel, C. et al. (Sept. 2022). "Mapping of the magnetic field to correct systematic effects in a neutron electric dipole moment experiment". In: *Physical Review A* 106.3. DOI: 10.1103/physreva.106.032808. URL: https://doi.org/10.1103/PhysRevA.106.032808.

Afach, S. et al. (Oct. 2015). "Measurement of a false electric dipole moment signal from 199Hg atoms exposed to an inhomogeneous magnetic field". In: *The European Physical Journal D* 69.10, p. 225. ISSN: 1434-6079. DOI: 10.1140/epjd/e2015-60207-4. URL: https://doi.org/10.1140/epjd/e2015-60207-4.

Aghanim, N. et al. (Sept. 2020). "Planck 2018 results". In: *Astronomy and Astrophysics* 641, A6. DOI: 10.1051/0004-6361/201833910. URL: https://doi.org/10.1051/0004-6361/201833910.

Ahmed, M.W. et al. (Nov. 2019). "A new cryogenic apparatus to search for the neutron electric dipole moment". In: *Journal of Instrumentation* 14.11, P11017. DOI: 10.1088/1748-0221/14/11/P11017. URL: https://dx.doi.org/10.1088/1748-0221/14/11/P11017.

al., N.J. Ayres et (2022). "The design of the n2EDM experiment". In: *European Physics Journal C* 81.512. DOI: https://doi.org/10.1140/epjc/s10052-021-09298-z.

Altarev, I. et al. (June 2015). "Minimizing magnetic fields for precision experiments". In: *Journal of Applied Physics* 117.23, p. 233903. ISSN: 0021-8979. DOI: 10.1063/1.4922671. eprint: https://pubs.aip.org/aip/jap/article-pdf/doi/10.1063/1.4922671/15164164/233903_1_online.pdf. URL: https://doi.org/10.1063/1.4922671.

Altarev, I.S. et al. (1980). "A search for the electric dipole moment of the neutron using ultracold neutrons". In: *Nuclear Physics A* 341.2, pp. 269–283. ISSN: 0375-9474. DOI: https://doi.org/10.1016/0375-9474(80)90313-9. URL: https://www.sciencedirect.com/science/article/pii/0375947480903139.

Ayres, N. J. et al. (Sept. 2022). "The very large n2EDM magnetically shielded room with an exceptional performance for fundamental physics measurements". In: *Review of Scientific Instruments* 93.9, p. 095105. DOI: 10.1063/5.0101391. URL: https://doi.org/10.1063/5.0101391.

Baker, C. A. et al. (Sept. 2006). "Improved Experimental Limit on the Electric Dipole Moment of the Neutron". In: *Phys. Rev. Lett.* 97 (13), p. 131801. DOI: 10.1103/

PhysRevLett.97.131801. URL: https://link.aps.org/doi/10.1103/PhysRevLett.97.131801.

Barabanov, A. L., R. Golub, and S. K. Lamoreaux (Nov. 2006). "Electric dipole moment searches: Effect of linear electric field frequency shifts induced in confined gases". In: *Phys. Rev. A* 74 (5), p. 052115. DOI: 10.1103/PhysRevA.74.052115. URL: https://link.aps.org/doi/10.1103/PhysRevA.74.052115.

Bhattacharya, Tanmoy et al. (Nov. 2015). "Neutron Electric Dipole Moment and Tensor Charges from Lattice QCD". In: *Phys. Rev. Lett.* 115 (21), p. 212002. DOI: 10.1103/PhysRevLett.115.212002. URL: https://link.aps.org/doi/10.1103/PhysRevLett.115.212002.

Bhattacharya, Tanmoy et al. (June 2021a). "Contribution of the QCD term to the nucleon electric dipole moment". In: *Physical Review D* 103.11. DOI: 10.1103/physrevd.103.114507. URL: https://doi.org/10.1103/physrevd.103.114507.

— (June 2021b). "Contribution of the QCD theta-term to the nucleon electric dipole moment". In: *Phys. Rev. D* 103 (11), p. 114507. DOI: 10.1103/PhysRevD.103.114507. URL: https://link.aps.org/doi/10.1103/PhysRevD.103.114507.

Chanel, Estelle et al. (2019). "The pulsed neutron beam EDM experiment". In: *EPJ Web Conf.* 219, p. 02004. DOI: 10.1051/epjconf/201921902004. URL: https://doi.org/10.1051/epjconf/201921902004.

Chiu, Pin-Jung (2021). "Search for a New Interaction Mediated by Axionlike Particles". PhD thesis. Zurich, ETH. DOI: 10.3929/ethz-b-000509133.

Chupp, Timothy and Michael Ramsey-Musolf (Mar. 2015). "Electric dipole moments: A global analysis". In: *Phys. Rev. C* 91 (3), p. 035502. DOI: 10.1103/PhysRevC.91.035502. URL: https://link.aps.org/doi/10.1103/PhysRevC.91.035502.

Clayton, Steven M. (2011). "Spin relaxation and linear-in-electric-field frequency shift in an arbitrary, time-independent magnetic field". In: *Journal of Magnetic Resonance* 211.1, pp. 89–95. ISSN: 1090-7807. DOI: https://doi.org/10.1016/j.jmr.2011.04.008. URL: https://www.sciencedirect.com/science/article/pii/S1090780711001418.

Cline, James M. (2007). "Course 2 - Baryogenesis". In: *Particle Physics and Cosmology: The Fabric of Spacetime*. Ed. by Francis Bernardeau, Christophe Grojean, and Jean Dalibard. Vol. 86. Les Houches. Elsevier, pp. 53–116. DOI: https://doi.org/10.1016/S0924-8099(07)80028-X. URL: https://www.sciencedirect.com/science/article/pii/S092480990780028X.

Demir, Durmu, Maxim Pospelov, and Adam Ritz (Jan. 2003). "Hadronic electric dipole moments, the Weinberg operator, and light gluinos". In: *Phys. Rev. D* 67 (1), p. 015007. DOI: 10.1103/PhysRevD.67.015007. URL: https://link.aps.org/doi/10.1103/PhysRevD.67.015007.

Dragos, Jack et al. (Jan. 2021). "Confirming the existence of the strong CP problem in lattice QCD with the gradient flow". In: *Physical Review C* 103.1. DOI: 10.1103/physrevc.103.015202. URL: https://doi.org/10.1103/physrevc.103.015202.

Dress, W. B. et al. (Jan. 1977). "Search for an electric dipole moment of the neutron". In: *Phys. Rev. D* 15 (1), pp. 9–21. DOI: 10.1103/PhysRevD.15.9. URL: https://link.aps.org/doi/10.1103/PhysRevD.15.9.

Engel, Jonathan, Michael J. Ramsey-Musolf, and U. van Kolck (2013). "Electric dipole moments of nucleons, nuclei, and atoms: The Standard Model and beyond". In: *Progress in Particle and Nuclear Physics* 71. Fundamental Symmetries in the Era of the LHC, pp. 21–74. ISSN: 0146-6410. DOI: https://doi.org/10.1016/j.ppnp.2013.03.003. URL: https://www.sciencedirect.com/science/article/pii/S0146641013000227.

Ferraris-Bouchez, Laura (June 2020). "Mesure du moment dipolaire electrique du neutron : correction de l'effet systematique du champ fantome". Theses. Universite Grenoble Alpes [2020-....] URL: https://theses.hal.science/tel-03130525.

Flaux, Pierrick (Oct. 2019). "Measurement of the neutron electric dipole moment at the Paul Scherrer Institute : production of magnetic fields". Theses. Normandie Université. URL: https://theses.hal.science/tel-02409339.

Golub, R. et al. (Dec. 2015). "Geometric phases in electric dipole searches with trapped spin-1/2 particles in general fields and measurement cells of arbitrary shape with smooth or rough walls". In: *Phys. Rev. A* 92 (6), p. 062123. DOI: 10.1103/PhysRevA.92.062123. URL: https://link.aps.org/doi/10.1103/PhysRevA.92.062123.

Graner, B. et al. (Apr. 2016). "Reduced Limit on the Permanent Electric Dipole Moment of 199Hg". In: *Physical Review Letters* 116.16. DOI: 10.1103/physrevlett.116.161601. URL: https://doi.org/10.1103/physrevlett.116.161601.

Gupta, Rajan et al. (Nov. 2018). "Flavor diagonal tensor charges of the nucleon from $(2+1+1)$-flavor lattice QCD". In: *Phys. Rev. D* 98 (9), p. 091501. DOI: 10.1103/PhysRevD.98.091501. URL: https://link.aps.org/doi/10.1103/PhysRevD.98.091501.

Hisano, Junji et al. (June 2012). "Reevaluation of neutron electric dipole moment with QCD sum rules". In: *Phys. Rev. D* 85 (11), p. 114044. DOI: 10.1103/PhysRevD.85.114044. URL: https://link.aps.org/doi/10.1103/PhysRevD.85.114044.

Huet, Patrick and Eric Sather (1995). "Electroweak baryogenesis and standard model CP violation". In: *Phys. Rev. D* 51, pp. 379–394. DOI: 10.1103/PhysRevD.51.379. arXiv: hep-ph/9404302.

Ito, T. M. et al. (Jan. 2018). "Performance of the upgraded ultracold neutron source at Los Alamos National Laboratory and its implication for a possible neutron electric dipole moment experiment". In: *Phys. Rev. C* 97 (1), p. 012501. DOI: 10.1103/PhysRevC.97.012501. URL: https://link.aps.org/doi/10.1103/PhysRevC.97.012501.

Khintchine, A. (Dec. 1934). "Korrelationstheorie der stationaren stochastischen Prozesse". In: *Mathematische Annalen* 109.1, pp. 604–615. ISSN: 1432-1807. DOI: 10.1007/BF01449156. URL: https://doi.org/10.1007/BF01449156.

Kirch, Klaus and Bernhard Lauss (2020). "Ultracold Neutrons". In: DOI: 10.48550/ARXIV.2006.04568. URL: https://arxiv.org/abs/2006.04568.

Kobayashi, Makoto and Toshihide Maskawa (Feb. 1973). "CP-Violation in the Renormalizable Theory of Weak Interaction". In: *Progress of Theoretical Physics* 49.2, pp. 652–657. ISSN: 0033-068X. DOI: 10.1143/PTP.49.652. eprint: https://academic.oup.com/ptp/article-pdf/49/2/652/5257692/49-2-652.pdf. URL: https://doi.org/10.1143/PTP.49.652.

Lamoreaux, S. K. (June 1996). "Additional motional-magnetic-field considerations for electric-dipole-moment experiments". In: *Phys. Rev. A* 53 (6), R3705–R3708. DOI: 10.1103/PhysRevA.53.R3705. URL: https://link.aps.org/doi/10.1103/PhysRevA.53.R3705.

Lamoreaux, S. K. and R. Golub (Mar. 2005). "Detailed discussion of a linear electric field frequency shift induced in confined gases by a magnetic field gradient: Implications for neutron electric-dipole-moment experiments". In: *Phys. Rev. A* 71 (3), p. 032104. DOI: 10.1103/PhysRevA.71.032104. URL: https://link.aps.org/doi/10.1103/PhysRevA.71.032104.

Lebedev, Oleg et al. (July 2004). "Probing CP violation with the deuteron electric dipole moment". In: *Phys. Rev. D* 70 (1), p. 016003. DOI: 10.1103/PhysRevD.70.016003. URL: https://link.aps.org/doi/10.1103/PhysRevD.70.016003.

Morrissey, David E and Michael J Ramsey-Musolf (Dec. 2012). "Electroweak baryogenesis". In: *New Journal of Physics* 14.12, p. 125003. DOI: 10.1088/1367-2630/14/12/125003. URL: https://doi.org/10.1088/1367-2630/14/12/125003.

Pais, Duarte (2021). "Development of the caesium magnetometer array for the n2EDM experiment". en. Doctoral Thesis. Zurich: ETH Zurich. DOI: 10.3929/ethz-b-000511496.

Papoulis, Athanasios and S. Unnikrishna Pillai (2002). *Probability, Random Variables, and Stochastic Processes*. Fourth. McGraw Hill.

Particle Physics Preparatory Group, European Strategy for (2020). *Physics Briefing Book*. arXiv: 1910.11775 [hep-ex].

Pendlebury, J. M. et al. (Sept. 2004). "Geometric-phase-induced false electric dipole moment signals for particles in traps". In: *Phys. Rev. A* 70 (3), p. 032102. DOI: 10.1103/PhysRevA.70.032102. URL: https://link.aps.org/doi/10.1103/PhysRevA.70.032102.

Picker, Ruediger (n.d.). "How the Minuscule Can Contribute to the Big Picture: The Neutron Electric Dipole Moment Project at TRIUMF". In: *Proceedings of the 14th International Conference on Meson-Nucleon Physics and the Structure of the Nucleon (MENU2016)*. DOI: 10.7566/JPSCP.13.010005. eprint: https://journals.jps.jp/doi/pdf/10.7566/JPSCP.13.010005. URL: https://journals.jps.jp/doi/abs/10.7566/JPSCP.13.010005.

Pignol, G. et al. (Nov. 2015). "Frequency shifts and relaxation rates for spin-1/2 particles moving in electromagnetic fields". In: *Phys. Rev. A* 92 (5), p. 053407. DOI: 10.1103/PhysRevA.92.053407. URL: https://link.aps.org/doi/10.1103/PhysRevA.92.053407.

Pignol, Guillaume (Aug. 2015). "Probing Dark Energy models with neutrons". In: *International Journal of Modern Physics A* 30.24, p. 1530048. DOI: 10.1142/s0217751x15300483. URL: https://doi.org/10.1142/s0217751x15300483.

— (2019). "A magic magnetic field to measure the neutron electric dipole moment". In: *Physics Letters B* 793, pp. 440–444. ISSN: 0370-2693. DOI: https://doi.org/10.1016/j.physletb.2019.05.014. URL: https://www.sciencedirect.com/science/article/pii/S0370269319303235.

Pignol, Guillaume and Stéphanie Roccia (Apr. 2012). "Electric-dipole-moment searches: Reexamination of frequency shifts for particles in traps". In: *Phys. Rev. A* 85 (4), p. 042105. DOI: 10.1103/PhysRevA.85.042105. URL: https://link.aps.org/doi/10.1103/PhysRevA.85.042105.

Pospelov, Maxim and Adam Ritz (Mar. 2001). "Neutron electric dipole moment from electric and chromoelectric dipole moments of quarks". In: *Phys. Rev. D* 63 (7), p. 073015. DOI: 10.1103/PhysRevD.63.073015. URL: https://link.aps.org/doi/10.1103/PhysRevD.63.073015.

— (2005). "Electric dipole moments as probes of new physics". In: *Annals of Physics* 318.1. Special Issue, pp. 119–169. ISSN: 0003-4916. DOI: https://doi.org/10.1016/j.aop.2005.04.002. URL: https://www.sciencedirect.com/science/article/pii/S0003491605000539.

Purcell, E. M. and N. F. Ramsey (June 1950). "On the Possibility of Electric Dipole Moments for Elementary Particles and Nuclei". In: *Phys. Rev.* 78 (6), pp. 807–807. DOI: 10.1103/PhysRev.78.807. URL: https://link.aps.org/doi/10.1103/PhysRev.78.807.

Ramsey, Norman F. (June 1950). "A Molecular Beam Resonance Method with Separated Oscillating Fields". In: *Phys. Rev.* 78 (6), pp. 695–699. DOI: 10.1103/PhysRev.78.695. URL: https://link.aps.org/doi/10.1103/PhysRev.78.695.

Rawlik, Michał (2018). "Active Magnetic Shielding and Axion-Dark-Matter Search". en. Doctoral Thesis. Zurich: ETH Zurich. DOI: 10.3929/ethz-b-000273039.

Redfield, A. G. (1957). "On the Theory of Relaxation Processes". In: *IBM Journal of Research and Development* 1.1, pp. 19–31. DOI: 10.1147/rd.11.0019.

Saenz, William (Dec. 2022). "Neutron to Hidden Neutron Oscillations in Ultra-Cold Neutron Beams". Theses. Normandie Université. URL: https://theses.hal.science/tel-04023774.

Sakharov, A. D. (1967). "Violation of CP Invariance, C asymmetry, and baryon asymmetry of the universe". In: *Pisma Zh. Eksp. Teor. Fiz.* 5, pp. 32–35. DOI: 10.1070/PU1991v034n05ABEH002497.

Smith, J. H., E. M. Purcell, and N. F. Ramsey (Oct. 1957). "Experimental Limit to the Electric Dipole Moment of the Neutron". In: *Phys. Rev.* 108 (1), pp. 120–122. DOI: 10.1103/PhysRev.108.120. URL: https://link.aps.org/doi/10.1103/PhysRev.108.120.

Swank, C. M., A. K. Petukhov, and R. Golub (June 2016). "Random walks with thermalizing collisions in bounded regions: Physical applications valid from the ballistic to diffusive regimes". In: *Phys. Rev. A* 93 (6), p. 062703. DOI: 10.1103/PhysRevA.93.062703. URL: https://link.aps.org/doi/10.1103/PhysRevA.93.062703.

Swank, C.M., A.K. Petukhov, and R. Golub (2012). "Correlation functions for restricted Brownian motion from the ballistic through to the diffusive regimes". In: *Physics Letters A* 376.34, pp. 2319–2324. ISSN: 0375-9601. DOI: https://doi.org/10.1016/j.physleta.2012.05.038. URL: https://www.sciencedirect.com/science/article/pii/S0375960112006330.

Thiel, F. et al. (Mar. 2007). "Demagnetization of magnetically shielded rooms". In: *Review of Scientific Instruments* 78.3, p. 035106. ISSN: 0034-6748. DOI: 10.1063/1.2713433. eprint: https://pubs.aip.org/aip/rsi/article-pdf/doi/10.1063/1.2713433/14005773/035106_1_online.pdf. URL: https://doi.org/10.1063/1.2713433.

Voigt, Jens et al. (2013). "Measures to reduce the residual field and field gradient inside a magnetically shielded room by a factor of more than 10". In: *Metrology and Measurement Systems* No 2, pp. 239–248. DOI: 10.2478/mms-2013-0021. URL: http://journals.pan.pl/Content/90119/PDF/Journal10178-VolumeXXIssue2_08.pdf.

Wiener, Norbert (1930). "Generalized harmonic analysis". In: *Acta Mathematica* 55.none, pp. 117 –258. DOI: 10.1007/BF02546511. URL: https://doi.org/10.1007/BF02546511.

Wu, C. S. et al. (Feb. 1957). "Experimental Test of Parity Conservation in Beta Decay". In: *Phys. Rev.* 105 (4), pp. 1413–1415. DOI: 10.1103/PhysRev.105.1413. URL: https://link.aps.org/doi/10.1103/PhysRev.105.1413.

Wurm, David et al. (2019). "The PanEDM neutron electric dipole moment experiment at the ILL". In: *EPJ Web Conf.* 219, p. 02006. DOI: 10.1051/epjconf/201921902006. URL: https://doi.org/10.1051/epjconf/201921902006.